5-8-2015

Metals on Titania/HOPG as Models for Heterogeneous Catalysts

Randima Piyumalie Galhenage
University of South Carolina - Columbia

METALS ON TITANIA/HOPG AS MODELS FOR HETEROGENEOUS CATALYSTS

by

Randima Piyumalie Galhenage

Bachelor of Science
Institute of Chemistry, Sri Lanka, 2008

Bachelor of Science
University of Colombo, Sri Lanka, 2009

Submitted in Partial Fulfillment of the Requirements

For the Degree of Doctor of Philosophy in

Chemistry

College of Arts and Sciences

University of South Carolina

2015

Accepted by:

Donna A. Chen, Major Professor

Michael L. Myrick , Chairman, Examining Committee

Ken D. Shimizu, Committee Member

John W. Weidner, Committee Member

Lacy Ford, Vice Provost and Dean of Graduate Studies

Dedication

This work is dedicated to my mother and father, Indrani Jinananda and Galhenage Jinananda, for their unconditional love and support.

Acknowledgements

I would like to express my gratitude to the people who were a great help to me throughout my Ph.D. First and foremost I would like to thank my research advisor, Prof. Donna Chen, for being such a wonderful mentor to me. All that time you spent to give me advice, to make everything a little bit better, for the effort you put to bring the best out of me are all really appreciated. I could not have asked for more and do not have enough words to express my gratitude, but I will promise to do my best at my next stop to protect the confidence you had in me. Then I would like to thank my committee members, Prof Michael Myrick, Prof. Ken Shimizu and Prof. John Weidner for all their advice for my graduate work.

Next, I would like to thank all the members of Chen group, past and present, Dr. Samuel Tenney, Dr. Hui Yan, Audrey Duke, Kangmin Xie, Mara Levine, Brett Cagg, Grant Seuser, Nhat Nagyun, Thathsara Maddumapatabandi, Amy Brandt and Tyler Hernandez. I am truly blessed to have such a wonderful group of people to work with. Then I want to acknowledge all the help given by Arthur Illingworth and Allen Frye in Machine Shop. They do miracles. Matt Roberts, Alex Skripnik and Dave Wynia from Omicron for all their support given to troubleshoot the problems I had with my UHV chamber. All the support I received from the wonderful faculty/staff members in the chemistry department is greatly appreciated. I acknowledge the funding agencies, DOE, NSF and USC for the ASPIRE grant for their funds to carry out the research in this thesis.

Then I want to thank all my friends here in US and back in Sri Lanka, for their constant love and support which helped me to get through difficult times. I thank Sahan for all his efforts and support given to me. Last but not least I thank my family for being there for me no matter what. I specially thank my parents for their unconditional love and support and for encouraging me to do what I am passionate about and keep having faith in me to make my own decisions.

Abstract

The work done in this thesis is mainly focused on understanding the nanoscale morphology and activity of model heterogeneous catalysts. In order to do this we design and prepare model catalytic surfaces in ultrahigh vacuum (UHV) and study these surfaces using electron and ion based microscopies and spectroscopies. The nucleation, growth and chemical activity of mono and bimetallic clusters on TiO_2(110) were investigated in order to understand how activity is influenced by cluster sizes, interactions with the oxide support and surface compositions of the bimetallic clusters. For example, Au-based and Pt-based bimetallic clusters such as Co-Au, Co-Pt, and Pt-Re were grown on titania and their activity for CO adsorption as well as methanol reaction were investigated. The nucleation and growth of these metals were found to be dependent upon the mobility of each metal on the titania surface. Furthermore, bimetallic clusters can be grown on the surface by taking advantage of the relative surface mobilities; when clusters of the less mobile metal are deposited first, the subsequent deposition of the second, more mobile metal results in nucleation exclusively at the existing seed clusters. Furthermore, bimetallic Pt-Ru clusters on highly oriented pyrolytic graphite (HOPG) have been studied as model systems for understanding direct methanol fuel cell catalysts. For Pt-Ru clusters deposited on powdered carbon supports, the novel electroless deposition (ED) method produces exclusively bimetallic clusters in contrast to the existing wet impregnation methods. The ED grown clusters were compared with clusters grown via vapor deposition by sequential deposition

of Pt on Ru seed clusters. For both ED and vapor deposition, exclusively bimetallic clusters were produced since the deposition of Pt did not result in the formation of new clusters. In addition to bimetallic clusters, we have also successfully synthesized MoS_2 clusters on titania to understand the structural changes that occurs in the presence of different reactant molecules since the activity of MoS_2 towards hydrodesulphurization type reactions is very sensitive to the structure of the clusters. What we have discovered was that these structures are very stable towards adsorption of MeOH, CO, H_2O and H_2 in UHV.

Table of contents

List of figures

List of tables

Chapter 1. Introduction

1.1 Introduction to catalysis

"There is probably no chemical reaction which cannot be influenced catalytically" - *Wilhelm Ostwald*

Catalysis is an action of a chemical substance (a catalyst) to increase the rate of a reaction towards a desired product. Homogeneous and heterogeneous catalysis are the two primary forms of catalysis. In homogeneous catalysis, the catalyst is in the same physical state as the reactants, and in heterogeneous catalysis, the catalyst and the reactants are in different physical states. Initial evidence of catalysis appeared when mankind began to produce alcohol by fermentation. In 1835, J. J. Berzelius introduced the term "catalysis" by systematic investigations of recorded observations.[1,2] Catalysts were used widely during World War I and World War II in producing materials like explosives and synthetic fuels. Since those early times catalysis has had major turning points and success including Nobel prizes and other significant achievements.[2]

In chemical industries reactions mainly occur at the surfaces of heterogeneous catalysts. There is a great deal of ongoing scientific research on heterogeneous catalysts in order to study the surfaces and thereby to gain a fundamental understanding of the nature of the reaction occuring at the surface. Understanding the basic aspects of complex industrial catalysts is rather difficult due to the nature of the complexity. For example, most industrial catalysts are supported metal clusters. A clear understanding of active sites, metal-support interfaces, and metal-metal interactions are therefore, harder to decouple to obtain a better structure-activity relationship. Financial benefits that can be gained by being able to design catalysts rationally are tremendous. Industrial catalytic materials most often have drawbacks in catalyst stability due to poisoning, and some of the materials are often

wasted due to the fact that the surfaces are not well-engineered to gain the best surface to volume ratio. To this date, the fundamental knowledge of catalysts is limited in order to rationally design catalysts with the knowledge of structure-activity relationship. Studying models of the complex catalytic systems is one approach to help the rational design of smarter catalysts.

1.2 Motivations and objectives

The research conducted in our laboratory is mainly focused on understanding bimetallic clusters on single crystal supports as models for heterogeneous catalysts. Bimetallic catalysts are known to exhibit enhanced activity compared to their monometallic counterparts.[3-10] Enhanced activity of bimetallic catalysts can be explained by bimetallic effects, namely bi-functional effects, electronic effects and ensemble effects. Bi-functional effects are present when the catalyst demonstrates the activity of both metals in the bimetallic form with no significant modification in activity. Bimetallic clusters that show different activity and selectivity compared to their monometallic counterparts due to electronic interactions are termed electronic effects. In some bimetallic systems geometric differences in the bimetallic forms act as altered active sites that either enhance the activity or change the selectivity. Most of the catalysts used today for energy generation type of reactions are bimetallic clusters on oxide supports. They are designed by trial and error fashion rather than by rational design. Most often therefore materials are wasted without having been used effectively. Our motivation is to design model systems in extremely controlled environments to understand the fundamental aspects such as structure-activity relationships to help the rational design of catalysts.

We have studied the growth of catalytically relevant metals such as Au, Ni, Co, Pt, Re and Ru on rutile TiO_2(110) and HOPG. The Co-Au bimetallic system is known to exhibit interesting catalytic properties, such as in Fisher-Tropsch reaction.[11,12] The Co-Au system has been studied as a part of larger study where Pt-Au and Ni-Au were also investigated as model catalysts for steam reforming type reactions.[13-15] An extended study of Au-based bimetallic systems was done with the motivation of designing model bimetallic catalysts for conversion of alcohols to H_2. In comparison to bulk immiscible bimetallic systems, i.e. Co-Au, the Co-Pt system, which is a bulk miscible bimetallic system, was studied. Co-Pt is known to have catalytic activity towards electro-oxidation of methanol in fuel cells.[16-19] The conventional Pt catalyst becomes poisoned by CO, which is a byproduct of the reaction.[20-23] Co is known to modify Pt sites so that Pt sites are less susceptible to poisoning by CO.[24,25] Similar effects have been seen in Pt-Re bimetallic systems as well. Pt-Re bimetallic clusters on titania were also studied as a model catalytic system for the aqueous reforming of alcohols. Addition of Re to Pt is believed to suppress poisoning by the CO byproduct, and the presence of Re oxides is also reported to play a role in enhanced activity for oxidation reactions.[26-30] The role of the second metal in these bimetallic systems on titania is not precisely known. Studying models of these catalytic systems could shed light on why these enhanced activity is observed in bimetallic catalysts. A Pt-Ru model system was prepared via electroless deposition (ED) method as a proof of principle study to investigate the design of models using industrially relevant methods. Carbon supported Pt-Ru catalysts have shown superior activity as anode catalysts compared to pure Pt for electro-oxidation of methanol in direct methanol fuel cells.[31-34] Similar to the bimetallic systems on titania, here also the second metal, Ru, is known to suppress the poisoning of

the Pt sites by CO.[35-38] In addition to bimetallic clusters, we have also successfully synthesized MoS_2 clusters on titania to understand the structural changes that occur in the presence of different reactant molecules. MoS_2 is use to catalyze hydrodesulphurization reactions.[39,40]

The nucleation, growth and chemical activity of mono and bimetallic clusters were investigated to understand how activity is influenced by cluster sizes, interactions with the oxide support and surface compositions of the bimetallic clusters. The metal-titania bond strength dictates how metals such as Co, Au, Pt, Ni and Re grow on titania. When the metal-titania bond strength is weak, the mobility of metals on titania is high. Au-titania has the lowest bond strength followed by Ni, Pt, Co, and Re. Therefore, Re shows the lowest mobility on titania, with smaller cluster sizes and higher cluster densities compared to more mobile metals such as Au, Ni, Pt and Co. Furthermore, we have discovered that the metal-titania bond strengths follow the same trend as the metal-oxygen bond strengths. Therefore, if metal-oxygen bond strengths are known, one can predict the growth of metals on titania. Exclusive formation of bimetallic clusters was achieved for Co-Au, Co-Pt, and Pt-Re on titania. Bimetallic clusters can be designed by taking advantage of the relative mobilities of metals, which involves deposition of the low mobile metal first followed by deposition of the more mobile metal second. For metals such as Pt and Co, where the relative mobilities are not drastically different, bimetallic clusters can be prepared in either order of deposition as long as the first deposition provides enough seed clusters to act as nucleation sites for the second metal. Sintering of clusters at higher temperatures was observed for metals in their monometallic and bimetallic forms.

Unlike titania, HOPG is an inert carbon support therefore, defect sites govern the nucleation density of metals on HOPG. Defect density was controlled by Ar^+ ion sputtering. Exclusive formation of Pt-Ru bimetallic clusters was achieved by depositing the first metal on modified HOPG followed by the deposition of the second metal. Both orders of deposition resulted in bimetallic clusters, provided that the initial deposition created enough seed clusters. Significant sintering takes place when mono/bimetallic clusters on HOPG are heated to temperatures as low as 400 K, due to very weak metal-support interactions. Pt-Ru bimetallic clusters were successfully prepared via ED of Pt on Ru seed clusters on lightly modified HOPG.

Growth of MoS_2 on titania was successfully achieved by previously developed synthesis method. Sulfiding conditions and the temperature at which the synthesis was done dictate the size distribution of MoS_2 nanostructures. MoS_2 did not show sintering unlike the other metallic systems that we studied on titania.

The surface composition of bimetallic clusters was determined by low energy ion scattering spectroscopy. For bimetallic clusters such as Co-Au, where metals are bulk immiscible, the surface composition is governed by the surface free energies. The surface of Co-Au bimetallic clusters were Au rich, and therefore, a core-shell type structure with Au at the shell was observed. For bulk miscible metals such as Co and Pt, the surfaces were composed of a mixture of two metals. In contrast, even though Pt and Re are bulk miscible, the surfaces of the bimetallic clusters were found to be Pt rich. In this system, Re-TiO_2 interactions play a vital role in determining the surface composition. Re shows very strong metal support interactions; therefore, there it is likely that Re migrate onto the support. This facilitate the segregation of Pt to the surface, which is favorable according to the lower

surface free energy of Pt. Similar behavior was observed for the Pt-Ru bimetallic clusters even though Pt and Ru are bulk miscible. Bimetallic Pt-Ru clusters were Pt rich, core-shell type structures which can be explained by the lower surface free energy of Pt compared to Ru and Pt has very weak interactions with the support compared to Ru. Determining the surface composition of Pt-Ru bimetallic clusters are prepared via ED was not achievable using LEIS studies because the clusters are exposed to solution and air therefore, the first atomic layer is contaminated.

Encapsulation of metals with titania was observed at higher temperatures for metals such as Pt and Co but not on Au. Encapsulation, segregation of the support on metals, is an indication of the presence of strong metal-support interactions. Pt and Co become encapsulated in both Co-Pt and Co-Au bimetallic clusters. Metals, being in bimetallic form did not prevent the individual metals from being encapsulated by the support. Re was encapsulated even at room temperature due to strong metal-support interactions. The titania became reduced upon the deposition of Re, which was not observed for Au, Pt or Co, which is further evidence of strong support interactions with Re. Metal-metal interactions, were not studied in Co-Au, Co-Pt and Pt-Ru systems where the bimetallic clusters were made in submonolayer coverages. At these coverages, it is difficult to decouple the cluster size effects and metal-metal interactions using XPS. For higher coverages of Pt-Re bimetallic clusters, Pt-Re interactions were present when Re was deposited on Pt. When Re was deposited first, Re-support interactions dominated over Pt-Re interactions.

Active sites of Pt-Co, Co-Au, Pt-Re and MoS_2 on titania were studied using TPD. The presence of probe molecule, such as CO, induced changes in the surface composition of Co-Au bimetallic clusters. Even though the surface is rich in Au, CO desorption from

Co sites was observed due to adsorbate-induced metal segregation. This phenomenon has previously been observed in other bulk immiscible bimetallic systems such as Pt-Au and Ni-Au. Whereas for metals that are miscible in bulk such as Pt and Co, CO desorption was observed from both Pt and Co sites. Significant changes in the surface composition, after reaction, were not observed. Furthermore, bimetallic effects were more evident in the Co-Pt system. The selectivity of the methanol reaction was different for Co-Pt bimetallic clusters in comparison to that of pure Co and pure Pt. There was also stabilization of the C-H bond in the methanol reaction that is preferable in a catalyst for methanol oxidation reactions. Such effects can be anticipated to be seen in a system where the metals ae known to mix in bulk, which can lead to more electronic interactions as opposed to a system like Co-Au, where the metals do not mix in the bulk. In the Pt-Re system, even though Pt-Re is known to mix in the bulk, CO desorption was mostly dominated by Pt sites, which is consistent with the LEIS data. CO desorption from Pt sites can be structure sensitive, but in this work, the structure of the Pt was not investigated.

The activity and stability of MoS_2 were investigated using TPD and XPS. MoS_2 structures were remarkably stable upon adsorption of gases in UHV. MoS_2 disintegrates upon exposure to extreme oxidation conditions. Adsorption of CO confirms the presence of a metallic character in MoS_2 particles.

1.3 References

(1) Lindstrom, B.; Pettersson, L. J. A Brief History of Catalysis Cattech **2003**, 7, 130-138.

(2) Wisniak, J. The HIstory of Catalysis. From Begining to Nobel Prizes Educ.Quim **2010**, 21, 60-69.

(3) Rodriguez, J. A.; Kuhn, M. Chemical and electronic properties of Pt in bimetallic surfaces: Photoemission and CO-chemisorption studies for Zn/Pt(111). The Journal of chemical physics **1995**, 102, 4279.

(4) Lee, Y.; Rhee, J.; Whang, C.; Lee, Y. Electronic structure of Co-Pt alloys: X-ray spectroscopy and density-functional calculations. Physical Review B **2003**, 68.

(5) Chui, Y. H.; Chan, K.-Y. Structures and Energetics of Platinum–Cobalt Bimetallic Clusters. Molecular Simulation **2004**, 30, 679-690.

(6) Galhenage, R. P.; Ammal, S. C.; Yan, H.; Duke, A. S.; Tenney, S. A.; Heyden, A.; Chen, D. A. Nucleation, Growth, and Adsorbate-Induced Changes in Composition for Co–Au Bimetallic Clusters on TiO2. The Journal of Physical Chemistry C **2012**, 116, 24616-24629.

(7) Tenney, S. A.; Shah, S. I.; Yan, H.; Cagg, B. A.; Levine, M. S.; Rahman, T. S.; Chen, D. A. Methanol Reaction on Pt-Au Clusters on TiO_2 (110): Methoxy-induced Diffusion of Pt. J.Phys.Chem.C **2013**, 117, 26998–27006.

(8) Cheng, D.; Wang, W.; Huang, S. Core–shell-structured bimetallic clusters and nanowires. Journal of Physics: Condensed Matter **2007**, 19, 356217.

(9) Kiss, J.; Óvári, L.; Bugyi, L.; Berkó, A. Characterization Of Au-Rh And Au-Mo Bimetallic Nanoclusters On TiO_2(110): A Comparative Study. React.Kinet.Catal.Lett. **2009**, 96.

(10) Rodriguez, J. A.; Goodman, W. W. Surface Sclence Studies of the Electronic and Chemlcai Properties of Bimetallic

Systems. Journal of Physical Chemistry, 95.

(11) Jalama, K.; Coville, N. J.; Xiong, H. F.; Hildebrandt, D.; Glasser, D.; Taylor, S.; Carley, A.; Anderson, J. A.; Hutchings, G. J. A comparison of Au/Co/Al2O3 and Au/Co/SiO2 catalysts in the Fischer-Tropsch reaction. Appl. Catal. A-Gen. **2011**, 395, 1-9.

(12) Jalama, K.; Coville, N. J.; Hildebrandt, D.; Glasser, D.; Jewell, L. L.; Anderson, J. A.; Taylor, S.; Enache, D.; Hutchings, G. J. Effect of the addition of Au on Co/TiO2 catalyst for the Fischer-Tropsch reaction. Top. Catal. **2007**, 44, 129-136.

(13) Tenney, S. A.; Ratliff, J. S.; He, W.; Roberts, C. C.; Ammal, S. C.; Heyden, A.; Chen, D. A. Adsorbate-induced Changes in the Surface Composition of Bimetallic Clusters: Au-Pt on TiO_2(110). Journal of Physical Chemistry C **2010**, 114, 21652-21663.

(14) Tenney, S. A.; He, W.; Ratliff, J. S.; Mullins, D. R.; Chen, D. A. Characterization of Pt–Au and Ni–Au Clusters on TiO2(110). Topics in Catalysis **2011**, 54, 42-55.

(15) Tenney, S. A.; He, W.; Roberts, C. C.; Ratliff, J. S.; Shah, S. I.; Shafai, G. S.; Turkowski, V.; Rahman, T. S.; Chen, D. A. CO-Induced Diffusion of Ni Atoms to the

Surface of Ni–Au Clusters on TiO2(110). The Journal of Physical Chemistry C **2011**, 115, 11112-11123.

(16) Antolini, E.; Salgado, J. R. C.; Gonzalez, E. R. The methanol oxidation reaction on platinum alloys with the first row transition metals - The case of Pt-Co and -Ni alloy electrocatalysts for DMFCs: A short review. Appl. Catal. B **2006**, 63, 137-149.

(17) Stamenkovic, V.; Schmidt, T. J.; Ross, P. N.; Markovic, N. M. Surface composition effects in electrocatalysis: Kinetics of oxygen reduction on well-defined Pt_3Ni and Pt_3Co alloy surfaces. Journal of Physical Chemistry B **2002**, 106, 11970-11979.

(18) Stamenkovic, V. R.; Mun, B. S.; Mayrhofer, K. J. J.; Ross, P. N.; Markovic, N. M. Effect of surface composition on electronic structure, stability, and electrocatalytic properties of Pt-transition metal alloys: Pt-skin versus Pt-skeleton surfaces. J. Am. Chem. Soc. **2006**, 128, 8813-8819.

(19) Stamenkovic, V. R.; Mun, B. S.; Arenz, M.; Mayrhofer, K. J. J.; Lucas, C. A.; Wang, G. F.; Ross, P. N.; Markovic, N. M. Trends in electrocatalysis on extended and nanoscale Pt-bimetallic alloy surfaces. Nat. Mater. **2007**, 6, 241-247.

(20) Urban, P. M.; Funke, A.; Muller, J. T.; Himmen, M.; Docter, A. Catalytic processes in solid polymer electrolyte fuel cell systems. Appl. Catal. A-Gen. **2001**, 221, 459-470.

(21) Sun, S. G.; Clavilier, J. ELECTROCHEMICAL STUDY ON THE POISONING INTERMEDIATE FORMED FROM METHANOL DISSOCIATION AT LOW INDEX AND STEPPED PLATINUM SURFACES. J. Electroanal. Chem. **1987**, 236, 95-112.

(22) Wilhelm, S.; Iwasita, T.; Vielstich, W. COH AND CO AS ADSORBED INTERMEDIATES DURING METHANOL OXIDATION ON PLATINUM. J. Electroanal. Chem. **1987**, 238, 383-391.

(23) Markovic, N. M.; Gasteiger, H. A.; Ross, P. N.; Jiang, X. D.; Villegas, I.; Weaver, M. J. ELECTROOXIDATION MECHANISMS OF METHANOL AND FORMIC-ACID ON PT-RU ALLOY SURFACES. Electrochim. Acta **1995**, 40, 91-98.

(24) Xu, Y.; Ruban, A. V.; Mavrikakis, M. Adsorption and Dissociation of O2 on Pt-Co and Pt-Fe

Alloys. JACS **2004**, 126, 4717-4725.

(25) Neergat, M.; Shukla, A. K.; Gandhi, K. S. Platinum-based alloys as oxygen-reduction catalysts for solid-polymer-electrolyte direct methanol fuel cells. J. Appl. Electrochem. **2001**, 31, 373-378.

(26) Querini, C. A.; Fung, S. C. Coke and Product Profiles Formed along the Catalyst Bed during n-Heptane Reforming

i. Nonsulfided Pt/Al_2O_3 and $Pt-Re/Al_2O_3$. Journal of Catalysis **1993**, 141, 389-406.

(27) Biswas, J.; Bickle, G. M.; Gray, P. G.; Do, D. D.; Barbier, J. The Role of Deposited Poisons and Crystallite Surface Structure in the Activity and Selectivity of Reforming Catalysts. Catal.Rev.-Sci.Eng **1988**, 30, 161-247.

(28) Azzam, K. G.; Babich, I. V.; Seshan, K.; Mojet, B. L.; Lefferts, L. Stable and Effecient $Pt-Re/TiO_2$ cata;yts for Water Gas Shift: On the Effect of Rhenium. ChemCatChem **2013**, 5, 557-564.

(29) Azzam, K. G.; Babich, I. V.; Sehan, K.; Lefferts, L. Role of Re in Pt-Re/TiO_2 catalyts for water gas shift reaction: A mechanistic and Kinetic Study. Applied Catalysis B: Environmental **2008**, 80, 129-140.

(30) Azzam, K.; Babich, I.; Seshan, K.; Lefferts, L. A bifunctional catalyst for the single-stage water–gas shift reaction in fuel cell applications. Part 2. Roles of the support and promoter on catalyst activity and stability. Journal of Catalysis **2007**, 251, 163-171.

(31) Arico, A. S.; Srinivasan, S.; Antonucci, V. DMFCs: From Fundamental Aspects to Technology Development. Fuel Cells **2001**, 1, 133-161.

(32) Liu, H. S.; Song, C. J.; Zhang, L.; Zhang, J. J.; Wang, H. J.; Wilkinson, D. P. A review of anode catalysis in the direct methanol fuel cell. J. Power Sources **2006**, 155, 95-110.

(33) Lamy, C.; Leger, J. M.; Srinivasan, S.: Direct Methanol Fuel Cells: From a Twentieth Centry Electrochemist's Dream to a Twenty-first Century Emerging Technology. In Modern Aspects of Electrochemistry; Bockris, O. M., Conway, B. E., White, R. E., Eds.; Plenum Press: New York, 2000; Vol. 34; pp 53-115.

(34) Roth, C.; Papworth, A. J.; Hussain, I.; Nichols, R. J.; Schiffrin, D. J. A Pt/Ru nanoparticulate system to study the bifunctional mechanism of electrocatalysis. J. Electroanal. Chem. **2005**, 581, 79-85.

(35) Watanabe, M.; Motoo, S. ELECTROCATALYSIS BY AD-ATOMS .2. ENHANCEMENT OF OXIDATION OF METHANOL ON PLATINUM BY RUTHENIUM AD-ATOMS. Journal of Electroanalytical Chemistry **1975**, 60, 267-273.

(36) Liu, P.; Norskov, J. K. Kinetics of the Anode Processes in PEM Fuel Cells - The Promoting Effect of Ru in PtRu Anodes. Fuel Cells **2001**, 1, 192-201.

(37) Waszczuk, P.; Lu, G. Q.; Wieckowski, A.; Lu, C.; Rice, C.; Masel, R. I. UHV and electrochemical studies of CO and methanol adsorbed at platinum/ruthenium surfaces, and reference to fuel cell catalysis. Electrochim. Acta **2002**, 47, 3637-3652.

(38) Christoffersen, E.; Liu, P.; Ruban, A.; Skriver, H. L.; Norskov, J. K. Anode materials for low-temperature fuel cells: A density functional theory study. Journal of Catalysis **2001**, 199, 123-131.

(39) Lauritsen, J. V.; Nyberg, M.; Nørskov, J. K.; Clausen, B. S.; Topsøe, H.; Lægsgaard, E.; Besenbacher, F. Hydrodesulfurization reaction pathways on MoS2 nanoclusters revealed by scanning tunneling microscopy. Journal of Catalysis **2004**, 224, 94-106.

(40) Bollinger, M.; Lauritsen, J.; Jacobsen, K.; Nørskov, J.; Helveg, S.; Besenbacher, F. One-Dimensional Metallic Edge States in MoS2. Physical Review Letters **2001**, 87.

Chapter 2. Experimental section

2.1 UHV chamber

Preparation and characterization of the model catalytic system are done in an ultra-high vacuum (UHV) Chamber. The base pressure of this chamber is below 1 x 10^{-10} Torr. Figure 2.1 a) shows a schematic of the UHV chamber and b) shows an image of the chamber.

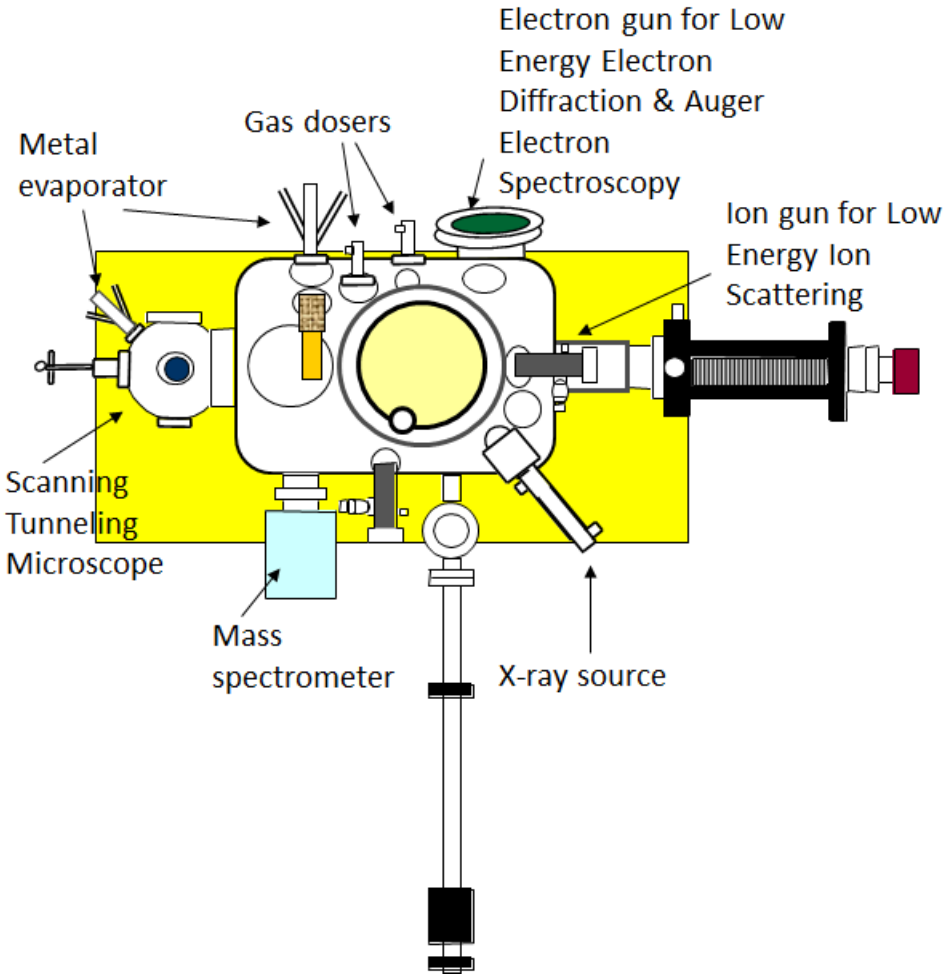

Figure 2.1.a) Schematic of the Ultra High Vacuum Chamber

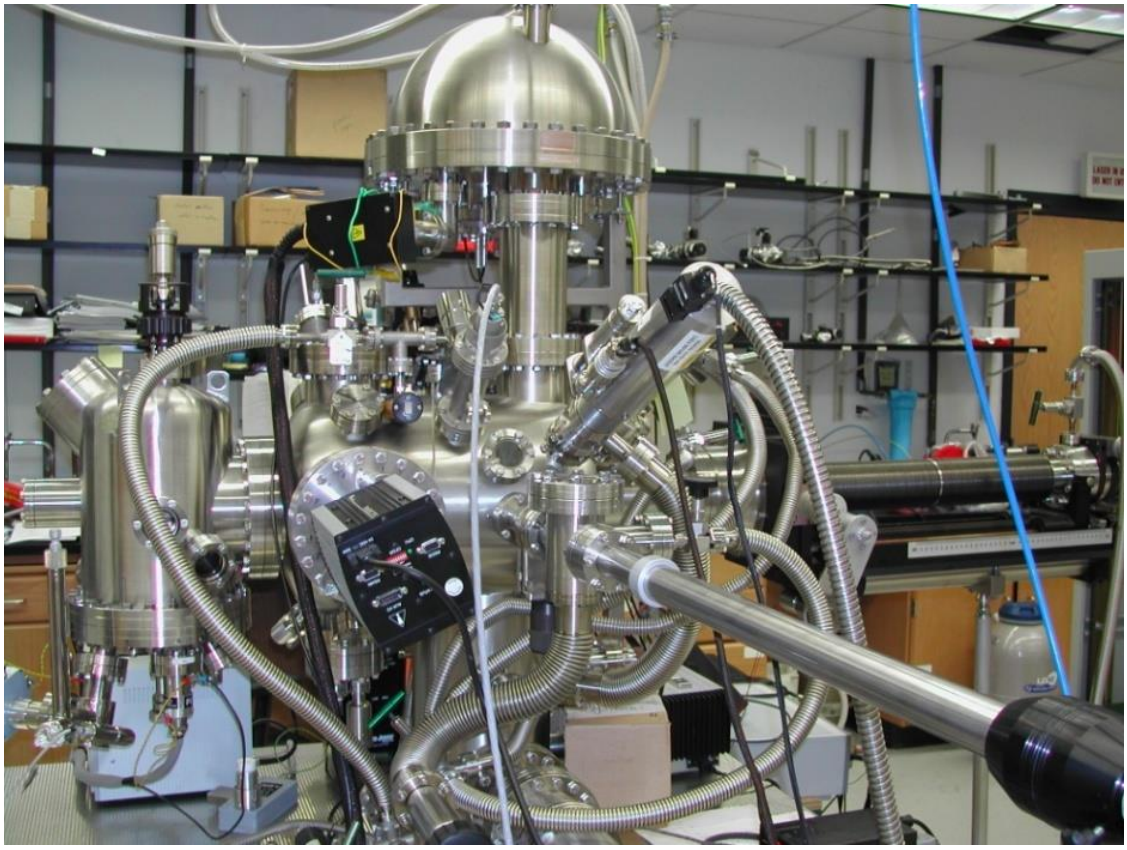

Figure 2.1.b. Ultra High Vacuum Chamber

The chamber is equipped with a manipulator arm to hold the sample and move it to different positions. The sample holder is capable of heating samples via electron beam bombardment of a back plate where the sample has been mounted. The main chamber is connected to a load lock chamber that is isolated with a gate valve in order to provide the ability to introduce a sample without opening the entire chamber. Inside the chamber, there is a carrousel that can retain six different samples. The chamber is equipped with an ion gun for sputtering, metal dosers for the physical vapor deposition of metals and gas dosers, to allow insitu preparation of model surfaces. UHV chamber is also equipped with an ion gun for Low Energy Ion Scattering spectroscopy (LEIS), an electron gun for low energy electron diffraction (LEIS) and Auger Electron Spectroscopy (AES), an X-ray source for

X-ray Photoelectron Spectroscopy (XPS), a mass spectrometer for Temperature Programmed Desorption (TPD) and a Scanning Tunneling Microscope (STM) .

2.2 Scanning Tunneling Microscopy (STM)

The concept of STM was first introduced by Binnig and Rohrer, who won the Nobel Prize in physics in 1986. STM can be used to image with atomic resolution. Figure 2.2 shows the working principle of STM.

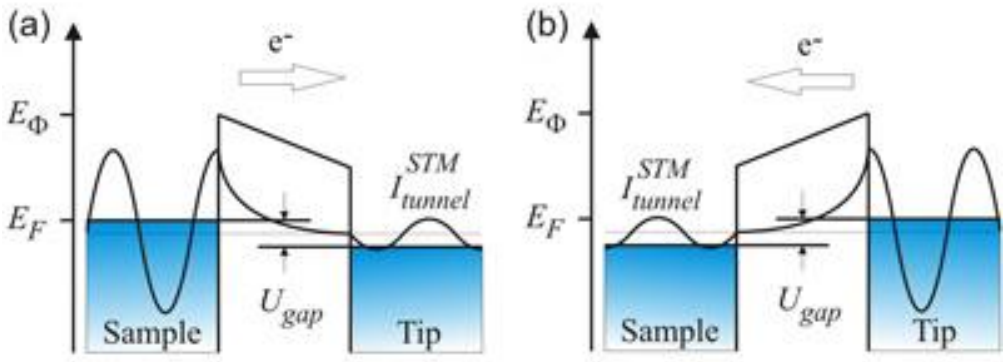

Figure 2.2 Concept of Scanning Tunneling Microscope

The technique is based on the quantum tunneling effects. As shown in the figure 2.2, when a sharp metallic tip is rastered across a conductive sample, to which a positive or a negative bias is applied, electrons tunnel across the vacuum gap from the sample to tip or tip to sample, respectively. The applied voltage determines the direction of the tunneling electrons. If the sample is negatively biased with respect to the tip (figure 2.2a) electrons tunnel from the occupied states of the sample to the unoccupied states of the tip; when the sample is biased positively with respect to the tip (figure 2.2b) then the electrons tunnel from the tip to the sample. Even though, STM does not provide direct chemical

information; it is a powerful tool for determining the morphology of a surface. Morphology of the surface is generated by the movement of the tip in z-direction. Resolution down to the atomic level allow for identification of specific sites on the surface. STM experiments that have been done in the work described here was done by applying a positive voltage to the sample. Furthermore, there are two modes in which STM can be operated, constant current mode and constant height mode. Constant current mode or constant height mode control the movement along the z-axis. Constant current mode maintains a constant current between the sample and the tip, to give the morphology of the surface. In constant height mode, the height is kept constant so that the change in the current develop the morphology of the surface. In our lab, we use constant current mode. Changing parameters such as a bias voltage and current helps to tune the quality of the image.

It is of vital importance that a very sharp tip is used in STM experiments. Imaging with a tip that does not have close to a single atom apex can result in the contribution to the tunneling current from multiple atoms at the tip, and, therefore, the lateral resolution is diminished. The tips that were used for these experiments were prepared by electrochemical etching of a 0.38 mm tungsten wire in 8 M sodium hydroxide solution. Tips are conditioned for better quality by sputtering with a 8 uA, Ar^+ ion beam at 3 kV and applying high voltages (pulsing) while scanning a cleaned support such as TiO_2 inside the UHV chamber (figure 2.1.b).

Surfaces were imaged by STM, and cluster sizes for the mono/bimetallic clusters on the model support were analyzed either using the SCALA 4.1 software from Omicron or an in-house program STATS. Analysis of the STM images provides insight into the

growth and cluster distribution, which are essential factors in determining surface morphology and activity relationship.

2.3 X-ray Photoelectron Spectroscopy (XPS)

XPS measurements are obtained by irradiating the surface to be analyzed with x-rays. The irradiated atoms eject core level electrons (photoelectrons) and are collected by an electrostatic analyzer. Photoelectrons are separated according to their binding energies that are fingerprints of the elements from which the electrons are ejected, and the number of electrons is proportional to the concentration of that element. Figure 2.3 shows the basic concept of XPS. When atoms are irradiated with x-rays, one of three phenomena can take place. 1) photons can pass without any interactions 2) photons can scattered by atomic orbitals that lead to an energy loss and 3) photons can interact with atom with total transfer of energy to an electron leading to the electron emission. Third process is the process that gives chemical information about the elements in an XPS experiment.

When the photon energy is equal or greater to the threshold energy required to remove an electron from an atom, energy is transferred to the electron and eject from the atom. Excess energy gives rise to the kinetic energy (KE) of that ejected electrons. Binding energy of the ejected electron is calculated by the equation 1.

$$E_B = h\upsilon - KE \text{ ------ } (1)$$

E_B is the binding energy of the electron to the atom, h is the Plank's constant, υ is the frequency of the photon and KE is the kinetic energy of the electron. An electrostatic analyzer collects the ejected electrons and measures the kinetic energy, and from that

information binding energies can be calculated. Each element has a set of characteristic binding energies, which serve as atomic "fingerprints".

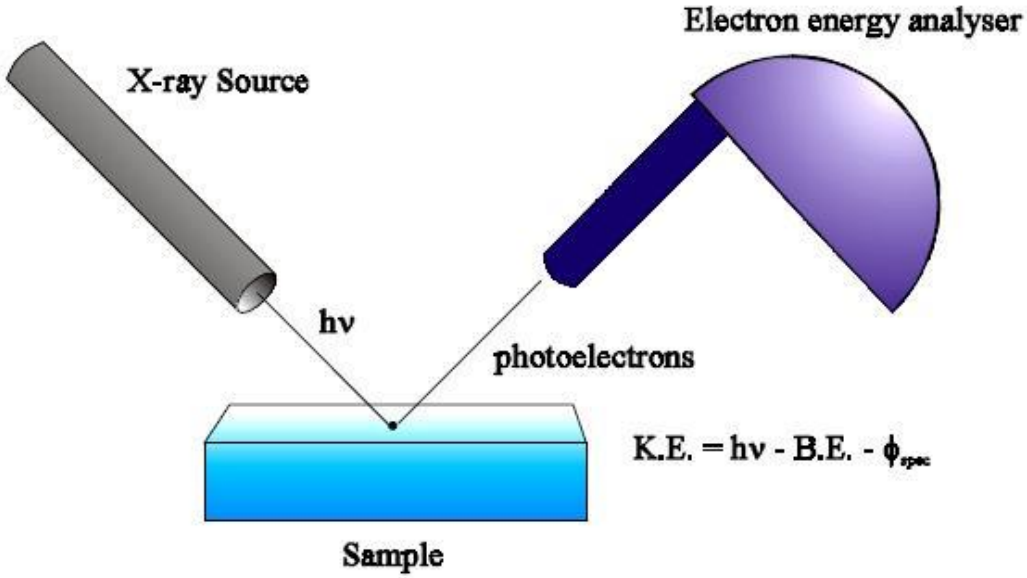

Figure 2.3. Concept of X-ray Photoelectron Spectroscopy

Furthermore binding energy of an ejected electron provides information about the chemical environment of a particular element on the surface. For example, Fe^{2+} and Fe^{3+} can be distinguished by differences in their binding energies; Fe(3+) has a higher binding energy because the effective nuclear charge experienced by the core level electrons is greater in the +3 valency. Not only the oxidation states, but significant differences in the chemical environments also can be identified by XPS.

X-rays for the XPS experiment are generated by a dual anode that consists of an Al anode and a Mg anode. To generate X-rays, thoria-coated iridium filament is heated to emit electrons, and the emitted electrons are accelerated to the anode which has a voltage of 15 kV. Electron bombardment of the anode surface generates x-rays. This process creates significant thermal energy, and, therefore, the anode needs to be water cooled. The excited

Mg or Al targets emit x-rays with an energy of 1253.6 eV or 1486.6 eV, respectively. The probe depth of the XPS experiments is about 10 nm into the bulk due to the mean free path of the ejected electrons.

2.4 Low Energy Ion Scattering (LEIS)

LEIS is a technique in which the first atomic layer of a surface can be probed. In the LEIS experiment, the surface is exposed to a stream of noble gas ions of low energy (>600 eV) (He^+, Ne^+, Ar^+), and the back scattered ions are collected by an electrostatic analyzer to measure the kinetic energy. The kinetic energy of the backscattered ion depends on the mass of the surface atom with which the ion collides. To a first approximation, the scattering event can be treated as a classical two-body elastic collision. The mass of the element on the surface is calculated by conservation of momentum and energy for the system. Figure 2.4 shows a simple schematic of the scattering process occurring in a LEIS experiment.

Surface sensitivity of a LEIS experiment arises from the neutralization of ions that penetrate beyond the first atomic layer. Ions that penetrate deeper into the surface get neutralized before they escape the surface, therefore, are not detected by the electrostatic analyzer. The relative sensitivity of LEIS to different elements is different. Therefore, a sensitivity correction factor must be applied to quantitative analysis of the elemental composition at the surface. Unlike XPS, which probes around 10 nm into the surface, LEIS only probes the first atomic layer that makes it the most surface sensitive technique.

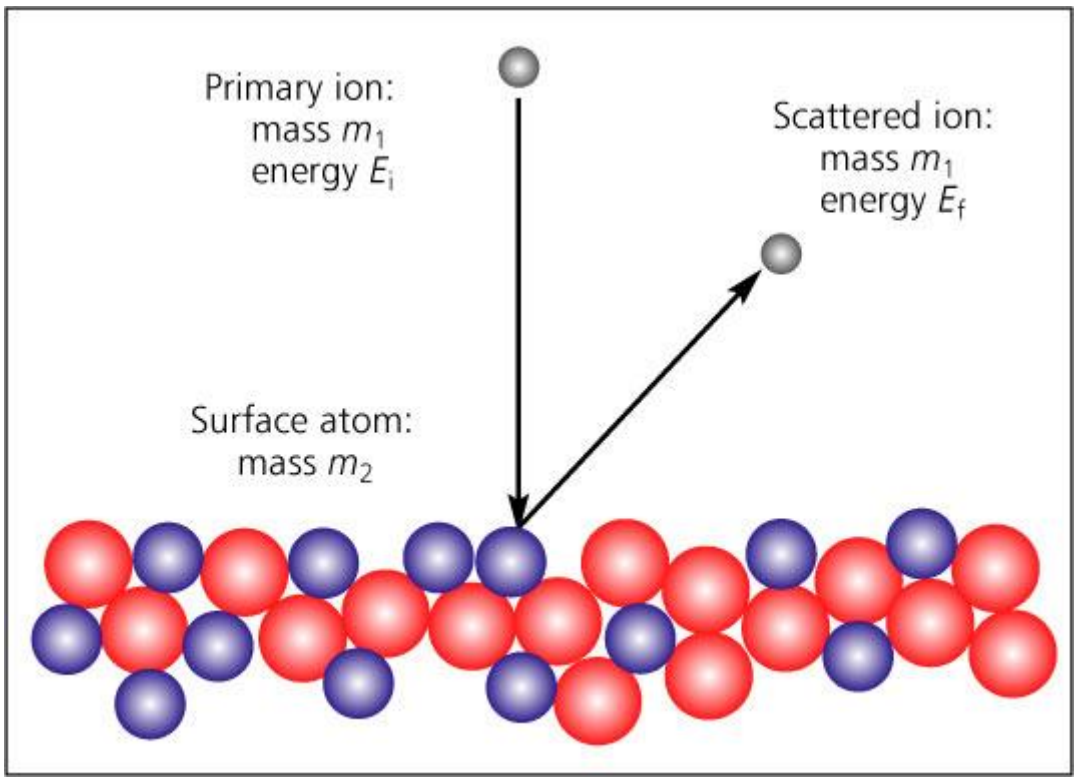

Figure 2.4. Scattering process of low energy ion scattering spectroscopy

2.5 Temperature Programmed Desorption (TPD)

TPD is used to understand the active sites of the model surface. The experiment is performed by, first preparing the model catalyst surface, exposing the surface to a gas-phase probe molecule, and heating the surface in front of a quadrupole mass spectrometer. The desorbing products are detected by the mass spectrometer. From the mass fragmentation pattern, the products can be identified, and from the integration of the peaks, the product yield can be estimated. Figure 2.5 shows the TPD setup that is being used in our lab. The mass spectrometer is shielded with a Au-covered flag that has a ~2mm diameter, hole in the center of the flag. The sample is placed approximately 3 mm from the aperture, which helps to eliminate any contribution from molecules that desorb from the

rest of the sample holder or manipulator. The sample is biased at -100 V to prevent electron-induced chemistry on the surface.

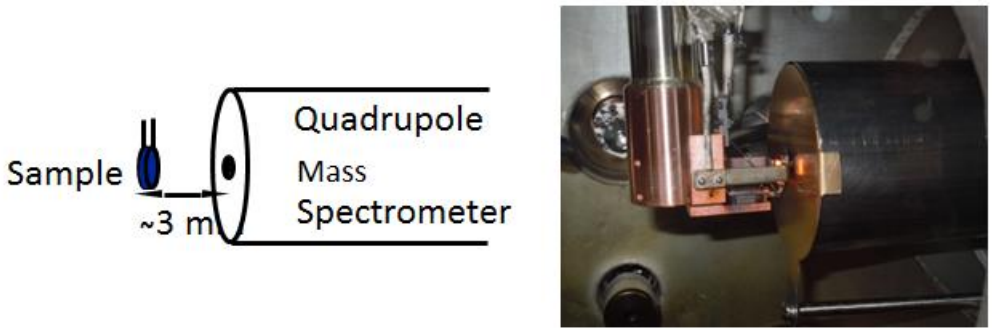

Figure 2.5. Temperature Programmed Desorption set up

2.6 Model system

The model system is prepared in a highly controlled environment, i.e. inside the UHV chamber. The insitu preparation of metal clusters are done using physical vapor deposition. Physical vapor deposition is achieved by electron beam heating of a metal rod or a crucible which filled with the metal. Electron beam heating is achieved by accelerating electrons from a thoriated tungsten wire to a positively biased metal rod or a crucible. Characterization of these systems has been done using following characterization methods.

In an industrial catalyst, active metal component which is responsible to catalyze the reaction is supported on oxides or carbon. Single crystal supports of these oxide surfaces or carbon supports such as rutile TiO_2 (110) and HOPG respectively serve as model supports due to their simplicity and the order. There are other methods of preparing these oxide supports such as preparing thin films on conductive supports. The workd done

in this thesis, was done using TiO_2 (110) single crystal as a model oxide support and Highly Ordered Pyrolytic Graphite (HOPG) as a model carbon support.

Titania crystal structure has been studied extensively in literature.[1-5] Furthermore titania is a reducible oxide which could effectively participate in a reaction and, therefore, catalytically relevant. For these reasons rutile TiO_2(110) serve as a good model support. Structure of the titania in stick and ball model is shown in figure 2.6 a) and 2.6 b) shows an STM image of TiO_2 (110) single crystal. The rutile titania crystal structure consists of octahedral titanium atoms bonded to 6 oxygen atoms with the octahedra alternating their orientation between the rows. The (110) surface of the crystal (Figure 2.6.b) results in the cleavage of one of these oxygen-titania bonds yielding two different types of titanium atoms with 5-fold and 6-fold coordination in addition to two types of oxygen atoms, in plane and out of plane.[1] In figure 2.6.b) an STM image of cleaned titania is shown. We use Ar^+ ion sputtering to remove the contaminants from the support. This sputtering process make a rough surface therefore, the surface is heated to ~1000 K for 3 minutes to create large enough flat terraces. Sputtering annealing process drive the lattice oxygen off making the support an n-type semiconductor. The support after the preparation procedure is conductive enough for ion and electron based spectroscopies and microscopies. In the STM image bright rows correspond to Ti atoms and the dark rows correspond to oxygen atoms. There always is an uncertainty between whether STM probe the geometric structure or the electronic structure. In this case clearly STM has probed the electronic structure because otherwise the bright rows are supposed to be oxygen because geometrically oxygen lies a layer above Ti atoms. This has been the case for STM images on titania, where unoccupied states of Ti is imaged when the sample is positively biased.[1]

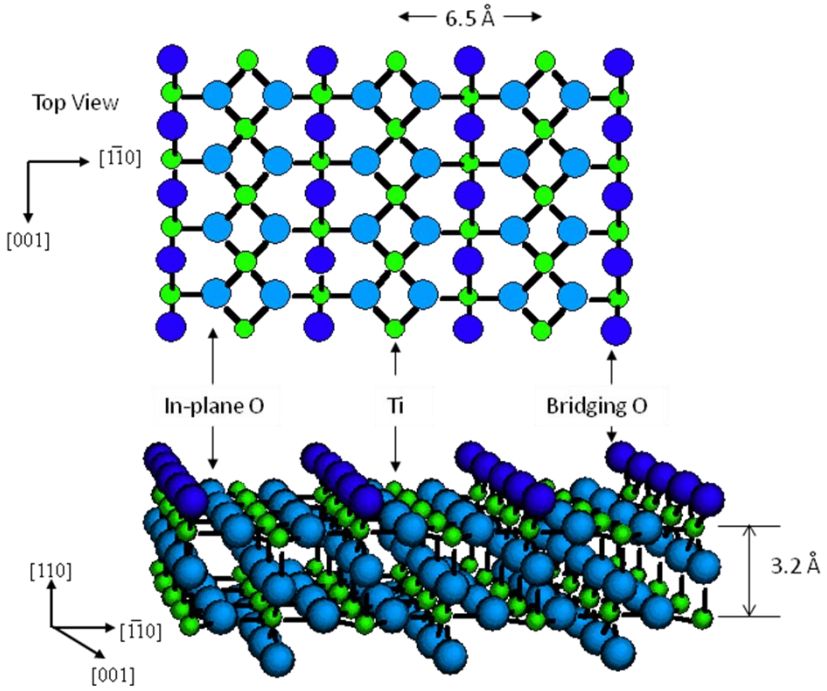

Figure 2.6. a) Stick and ball model of the TiO_2(110)

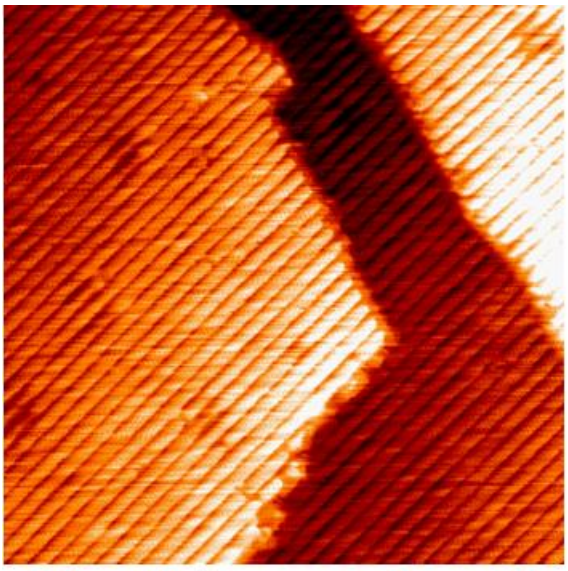

Figure 2.6. b) STM image of TiO_2(110)

Cleanliness and the order of the support has been determined using surface characterization techniques such as XPS, STM, LEED and LEIS.

Metal deposition in order to make metal cluster on supports was achieved either by physical vapor deposition of metals or electroless deposition of metals. Model catalytic systems are prepared in a very controlled environment such as in Ultra High Vacuum conditions. Unlike in real catalytic conditions surface can be analyzed with minimum amount of contamination in a UHV chamber.

2.7. References

(1) Diebold, U. The Surface Science of Titanium Dioxide Surface Science Reports **2003**, 48, 53-229.

(2) Du, Y.; Deskins, N. A.; Zhang, Z.; Dohnalek, Z.; Dupuisb, M.; Lyubinetsky, I. Formation of O Adatom Pairs and Charge Transfer Upon O_2 Dissociation on Reduced TiO_2(110). PCCP **2010**, 12, 6337-6344.

(3) Li, M.; Hebenstreit, W.; Gross, L.; Diebold, U.; Henderson, M. A.; Jennison, D. R.; Schultz, P. A.; c, M. P. S. Oxygen-Induced Restructuring of the TiO_2(110) Surface: a Comprehensive Study. Surface Science **1999**, 437, 173-190.

(4) Zhang, Z.; Lee, J.; John T. Yates, J.; Bechstein, R.; Lira, S.; Hansen, J. Ø.; Wendt, S.; Besenbacher, F. Unraveling the Diffusion of Bulk Ti Interstitials in Rutile TiO_2(110) by Monitoring Their

Reaction with O Adatoms. J Phys Chem C **2010**, 114, 3059-3062.

(5) Wang, Y.; Sun, H.; Tan, S.; Feng, H.; Cheng, Z.; Zhao, J.; Zhao, A.; Wang, B.; Luo, Y.; Yang, J.; Hou, J. G. Role of point defects on the reactivity of reconstructed anatase titanium dioxide (001) surface. Nature communications **2013**, 4, 2214.

Chapter 3. Understanding the nucleation and growth of metals on TiO_2: Co compared to Au, Ni and Pt

3.1 Introduction

Understanding the growth of metals on oxide surfaces is of critical importance for a wide variety of applications, including those involving heterogeneous catalysis, electronic devices and gas sensors.[1-4] In catalysis, the number of active sites depends on the exposed surface area of the supported metal clusters, and therefore the growth mode of the metal clusters is crucial for determining the activity of the supported clusters.[2,5,6] In the fabrication of gas sensors and other electronic devices, the ability of metal films to adhere to the oxide substrate depends on the nature of bonding at the metal-oxide interface.[3,7-9]

Co is an important Fischer-Tropsch catalyst for the synthesis of hydrocarbons from CO and H_2 (syngas).[10,11] The attractiveness of Co as a catalyst for the Fischer-Tropsch reaction stems from its high activity,[10-12] high selectivity for longer chain hydrocarbons,[13] and low activity for the undesired water-gas shift side reaction.[11,14] Furthermore, titania is a preferred support for the Co-based Fischer-Tropsch catalysts,[12,15-22] due to its excellent thermal stability under reaction conditions and good mechanical properties.[23] The Co-TiO_2 system has also been used for other industrially relevant catalytic processes, including the steam reforming of ethanol,[24] preferential oxidation of CO in hydrogen[25] and oxidative dehydrogenation of ethane.[26] The nature of the Co-titania interface is believed to influence the chemical activity of the supported Co clusters. For example, the number of active sites is altered by the extent of sintering or agglomeration of the clusters during heating as well as the initial wetting ability of the Co on titania. While strong Co-titania interactions favor higher activity through greater dispersion, the formation of a Co-titanate compound is known to deactivate Co catalysts.[14] It has also been reported that this interfacial reaction,

which occurs during reduction with H_2, inhibits the reduction of Co.[27] Previous studies of Co on titania catalysts report strong metal support interaction (SMSI) effects, such as the decreased adsorption of CO and H_2 after heating the system in a reducing environment.[19,20,28,29] Recent investigations of Co on TiO_2(110) from our group show that the Co clusters become partially encapsulated by titania upon heating in vacuum,[30] and other investigations of Co on TiO_2(110) observe decreased Co photoemission upon annealing,[29] which is also consistent with encapsulation.

In order to better understand the growth of Co on titania and the nature of the Co-titania interfacial interactions, we have studied vapor-deposited Co clusters on rutile TiO_2(110) using techniques such as scanning tunneling microscopy (STM) and X-ray photoelectron spectroscopy (XPS) under ultrahigh vacuum (UHV) conditions. The deposition of Co on titania at room temperature results in greater cluster densities and smaller cluster sizes compared to other transition metals grown on TiO_2(110). Co remains predominantly metallic and does not induce significant reduction of the titania support. Upon heating the surface, the Co clusters undergo sintering to form larger clusters. Density functional theory (DFT) studies were carried out to calculate the binding energy of a single metal atom on vacuum-annealed (reduced) TiO_2 for Co as well as other transition metals like Au, Ni and Pt. This binding energy scales with the strength of oxygen metal bonds formed on close-packed single crystal surfaces of the metals. The relative cluster sizes and densities for various metals on TiO_2 are successfully predicted based on the metal-titania binding energies: stronger metal-titania binding results in slower diffusion rates and smaller clusters with higher cluster densities. Furthermore, diffusion rates for metals

deposited on oxidized TiO_2 were lower than on reduced TiO_2 for all four metals (Au, Ni, Pt, Co) due to the formation of strong admetal-oxygen bonds.

3.2 Experimental methods

All experiments were conducted in two ultrahigh vacuum chambers. The first chamber has a base pressure of $<5x10^{-11}$ Torr and is equipped with a variable-temperature scanning tunneling microscope (Omicron, VT-25), hemispherical analyzer (Omicron, EA125) for X-ray photoelectron and low energy ion scattering experiments, low energy electron diffraction optics (Omicron SPEC3), and a quadrupole mass spectrometer (Leybold-Inficon Transpector 2). A more detailed description of the chamber, as well as sample heating and metal deposition procedures, can be found elsewhere.[31-36] The second chamber has a base pressure of $\leq 2x10^{-10}$ Torr and was used to conduct soft X-ray photoelectron spectroscopy (sXPS) experiments on the U12a beamline at the National Synchrotron Light Source.[37-40] The rutile TiO_2(110) crystals (Princeton Scientific) were cleaned by several cycles of Ar ion sputtering at 1 kV for 20 min followed by annealing to 950-1000 K for 1-3 min. Preferential loss of oxygen from the crystals through this treatment resulted in crystals that were reduced and sufficiently conductive for STM and XPS experiments. All TiO_2(110) surfaces were subjected to this treatment unless otherwise specified, and these surfaces are referred to as vacuum-annealed or reduced TiO_2(110). Surface cleanliness and order were confirmed by a combination of XPS, STM and LEED. Temperatures were measured by type K or C thermocouples spotwelded to the backplate of the crystal and independently calibrated with an infrared pyrometer.[31]

In the first chamber, metals were deposited via a commercial metal evaporator (Oxford Applied Research, EGC04) using electron beam heating of pure Co, Pt and Ni

rods and Au pellets contained in a Mo crucible. In the second chamber, Co was evaporated from a 0.25 mm pure Co wire (99.995%, ESPI) wrapped around a 0.50 mm W wire (ESPI), through which current was passed to heat the Co. Metal coverages and fluxes were measured by a quartz crystal microbalance, which was independently calibrated.[30] Deposition rates for all of the metals were ~0.1 ML/min, where one monolayer (ML) is defined by the packing densities of the Co(0001), Pt(111), Ni(111) and Au(111) surfaces. Oxygen (Matheson, 99.997%) exposures were carried out at room temperature with a pressure rise of $1x10^{-7}$ Torr for 5 min using a stainless steel directed dosing tube positioned 5 mm from the face of the crystal.

XPS data for the Co(2p) region were collected with an Al K□ source using a 0.2s dwell time and 0.03 eV step size. The Ti(2p) region was collected with a photon energy of 600 eV, step size of 0.1 eV, and dwell time of 0.1 s. STM studies were conducted at a sample bias of +2.3 V and a tunneling current of 0.05-0.1 nA with electrochemically etched tungsten tips.[33] Measurements of cluster heights in the STM images were carried out with an in-house analysis program that has been described elsewhere.[30,41] Cluster heights are used as measure of cluster size since the diameters are known to be overestimated due to tip convolution effects.[30,33]

Computational Methods

Density functional theory calculations[42,43] of metal binding to TiO_2 were performed with the Vienna Ab-initio Simulation Package.[44,45] Core electrons were described by projector augmented-wave potentials [45,46] and valence electrons with a plane wave basis using an energy cutoff of 300 eV. Electron correlation was modeled within the generalized gradient approximation using the PW91 functional of Perdew and Wang.[47] A Dudarev +U

correction of U_{eff} = 4 eV was applied to the Ti d states.[48,49] All calculations were spin polarized. The Brillouin zone was sampled at the Γ-point. A dipole correction was applied in the direction normal to the TiO_2 surface.

The calculated lattice constant of bulk rutile TiO_2 (a = 4.68 Å, c = 3.03 Å, c/a = 0.64) was found to be in good agreement with literature values.[50] To study the binding of metal atoms, we used a rutile (110) slab structure having three stoichiometric layers and a 3 × 2 surface supercell. We prepared a reduced TiO_2 surface by removing one bridging oxygen atom from a stoichiometric slab, and an oxidized surface by adding an oxygen atom on top of the fivefold (5f) Ti site. The bottom TiO_2 layer was held fixed in bulk lattice positions during geometry optimization, and the topmost two layers were free to relax. Binding energies of various metal atoms on the TiO_2 (110) slabs were calculated as $E_b = E_{metal/slab} - E_{metal} - E_{slab}$, with $E_{metal/slab}$, E_{metal}, and E_{slab} being the energy of the bound system, metal in gas phase, and TiO_2 slab, respectively.

3.3 Results

Scanning tunneling microscopy experiments were carried out on various coverages of Co deposited on TiO_2(110) at room temperature (Figure 3.1). For the lowest coverage of 0.02 ML, relatively small clusters are formed with an average height of 3.3± 0.9 Å and a cluster density of 4.17×10^{12} clusters/cm^2 (Figure 3.1a). Although three-dimensional clusters are grown on the surface, many of the clusters are only 1-2 atomic layers thick, suggesting strong interactions between the TiO_2 support and the Co clusters. Furthermore, there is no preference for the clusters to reside at the step edges, which are the high coordination sites, and this implies that the diffusion length of the Co atoms on TiO_2 is shorter than the distance between steps on the titania surface. As the coverage is increased

to 0.06 ML and 0.13 ML, the number of clusters on the surface and the average cluster height increases, with the height reaching 4.4±1.2 Å at 0.13 ML (Figure 3.1 b,c). These same trends continue as the Co coverage is increased to 0.19 ML and then 0.25 ML, where the surface appears to be completely covered with clusters with an average height of 5.2 ±1.6 Å (Figure 3.1d,e).

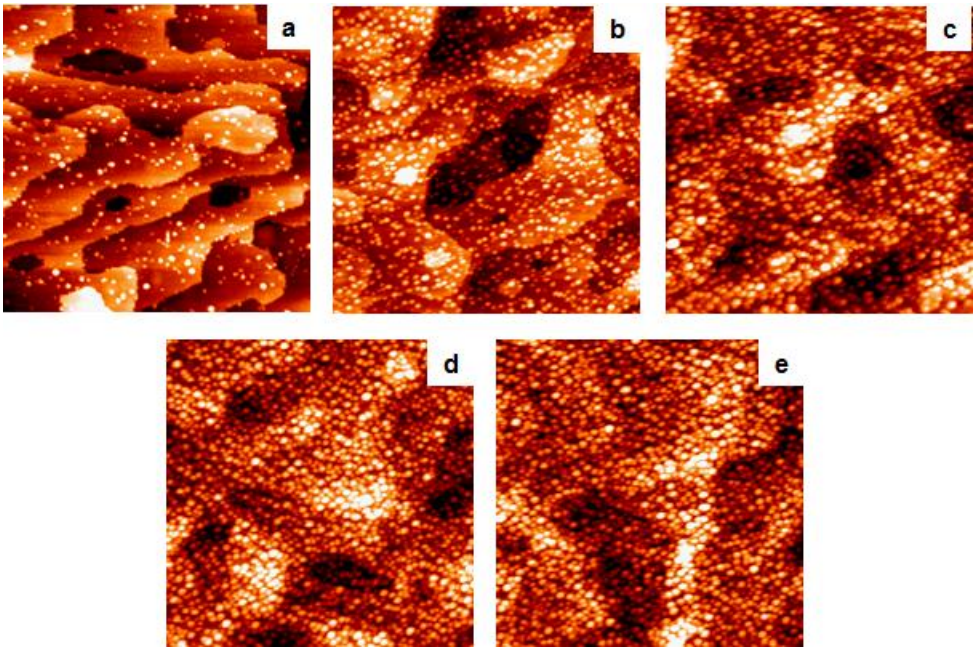

Figure 3.1: STM images of the following coverages of Co deposited on TiO_2(110) at room temperature: a) 0.02 ML; b) 0.06 ML; c) 0.13 ML; d) 0.19 ML and e) 0.25 ML. All images are 1000 Åx1000 Å.

A quantitative comparison of cluster height and densities as a function of coverage is shown in Figure 3.2. From 0.02 to 0.06 ML, the number of clusters on the surface increases linearly, with the number of clusters increasing by a factor of 2.8 (Figure 3.2a). Between 0.06 and 0.19 ML, the clusters density increases less sharply as the surface becomes covered with clusters, and therefore the probability of an incoming Co atom joining an existing cluster becomes high despite the short diffusion length of Co on TiO_2.

In the highest coverage regime of 0.19 to 0.25 ML, the number of clusters nearly plateaus, presumably because there is little exposed titania on which new clusters can nucleate, and consequently the incoming Co atoms are likely to contribute to the growth of existing clusters. Although the average heights of the clusters also increase nearly linearly from the lowest to highest coverage studied (Figure 3.2b), the total increase in height between 0.02 and 0.25 ML is only ~2 Å, which roughly corresponds to a single atomic layer.

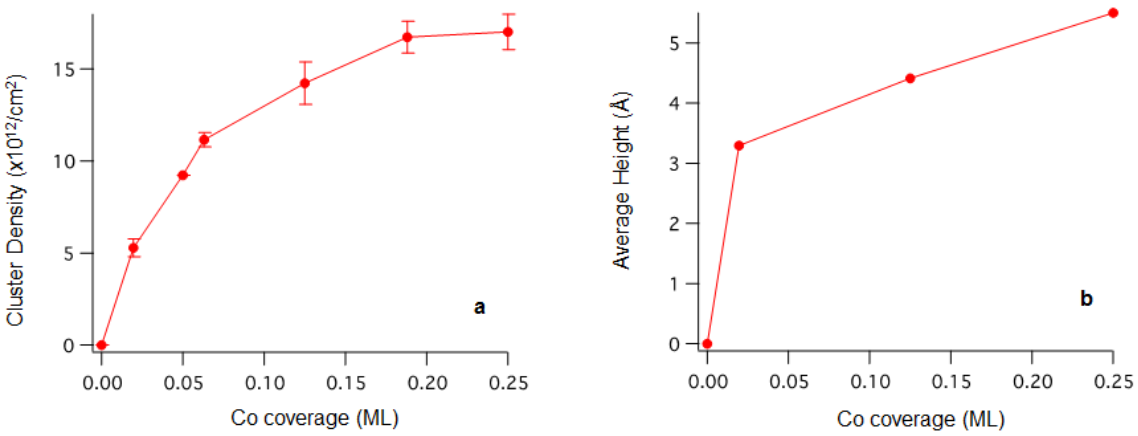

Figure 3.2: Cluster densities (a) and average cluster heights (b) as a function of increasing Co coverage on TiO_2(110). The error bars for the cluster densities are the standard deviations from counting the clusters in three 1000Åx1000Å images from the same experiment except for the 0.19 ML clusters, where only two images were counted.

At a coverage of 0.02 ML of Co, the height distribution is very narrow, with 80% of the clusters in the 2-4 Å range and 20% in the 4-6 Å range (Figure 3.3). As the coverage is increased to 0.13 ML, the distribution becomes slightly broader; larger clusters appear with heights of 8 Å, and only 40% of the clusters are 2-4 Å high. Furthermore, at 0.25 ML, clusters as large as 10 Å are observed, and the smaller 2-4 Å clusters comprise <20% of the total distribution.

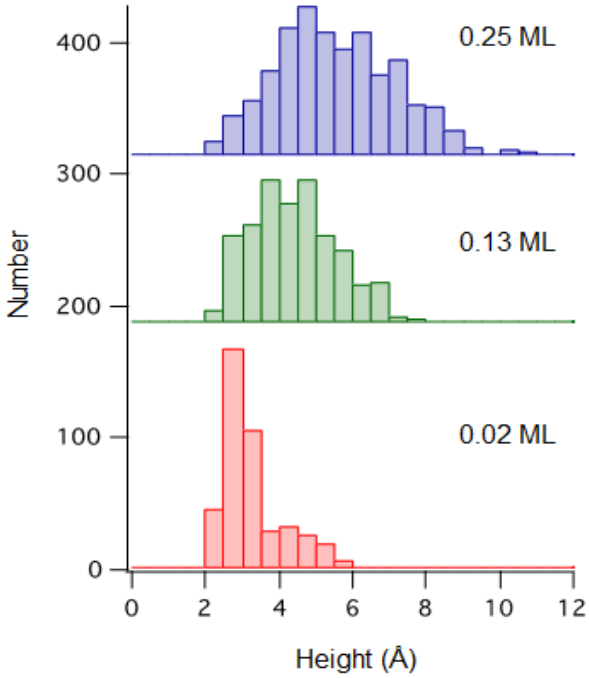

Figure 3.3: Cluster height distributions for various coverages of Co deposited on TiO_2 at room temperature. Heights were determined from STM images using an in-house cluster measurement program, and the following image sizes were used for the analysis: 1000Åx1000Å for 0.02 ML, 500Åx1000Å for 0.13 and 0.25 ML.

The broadening of the size distribution with increasing coverage is explained as follows: at the higher coverages, incoming Co atoms can both nucleate new clusters, which contribute to the smallest cluster sizes, or become incorporated into existing clusters, which contributes to the larger cluster sizes. In contrast, at the lower coverages, almost all of the Co atoms nucleate new clusters because the diffusion length is not large enough for these atoms to reach existing clusters. In general, our group has observed that the size distribution for metals grown on TiO_2 becomes narrower as the diffusion length decreases; for example, on a TiO_2 surface that was intentionally made defective by heating to induce

partial reconstruction of the surface, the deposition of Cu clusters resulted in a more uniform size distribution than on stoichiometric TiO_2(110)-(1x1).[51,52] The same behavior has been reported for the growth of Pd,[53] Ag[54] and Pt[55] on reconstructed TiO_2(110)-(1x2) surfaces.

The most striking feature of the growth of Co on TiO_2 is that the nucleation density for Co is much higher than for other mid-late transition metals on TiO_2(110),[33,36,52,54,56-64] implying a lower diffusion rate for Co on TiO_2. A more direct comparison of the growth of Co with Au, Ni and Pt is shown in the STM images in Figure 3.4, where 0.25 ML of each metal is deposited at room temperature. Because the four metals have different rates of diffusion on TiO_2, the resulting cluster sizes and densities are also different, and cluster heights and densities for these surfaces are presented in Table 3.1.

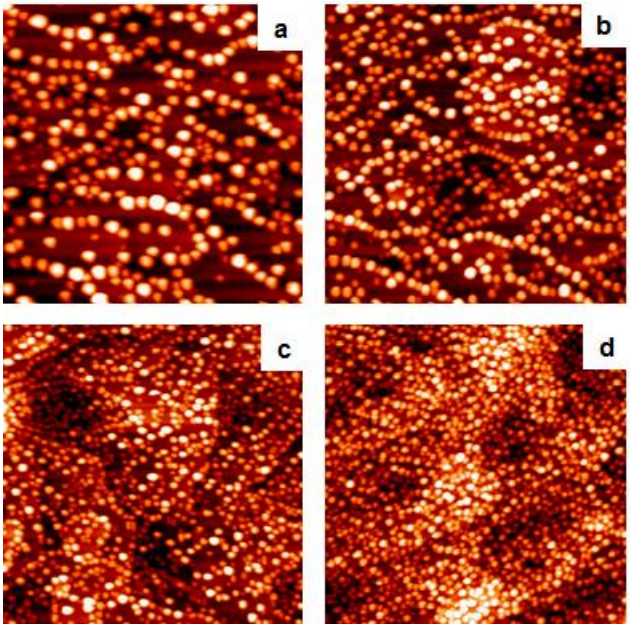

Figure 3.4: STM images of 0.25 ML of the following metals deposited at room temperature on TiO_2(110): a) Au; b) Ni; c) Pt; and d) Co. All images are 1000 Åx1000Å.

Au clusters (Figure 3.4a) have the largest average cluster heights of the four metals (12.7±4.3 Å) and the lowest cluster density, indicating that Au atoms have the greatest mobility on TiO_2.

Table 3.1. Average cluster heights and densities for 0.25 ML of metal deposited on vacuum-annealed TiO_2(110) at room temperature. These statistics are based on measurements of all clusters in 1000x1000 $Å^2$ images, which contained a minimum of 300 clusters.

Surface	Average height (Å)	Cluster density (clusters/cm^2)
0.25 ML Au	12.7 ± 4.3	$3.02x10^{12}$
0.25 ML Ni	11.1 ± 2.8	$5.24x10^{12}$
0.25 ML Pt	6.0 ± 2.1	$1.17x10^{13}$
0.25 ML Co	5.2 ± 1.6	$1.63x10^{13}$

Furthermore, the Au clusters exhibit a tendency to reside at the step edges since the Au atoms are able to diffuse across the terraces. Ni atoms diffuse slightly less readily than Au; the average cluster height is smaller (11.1±2.8 Å) and the cluster density for Ni is a factor of 1.7 higher than for Au although the Ni clusters are still preferentially located at step edges (Figure 3.4b). In the case of Pt, a significant fraction of the clusters appear on the terraces, but the step edge sites are also occupied by clusters (Figure 3.4c). The average cluster height for Pt decreases to 6.0±2.1 Å, and the cluster density is more than twice that of Ni. The Co clusters have no preference for nucleation at step edges, as well as the smallest cluster height (5.2+1.6 Å) and a cluster density that is 1.4 times greater than Pt (Figure 3.4d).

The binding energies of these metals on TiO_2(110) were calculated by DFT in order to explain the experimental differences in metal nucleation and growth (Table 3.2). The

vacuum-annealed (reduced) TiO_2 surfaces used for the experiments contain ~7% oxygen vacancies as determined by counting the number of these features in high resolution STM images, and this number is consistent with the values reported in the literature for similarly prepared TiO_2(110) surfaces.[3] The DFT calculations demonstrate that the metal atoms bind preferentially at the oxygen vacancies, as also reported in the literature for Pt and Au on TiO_2(110);[65,66] it has generally been observed that for growth on oxide surfaces, defects play an important role in the nucleation of the metal clusters.[1] Co binds most strongly to the bridging oxygen vacancy, followed by Pt, Ni, and finally Au. Furthermore, the Co atom binds asymmetrically to one Ti (5f) atom and one bridging oxygen atom, in contrast to the symmetric Ti (5f)–metal–Ti (5f) bond of Pt, Ni, and Au, as shown in Figure 3.5 (circles, top). The distinct bonding geometry of Co-TiO_2 can be understood in terms of the stronger affinity of Co for oxygen compared with the Pt, Ni, and Au cases. The calculated oxygen binding energies on the (111) surfaces of Au, Pt and Ni and the (0001) surface of Co are given in Table 3.2 to illustrate that the metal-titania binding energies are correctly predicted by the admetal-oxygen bond strengths. Likewise, a review article by Campbell on the growth of metals on oxides reports that for metal deposition on alumina, the interfacial energy scales with the strength of the admetal-oxygen bond.[1]

From the calculated binding energies of metals, there is a clear trend between binding energy and cluster size/density; specifically, the larger binding energies lead to smaller cluster sizes and higher cluster densities. This behavior can be understood if the rate of diffusion for the metal on titania is assumed to be related to the metal-titania binding energy, with slower rates of diffusion and shorter diffusion lengths associated with strong metal-titania binding.

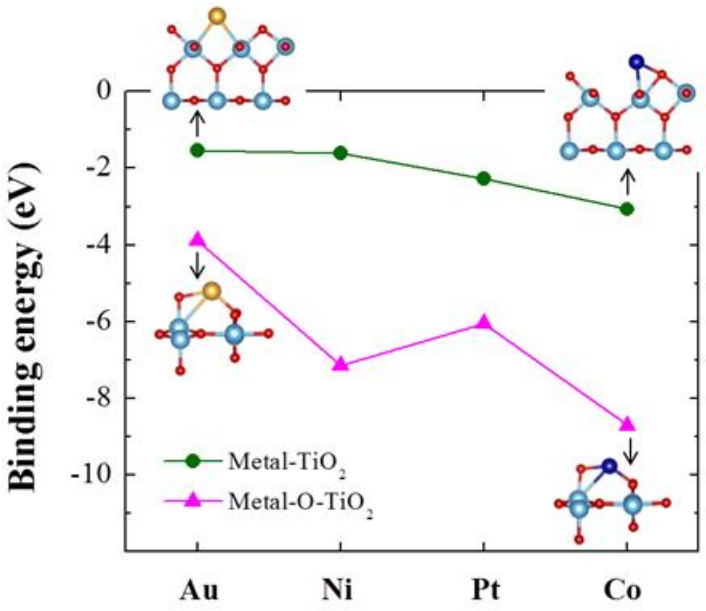

Figure 3.5: Calculated binding energies of metal atoms on vacuum-annealed (reduced) TiO_2 and oxidized TiO_2 (O-TiO_2) surfaces.

The Bronsted-Evans-Polyani (BEP) relationship suggests that the activation energy barrier for metal diffusion should scale with the adsorption energy of the metal.[67-69] According to the BEP equation, the change in activation energy is equal to a constant times the change in reaction energy for reactions of the same type, and this relationship has been successfully applied to understanding the elementary steps in surface reactions.[67-72] Thus, the activation energies obtained from transition state theory can be directly determined from the more easily calculated thermodynamic properties.[69] More recent work by Norskov and coworkers have shown through DFT calculations that there is a "universal" linear relationship between the activation energy of reaction and the adsorption energies of the atomic species for the dissociation of diatomic molecules (N_2, CO, NO, O_2) on many transition metal surfaces.[73,74] Other DFT investigations have also demonstrated this same

relationship between activation energy of reaction and adsorption energies for C-H bond breaking in ethylene,[75] CO dissociation[76] and N_2 dissociation.[74] Consequently, the rate of diffusion of the metal atoms on the surface should decrease with increasing metal-titania binding. The calculated binding energies in Table 3.2 are consistent with the diffusion rates for the metals on TiO_2 following the order of Au>Ni>Pt>Co for diffusion rates.

Table 3.2. Calculated metal binding energy on the vacuum-annealed (reduced) and the oxidized TiO_2 (110) surface. Also reported is the oxygen binding energy to the metal(111) surface for Au, Ni and Pt, and to (0001) for Co.

Metal	Metal binding energy on reduced TiO_2 (eV)	Metal binding energy on oxidized TiO_2 (eV)	Oxygen binding energy on metal (eV)
Au	-1.54	-3.89	-3.67
Ni	-1.61	-7.23	-4.02
Pt	-2.28	-6.05	-4.56
Co	-3.07	-8.70	-6.02

The metals with the greatest mobility on the surface exhibit the largest cluster sizes, the smallest cluster densities and the greatest tendency for the clusters to occupy the high-coordination step edge sites.

The growth of Co, Au and Ni is substantially altered when the vacuum-annealed TiO_2 surface is exposed to O_2 at 295 K before metal deposition. XPS studies report that this oxygen treatment decreases the Ti^{+3} low binding energy shoulder at ~458 eV in the Ti($2p_{3/2}$) spectrum. The oxidation process is proposed to involve O_2 dissociation at oxygen vacancies and subsequent filling of these vacancies by oxygen adatoms, leaving the remaining oxygen adatoms on the surface.[77,78]

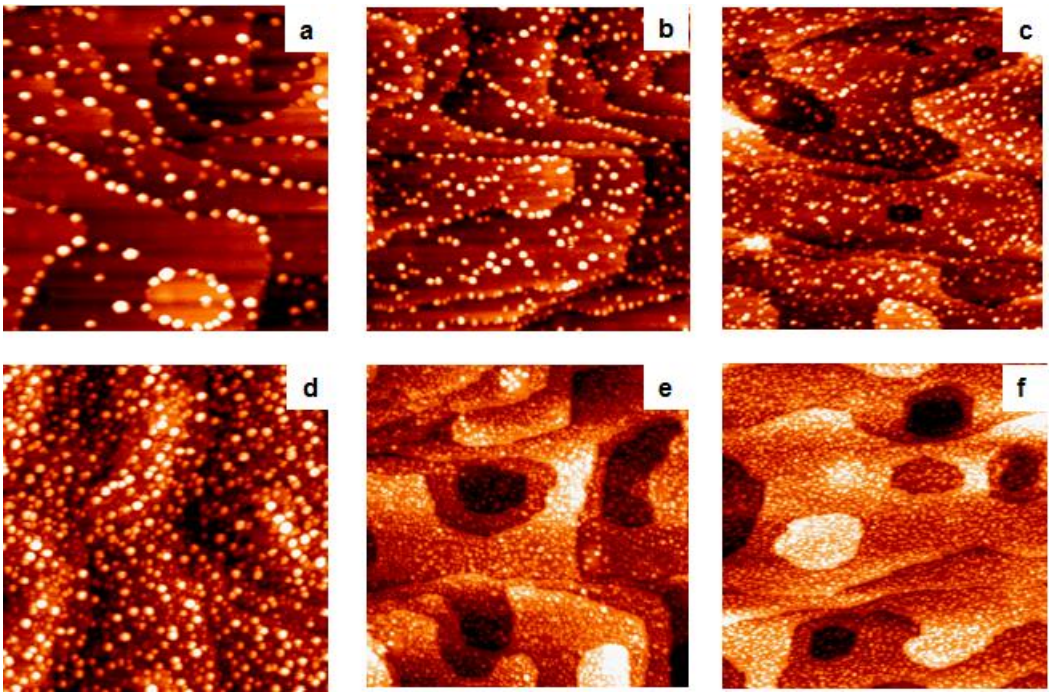

Figure 3.6: STM images of 0.05 ML of the following metals deposited on: vacuum-annealed TiO_2(110): a) Au; b) Ni; and c) Co; and TiO_2 exposed to O_2 at 295 K: d) Au, e) Ni; and f) Co. All metals were deposited at room temperature, and images are 1000Åx1000 Å.

STM images in Figure 3.6 illustrate that for 0.05 ML coverages of various metals, the number of clusters is significantly increased for the oxidized surface compared to reduced TiO_2 in all cases. Similarly, the average cluster heights are all smaller for deposition on oxidized TiO_2 compared to the reduced surface.The changes in the cluster sizes and densities (Table 3.3) suggest that diffusion is inhibited on the oxidized surface due to stronger metal-support interactions. The most pronounced difference is observed for Au, given that the cluster density on the oxidized surface increases by a factor of ~6. Both Ni and Co exhibit smaller changes, with the cluster densities increasing by a factor of only ~3 or ~2, respectively, on oxidized TiO_2. Thus, Au, which diffuses most readily on reduced TiO_2 shows the most pronounced changes in growth. DFT calculations were conducted to compare the binding energies on the oxidized and reduced TiO_2 surfaces (Figure 3.5), and

the most stable binding sites of metal atoms on oxidized TiO_2 were adopted from the literature.[79] The calculations demonstrate that the binding energy of the metal is higher on oxidized TiO_2 (O-TiO_2) in all cases. Moreover, the binding energy of Au on O-TiO_2 is lower than that of Ni or Co, and this reflects the experimental behavior in which the Au clusters grown on O-TiO_2 have greater average heights (4.8$\pm$2.3 Å) than Co (3.0$\pm$0.4 Å) or Ni (2.7$\pm$1.5 Å), which have similar heights (Table 3.3). Likewise, STM studies of Ag[80] and Au[79] clusters on oxidized TiO_2(110) have reported stronger bonding of the metal to the oxidized surface compared to the vacuum-annealed surface.[80] This increased binding in the presence of oxygen is reflected in the experimental observation (Figure 3.6) that the average particle size for all investigated metals is smaller on the oxidized surface.

The difference in metal binding on the reduced and oxidized TiO_2 surfaces can be understood in terms of the relative electronegativities of the metals. The reduced TiO_2 (110) surface is electron rich whereas the oxidized TiO_2(110) surface is electron deficient,[79] and therefore a correlation between the relative electronegativities of the metals and the difference in binding to these surfaces is expected.[81] This was tested by explicitly calculating the binding energy difference, $\Delta E_b = E_b^{oTiO_2} - E_b^{rTiO_2}$, where $E_b^{oTiO_2}$ and $E_b^{rTiO_2}$ are the metal binding energies on the oxidized and reduced TiO_2 (110) surfaces, respectively. Figure 3.7 shows that the binding energy difference is well-correlated with the Pauling electronegativity of the metals.[82] Co, which has the lowest electronegativity, most strongly prefers the oxidizing environment.

Table 3.3. Average cluster heights and densities for 0.05 ML of metal deposited at room temperature on vacuum-annealed (reduced) TiO_2(110) and TiO_2(110) exposed to O_2 at 295 K (oxidized, O-TiO_2). These statistics are based on measurements of all clusters in 500x1000 $Å^2$ or 1000x1000 $Å^2$ images, which included 180-940 clusters.

Surface	Average height (Å)	Cluster density (clusters/cm^2)
0.05 ML Co/TiO_2	3.7±1.2	$9.32x10^{12}$
0.05 ML Co/O-TiO_2	3.0±0.4	$1.57x10^{13}$
0.05 ML Au/TiO_2	8.0±2.7	$1.88x10^{12}$
0.05 ML Au/O-TiO_2	4.8±2.3	$1.16x10^{13}$
0.05 ML Ni/TiO_2	4.4±1.5	$5.44x10^{12}$
0.05 ML Ni/O-TiO_2	2.7±0.6	$1.42x10^{13}$

In contrast, Au has the highest electronegativity and the smallest magnitude of ΔE_b. Although Au has the smallest ΔE_b of the three metals, the ratio of number of clusters on the oxidized compared to TiO_2 surface is the greatest for Au.

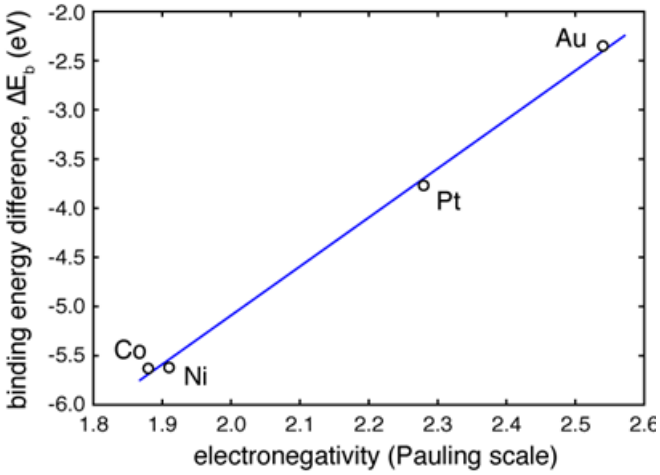

Figure 3.7: Correlation between the ΔE_b values of metal atoms on TiO_2 with their electronegativities.

This behavior is explained by the fact that the reduced TiO_2 surface has very few nucleation sites for Au compared to Ni or Co, and therefore the creation of new nucleation sites on the oxidized surface has the most pronounced effect on the cluster density for Au.

To investigate the interactions between the TiO_2 support and the Co clusters, sXPS experiments were carried out at the U12a beamline at the National Synchrotron Light Source. The surface sensitivity of the experiments was enhanced by using an incident energy of 600 eV so that the photoelectrons have lower kinetic energy than those generated with a conventional Al K□ X-ray source. For these experiments, a higher metal coverage of 2 ML was deposited in order to increase the likelihood of observing the effects of Co-titania interactions. The Ti($2p_{3/2}$) spectrum of the clean TiO_2(110) surface is fit with a main peak at 459.2 eV, which is assigned to Ti^{+4} and accounts for 90% of the total intensity; a smaller feature at 457.7 eV, which is assigned to Ti^{+3}, accounts for the remaining 10% (Figure 3.8a).[39,83,84] After the deposition of 2 ML of Co (Figure 3.8b), the Ti^{+4} and Ti^{+3} peaks comprise 80% and 15% of the total intensity, respectively, and a small feature at 456.5 eV appears, which is assigned to Ti^{+2} and accounts for 5% of the intensity. The ~10% decrease in the Ti^{+4} peak compared to clean TiO_2 suggests that a small fraction of Ti^{+4} is reduced by Co. Previous studies of Co clusters annealed at 800 K showed that the clusters were encapsulated by titania,[30] as has also been observed for many other metals such as Pt,[39,84,85] Rh,[39,86] Pd[87-89] and Ni[32,35,84,90] heated on TiO_2(110) in a reducing environment like UHV. After annealing to 800 K, the Ti($2p_{3/2}$) peak shape is nearly identical to that of the unannealed surface with Ti^{+4}, Ti^{+3} and Ti^{+2} contributions of 85%, 12% and 3%, respectively (Figure 3.8c), and this peak shape is also very similar to the clean TiO_2 surface. Thus, the Co clusters appear to be encapsulated by stoichiometric

titania, as also observed for encapsulated Ni clusters,[84] whereas Pt clusters are encapsulated by reduced titania.[39,84,85,91,92]

XPS data for the Co(2p) region indicate that the 0.25 ML Co clusters on TiO_2 consist predominantly of metallic Co (Figure 3.9). After deposition at room temperature, the Co(2p) peak shape is similar to that of metallic Co with a Co($2p_{3/2}$) binding energy of 778.5 eV (Figure 3.9a).[93] However, the peak is slightly broader than what is observed for bulk Co surfaces, with greater intensity in the shoulder around 781 eV.

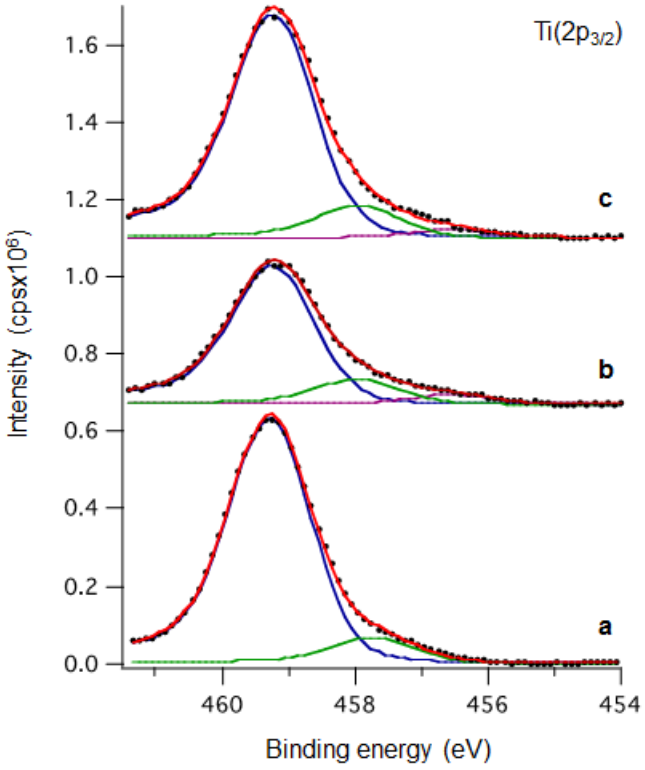

Figure 3.8: Soft X-ray photoelectron spectroscopy data for the Ti($2p_{3/2}$) region for: a) clean TiO_2(110); and 2 ML of Co deposited on TiO_2(110) after room temperature deposition (b) and after heating to 800 K for 1 min (c). The incident photon energy was 600 eV.

One possibility for the origin of this shoulder is that a small fraction of the Co is oxidized from interaction between the Co clusters and the TiO_2 support; note that Co is not expected to be oxidized by background gases upon deposition in UHV, given that pure metallic Co films have been observed on metal surfaces like Mo in UHV.[94] A similar Co(2p) peak shape has been observed for Co deposited on vanadia thin films, and the spectral intensity around ~ 781 eV was assigned to a shakeup satellite arising from d-d correlation, rather than oxidation of Co.[95]

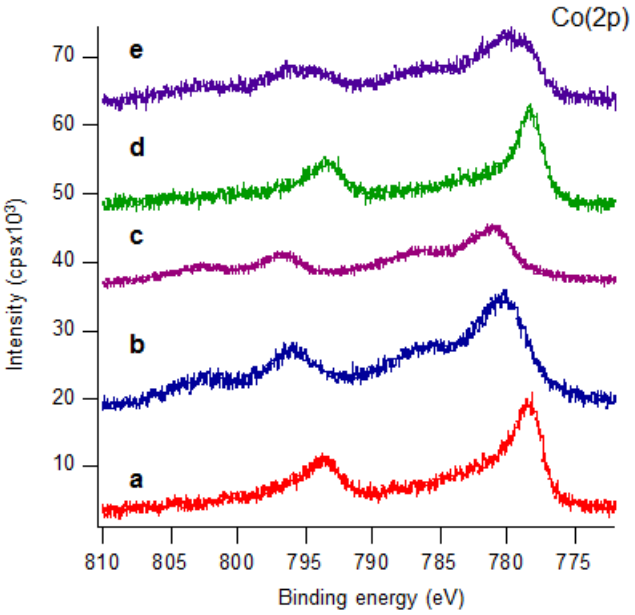

Figure 3.9: XPS data for the Co(2p) region for 0.25 ML of Co deposited on TiO_2(110) at room temperature: a) as deposited; b) exposed to O_2 at room temperature; c) exposed to air for 24 hours; d) annealed to 800 K for one minute; and e) annealed to 800 K for one minute and exposed to O_2 at room temperature. The O_2 was dosed in UHV at a pressure rise of $1x10^{-7}$ Torr for 5 minutes via a directed dosing tube.

Based on the lower heat of formation of cobalt oxide compared to vanadium oxide, it is unlikely that the Co would be oxidized by the vanadia support,[95] and a similar argument would suggest that Co should not be oxidized by the titania support either. XPS studies of Co thin films grown on Cu and oxidized Cu have attributed the Co($2p_{3/2}$) shoulder to correlation-induced satellite features, and the intensity of this satellite feature is reported to be very sensitive to film thickness, with greater intensity for thinner films.[96-98] In addition to d-d interaction, the Cu 4s-Co 3d hybridization also contributes to the Co($2p_{3/2}$) satellite structure for the Co films on Cu. Furthermore, theoretical studies confirm that the d-d correlation is expected to contribute to the satellite structure.[99,100] Therefore, the appearance of the shoulder in the Co($2p_{3/2}$) spectrum of Co on TiO_2 is not exclusively attributed to oxidation, given that the slight reduction of the titania surface is consistent with the presence of only a small fraction of Co oxide.

In order to understand changes in the Co(2p) spectrum due to oxidation, the 0.25 ML Co clusters were exposed to O_2 at a pressure of $1x10^{-7}$ Torr for 5 min. The resulting spectrum begins to resembles that of Co oxide[93] as the $2p_{3/2}$ binding energy shifts to 780.5 eV and distinct shoulders appear at a binding energies 5.7 eV higher than the main 2p peaks (Figure 3.9b). For comparison, the spectrum of 0.25 ML of Co exposed to air for 24 hours is shown in Figure 3.9c to illustrate that the clusters exposed to oxygen in UHV are not fully oxidized. In the spectrum of the Co clusters exposed to air, the $2p_{3/2}$ peak continues to shift to high binding energy (781.1 eV), indicating that this Co surface is more fully oxidized than the one treated in UHV. The Co(2p) spectrum of the clusters annealed to 800 K for one minute (Figure 3.9d) shows only a ~20% decrease in the integrated Co intensity, but the Co($2p_{3/2}$) peak also becomes slightly narrower, which could result from

decomposition of the small fraction of Co oxide. Indeed, when the Co clusters are oxidized in UHV and then heated to 800 K, the metallic peak shape is restored as the decomposition of Co oxide occurs at this temperature. However, because the intensity of the shoulder at ~781 eV is dependent on the thickness of the Co overlayers, the changes at 800 K could also be ascribed to a morphological change.[96-98] After annealing to 800 K, the partially encapsulated Co clusters are exposed to O_2 at 295 K (Figure 3.9e), and there is a significant change in peak shape and a shift in Co($2p_{3/2}$) binding energy to 779.7 eV. This suggests that the Co clusters become oxidized even after partial encapsulation by titania although the extent of oxidation is not as great as for the unencapsulated Co clusters, based on the smaller shift to higher binding energy.

3.4 Discussion

A comparison of Co, Pt, Ni and Au growth on TiO_2(110) demonstrates that information about the kinetics of cluster growth can be extracted from thermodynamic properties like the admetal-oxygen bond strengths. The relative rates of diffusion increase with decreasing admetal-oxygen bond strengths, and higher diffusion rates lead to larger clusters and lower cluster densities. Co exhibits the lowest diffusion rate since it has the strongest metal-titania bonding, and Au exhibits the highest diffusion rate since it has the weakest metal-titania bonding; Ni and Pt follow the same trend of increasing diffusion rates with weaker metal-TiO_2 bonding. Consequently, cluster sizes increase in the order of Co<Pt<Ni<Au. For Co, its less active neighbors in the periodic table (Rh, Ni) exhibit much higher metal atom diffusion at room temperature,[59,62] implying significantly weaker metal-titania binding compared to Co. Many of the mid-late transition metals have been imaged by STM on TiO_2(110), and the reported spatial distributions also follow the trends

predicted by the metal-oxygen bond strengths. Metals like Cu,[58,59] Ag[57,61,101], Rh[62] and Pd[53,60] are mobile on the surface at room temperature compared to Pt and Co, which have higher metal-oxygen bond strengths, and therefore the Cu, Ag, Rh and Pd clusters are preferentially located at the high-coordination step sites. Similarly, metals like Mo[102,103] and Al[104] with stronger metal-oxygen bonds form clusters that show no preference for nucleation at step edges due to the short diffusion lengths.

Diebold and Madey have compared the growth of many transition metals on TiO_2(110) and found that the mode of film growth can also be predicted from thermodynamic properties.[3,4,105] Specifically, the wetting ability of the admetal film depends on the activity of the admetal for reaction with oxygen. Late transition metals like Cu[105] and Au,[56,106] which are not active for reaction with oxygen, grow as three dimensional islands that do not wet the surface; in contrast early transition metals like Cr[107] and Mn[108] are active for reaction with lattice oxygen and form flatter islands that wet more of the titania surface. In general, the admetal's activity for reaction with lattice oxygen follows the heat of formation of the oxides per mole of oxygen,[4] similar to the trend observed for reduction of the titania by the admetal. Moreover, a review by Campbell demonstrated that the growth mode for metals on oxides can be predicted from trends in the heats of formation of the admetal oxide.[1] Three-dimensional film growth is expected when $\gamma_o < \gamma_m + \gamma_{m/o}$, where γ_o and γ_m are the surface free energies of the oxide and admetal, respectively, and $\gamma_{m/o}$ is the energy of the admetal-oxide interface. Since the surface free energy of the metal is usually higher than that of oxide,[109] the interfacial energy often controls the mode of film growth, with strong admetal-titania interaction favoring more 2-dimensional growth. Given that the interfacial energy has been shown to scale with the

heats of formation for the admetal oxides,[1] two-dimensional growth is expected for admetals with higher heats of formation of the associated admetal oxide.

The general trend observed for transition metals on TiO_2 is that the extent of reduction at the admetal-titania interface increases with the heat of adsorption of oxygen on the admetal.[102] Tanaka and coworkers showed that the heat of adsorption for oxygen follows the standard heat of formation (per metal atom) of the highest oxide,[110] and therefore, the extent of titania reduction by the admetal should increase with increasing heat of formation of the oxide. Fe, which is directly to the left of Co in the periodic table, exhibits greater reduction of the titania surface than Co,[105,111] and the early transition metals such as Cr,[107] V,[4,112] Mo[113,114] and Mn[108] also reduce titania significantly upon room temperature deposition. In addition, metals in the periodic table that are in or to the left of the Fe group[111] reduce titania while the admetal itself becomes oxidized, and this interfacial reaction enhances wetting ability.[4] For the mid-late transition metals deposited on TiO_2(110) in this study (Au, Pt, Ni, Co), the extent of titania reduction for equivalent coverages of metal also reflects the relative strengths of the admetal-titania bonds even though none of these metals reduce titania substantially.[84] In the case of Au, which has the weakest metal-titania interaction, there is only a ~3% reduction of Ti^{+4} to Ti^{+3} after deposition. Ni deposition on titania induces a 6% reduction of Ti^{+4} to Ti^{+3} and 3% reduction of Ti^{+3} to Ti^{+2}. Co and Pt, with the strongest metal-oxygen bonds, cause a ~10% reduction of Ti^{+4} to Ti^{+3} and a ~5% reduction of Ti^{+3} to Ti^{+2}.

For the deposition of Co on metal oxide surfaces, the extent to which Co is oxidized by the support increases with decreasing heats of formation of the metal oxide. For example, Co becomes oxidized when deposited on niobia thin films[115] and ZnO surfaces[116-

[118], but Co remains metallic when deposited on alumina,[115,119,120] vanadia thin films[95] and the TiO_2(110) single-crystal surfaces reported here. The heats of formation of the metal oxides (per mole oxygen) for the most stable metal oxide follow the order alumina>titania>vanadia>niobia>ZnO.[1,121] Thus, deposited Co is less likely to become oxidized by the support for metal oxides that have the strongest bonds with lattice oxygen. The observed lack of oxidation of Co on TiO_2 is expected based on the heats of formation of titania compared with alumina and vanadia, which also do not oxidize Co clusters.

3.5 Conclusions

The growth of Co clusters on TiO_2(110) results in small clusters 3-5 Å high for coverages up to 0.25 ML, accompanied by a relatively high cluster density and no preferential nucleation at step edges. These results demonstrate that Co is less mobile on the surface compared to other mid-late transition metals, which form larger clusters and nucleate at step edges. Room temperature deposition of Co induces only a minor reduction of the titania surface, and Co is not significantly oxidized by the titania support. A comparison of the growth of Au, Ni and Pt clusters on TiO_2(110) with Co at the same coverage demonstrates that Co forms the smallest clusters and highest cluster densities due to the lowest rates of the diffusion. DFT calculations for the binding energies of these metals on titania show that the diffusion rate decreases with metal-titania bond strength, which also follows the binding energy of oxygen on the close-packed metal surfaces. Therefore, the rate of diffusion and corresponding clusters size can be predicted based on the metal-titania and admetal-oxygen binding energies. Co, with the strongest binding, has the greatest diffusion barrier and therefore forms the smallest clusters; Au, with the weakest binding, is the most mobile and result in the largest clusters. On oxidized TiO_2(110)

surfaces, diffusion of four metals is slower due to strong bonding between the metals and surface oxygen.

3.7 References

(1) Campbell, C. T. Ultrathin Metal Films and Particles on Oxide Surface: Structural, Electronic and Chemisorptive Properties. Surf. Sci. Rep., **1997**, 27, 1-111.

(2) Henrich, V. E.; Cox, P. A. The Surface Science of Metal Oxides; Cambridge University Press: Cambridge, 1996.

(3) Diebold, U. The Surface Science of Titanium Dioxide. Surf. Sci. Rep., **2003**, 48, 53-230.

(4) Diebold, U.; Pan, J. M.; Madey, T. E. Ultrathin Metal-Film Growth on TiO_2(110): An Overview. Surf. Sci., **1995**, 333, 845-854.

(5) Goodman, D. W. Model Studies in Catalysis Using Surface Science Probes. Chem. Rev., **1995**, 95, 523-536.

(6) Bäumer, M.; Freund, H. J. Metal Deposits on Well-Ordered Oxide Films. Prog. in Surf. Sci., **1999**, 61, 127-198.

(7) Fu, Q.; Wagner, T. Interaction of Nanostructured Metal Overlayers with Oxide Surfaces. Surf. Sci. Rep., **2007**, 62, 431-498.

(8) Semancik, S.; Cavicchi, R. E. The Use of Surface and Thin-Film Science in the Development of Advanced Gas Sensors. Appl. Surf. Sci., **1993**, 70-1, 337-346.

(9) Novak, D.; Garfunkel, E.; Gustafsson, T. Scanning Tunneling Microscopy Study of the Atomic-Scale Structure of TiO_2(110)-(1x1). Phys. Rev. B, **1994**, 50, 5000-5003.

(10) Withers, H. P.; Eliezer, K. F.; Mitchell, J. W. Slurry-Phase Fischer-Tropsch Synthesis and Kinetic-Studies over Supported Cobalt Carbonyl Derived Catalysts. Ind. Eng. Chem. Res., **1990**, 29, 1807-1814.

(11) Iglesia, E. Design, Synthesis, and Use of Cobalt-Based Fischer-Tropsch Synthesis Catalysts. Appl. Catal. A, **1997**, 161, 59-78.

(12) Dry, M. E. Fischer-Tropsch Catalysts. In Studies in Surface Science and Catalysis: Fischer-Tropsch Technology; Steynberg, A., Dry, M., Eds.; Elsevier: Amsterdam, 2004; Vol. 152; pp 533-600.

(13) Coville, N. J.; Li, J. Effect of Boron Source on the Catalyst Reducibility and Fischer-Tropsch Synthesis Activity of Co/TiO_2 Catalysts. Catal. Today, **2002**, 71, 403-410.

(14) Jongsomjit, B.; Sakdamnuson, C.; Goodwin, J. G.; Praserthdam, P. Co-Support Compound Formation in Titania-Supported Cobalt Catalyst. Catal. Lett., **2004**, 94, 209-215.

(15) Jacobs, G.; Das, T. K.; Zhang, Y. Q.; Li, J. L.; Racoillet, G.; Davis, B. H. Fischer-Tropsch Synthesis: Support, Loading, and Promoter Effects on the Reducibility of Cobalt Catalysts. Appl. Catal. A, **2002**, 233, 263-281.

(16) Li, J. L.; Jacobs, G.; Das, T.; Davis, B. H. Fischer-Tropsch Synthesis: Effect of Water on the Catalytic Properties of a Ruthenium Promoted Co/TiO2 Catalyst. Appl. Catal. A, **2002**, 233, 255-262.

(17) Li, J. L.; Xu, L. G.; Keogh, R.; Davis, B. Fischer-Tropsch Synthesis. Effect of CO Pretreatment on a Ruthenium Promoted Co/TiO_2. Catal. Lett., **2000**, 70, 127-130.

(18) Jongsomjit, B.; Wongsalee, T.; Praserthdam, P. Study of Cobalt Dispersion on Titania Consisting Various Rutile: Anatase Ratios. Mater. Chem. Phys., **2005**, 92, 572-577.

(19) Duvenhage, D. J.; Coville, N. J. Fe : Co/TiO2 Bimetallic Catalysts for the Fischer-Tropsch Reaction Part 2. The Effect of Calcination and Reduction Temperature. Appl. Catal. A, **2002**, 233, 63-75.

(20) Li, J. L.; Coville, N. J. The Effect of Boron on the Catalyst Reducibility and Activity of Co/TiO_2 Fischer-Tropsch Catalysts. Appl. Catal. A, **1999**, 181, 201-208.

(21) Jalama, K.; Kabuba, J.; Xiong, H. F.; Jewell, L. L. Co/TiO_2 Fischer Tropsch Catalyst Activation by Synthesis Gas. Catal. Commun., **2012**, 17, 154-159.

(22) Zennaro, R.; Tagliabue, M.; Bartholomew, C. H. Kinetics of Fischer-Tropsch Synthesis on Titania-Supported Cobalt. Catal. Today, **2000**, 58, 309-319.

(23) Bartholomew, C. H.; Reuel, R. C. Cobalt Support Interactions - Their Effects on Adsorption and CO Hydrogenation Activity and Selectivity Properties. Ind. Eng. Chem. Prod. RD, **1985**, 24, 56-61.

(24) Llorca, J.; Homs, N.; Sales, J.; de la Piscina, P. R. Efficient Production of Hydrogen over Supported Cobalt Catalysts from Ethanol Steam Reforming. J. Catal., **2002**, 209, 306-317.

(25) Epling, W. S.; Cheekatamarla, P. K.; Lane, A. M. Reaction and Surface Characterization Studies of Titania-Supported Co, Pt and Co/Pt Catalysts for the Selective Oxidation of CO in H-2-Containing Streams. Chem. Eng. J., **2003**, 93, 61-68.

(26) Brik, Y.; Kacimi, M.; Bozon-Verduraz, F.; Ziyad, M. Characterization and Comparison of the Activity of Boron-Modified Co/TiO_2 Catalysts in Butan-2-Ol Conversion and Oxidative Dehydrogenation of Ethane. J. Catal., **2002**, 211, 470-481.

(27) Riva, R.; Miessner, H.; Vitali, R.; Del Piero, G. Metal-Support Interaction in Co/SiO2 and Co/TiO_2. Appl. Catal. A, **2000**, 196, 111-123.

(28) O'Shea, V. A. D.; Galvan, M. C. A.; Prats, A. E. P.; Campos-Martin, J. M.; Fierro, J. L. G. Direct Evidence of the SMSI Decoration Effect: The Case of Co/TiO_2 Catalyst. Chem. Commun., **2011**, 47, 7131-7133.

(29) Shao, Y.; Chen, W.; Wold, E.; Paul, J. Dispersion and Electronic-Structure of TiO_2-Supported Cobalt and Cobalt Oxide. Langmuir, **1994**, 10, 178-187.

(30) Galhenage, R. P.; Ammal, S. C.; Yan, H.; Duke, A.; Tenney, S. A.; Heyden, A.; Chen, D. A. Nucleation, Growth and Adsorbate-Induced Changes in Composition for Co-Au Bimetallic Clusters on TiO_2. J. Phys. Chem. C, **2012**, 116, 24616-24629.

(31) Park, J. B.; Ratliff, J. S.; Ma, S.; Chen, D. A. Understanding the Reactivity of Oxide-Supported Bimetallic Clusters: Reaction of NO with CO on TiO_2(110)-Supported Pt-Rh Clusters. J. Phys. Chem. C, **2007**, 111, 2165-2176.

(32) Zhou, J.; Ma, S.; Kang, Y. C.; Chen, D. A. Dimethyl Methylphosphonate Decomposition on Titania-Supported Ni Clusters and Films: A Comparison of Chemical Activity on Different Ni Surfaces. J. Phys. Chem. B, **2004**, 108, 11633-11644.

(33) Park, J. B.; Conner, S. F.; Chen, D. A. Bimetallic Pt-Au Clusters on TiO_2(110): Growth, Surface Composition and Metal-Support Interactions. J. Phys. Chem. C, **2008**, 112, 5490-5500.

(34) Tenney, S. A.; Ratliff, J. S.; He, W.; Roberts, C. C.; Ammal, S. C.; Heyden, A.; Chen, D. A. Adsorbate-Induced Changes in the Surface Composition of Bimetallic Clusters: Au-Pt on TiO_2(110). J. Phys. Chem. C, **2010**, 114, 21652-21663.

(35) Tenney, S. A.; He, W.; Roberts, C. C.; Ratliff, J. S.; Shah, S. I.; Shafai, G. S.; Turkowski, V.; Rahman, T. S.; Chen, D. A. CO-Induced Diffusion of Ni Atoms to the Surface of Ni–Au Clusters on TiO_2(110). J. Phys. Chem. C, **2011**, 115, 11112-11123.

(36) Tenney, S. A.; Cagg, B. A.; Levine, M. S.; He, W.; Manandhar, K.; Chen, D. A. Enhanced Activity for Supported Au Clusters: Methanol Oxidation on Au/TiO_2(110). Surf. Sci., **2012**, 606, 1233-1243.

(37) Mullins, D. R.; Overbury, S. H.; Huntley, D. R. Electron Spectroscopy of Single Crystal and Polycrystalline Cerium Oxide Surfaces. Surf. Sci., **1998**, 409, 307-319.

(38) Mullins, D. R.; Zhang, K. Z. Metal-Support Interactions between Pt and Thin Film Cerium Oxide. Surf. Sci., **2002**, 513, 163-173.

(39) Ozturk, O.; Ma, S.; Park, J. B.; Ratliff, J. S.; Zhou, J.; Mullins, D. R.; Chen, D. A. Probing the Interactions of Pt, Rh and Bimetallic Pt-Rh Clusters with the TiO_2(110) Support. Surf. Sci., **2007**, 601, 3099-3113.

(40) Chen, D. A.; Ratliff, J. S.; Hu, X.; Gordon, W. O.; Senanayake, S. D.; Mullins, D. R. Dimethyl Methylphosphonate Decomposition on Fully Oxidized and Partially Reduced Ceria Thin Films. Surf. Sci., **2010**, 604, 574-587.

(41) Ratliff, J. S. The Morphology and Catalytic Activity of Bimetallic Nanoclusters Supported on TiO_2(110). PhD Dissertation, University of South Carolina, 2009.

(42) Hohenberg, P.; Kohn, W. Inhomogeneous Electron Gas. Phys. Rev. B, **1964**, 136, B864-&.

(43) Kohn, W.; Sham, L. J. Self-Consistent Equations Including Exchange and Correlation Effects. Phys. Rev., **1965**, 140, 1133-&.

(44) Kresse, G.; Furthmuller, J. Efficiency of Ab-Initio Total Energy Calculations for Metals and Semiconductors Using a Plane-Wave Basis Set. Comput. Mat. Sci., **1996**, 6, 15-50.

(45) Kresse, G.; Furthmuller, J. Efficient Iterative Schemes for Ab Initio Total-Energy Calculations Using a Plane-Wave Basis Set. Phys. Rev. B, **1996**, 54, 11169-11186.

(46) Blochl, P. E. Projector Augmented-Wave Method. Phys. Rev. B, **1994**, 50, 17953-17979.

(47) Perdew, J. P.; Wang, Y. Accurate and Simple Analytic Representation of the Electron-Gas Correlation-Energy. Phys. Rev. B, **1992**, 45, 13244-13249.

(48) Islam, M. M.; Calatayud, M.; Pacchioni, G. Hydrogen Adsorption and Diffusion on the Anatase TiO_2(101) Surface: A First-Principles Investigation. J. Phys. Chem. C, **2011**, 115, 6809-6814.

(49) Finazzi, E.; Di Valentin, C.; Pacchioni, G.; Selloni, A. Excess Electron States in Reduced Bulk Anatase TiO_2: Comparison of Standard GGA, GGA Plus U, and Hybrid DFT Calculations. J. Chem. Phys., **2008**, 129.

(50) Arroyo-de Dompablo, M. E.; Morales-Garcia, A.; Taravillo, M. DFT Plus U Calculations of Crystal Lattice, Electronic Structure, and Phase Stability under Pressure of TiO_2 Polymorphs. J. Chem. Phys., **2011**, 135.

(51) Reddic, J. E.; Zhou, J.; Chen, D. A. Scanning Tunneling Microscopy Studies of the Growth of Cu Clusters on a Reconstructed TiO_2(110)-(1x2) Surface. Surf. Sci., **2001**, 494, L767-L772.

(52) Zhou, J.; Chen, D. A. Controlling Size Distributions of Copper Islands Grown on TiO_2(110)-(1x2). Surf. Sci., **2003**, 527, 183-187.

(53) Jak, M. J. J.; Konstapel, C.; van Kreuningen, A.; Chrost, J.; Verhoeven, J.; Frenken, J. W. M. The Influence of Substrate Defects on the Growth Rate of Palladium Nanoparticles on a TiO_2(110) Surface. Surf. Sci., **2001**, 474, 28-36.

(54) Luo, K.; St. Clair, T. P.; Lai, X.; Goodman, D. W. Silver Growth on TiO_2(110) (1x1) and (1x2). J. Phys. Chem. B, **2000**, 104, 3050-3057.

(55) Gan, S.; Liang, Y.; Baer, D. R.; Grant, A. W. Effects of Titania Surface Structure on the Nucleation and Growth of Pt Nanoclusters on Rutile TiO_2(110). Surf. Sci., **2001**, 475, 159-170.

(56) Valden, M.; Lai, X.; Goodman, D. W. Onset of Catalytic Activity of Gold Clusters on Titania with the Appearance of Nonmetallic Properties. Science, **1998**, 281, 1647-1650.

(57) Lai, X.; St. Clair, T. P.; Goodman, D. W. Oxygen-Induced Morphological Changes of Ag Nanoclusters Supported on TiO_2(110). Faraday Discuss., **1999**, 114, 279-284.

(58) Chen, D. A.; Bartelt, M. C.; McCarty, K. F.; Hwang, R. Q. Self-Limiting Growth of Cu Islands on TiO_2(110). Surf. Sci., **2000**, 450, 78.

(59) Zhou, J.; Kang, Y. C.; Chen, D. A. Controlling Island Size Distributions: A Comparison of Nickel and Copper Growth on TiO_2(110). Surf. Sci., **2003**, 537, L429-L434.

(60) Xu, C.; Lai, X.; Zajac, G. W.; Goodman, D. W. Scanning-Tunneling-Microscopy Studies of the TiO_2(110) Surface : Structure and the Nucleation Growth of Pd. Phys. Rev. B, **1997**, 56, 13464-13482.

(61) Chen, D. A.; Seutter, S. M.; Bartelt, M. C.; McCarty, K. F. Small, Uniform, and Thermally Stable Silver Particles on TiO_2(110)-(1x1). Surf. Sci., **2000**, 464, L708-L714.

(62) Park, J. B.; Ratliff, J. S.; Ma, S.; Chen, D. A. In Situ Scanning Tunneling Microscopy Studies of Bimetallic Cluster Growth: Pt-Rh on TiO_2(110). Surf. Sci., **2006**, 600, 2913-2923.

(63) Jak, M. J. J.; Konstapel, C.; van Kreuningen, A.; Verhoeven, J.; Frenken, J. W. M. Scanning Tunneling Microscopy Study of the Growth of Small Palladium Particles on TiO_2(110). Surf. Sci., **2000**, 457, 295-310.

(64) Berkó, A.; Klivényi, G.; Solymosi, F. Fabrication of Ir/TiO_2(110) Planar Catalysts with Tailored Particle Size and Distribution. J. Catal., **1999**, 182, 511-514.

(65) Iddir, H.; Ögüt, S.; Browning, N. D.; Disko, M. M. Adsorption and Diffusion of Pt and Au on the Stoichiometric and Reduced TiO_2 Rutile (110) Surfaces. Phys. Rev. B, **2005**, 72, 081407R.

(66) Chen, M. S.; Goodman, D. W. Catalytically Active Gold on Ordered Titania Supports. Chem. Soc. Rev., **2008**, 37, 1860-1870.

(67) Masel, R. I. Principles of Adsorption and Reaction on Solid Surfaces; John Wiley and Sons, Inc.: New York, 1996.

(68) Bligaard, T.; Norskov, J. K.; Dahl, S.; Matthiesen, J.; Christensen, C. H.; Sehested, J. The Bronsted-Evans-Polanyi Relation and the Volcano Curve in Heterogeneous Catalysis. J. Catal., **2004**, 224, 206-217.

(69) van Santen, R. A.; Neurock, M.; Shetty, S. G. Reactivity Theory of Transition-Metal Surfaces: A Bronsted-Evans-Polanyi Linear Activation Energy-Free-Energy Analysis. Chem. Rev., **2010**, 110, 2005-2048.

(70) Evans, M. G.; Polyani, M. Inertia and Driving Force of Chemical Reactions. Trans. Faraday Soc., **1938**, 34, 11-29.

(71) Bronsted, J. N. Acid and Basic Catalysis. Chem. Rev., **1928**, 5, 231-338.

(72) Hammer, B.; Norskov, J. K. Theoretical Surface Science and Catalysis - Calculations and Concepts. In Advances in Catalysis; Academic Press Inc: San Diego, 2000; Vol. 45; pp 71-129.

(73) Norskov, J. K.; Bligaard, T.; Logadottir, A.; Bahn, S.; Hansen, L. B.; Bollinger, M.; Bengaard, H.; Hammer, B.; Sljivancanin, Z.; Mavrikakis, M.; et. al. Universality in Heterogeneous Catalysis. J. Catal., **2002**, 209, 275-278.

(74) Logadottir, A.; Rod, T. H.; Norskov, J. K.; Hammer, B.; Dahl, S.; Jacobsen, C. J. H. The Bronsted-Evans-Polanyi Relation and the Volcano Plot for Ammonia Synthesis over Transition Metal Catalysts. J. Catal., **2001**, 197, 229-231.

(75) Pallassana, V.; Neurock, M. Electronic Factors Governing Ethylene Hydrogenation and Dehydrogenation Activity of Pseudomorphic Pd(ML)/Re(0001), Pd(ML)/Ru(0001), Pd(111), and Pd(ML)/Au(111) Surfaces. J. Catal., **2000**, 191, 301-317.

(76) Liu, Z. P.; Hu, P. General Trends in CO Dissociation on Transition Metal Surfaces. J. Chem. Phys., **2001**, 114, 8244-8247.

(77) Epling, W. S.; Peden, C. H. F.; Henderson, M. A.; Diebold, U. Evidence for Oxygen Adatoms on TiO_2(110) Resulting from O_2 Dissociation at Vacancy Sites. Surf. Sci., **1998**, 412-13, 333-343.

(78) Du, Y. G.; Dohnalek, Z.; Lyubinetsky, I. Transient Mobility of Oxygen Adatoms Upon O_2 Dissociation on Reduced TiO_2(110). J. Phys. Chem. C, **2008**, 112, 2649-2653.

(79) Matthey, D.; Wang, J. G.; Wendt, S.; Matthiesen, J.; Schaub, R.; Laegsgaard, E.; Hammer, B.; Besenbacher, F. Enhanced Bonding of Gold Nanoparticles on Oxidized TiO_2(110). Science, **2007**, 315, 1692-1696.

(80) Hansen, J. O.; Lira, E.; Galliker, P.; Wang, J. G.; Sprunger, P. T.; Li, Z. S.; Laegsgaard, E.; Wendt, S.; Hammer, B.; Besenbacher, F. Enhanced Bonding of Silver Nanoparticles on Oxidized TiO_2(110). J. Phys. Chem. C, **2010**, 114, 16964-16972.

(81) Martinez, U.; Hammer, B. Adsorption Properties Versus Oxidation States of Rutile TiO_2(110). J. Chem. Phys., **2011**, 134.

(82) Pauling, L. The Nature of the Chemical Bond, 3rd ed.; Cornell University: New York, 1960.

(83) Mayer, J. T.; Diebold, U.; Madey, T. E.; Garfunkel, E. Titanium and Reduced Titania Overlayers on Titanium Dioxide(110). J. Electron. Spectrosc., **1995**, 73, 1-11.

(84) Tenney, S. A.; He, W.; Ratliff, J. S.; Mullins, D. R.; Chen, D. A. Characterization of Pt-Au and Ni-Au Clusters on TiO_2(110). Top. Catal., **2011**, 54, 42-45.

(85) Pesty, F.; Steinrück, H.-P.; Madey, T. E. Thermal Stability of Pt Films on TiO_2(110): Evidence for Encapsulation. Surf. Sci., **1995**, 339, 83-95.

(86) Majzik, Z.; Balazs, N.; Berko, A. Ordered SMSI Decoration Layer on Rh Nanoparticles Grown on TiO_2(110) Surface. J. Phys. Chem. C, **2011**, 115, 9535-9544.

(87) Bowker, M.; Fourre, E. Direct Interactions between Metal Nanoparticles and Support: STM Studies of Pd on TiO_2(110). Appl. Surf. Sci., **2008**, 254, 4225-4229.

(88) Bennett, R. A.; Stone, P.; Bowker, M. Pd Nanoparticle Enhanced Re-Oxidation of Non-Stoichiometric TiO_2: STM Imaging of Spillover and a New Form of SMSI. Catal. Lett., **1999**, 59, 99-105.

(89) Bowker, M.; Stone, P.; Morrall, P.; Smith, R.; Bennett, R.; Perkins, N.; Kvon, R.; Pang, C.; Fourre, E.; Hall, M. Model Catalyst Studies of the Strong Metal-Support Interaction: Surface Structure Identified by STM on Pd Nanoparticles on TiO_2(110). J. Catal., **2005**, 234, 172-181.

(90) Ozturk, O.; Park, J. B.; Black, T. J.; Rodriguez, J. A.; Hrbek, J.; Chen, D. A. Methanethiol Chemistry on TiO_2-Supported Ni Clusters. Surf. Sci., **2008**, 602, 3077-3088.

(91) Dulub, O.; Hebenstreit, W.; Diebold, U. Imaging Surfaces with Atomic Resolution: The Strong Metal-Support Interaction State of Pt Supported TiO_2(110). Phys. Rev. Lett., **2000**, 84, 3646-3649.

(92) Jennison, D. R.; Dulub, O.; Hebenstreit, W.; Diebold, U. Structure of an Ultrathin TiO_x Film, Formed by the Strong Metal Support Interaction (SMSI) on Pt Nanocrystals on TiO_2(110). Surf. Sci., **2001**, 492, L677-L687.

(93) Wagner, C. D.; Riggs, W. M.; Davis, L. E.; Moulder, J. F. Handbook of X-Ray Photoelectron Spectroscopy; Perkin Elmer Corporation: Eden Prairie, MN, 1978.

(94) Chen, D. A.; Friend, C. M. Adsorbate-Induced Structural Changes of Metal Thin Films: Cobalt-Oxygen and Cobalt-Sulfur Overlayers on Mo(110). Surf. Sci., **1997**, 371, 131-142.

(95) Parteder, G.; Allegretti, F.; Surnev, S.; Netzer, F. P. Growth of Cobalt on a Vo(111) Surface: Template, Surfactant or Encapsulant Role of the Oxide Nanolayer? Surf. Sci., **2008**, 602, 2666-2674.

(96) Schneider, C. M.; Pracht, U.; Kuch, W.; Chasse, A.; Krischner, J. Magnetic Dichroism in Photoemission as a Spin-Resolving Probe for Electronic Correlations. Phys. Rev. B, **1996**, 54, 15618-15621.

(97) Nath, K. G.; Haruyama, Y.; Kinoshita, T. Observation of the Satellite Signal in Co 2p Photoemission Spectra: Evidence of a Localized Electronic Structure in Thin Films. Phys. Rev. B, **2001**, 64.

(98) Nath, K. G.; Haruyama, Y.; Kinoshita, T. Surface Superstructure Formation, Electronic Structure Modification and Magnetic Stability of Co Films on Oxygen-Rich Cu(001): Confirmation of Oxygen-Surfactant Effect. Surf. Sci., **2001**, 486, 185-193.

(99) Chen, C. F. Novel Many-Body Effects in the Photoemission Spectrum of Ultrathin Bcc-Cobalt Films. Phys. Rev. Lett., **1990**, 64, 2176-2179.

(100) Chen, C. F. Photoemission as a Probe of Electronic States in Ultrathin Magnetic Overlayers - Correlation and Hybridization Effects. Phys. Rev. B, **1993**, 48, 1318-1321.

(101) Santra, A. K.; Yang, F.; Goodman, D. W. The Growth of Ag-Au Bimetallic Nanoparticles on TiO_2(110). Surf. Sci., **2004**, 548, 324-332.

(102) Kitchin, J. R.; Barteau, M. A.; Chen, J. G. G. A Comparison of Gold and Molybdenum Nanoparticles on TiO_2(110) 1x2 Reconstructed Single Crystal Surfaces. Surf. Sci., **2003**, 526, 323-331.

(103) Berko, A.; Magony, A.; Szoko, J. Characterization of Mo Deposited on a TiO2(110) Surface by Scanning Tunneling Microscopy and Auger Electron Spectroscopy. Langmuir, **2005**, 21, 4562-4570.

(104) Lai, X.; Xu, C.; Goodman, D. W. Synthesis and Structure of Al Clusters Supported on TiO_2(110) : A Scanning-Tunneling-Microscopy Study. J. Vac. Sci. Technol. A, **1998**, 16, 2562-2566.

(105) Pan, J. M.; Maschhoff, B. L.; Diebold, U.; Madey, T. E. Structural Study of Ultrathin Metal-Films on TiO_2 Using LEED ; Arxps and Meed. Surf. Sci., **1993**, 291, 381-394.

(106) Zhang, L.; Persaud, R.; Madey, T. E. Ultrathin Metal-Films on a Metal-Oxide Surface: Growth of Au on TiO_2(110). Phys. Rev. B, **1997**, 56, 10549-10557.

(107) Pan, J. M.; Diebold, U.; Zhang, L. Z.; Madey, T. E. Ultrathin Reactive Metal-Films on TiO_2(110): Growth ; Interfacial Interaction and Electronic-Structure of Chromium Films. Surf. Sci., **1993**, 295, 411-426.

(108) Diebold, U.; Shinn, N. D. Adsorption and Thermal-Stability of Mn on TiO_2(110) : 2p X-Ray-Absorption Spectroscopy and Soft-X-Ray Photoemission. Surf. Sci., **1995**, 343, 53-60.

(109) Overbury, S. H. Chem. Rev., **1975**, 75, 547.

(110) Tanaka, K.; Tamaru, K. A General Rule in Chemisorption of Gases on Metals. J. Catal., **1963**, 2, 366-370.

(111) Diebold, U.; Tao, H. S.; Shinn, N. D.; Madey, T. E. Electronic-Structure of Ultrathin Fe Films on TiO_2(110) Studied with Soft-X-Ray Photoelectron-Spectroscopy and Resonant Photoemission. Phy. Rev. B, **1994**, 50, 14474-14480.

(112) Zhang, Z.; Henrich, V. E. Electronic Interactions in the Vanadium/TiO_2(110) and Vanadia/TiO_2(110) Model Catalyst System. Surf. Sci., **1992**, 277, 263-272.

(113) Domenichini, B.; Petigny, S.; Blondeau-Patissier, V.; Steinbrunn, A.; Bourgeois, S. Effect of the Surface Stoichiometry on the Interaction of Mo with TiO_2 (110). Surf. Sci., **2000**, 468, 192-202.

(114) Domenichini, B.; Blondeau-Patissier, V.; Casanove, M. J.; Lian, G. D.; Bourgeois, S. Effect of the Mo Atom Flow on the Molybdenum Growth on TiO_2(110) Surface. J. Cryst. Growth, **2004**, 263, 256-262.

(115) Mendes, F. M. T.; Uhl, A.; Starr, D. E.; Guimond, S.; Schmal, M.; Kuhlenbeck, H.; Shaikhutdinov, S. K.; Freund, H. J. Strong Metal Support Interaction on Co/Niobia Model Catalysts. Catal. Lett., **2006**, 111, 35-41.

(116) Law, Y. T.; Skala, T.; Pis, I.; Nehasil, V.; Vondracek, M.; Zafeiratos, S. Bimetallic Nickel-Cobalt Nanosized Layers Supported on Polar Zno Surfaces: Metal-Support Interaction and Alloy Effects Studied by Synchrotron Radiation X-Ray Photoelectron Spectroscopy. J. Phys. Chem. C, **2012**, 116, 10048-10056.

(117) Hyman, M. P.; Martono, E.; Vohs, J. M. Studies of the Structure and Interfacial Chemistry of Co Layers on ZnO(0001). J. Phys. Chem. C, **2010**, 114, 16892-16899.

(118) Su, S. H.; Lai, J. H.; Chen, H. H.; Lee, T. H.; Hsu, Y. J.; Wang, R. L.; Huang, J. C. A. Elucidating the Structure and Chemical State of Co Growth on the ZnO(10-10) Surface. J. Phys. Chem. C, **2012**, 116, 9917-9924.

(119) Carlsson, A. F.; Baumer, M.; Risse, T.; Freund, H. J. Surface Structure of Co-Pd Bimetallic Particles Supported on Al_2O_3 Thin Films Studied Using Infrared Reflection Absorption Spectroscopy of CO. J. Chem. Phys., **2003**, 119, 10885-10894.

(120) Hill, T.; Mozaffari-Afshar, M.; Schmidt, J.; Risse, T.; Stempel, S.; Heemeier, M.; Freund, H. J. Influence of CO Adsorption on the Magnetism of Small Co Particles Deposited on Al_2O_3. Chem. Phys. Lett., **1998**, 292, 524-530.

(121) CRC Handbook of Chemistry and Physics; 67th ed.; Weast, R. C., Ed.; CRC Press, Inc.: Boca Raton, Florida, 1986-1987.

Chapter 4. Nucleation, growth and adsorbate-induced changes in composition for Co-Au bimetallic clusters on TiO_2

4.1 Introduction

The ability to systematically tailor the activity and selectivity of catalytic materials has long been a goal in heterogeneous catalysis. Control over active sites is key to the development of superior catalysts. New active sites can be created on bimetallic surfaces, where electronic modification due to strain effects[1-4] or metal-metal interactions, [2,4-12] the formation of mixed metal sites,[13-15] or other structural changes such as site-blocking [16] gives rise to new chemical activity.[17-21] For example, Chen and coworkers have shown that Pt-Ni bimetallic surfaces exhibit unique chemical activity for a variety of reactions, including hydrogenation of cyclohexene[22-24] and benzene,[23] selective hydrogenation of acrolein,[25] reforming of methanol and ethylene glycol to CO and H_2,[26] hydrodeoxygenation of meta-cresol[27] and hydrodesulfurization of thiophene.[28] A number of DFT studies have also reported that adsorption and dissociation of surface species like H_2[2,12,29], O_2[12,30] ethylene[10], CO[11] and OH[31,32] are different on surface alloys compared to bulk metals. Furthermore, the adsorption of CO is known to be different on pure metal surfaces compared to thin metal films on metal substrates.[5-7,9] In addition to creating new sites via bimetallic surfaces, interactions between the metal clusters and a reducible oxide support can result in new chemical activity. For instance, an "inverse" catalyst composed of titania clusters supported on Au exhibits the same enhanced activity for the water gas shift reaction as Au clusters supported on titania, illustrating the importance of cluster-support interfacial sites.[33] For supported metal clusters on ceria, oxygen from ceria participates in oxidation processes, forming gaseous products containing lattice oxygen from the ceria support.[34-39] In the three way catalysts for the conversion of CO, NO_x and hydrocarbons

into CO_2, water and N_2, the ceria support also plays an important role in oxygen storage.[40-42]

The Co-Au bimetallic clusters on TiO_2(110) present a model system for understanding the nature of metal-metal interactions and metal-support interactions. This study is part of a larger research effort that includes investigations of the growth and activity of Ni-Au and Pt-Au clusters on TiO_2(110),[43-47] and the behavior of the Co-Au system will be compared. The Co-Au on titania system is of specific interest because it has the potential to serve as an excellent catalyst for the conversion of alcohols to H_2. Although Co itself is highly active for C-C and C-H scission in alcohols,[48] decomposition of the alcohol results in the production of CO, which blocks active sites and poisons the catalyst.[49] The oxidation of CO to CO_2 is known to be catalyzed by Au particles supported on titania,[50-54] and there is strong evidence that this reaction occurs at Au-titania interfacial sites.[54-56] Therefore, the Co-Au bimetallic surfaces could potentially improve conversion of alcohols to H_2 by providing sites at which the C-C and C-H bonds are cleaved, as well as sites for the removal of CO. Co also has greater selectivity for H_2 production compared to other catalysts like Pt and Ni due to the ability of Co to suppress the methanation side reaction.[57-61]

Furthermore, the Co-Au bimetallic system exhibits interesting catalytic properties, and there are a number of reactions in which the bimetallic surface has superior activity and selectivity compared to the pure metals. The catalytic activity of Co-based clusters is reported to be improved when the Co is alloyed with noble metals like Au. For example, the activity of Co on a TiO_2 catalyst used in the Fischer-Tropsch reaction is increased upon the addition of Au,[62] and the same is true for Co on Al_2O_3 and SiO_2.[63] Moreover, the

presence of Au in the Co clusters lowers the temperature at which Co oxide can be reduced,[62-64] and other noble metals such as Ru,[65] Re,[65] and Pt[66] mixed with Co exhibit the same effect. A recent study also reports enhanced activity for Co oxide on Au in the electrochemical evolution of oxygen; specifically, the turnover frequency is ~40 times higher for 0.4 ML Co oxide on Au compared to Co on bulk Co oxide.[67] The addition of Au to a kaolin-supported Co catalyst increases the conversion of 1,4-butanediol to 2,3-dihydrofuran, and XRD studies show that the structure of the Co catalyst is modified by the Au.[64] Another example is the addition of Co to an oxide-supported Au catalyst for the gas phase epoxidation of propene using a H_2/O_2 mixture.[68] The Co-Au bimetallic clusters are more active for propene oxide formation compared to pure Au, and the bimetallic surfaces are also less susceptible to deactivation compared to pure Au.

In the work reported here, Co-Au bimetallic clusters are grown on rutile TiO_2(110) by nucleating Au atoms at existing Co clusters, based on the slower diffusion of Co compared to Au. The resulting cluster surfaces are >80% Au for bulk Au fractions of >50%, as dictated by the lower surface free energy of Au compared to Co. Although the pure Co clusters are significantly smaller than the Au clusters at room temperature due to the increased nucleation density for Co (5.5 vs. 12.7 Å average height), addition of Co to the Au clusters does not suppress cluster sintering. Pure Co clusters become encapsulated by titania upon annealing to 800 K, and for annealed Co-Au clusters, surface Co atoms are selectively encapsulated while the Au atoms remain uncovered. Exposure of the bimetallic clusters to CO results in diffusion of Co to the surface of the clusters, but this effect is less pronounced than what is observed in the Pt-Au and Ni-Au systems. DFT calculations

demonstrate that the CO-induced metal diffusion is thermodynamically driven by the formation of strong CO-metal bonds.

4.2 Experimental

Experiments were carried out in two ultrahigh vacuum chambers with base pressures below 5×10^{-11} Torr. The first chamber is equipped with a variable-temperature STM (Omicron, VT-25), hemispherical analyzer for XPS and LEIS experiments (Omicron, EA125), and a low energy electron diffraction (LEED)/Auger electron spectroscopy (AES) system (Omicron, SPEC3). The second chamber houses a quadrupole mass spectrometer (Hiden HAL 301/3F) for TPD experiments, a cylindrical mirror analyzer for AES (Omicron, CMA 150) and LEED optics (Specs). Both the first[43,44,47,69-71] and second,[44,47,71-73] chambers have been previously described in more detail.

The rutile TiO_2(110) crystals (Princeton Scientific Corporation, 1 cm x 1 cm x 0.1 cm) were cleaned by Ar^+ sputtering at 1 kV for 20 minutes and subsequent annealing to 950-1000 K for 3 minutes.[44] The resulting crystals were sufficiently conductive for STM as well as electron and ion spectroscopy experiments since this treatment preferentially removed oxygen from the crystal. The crystals were heated via electron bombardment of the Ta backplates,[73,74] and temperatures were monitored by type C or K thermocouples, which were calibrated with an infrared pyrometer.[69] The cleanliness and the order of the TiO_2(110)-(1x1) surface were confirmed by a combination of STM, XPS, LEIS and LEED and AES experiments.

In the first chamber, a commercial metal evaporator (Oxford Applied Research, EGC04) was used to deposit metals via heating by electron bombardment; Co (ESPI,

99.995%) was evaporated from a 2 mm diameter rod, and Au was evaporated from pure pellets (Alfa Aesar, 99.95%) housed in a molybdenum crucible. In the second chamber, Au was evaporated by passing current through a tungsten wire cage surrounding a pure Au pellet, and Co was deposited by passing current through a 0.50 mm diameter tungsten wire (ESPI) around which 0.25 mm diameter Co wire (ESPI, 99.995%) was wrapped. Metal fluxes were monitored using a quartz crystal microbalance (Inficon). The quartz crystal microbalance (QCM) was independently calibrated by depositing submonolayer coverages of Au and Pt onto Ru(0001) and imaging with STM to determine the total fraction of the surface covered. The QCM calibration was checked by depositing one monolayer of the metals on TiO_2(110) and confirming that the disappearance of the Ti LEIS signal occurred at this coverage. One monolayer (ML) is defined with respect to the packing densities of the Au(111) (1.39×10^{15} atoms/cm^2) and Co(0001) (1.83×10^{15} atoms/cm^2) surfaces, respectively. The deposition rate was approximately 0.1 ML/min for both metals.

LEIS experiments were conducted with 600 eV He^+ ions at a scattering angle of 130°, current to the crystal of 25 nA, step size of 0.2 eV, and dwell time of 0.05-0.2 s. Dwell times were adjusted for each surface in order to use the maximum value that resulted in a <10% decrease in the Co and Au signals after seven successive scans. This ensured that the metal signals were not changing due to sputtering effects over the course of heating and acquiring spectra at seven different temperatures. The Au peak was collected over 490-545 eV, while the Co and Ti features were collected over 365-465 eV. A scaled contribution from the Ti peak for clean TiO_2 was subtracted from the spectrum in order to generate a flat baseline for integration of the Co peak.

XPS experiments for the Co(2p) region were carried out with an Al K□ anode, a step size of 0.03 eV and dwell time of 0.2 s. For TPD experiments, the crystal was positioned in front of a shielded quadrupole mass spectrometer,[44,71] the heating rate was 2 K/s, and the crystal was biased at -100 V to avoid damage from electrons generated by the mass spectrometer filament. CO (National Welders, 99.99%) was adsorbed onto the surface at 295 K by positioning the crystal ~2 mm in front of the end of a stainless steel directed dosing tube and leaking CO into the chamber with a pressure rise of 3.0×10^{-10} Torr for 3 min. This exposure resulted in a saturation coverage of CO.

STM experiments were carried out with the sample biased at +2.3 V with respect to the tip using a tunneling current of 0.05 nA-0.1 nA. STM tips were prepared by electrochemically etching 0.38 mm diameter tungsten wire in NaOH,[43] and the tips were conditioned by a combination of Ar^+ ion sputtering and pulsing to high voltage.

Measurements of cluster heights and surface areas from STM images were carried out with an in-house analysis program that is described in more detailed elsewhere.[75] Briefly, this program follows the algorithm developed by Jak et al.[76] to remove steps from the titania surface before automatically measuring cluster heights and diameters. This program also measures the surface area of every cluster in a 1000 Å x1000 Å image. Average heights were determined by measuring the heights for clusters in a 1000 Å x1000 Å image with the exception of the room temperature 25%Co/75%Au and pure Co surfaces, in which 1000 Å x500 Å images containing more than 850 clusters were processed. The reported uncertainties for the room temperature heights are the standard deviations from the cluster height distributions. The reported uncertainties in the cluster densities are the sample standard deviations, which are calculated as the square root of the number of

clusters counted and assumes Poisson statistics. Note that the cluster height is taken as the measure of the cluster size since the diameters are known to be overestimated from tip convolution effects.[43] Typically the diameters are overestimated by a factor of 2.2, and this estimate is calculated from an average cluster diameter based on: the total number of atoms deposited as determined by the quartz crystal microbalance, the average cluster height, the number of clusters/cm^2 and assumes hcp/fcc packing densities for Co and Au. The calculated cluster surface areas were corrected by a factor of $(2.2)^2$ for the overestimation of the cluster diameters due to tip convolution effects.

Computational Methods

Fully spin-polarized periodic density functional theory (DFT) calculations were performed within the generalized gradient approximation (GGA) using the Vienna ab initio simulation package (VASP).[77-79] The revised Perdew-Burke-Ernzerhof (RPBE)[80,81] functional was used to describe the exchange-correlation effects. A (2×2×1) Monkhorst-Pack k-mesh with an energy cutoff of 400 eV was used for all structural relaxations. Energies were calculated with a (5×5×2) k-mesh. The Methfessel-Paxton method[82] of order one with a smearing of 0.2 eV was used to allow for partial occupancy near the Fermi level, and dipole corrections to the total energy were computed with Makov and Payne's modified method.[83] The metal (111) surface was modeled by a [3 × 3] supercell with a four-layer slab thickness and a vacuum spacing of 15 Å. Electronic energies were converged to 10^{-5} eV, and ionic relaxations were considered converged when the forces on the ions were less than 0.02 eV/Å. The atoms in the bottom layer of the slab model (typically Au) were fixed to the bulk position of the metal atoms of this layer, and all other atoms were allowed to relax to minimize the total energy. For all bimetallic calculations,

the equilibrium lattice constant for bulk Au (4.21 Å) was used; this value was calculated from the RPBE functional with a Monkhorst-Pack k-point grid of 11×11×11. Co-Au bimetallic structures were obtained by replacing Au atoms with Co atoms at various positions.

4.3 Results

Scanning Tunneling Microscopy Studies

STM studies of the sequential deposition of Co and Au at room temperature demonstrate that bimetallic clusters can be formed by depositing the more mobile Au atoms on the less mobile Co. The deposition of 0.02 ML of Co on TiO_2 results in clusters with average heights of 3.3±0.9 Å and a cluster density of 4.8±0.2 x10^{12}/cm^2 (Figure 1a). Compared to other metals like Pt,[43,84,85] Rh,[84,85] Ni,[47,86] Cu,[86] Ag and Au[43,51] on TiO_2(110), Co forms many more nucleation sites as well as smaller average cluster sizes. After the deposition of 0.1 ML of Au on the 0.02 ML Co clusters, there is only a small, ~6% increase in cluster density up to 5.1±0.2 x10^{12}/cm^2, indicating that the majority of Au atoms nucleate at existing Co sites (Figure 4.1b). This is consistent with the observed increase in average cluster height to 6.9±2.8 Å as the incoming Au atoms are incorporated into Co clusters to form bimetallic clusters. In the absence of Co clusters, the growth of 0.1 ML Au on TiO_2 (Figure 4.1c) results in much larger clusters (10.0±3.4 Å) with a lower cluster density (2.1±0.1 x10^{12}/cm^2), providing further evidence that Au nucleates at the existing Co clusters in Figure 4.1b. The lower cluster densities for pure Au compared to deposition of pure Co at a coverage five times lower demonstrate that Au is more mobile on the surface than Co. Moreover, the Au clusters are preferentially located at step edges, which are the

favored, high coordination sites on the surface, whereas Co clusters nucleate on terraces due to the inability of the Co atoms to diffuse to the step edge sites.

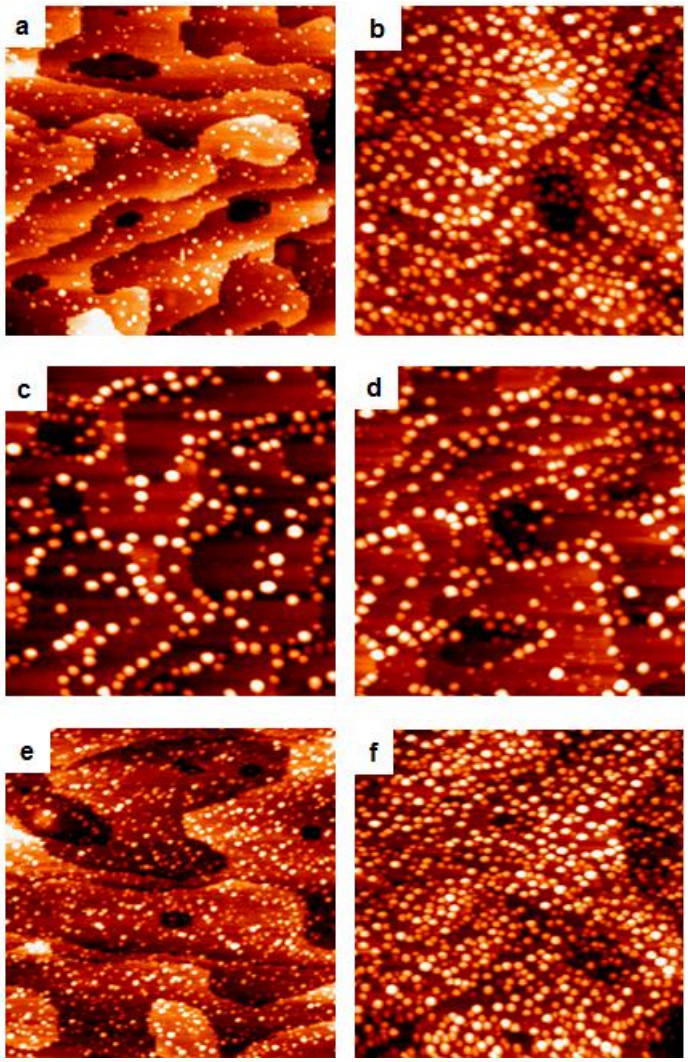

Figure 4.1: STM images of the following metal coverages deposited at room temperature on TiO_2(110): a) 0.02 ML of Co; b) 0.02 ML of Co + 0.1 ML of Au; and c) 0.1 ML of Au; d) 0.1 ML Au + 0.02 ML of Co; e) 0.05 ML of Co; and f) 0.05 ML of Co + 0.1 ML of Au. All images are 1000 Å x1000 Å.

For the reverse order of deposition of 0.02 ML of Co on 0.1 ML of Au (Figure 4.1d), the Co atoms do not nucleate exclusively at Au clusters. After Co deposition, the cluster

density increases to $4.3\pm0.2 \times 10^{12}/cm^2$, and a bimodal distribution consisting of very small clusters of pure Co (~3 Å) and larger, Au-rich clusters (~11 Å) is observed. Thus, the immobile Co atoms are not always able to diffuse to existing Au clusters, and pure Au and pure Co clusters coexist on the surface along with bimetallic clusters. When 0.1 ML of Au is deposited on a higher Co coverage of 0.05 ML (Figures 1e and 1f), the cluster density decreases from $9.2\pm0.3 \times 10^{12}$ to $8.0\pm0.3 \times 10^{12}/cm^2$. This implies that Au nucleates at Co clusters and that cluster coalescence occurs as the individual clusters grow. When the initial coverage of Co clusters is sufficiently high ($\geq$0.05 ML Co) to create a large number of nucleation sites, Au nucleates exclusively at the existing Co clusters.

Given that bimetallic clusters can be formed by the deposition of Co followed by Au, surfaces with varying bimetallic compositions were deposited at room temperature, keeping the total metal coverage fixed at 0.25 ML. The higher metal coverages were employed in order to increase the number of surface sites for chemical studies on Co-Au bimetallic clusters. Figure 4.2 shows STM images of clusters with average Co compositions of 0, 25, 50, 75 and 100%, corresponding to 0.25 ML Au, 0.06 ML Co + 0.19 ML Au, 0.13 ML Co + 0.13 ML Au, 0.19 ML Co + 0.06 ML Au and 0.25 ML Co, respectively.

The cluster densities as well as the average heights of the clusters are presented in Figure 4.3 as a function of Co fraction. The nucleation density increases almost linearly with increasing Co fraction. At the highest Co fractions, small clusters appear to cover almost the entire surface, in contrast to the pure Au clusters, which form larger clusters that leave the majority of the titania surface exposed.

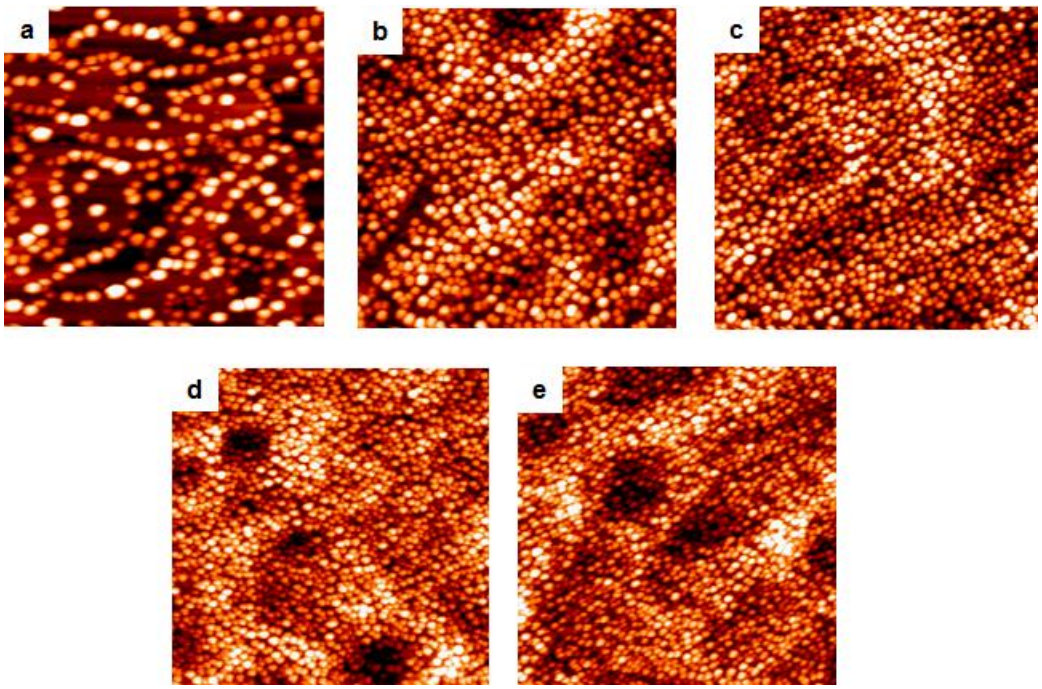

Figure 4.2: STM images of the following metal coverages deposited at room temperature on TiO_2(110): a) 0.25 ML of Au; b) 0.06 ML of Co + 0.19 ML of Au; c) 0.13 ML of Co + 0.13 ML of Au; d) 0.19 ML Co + 0.06 ML of Au; and e) 0.25 ML of Co. All images are 1000Å x1000Å.

Likewise, the average cluster heights at room temperature generally decrease with increasing Co fraction since the higher Co coverages provide a larger number of nucleation sites. The largest decrease in average height occurs between the pure Au clusters (12.7$\pm$4.3 Å) and the 25% Co clusters (8.1$\pm$2.3 Å), with the height then dropping more gradually to 5.5$\pm$1.6 Å for the pure Co clusters; height distributions are shown in Figure A.1a in appendix B.

Changes in surface morphology were studied by STM after heating to 500 K and 800 K for one minute at each temperature to address the effects of cluster sintering. Average heights and cluster densities for the clusters deposited at room temperature and then heated to 500 K and 800 K are shown in Figure 4.3 as a function of bulk Co

composition. Upon heating to 500 K, the average cluster heights increase, and the cluster densities decrease, but the

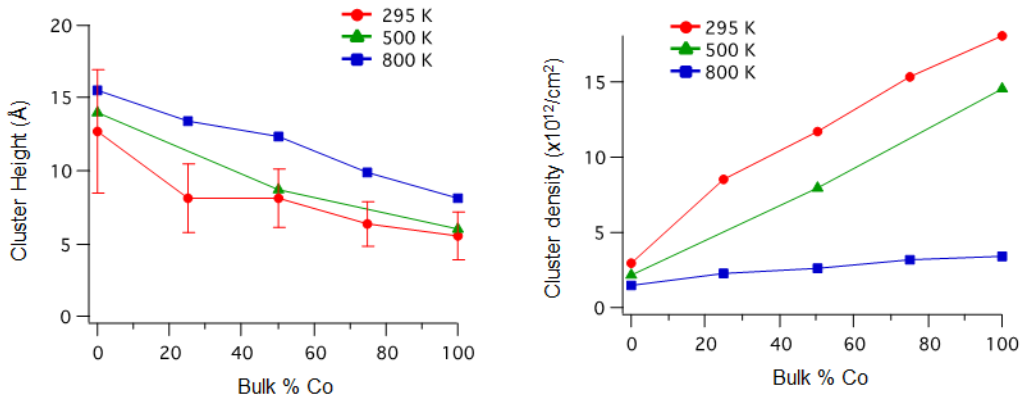

Figure 4.3: Average cluster heights (a) and cluster densities (b) as a function of bulk Co fraction at room temperature and after annealing at 500 K and 800 K for one minute at each temperature. All surfaces have a total metal coverage of 0.25 ML. The error bars shown for the room temperature heights are the standard deviations from the cluster height distributions. Standard deviations for the heights of clusters annealed to 500 K and 800 K are not shown for the sake of clarity but are given in Table S1 of the supporting information.

effects are relatively minor at all compositions compared to changes after heating at 800 K. At 800 K, the number of clusters on the surface is still larger for higher Co fractions, but the decrease in cluster density is only 50% for the pure Au clusters compared to ~70-80% for all of the Co-containing clusters (Figure 4.4). This behavior implies that the Co-containing clusters are more easily sintered than pure Au, and the smaller sizes for the 800 K-annealed clusters with high fraction of Co is attributed to the fact that these clusters have significantly smaller heights and higher cluster densities before annealing.

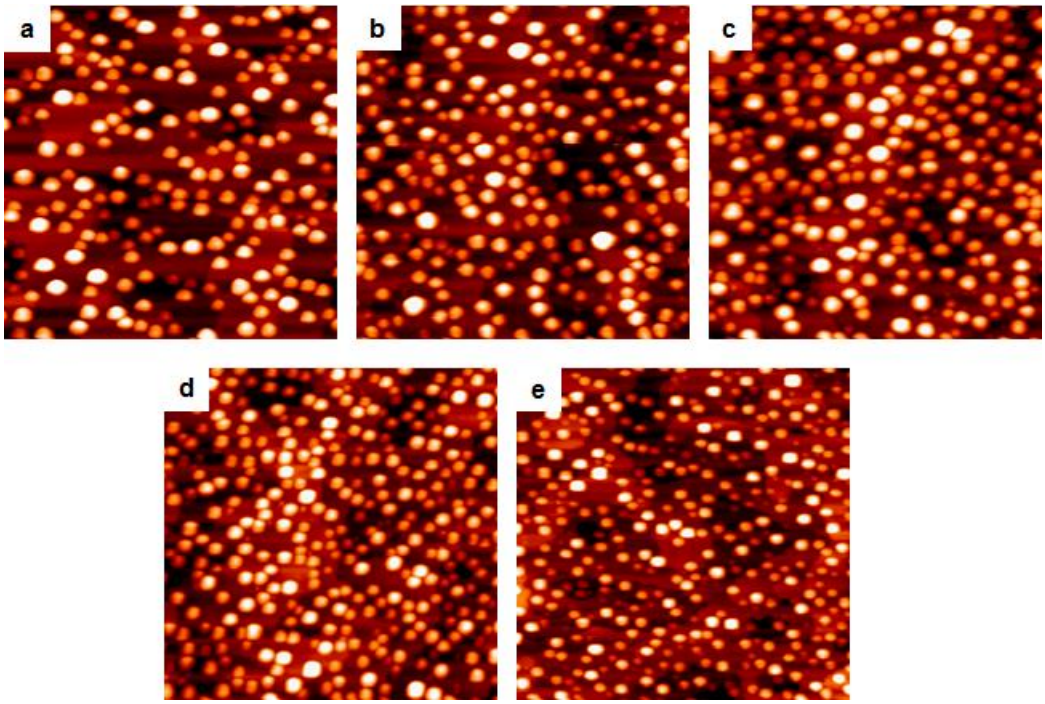

Figure 4.4: STM images of the following metal coverages deposited at room temperature on TiO_2(110) and annealed to 800 K for one minute: a) 0.25 ML of Au; b) 0.06 ML of Co + 0.19 ML of Au; c) 0.13 ML of Co + 0.13 ML of Au; d) 0.19 ML Co + 0.06 ML of Au; and e) 0.25 ML of Co. All images are 1000 Å x1000 Å.

For the pure Au clusters, there is a small increase in average cluster height from 12.7$\pm$4.3 Å at room temperature to 15.5$\pm$4.4 Å after annealing to 800 K. Although the difference in average height is similar for all Co fractions, the height distributions (Figure A.2, appendix B) show that the pure Co surfaces annealed at 800 K consist of small clusters with heights of ~3 Å in addition to larger clusters of 12-14 Å, and the same is true for the other Co-containing surfaces. For higher Co fractions, the number of ~3 Å clusters increases.

Thus, the average height is shifted to lower values by the presence of these small clusters and does not reflect the overall increase in cluster size, which is more apparent from the STM images. The appearance of the ~3 Å clusters after annealing to 800 K is attributed to

small Co clusters that are strongly bound to the TiO_2 surface, very likely at oxygen vacancy defects, and are therefore not mobile on the surface even at 800 K.

Low Energy Ion Scattering and X-ray Photoelectron Spectroscopy Studies

LEIS studies were carried out to characterize the composition of the first monolayer of the clusters. Based on the higher surface free energy for Co compared to Au (1.9 [87-89,90] vs. 1.1 J/cm^2 [87,88,90]) and the immiscibility of the two metals in the bulk,[91] it is expected that the surfaces of the clusters should be Au-rich when Au is deposited on top of Co seed clusters. The relative sensitivities for Co and Au were determined by depositing 10 ML of Co and 30 ML of Au, collecting LEIS data and determining the surface areas of the two films from STM images.[70] The sensitivity for Au is 3.4 times higher than Co in the LEIS experiment, and for these coverages, no Ti is exposed on the surface. A plot of surface Au composition as determined from LEIS vs. the bulk Au % deposited (Figure 4.5) shows that the clusters are rich in Au (85-100%) for Au fractions greater than 50%. However, it is still possible to prepare clusters with both Co and Au at the surface if the Au fraction is sufficiently low. For example, the clusters with 75% Co/25% Au (0.19 ML Co + 0.06 ML Au) have a surface composition of ~60% Au. A calculation of the total surface area of the 0.19 ML Co clusters from the STM images shows that the deposition of 0.06 ML of Au will leave ~40% of the Co surface exposed because the Au coverage is not high enough to completely cover the Co seed clusters. In contrast, a similar calculation for the 50% Co/50%Au clusters illustrates that 0.13 ML of Au provides sufficient Au atoms to completely cover the 0.13 ML Co seed clusters; the fact that cluster surfaces are ~15% Co at this coverage instead of 100% Au is explained by DFT calculations, which are discussed in a later section.

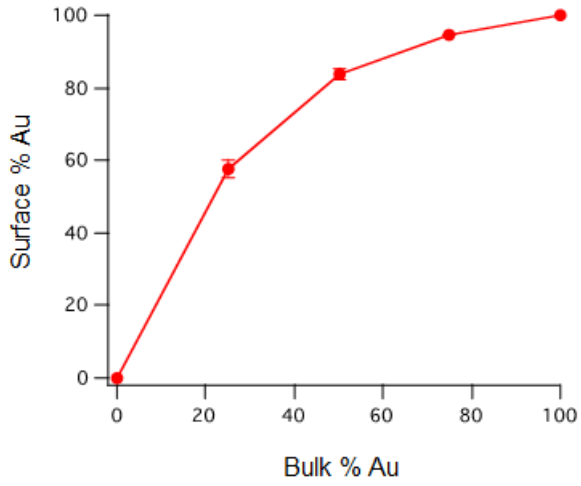

Figure 4.5: The surface % Au from LEIS experiments vs. bulk % Au deposited on the surface for Co-Au clusters of varying compositions. The total coverage of all surfaces was 0.25 ML, and Au was deposited on existing Co seed clusters in order to form bimetallic clusters. The error bars shown are the standard deviations from: 2 experiments at 75% Au, 3 experiments at 25% Au and 4 experiments at 50% Au. In the case of 75% Au, the error bar is smaller than the plot symbol.

It is also important to understand compositional changes in the bimetallic clusters that occur upon annealing. When metal clusters such as Pt,[45,84,92] Rh,[84] Ni,[45,47,70,72] and Pd[93-95] are heated on TiO_2(110) in a reducing environment such as ultrahigh vacuum (UHV), the clusters become encapsulated by TiO_x from the support, and this effect is known as a strong metal support interaction (SMSI).[96-99] It is not known whether Co clusters on titania will also encapsulate upon annealing in UHV, but it is likely that this will occur, given that encapsulation is observed for the neighbors of Co in the periodic table (Rh, Pd, Ni, Fe[100]). To address the issue of encapsulation, the intensity of the Co LEIS signal was monitored as a function of annealing temperature (Figure 4.6, circles).

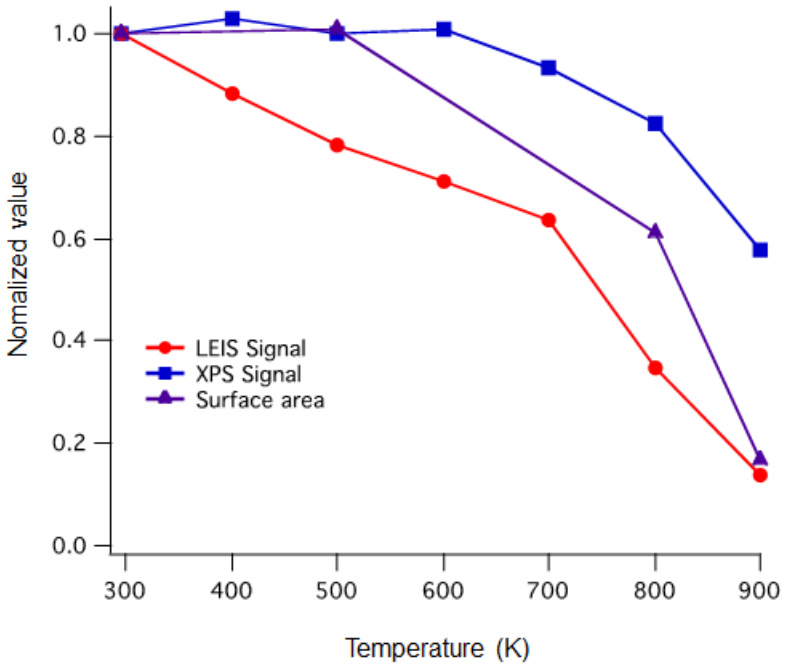

Figure 4.6: A plot of the integrated Co LEIS signal (circles), the integrated Co(2p) XPS signal (squares), and cluster surface area determined by STM (triangles) for 0.25 ML of Co deposited at room temperature and heated to various temperatures for 1 minute. All values are normalized to the values at room temperature.

Between room temperature and 700 K, the decrease in Co LEIS signal is almost linear, reaching 64% of the room temperature value at 700 K. Furthermore, at 800 K and 900 K, there is a more pronounced decrease in signal, which drops to ~14% of the original value after heating to 900 K. The loss in Co signal can be attributed to one of three processes: encapsulation, decrease in surface area due to sintering and Co desorption. Since the LEIS experiment detects only the top monolayer, the change in surface area determined from STM experiments is also plotted on the same graph in order to help distinguish loss of Co surface area due to sintering versus encapsulation (Figure 4.6, triangles). After heating to 500 K, there is no change in surface area, but the surface area then drops to 61% and 17%

of the initial value at 800 K and 900 K, respectively. Although the decrease in surface area and Co LEIS signal is similar at 900 K, the surface area does not diminish as rapidly as the Co LEIS signal at lower temperatures. This implies that the decrease in LEIS signal below 900 K is not solely due to cluster sintering and can be attributed in part to Co encapsulation by titania.

Changes in the XPS Co(2p) intensity for the 0.25 ML Co clusters were also monitored as a function of annealing temperature (Figure 4.6, squares). Up to 700 K, the decrease in the Co signal is less than 10% compared to the signal at room temperature before annealing. This small loss is assigned to either the onset of encapsulation or decrease in surface area due to sintering. At 800 K, the Co XPS signal decreases to 82% of the value at 295 K, and this is coincident with the substantial reduction in LEIS signal at 800 K. At 900 K, it appears that significant Co desorption occurs; the 43% drop in Co XPS signal from the 295 K value cannot be explained by encapsulation by one or two titania layers, which should attenuate the Co signal by only 9% and 17%, respectively,[101] assuming a mean free path for electrons in titania of 3.47 nm[102] at a kinetic energy of 708.6 eV for the Co(2p) photoelectrons excited by the Al K□ source. Note that XPS is much less sensitive to changes in cluster morphology and surface composition compared to LEIS, given that LEIS probes only the first surface monolayer while XPS probes multiple layers into the near-surface region. For average cluster heights of 6.3 Å and 11.9 Å at 295 and 800 K, respectively, the Co XPS signal from the clusters should be 74%-77% of Co signal for a surface where all of the Co atoms are deposited as a single monolayer; this calculation is based on a mean free path of 14 Å[101] and assumes a hemispherical cluster shape. In summary, it is concluded that the majority of the signal lost at 800 K both in the XPS and

LEIS experiments is due to Co encapsulation, whereas Co desorption becomes a significant factor around 900 K.

Changes in both the Co and Au LEIS signals as a function of temperature were studied for the bimetallic clusters of varying compositions with a total metal coverage of 0.25 ML (Figure 4.7). The normalized Co intensity for the pure Co clusters is shown again in order to compare directly with the Co signals for the bimetallic clusters (Figure 4.7a), and all LEIS signals are normalized to the values at room temperature so that relative changes can be seen more clearly. For the 75% Co clusters, the decrease in Co signal with annealing temperature closely follows that for the pure Co clusters. Encapsulation is not complete even at 900 K for the 75% Co and pure Co clusters since the Co signal does not drop to zero but remains at 10-15% of the room temperature value. The Co signals for the 50% Co and 25% Co clusters decrease slightly more rapidly than what is observed for the higher Co fractions, but in general the Co signals follow the same general trend: the loss in Co signal is significant at 800 K, and the Co signal decreases almost to zero at 900 K. The data suggest that the reduction in Co signal is greatest for the clusters with lower Co fractions, but given the low absolute signal intensity for the 25% and 50% Co clusters, it is possible that these differences are within experimental error. The normalized Au signal for the pure Au clusters also decreases with annealing temperature, reaching ~60% of the room temperature value at 800 K and ~40% at 900 K (Figure 4.7b). However, the Au signals for all of the cluster compositions do not drop as quickly as the Co signals. While the 25% Co and 50% Co clusters follow exactly the same trend as the pure Au clusters, the 75% Co clusters have slightly higher values at all temperatures. For example, the decrease in Au signal at 800 K is still ~70% of the room temperature value. This behavior is

attributed to the fact that the 75% Co clusters represent the only composition at which there are not enough Au atoms to completely cover the Co surface. When the surface area decreases after cluster sintering at the higher temperatures, all of the Au atoms can still be accommodated at the cluster surface, and therefore no Au signal is lost due to incorporation of Au atoms into the bulk of the clusters.

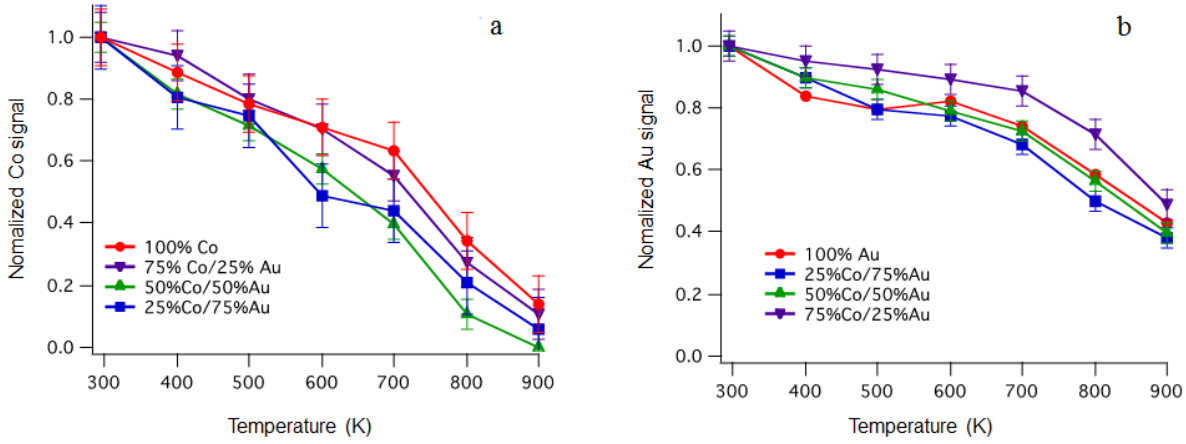

Figure 4.7: LEIS signals as a function of annealing for 1 minute at various temperatures for pure Co, pure Au and Co-Au clusters on TiO_2: a) normalized Co signal; and b) normalized Au signal. Signals are normalized to the initial values at 295 K. Au was deposited on Co clusters at room temperature for various compositions at a total metal coverage of 0.25 ML. The error bars shown are the standard deviations from: 2 experiments at 75% Au and 100% Co, 3 experiments at 25% Au and 4 experiments at 50% Au. For each composition, the maximum standard deviation in the temperature set was used.

Temperature Programmed Desorption Studies

Temperature programmed desorption experiments for CO adsorbed at room temperature were conducted to investigate the surface chemistry on the clusters. Figure 4.8 demonstrates that CO is evolved (28 amu) from pure 0.25 ML Co clusters in a

molecular desorption peak at 370 K and a high temperature peak at 755 K ascribed to recombination of carbon and oxygen atoms from dissociated CO. As the fraction of Au is increased in the 0.25 ML clusters, the CO desorption decreases. Since CO does not adsorb on pure 0.25 ML Au clusters or the TiO_2 support at room temperature, CO desorption is considered to be a measure of the fraction of Co at the cluster surface. The peak temperature for CO desorption shifts down to 350 K as the concentration of Au is initially increased to 25%, and the peak continues to shift to lower temperature (337 K) at 50% and 75% Au. This behavior suggests that the adsorption energy of CO on Co is decreased when the Co atoms are surrounded by Au atoms instead of Co atoms. Note that the change in desorption temperature cannot be attributed to a CO coverage effect; when the Au fraction is increased, the CO coverage should decrease and induce ta shift to higher desorption temperatures as a result of diminished repulsive CO-CO interactions at the lower coverage.[103]

A plot of normalized CO desorption yield and surface composition of Co from the LEIS experiments as a function of bulk Co fraction is shown in Figure 4.9a. The CO yields are normalized against the value for the pure 0.25 ML Co clusters. Since the normalized CO yield and the fraction of surface Co both have a maximum value of unity at a bulk Co composition of 100%, the relative changes for these two values can be easily compared. The CO desorption yield follows the same general trend as the Co surface composition, but for any given bimetallic composition, the normalized CO yields are ~ 10% higher than the fraction of Co atoms at the surface.

Thus, it appears that the strong bonding of CO to Co has a slight effect in inducing the diffusion of Co to the surface. Similar CO-induced diffusion of metals in Ni-Au and Pt-

Au clusters have been observed in previous work,[44,47] and these effects are more pronounced for Ni and Pt than for Co (Figure 4.9b, c), particularly at the 25% and 50% Ni or Pt compositions. In the case of Ni, the normalized CO desorption is 15% and 27 % higher than the fraction of Ni at the surface for the 25% and 50% Ni compositions, respectively. In the case of Pt, this difference is even greater, given that the 50% Pt clusters desorb 36% of the CO that is observed from the pure Pt clusters when the fraction of Pt at the surface is essentially zero in the absence of CO. This difference in the ability of CO to extract Co, Ni and Pt from the subsurface layers of the bimetallic clusters is explained by the relative strengths of the CO-metal bonds. The desorption temperatures for a saturation exposure of CO on the pure clusters are 380 K for Co, 400 K for Ni[47] and 500 K for Pt.[44] The metals with higher CO desorption temperatures form stronger bonds with CO, and CO-induced diffusion of these metals to the cluster surface should occur more readily for the strong metal-CO bonding.

Density Functional Theory Calculations

In order to understand the thermodynamics of Co-Au surfaces in the presence and absence of CO, DFT calculations were carried out on 50% Co/50% Au model surface structures. Four different surface configurations (Figure 4.10a-d) were considered by substituting 50% of the Au atoms with Co atoms in the surface model for pure Au. The relative energies (E_{rel}) of these surfaces with respect to the Au-terminated surface model (Au-Co-Co-Au, Figure 4.10a) are presented in Table 4.1. Based on these results, Co surface layers are highly unstable compared to Au-terminated surfaces, and this is again consistent with the higher surface free energy of Co (1.9 J/cm^2)[87-90] in comparison to Au (1.1. J/cm^2).[87,88,90]

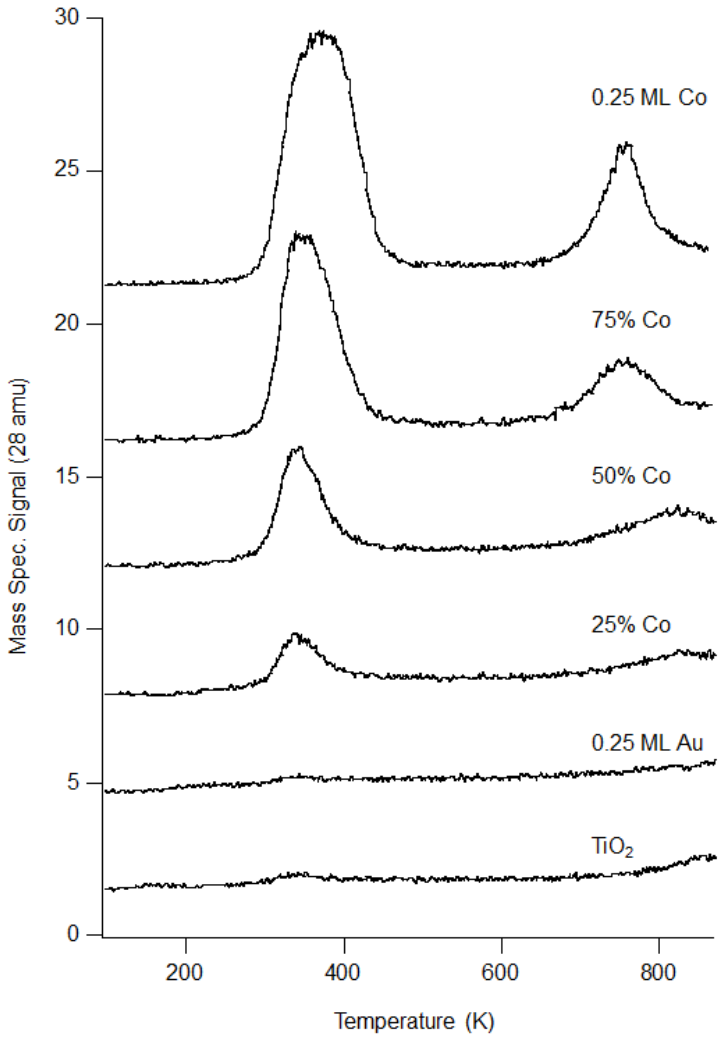

Figure 4.8: TPD experiments for CO adsorbed at room temperature on TiO_2 itself and on clusters ranging from 0-100% Co with a total metal coverage of 0.25 ML. In all cases, the Co was deposited on the surface first, and the heating rate during the TPD experiment was 2 K/s.

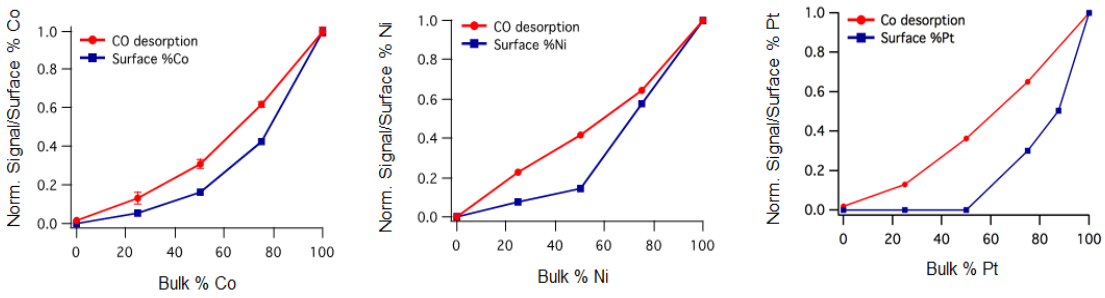

Figure 4.9: Normalized CO desorption yields from TPD experiments and surface % metal from LEIS experiments as a function of bulk % metal deposited on the surface for: a) Co-Au; b) Ni-Au and c) Pt-Au. The CO desorption is normalized to the value on the pure Pt, Ni or Co clusters. The total coverage of all surfaces was 0.25 ML, and Au was deposited on existing metal seed clusters in order to form bimetallic clusters. The error bars for the CO yields on Co are the standard deviations from: 3 experiments on 0.25 ML Co and the 25% Co clusters; 2 experiments on the 75% Co clusters; and 4 experiments on the 50% Co clusters.

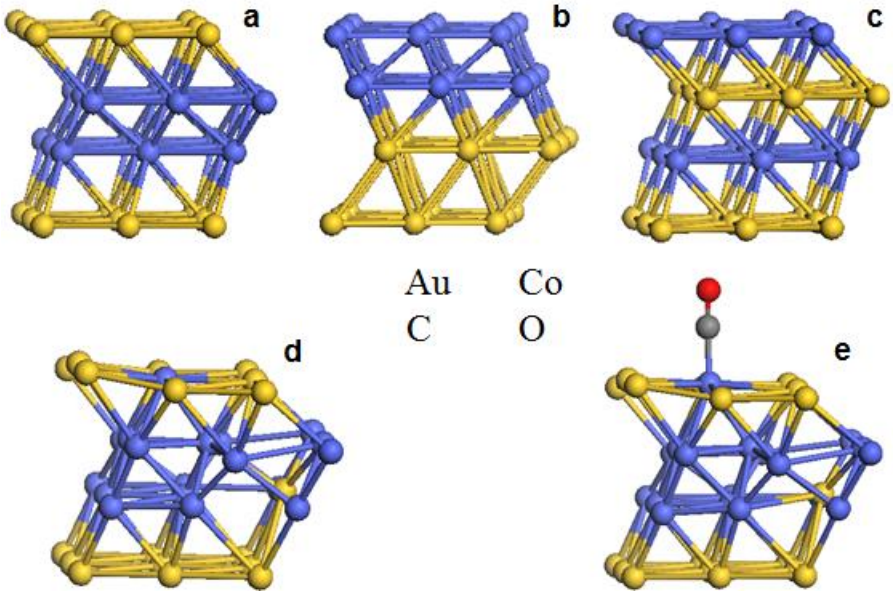

Figure 4.10: Model structures of 50% Co/50% Au surfaces where the bottom Au layer is fixed in bulk Au position: a) Au-Co-Co-Au; b) Co-Co-Au-Au; c) Co-Au-Co-Au; d) structure (a) with one Co atom exchanged from the third layer; and e) CO adsorbed on structure (d).

For the two Co-terminated surfaces, a higher relative energy (E_{rel} = 10.7 eV) was calculated for the configuration with alternating layers of Au and Co (Co-Au-Co-Au, Figure 4.10c). Thus, the immiscibility of the two metals in the bulk results in a preference for two layers of the same metal to cluster together, as in the structure Co-Co-Au-Au (Figure 4.10b, E_{rel} = 4.3 eV). Interestingly, when one Co atom from the third layer is exchanged into the top Au layer for the Au-Co-Co-Au structure (Figure 4.10d), the energy is decreased by 0.4 eV due to a better distribution of strain, and therefore the thermodynamically favored surface is predominantly Au, with a small fraction of Co. This is consistent with the LEIS data, which show that when the Au fraction is high enough for the Au atoms to completely cover the surface of the Co seed clusters, the surfaces are rich in Au (>80%) but still contain some small fraction of Co.

Table 4.1. Computed relative energies (E_{rel}) of the 50% Co/50% Au structures in the presence and absence of CO, and calculated adsorption energies (E_{ads}) of CO on these structures.

Structure	Co-Au clean surface	CO adsorbed on Co-Au	
	E_{rel} (eV)	E_{rel} (eV)	E_{ads} (eV)
Au-Co-Co-Au (Figure 4.10a)	0.0	0.0	-0.8
Co-Co-Au-Au (Figure 4.10b)	4.3	2.4	-2.6
Co-Au-Co-Au (Figure 4.10c)	10.7	8.3	-3.2
Au(Co_1)-Co-Co-(Au_1)-Au (Figure 4.10d)	-0.4	-0.7	-1.1

Next, the stability of these structures in the presence of a CO molecule was investigated. CO adsorption was considered at the atop site of a Au or Co atom on the four surface models (Figure 4.10a-d). The relative energies of these surfaces (Table 4.1) indicate that the Au-terminated surface with one Co atom on the surface (Figure 4.10e) is the most stable among the four surface models and becomes even more preferred than in the absence of CO due to the strong Co-CO bond. The CO adsorption energies (E_{ads}) given in Table 4.1 suggest that CO adsorbs more strongly on Co atoms than on Au atoms. However, CO adsorption is weaker by ~1.5 eV on Co surrounded by Au atoms ($Au(Co_1)$-Co-$Co(Au_1)$-Au, Figure 4.10d) compared to Co surrounded only by Co atoms (Figures 10b). This result is consistent with the TPD data, which demonstrates that the CO desorption temperature is shifted to lower values as the fraction of Au in the clusters is increased. Furthermore, Bader charge analysis indicates that there is a significant amount of charge transfer from Co to the neighboring Au atoms, and the surface Co atom in the $Au(Co_1)$-Co-$Co(Au_1)$-Au model is positively charged (q_{Co} = +0.33). Thus, back donation from the positively charged Co metal to the adsorbed CO is reduced (q_{CO} = -0.28), leading to weaker CO adsorption. In comparison, for the Co-terminated surface (Co-Co-Au-Au), the surface Co atoms are nearly charge neutral (q_{Co} = +0.02), resulting in more back donation of electrons to the adsorbed CO molecule (q_{CO} = -0.40) and a stronger metal-CO bond. Nevertheless, due to the high surface free energy of Co, the stronger CO adsorption is still not sufficient to bring more Co atoms to the surface.

In order to examine whether additional Co atoms can diffuse to the surface when the CO partial pressure is increased, the phase diagram for a 50% Co/50% Au system was

calculated in the presence of CO at a given temperature and CO partial pressure (Figure 4.11a). Approximate Gibbs free energies are calculated using the following equation:

$$\Delta G = E_{nCo(s)-nCO} - E_{1Co(s)} - n\left(E_{CO} + \Delta\mu_{CO}(T, 1\,atm) + k_B T \ln\left(\frac{P}{1\,atm}\right)\right) \quad (1)$$

where $E_{nCo(s)-nCO}$ corresponds to a structure with n Co atoms covered by adsorbed CO on the surface, $E_{1Co(s)}$ corresponds to the energy of the most stable surface in the absence of CO ($Au(Co_1)$-Co-$Co(Au_1)$-Au, Figure 4.10d), $\Delta\mu_{CO}$(T,1 atm) is the (ideal gas) reference chemical potential of CO at temperature T, and P is the partial pressure of CO. The calculated phase diagram in Figure 4.11a suggests that at room temperature and a CO partial pressure of 10^{-9}-10^{-10} atm, ~11-22% of the surface atoms (1-2 out of 9 surface atoms per unit cell) are Co atoms. A much higher partial pressure of CO (10^{-4} atm) is necessary to provide sufficient driving force for a ~33% Co surface composition (3 out 9 surface atoms per unit cell).

To compare this driving force for metal diffusion to the surface in the Co-Au system with the Ni-Au and Pt-Au systems, the phase diagrams for 50% Ni/50% Au and 50% Pt/50% Au structures were also calculated. A similar computational setup as described above for the Co-Au structures was used for Ni-Au and Pt-Au. The most stable structure in the absence of CO for the latter two systems is the Au-surface terminated structure. The diffusion of Ni or Pt atoms to the surface is not thermodynamically favored in the absence of CO, in contrast to the behavior of Co atoms in the Co-Au system.

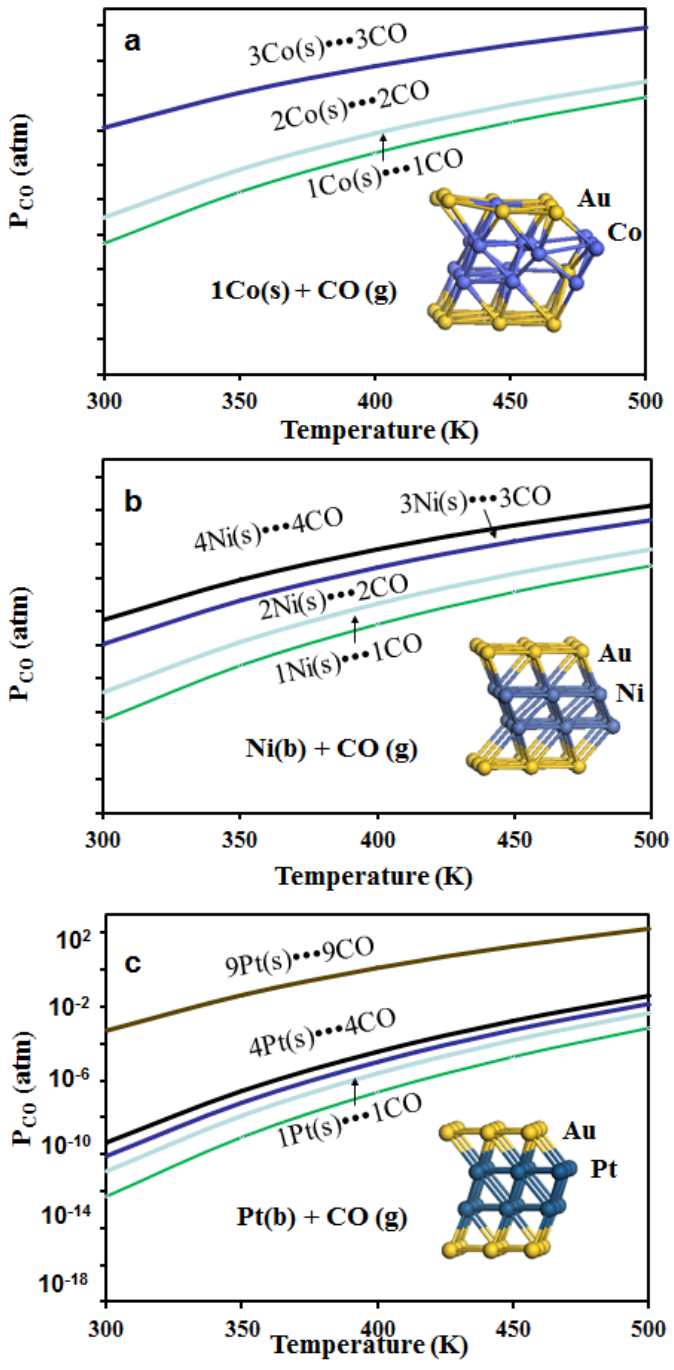

Figure 4.11: Phase diagrams for 50% M/50% Au model surfaces in the presence of CO calculated by constrained ab initio thermodynamics, where M=Co (a), Ni (b), and Pt (c). The most stable structure in the absence of CO is shown in the inset. All other structures are displayed in the supporting information.

The phase diagram for the Ni-Au system (Figure 4.11b) suggests that Ni comprises ~22% (2 out of 9 surface atoms per unit cell) of the surface atoms at room temperature and a CO partial pressure of $<10^{-10}$ atm. Furthermore, at a CO partial pressure of 10^{-6} atm, a surface with ~44% Ni atoms is stable. In the case of the Pt-Au system (Figure 4.11c), CO facilitates Pt migration at even lower CO partial pressures than for Ni in the Ni-Au structures. For example, Pt atoms comprise ~44% of the surface atoms at pressures just above 10^{-10} atm, and the surface consists of nearly pure Pt at CO pressures of $\sim10^{-3}$ atm. Thus, the thermodynamic driving force for CO to extract metal atoms out of the metal-Au systems is stronger for Pt and Ni compared to Co even though a larger fraction of Co atoms can be found at the bimetallic surface in the absence of CO. These computational results are consistent with experimental data illustrating that CO-induced diffusion of Pt and Ni occurs more readily than diffusion of Co in the metal-Au clusters.

4.4 Discussion

Growth, Sintering and Encapsulation

Bimetallic Co-Au clusters are formed on TiO_2(110) by sequential deposition due to the difference in diffusion rates for Co and Au on the surface. When the less mobile Co atoms are deposited first followed by the more mobile Au atoms, the incoming Au atoms nucleate almost exclusively at the existing Co seed clusters. In general, our group has shown that when there is a significant difference in the diffusion rates for the two metals, bimetallic clusters can be prepared via sequential deposition by depositing the less mobile metal first, followed by the more mobile metal; bimetallic cluster growth was observed for sequential deposition of Pt or Ni seed clusters followed by Au[43,44,47] since Pt and Ni also diffuse less readily on the surface compared to Au. Notably, in the reverse order of

deposition of Co deposited on existing Au clusters, Co does not nucleate preferentially at Au sites, and pure Co clusters coexist with clusters that are Au-rich. One major difference between the growth of Co-Au clusters compared to Ni-Au and Pt-Au is that pure Co clusters form many more nucleation sites than the other two metals. Consequently, the cluster density for Co-Au is higher than for the two other bimetallic systems. The high nucleation density for the Co clusters compared to other metals is attributed to the strong Co-titania interfacial energy, as discussed in more detail elsewhere.[104]

For the Co-Au clusters, there is no evidence that the addition of Co suppresses the sintering of the Au clusters, as was previously observed for Pt-Au and Ni-Au clusters on TiO_2(110).[43,44,47] However, the bimetallic Co-Au clusters are smaller than pure Au clusters both before and after annealing, given that Au nucleates at Co seed clusters, and that the slow diffusion of Co on TiO_2 results in a high cluster density. In the cluster sintering process, the first step involves detachment of an adatom from an existing cluster and the second step involves diffusion of the atom on the surface to reach another cluster and contribute to its growth. For metals such as Cu, Ni and Rh on TiO_2(110), previous studies have reported that the rate-limiting step in cluster sintering is adatom detachment rather than adatom diffusion,[85,86] and therefore the extent of sintering diminishes with increased metal-metal bond strength. This is likely to be the case for Au on TiO_2 as well because Au diffuses more readily on the surface than Cu, Ni or Rh; however, since Co diffuses less readily than these other metals, it is possible that adatom diffusion is the rate-limiting step in the sintering of Co clusters. For the Pt-Au clusters, the addition of Pt to Au clusters suppresses sintering because Pt-Pt and Pt-Au bonds are stronger than Au-Au. In the case of Ni, the Ni-Ni bond is only slightly stronger than the Au-Au, and therefore this effect is

much less pronounced. Based on the heats of sublimation for pure Co (425 kJ/mol)[105,106] and Au (370 kJ/mol),[107] the Co-Co bond is predicted to be slightly stronger than Au-Au. Consequently, the Co clusters should sinter less easily than Au clusters if metal-metal bond breaking is the rate-limiting step, in contrast to the STM results. The facile sintering of the Co clusters at higher temperatures is explained by the enhanced diffusion of Co atoms at 800 K, whereas the Au atoms are already sufficiently mobile even at room temperature due to the weaker metal-titania interactions.

In addition to cluster sintering upon annealing, other compositional and structural changes occur at the surfaces of the clusters. The annealing of TiO_2-supported Co clusters in UHV results in encapsulation of the clusters by titania, demonstrated by STM and XPS experiments. This same behavior has been previously reported for metals such as Pt, Ni, Pd, and Rh on TiO_2(110), [45,47,70,72,84,92-95,108] whereas metals like Au and Cu, which do not interact strongly with titania, do not undergo encapsulation.[99,109,110] For the annealed Co-Au clusters on TiO_2, the Co becomes encapsulated by titania while the Au remains exposed, resulting in a network of Au-titania sites at the surface. Similarly, studies of Pt-Au and Ni-Au on TiO_2 annealed in UHV report selective encapsulation of the Pt and Ni at the cluster surface.[43,44,47] A significant difference between the three bimetallic systems is that the clusters containing Co[104] and Ni[111] are encapsulated by stoichiometric titania, whereas the Pt-containing clusters are encapsulated by reduced titania.[45] These surfaces with extended Au-titania interfaces might be useful in increasing the activity of the Au-titania catalysts, assuming active sites are located at the cluster-support interface.[54-56]

Adsorbate-induced Changes in Surface Composition

In the absence of surface adsorbates, the surface composition of the Co-Au clusters is controlled by the relative surface free energies of Co (1.9 J/m^2)[87-90] and Au (1.1 J/m^2).[87,88,90] At bulk Au fractions of >50%, the surface is Au-rich due to the lower surface energy for Au compared to Co. At Au compositions of less than 50%, there is not enough Au present to completely cover the Co seed clusters, and therefore both Co and Au atoms reside at the surface. Likewise, the surfaces of Pt-Au[43,44] and Ni-Au[47] clusters on TiO_2(110) are Au-rich, as dictated by the lower surface free energy of Au, and mixed-metal surfaces can be formed for the Pt-Au and Ni-Au clusters at the lower Au fractions, when there is not enough Au to completely cover the clusters. The surface free energies of Ni (1.7 J/m^2)[87,90,112] and Co are very similar, resulting in nearly identical surface compositions of Au as a function of bulk Au fraction. Given that the Pt surface free energy (2.5 J/m^2)[113] is the highest of the four metals, it is not surprising that the Au fraction is also the highest at any given bulk Au fraction. In other bimetallic systems, the composition of the surface is determined by the relative surface free energies of the metals, as well as the strain energy arising from a mismatch in atomic sizes; thus, the surfaces of Co-Pt alloys are Pt-rich despite the higher surface free energy of Pt.[114,115] However, for the M-Au systems (M=Pt, Ni, Co) studied here, the relative surface free energies of the metals appear to be the dominant factor.

On Co-Au clusters that are rich in Au at the surface, the adsorption of CO results in activity associated with Co rather than Au, suggesting that CO induces the diffusion of Co to the surface. This effect has also been observed for Pt-Au and Ni-Au clusters on TiO_2(110) that are exposed to CO,[44,47] and the extent of CO-induced surface segregation

of Pt and Ni is more extensive than for Co. DFT studies show that metal surface segregation is thermodynamically driven by the formation of strong Co-CO, Pt-CO and Ni-CO bonds. Furthermore, the calculated phase diagrams for model 50% M/50% Au systems (M=Co, Pt, Ni) with Au-M-M-Au structures demonstrate that for a given pressure of CO, Pt atoms are most easily segregated to the surface, followed by Ni atoms and then Co atoms. This behavior is consistent with the relative strengths of the CO-metal bonds, given that on the pure metal clusters, CO has the lowest desorption temperature on Co, followed by Ni and then Pt, which has the highest desorption temperature.

Adsorbate-induced changes in the composition of other bimetallic surfaces have been experimentally observed in a number of systems where strong metal-adsorbate bonds are formed, particularly with oxygen.[116] For example, Chen and coworkers have investigated monolayer metal films of Ni and Co on Pt(111) by DFT, AES, HREELS.[117] After annealing these films to 600 K, Ni and Co diffuse into the surface, creating a Pt-M-Pt structure where M=Ni, Co. However, upon exposure to 400 L of O_2, surface segregation of Ni or Co occurs at 300-450 K. DFT studies show that oxygen binds more strongly to M-Pt-Pt compared to pure Pt, while oxygen binds less strongly to Pt-M-Pt. Thus, the oxygen-induced diffusion of Ni or Co to the surface is thermodynamically driven by formation of strong metal-oxygen bonds. Varga and coworkers' studies of single-crystal NiPt alloys of varying compositions have reported that exposure of these surfaces to oxygen induces segregation of Ni to the surface,[118] and investigations of a $Pt_3Co(110)$ alloy showed that oxygen exposure at 573-773 K induces Co segregation to the surface to form Co oxide.[119] $Cu_3Pt(110)$ alloy surfaces have also undergone Cu surface segregation upon exposure to oxygen at room temperature.[120] Furthermore, studies of PtRh alloy surfaces

indicate that exposure to O_2 or NO at >400 K induces Rh diffusion to the surface to make strong Rh-O bonds.[121-124] Similar to the effect of O_2, exposure to CO induces surface segregation of Pt and Pd at room temperature for AuPt[125] and AuPd[126] systems.

In addition to adsorbate-induced changes in the surfaces of single-crystal alloys and bimetallic films, changes in surface composition have been reported for supported bimetallic clusters. Somorjai and coworkers have shown that the surfaces of supported RhPd and RhPt nanoparticles are controlled by exposure to gases at 573 K and pressures of 100 mtorr. Specifically, reversible changes in surface composition are induced by exposure to an oxidizing (NO or O_2) or reducing (CO or H_2) gas environment. Under reducing conditions, Pd or Pt segregates to the surface, but under oxidizing conditions, the surfaces are Rh-rich due to the stability of Rh oxide compared to Pt or Pd oxide.[127,128]

Theoretical studies have also predicted adsorbate-induced changes in bimetallic surface composition. A DFT study of a AuPd alloy surface showed that CO induces Pd segregation to the surface.[129] Likewise, DFT investigations of PtPd and CoCr illustrated that adsorbed oxygen causes enrichment of Pd or Cr atoms at the surface due to the higher oxygen affinity of these metals compared to Pt and Co, respectively.[130] DFT calculations by Balbuena and coworkers reported that surface segregation in bimetallics can be directly correlated with metal-adsorbate bond strengths, and consequently, the surface segregation of metals for Pt_3M alloys (M=Fe, Co, Ni) is different in vacuum versus in an oxygen environment.[131] For PdAg alloys, Ag prefers to be at the surface under vacuum conditions, but the strong metal-oxygen bonds favor the diffusion of Pd to the surface in the presence of oxygen.[132] Similarly, the exposure of PdAg alloys to hydrogen induces Pd diffusion to the surface, given that the hydrogen binds more strongly to Pd than Ag.[133]

Diffusion of metal atoms from the bulk to the cluster surface is not expected to be kinetically limited at room temperature, and consequently, the bimetallic surface composition will change if exchange of metal atoms from the bulk to the surface of the clusters is thermodynamically favorable. For example, LEIS experiments for NiAu clusters on TiO_2(110) showed that the surfaces of 2 ML of Ni deposited on top of 2 ML Au was 80% Au, demonstrating that Au atoms are sufficiently mobile at room temperature to migrate to the cluster surface.[111] Reports of the CO-induced reconstruction of Pt surfaces at room temperature further support the idea that metal atoms are mobile at room temperature.[134-137] As discussed in the preceding paragraphs, many studies of adsorbate-induced surface segregation occur at or near room temperature, which also implies high mobility of atoms at room temperature.

4.5 Conclusions

Co-Au bimetallic clusters were grown on TiO_2(110) by sequential deposition of Co followed by Au. This resulted in preferential nucleation of Au at existing Co clusters due to the slower diffusion of Co on the surface compared to Au. Although the addition of Co to Au clusters does not inhibit cluster sintering, the sizes of the Co-Au clusters both before and after annealing decrease with increasing Co fraction, given the higher nucleation density of Co seed clusters for the larger Co coverages. At Au fractions of >50%, the cluster surface is rich in Au as a result of the higher surface free energy of Au compared to Co. Furthermore, annealing the Co-Au clusters causes encapsulation of the surface Co by TiO_x while the Au remains uncovered. Exposure of the Co-Au clusters to CO induces migration of Co from the bulk of the cluster to the surface in order to form the strong Co-CO bonds. This CO-induced metal diffusion has also been observed in Pt-Au and Ni-Au

surfaces, but the effect is less pronounced for Co due to the weaker metal-CO bonds. DFT calculations confirm that the surface of the Au clusters should be Au-rich for model bimetallic structures with a 50% Au fraction, and these calculations show that the CO-induced diffusion of metal to the cluster surface follows the trend of Pt>Ni>Co in other metal-Au systems.

4.7 References

(1) Khan, N. A.; Chen, J. G. J. Phys. Chem. B **2003**, 107, 4334-4341.

(2) Kitchin, J. R.; Norskov, J. K.; Barteau, M. A.; Chen, J. G. Phys. Rev. Lett. **2004**, 93, 156801.

(3) Mavrikakis, M.; Hammer, B.; Norskov, J. K. Phys. Rev. Lett. **1998**, 81, 2819-2822.

(4) Schlapka, A.; Lischka, M.; Gross, A.; Kasberger, U.; Jakob, P. Phys. Rev. Lett. **2003**, 91, 4.

(5) Rodriguez, J. A.; Goodman, D. W. Science **1992**, 257, 897-903.

(6) Kolodziej, J. J.; Pelhos, K.; Abdelrehim, I. M.; Keister, J. W.; Rowe, J. E.; Madey, T. E. Prog. Surf. Sci. **1998**, 59, 117-134.

(7) Rodriguez, J. A.; Goodman, D. W. J. Phys. Chem. **1991**, 95, 4196-4206.

(8) Campbell, R. A.; Rodriguez, J. A.; Goodman, D. W.; Ponec, V.; King, D. A.; Niemantsverdriet, H.; Vansanten, R.; Grunert, W.; Chadwick, D.; Bertolini, J. C.; et. al. Stud. Surf. Sci. Catal. **1993**, 75, 333-344.

(9) Rodriguez, J. A.; Campbell, C. T.; Goodman, D. W. Surf. Sci. **1994**, 309, 377-383.

(10) Watwe, R. M.; Cortright, R. D.; Mavrikakis, M.; Norskov, J. K.; Dumesic, J. A. J. Chem. Phys. **2001**, 114, 4663-4668.

(11) Zhou, W.-P.; Yang, X.; Vukmirovic, M. B.; Koel, B. E.; Jiao, J.; Peng, G.; Mavrikakis, M.; Adzic, R. R. J. Am. Chem. Soc. **2009**, 131, 12755-12762.

(12) Kitchin, J. R.; Norskov, J. K.; Barteau, M. A.; Chen, J. G. J. Chem. Phys. **2004**, 120, 10240-10246.

(13) Tsai, Y. L.; Koel, B. E. J. Phys. Chem. B **1997**, 101, 2895-2906.

(14) Tsai, Y. L.; Xu, C.; Koel, B. E. Surf. Sci. **1997**, 385, 37-59.

(15) Panja, C.; Saliba, N. A.; Koel, B. E. J. Phys. Chem. B **2001**, 105, 3786-3796.

(16) Besenbacher, F.; Chorkendorff, I.; Clausen, B. S.; Hammer, B.; Molenbroek, A. M.; Norskov, J. K.; Stensgaard, I. Science **1998**, 279, 1913-1915.

(17) Sinfelt, J. H. Bimetallic Catalysts. Discoveries, Concepts, and Applications; John Wiley and Sons: New York, 1983.

(18) Rodriguez, J. A. Surf. Sci. Rep. **1996**, 24, 223-287.

(19) Campbell, C. Annu. Rev. Phys. Chem. **1990**, 41, 775-837.

(20) Liu, P.; Norskov, J. K. Phys. Chem. Chem. Phys. **2001**, 3, 3814-3818.

(21) Sinfelt, J. H. Acc. Chem. Res. **1977**, 10, 15.

(22) Khan, N. A.; Zellner, M. B.; Chen, J. G. G. Surf. Sci. **2004**, 556, 87-100.

(23) Lu, S. L.; Lonergan, W. W.; Bosco, J. P.; Wang, S. R.; Zhu, Y. X.; Xie, Y. C.; Chen, J. G. J. Catal. **2008**, 259, 260-268.

(24) Hwu, H. H.; Eng, J.; Chen, J. G. G. J. Am. Chem. Soc. **2002**, 124, 702-709.

(25) Murillo, L. E.; Goda, A. M.; Chen, J. G. J. Am. Chem. Soc. **2007**, 129, 7101-7105.

(26) Stottlemyer, A. L.; Ren, H.; Chen, J. G. Surf. Sci. **2009**, 603, 2630-2638.

(27) Do, P. T. M.; Foster, A. J.; Chen, J.; Lobo, R. F. Green Chemistry **2012**, 14, 1388-1397.

(28) Khan, N. A.; Hwu, H. H.; Chen, J. G. J. Catal. **2002**, 205, 259-265.

(29) Greeley, J.; Mavrikakis, M. Nature Materials **2004**, 3, 810-815.

(30) Xu, Y.; Ruban, A. V.; Mavrikakis, M. J. Am. Chem. Soc. **2004**, 126, 4717-4725.

(31) Nilekar, A. U.; Xu, Y.; Zhang, J.; Vukmirovic, M. B.; Sasaki, K.; Adzic, R. R.; Mavrikakis, M. Top. Catal. **2007**, 46, 276-284.

(32) Friebel, D.; Viswanathan, V.; Miller, D. J.; Anniyev, T.; Ogasawara, H.; Larsen, A. H.; O'Grady, C. P.; Norskov, J. K.; Nilsson, A. J. Am. Chem. Soc. **2012**, 134, 9664-9671.

(33) Rodriguez, J. A.; Ma, S.; Liu, P.; Hrbek, J.; Evans, J.; Perez, M. Science **2007**, 318, 1757-1760.

(34) Tang, L. G.; Yamaguchi, D.; Burke, N.; Trimm, D.; Chiang, K. Catal. Commun. **2010**, 11, 1215-1219.

(35) Chen, D. A.; Ratliff, J. S.; Hu, X.; Gordon, W. O.; Senanayake, S. D.; Mullins, D. R. Surf. Sci. **2010**, 604, 574-587.

(36) Mullins, D. R.; Robbins, M. D.; Zhou, J. Surf. Sci. **2006**, 600, 1547-1558.

(37) Senanayake, S. D.; Mullins, D. R. J. Phys. Chem. C **2008**, 112, 9744-9752.

(38) Senanayake, S. D.; Gordon, W. O.; Overbury, S. H.; Mullins, D. R. J. Phys. Chem. C **2009**, 113, 6208-6214.

(39) Zhou, J.; Mullins, D. R. Surf. Sci. **2006**, 600, 1540-1546.

(40) Di Monte, R.; Kaspar, J. Top. Catal. **2004**, 28, 47-57.

(41) Kaspar, J.; Fornasiero, P.; Graziani, M. Catal. Today **1999**, 50, 285-298.

(42) Trovarelli, A. Catal. Rev. Sci. Eng. **1996**, 38, 439-520.

(43) Park, J. B.; Conner, S. F.; Chen, D. A. J. Phys. Chem. C **2008**, 112, 5490-5500.

(44) Tenney, S. A.; Ratliff, J. S.; He, W.; Roberts, C. C.; Ammal, S. C.; Heyden, A.; Chen, D. A. J. Phys. Chem. C **2010**, 114, 21652-21663.

(45) Tenney, S. A.; He, W.; Ratliff, J. S.; Mullins, D. R.; Chen, D. A. Top. Catal. **2011**, 54, 42-45.

(46) Ratliff, J. S.; Tenney, S. A.; Hu, X.; Conner, S. F.; Ma, S.; Chen, D. A. Langmuir **2009**, 25, 216-225.

(47) Tenney, S. A.; He, W.; Roberts, C. C.; Ratliff, J. S.; Shah, S. I.; Shafai, G. S.; Turkowski, V.; Rahman, T. S.; Chen, D. A. J. Phys. Chem. C **2011**, 115, 11112-11123.

(48) Haryanto, A.; Fernando, S.; Murali, N.; Adhikari, S. Energy & Fuels **2005**, 19, 2098-2106.

(49) Shabaker, J. W.; Davda, R. R.; Huber, G. W.; Cortright, R. D.; Dumesic, J. A. J. Catal. **2003**, 215, 344-352.

(50) Haruta, M.; Date, M. Appl. Catal. A **2001**, 222, 427-437.

(51) Valden, M.; Lai, X.; Goodman, D. W. Science **1998**, 281, 1647-1650.

(52) Haruta, M. Catal. Today **1997**, 36, 153-166.

(53) Haruta, M. Cattech **2002**, 6, 102-115.

(54) Haruta, M.; Tsubota, S.; Kobayashi, T.; Kageyama, H.; Genet, M. J.; Delmon, B. J. Catal. **1993**, 144, 175-192.

(55) Green, I. X.; Tang, W.; Neurock, M.; Yates, J. R. Science **2011**, 333, 736-739.

(56) Molina, L. M.; Hammer, B. Appl. Catal. A **2005**, 291, 21-31.

(57) Batista, M. S.; Santos, R. K. S.; Assaf, E. M.; Assaf, J. M.; Ticianelli, E. A. J. Power Sources **2003**, 124, 99-103.

(58) Haga, F.; Nakajima, T.; Yamashita, K.; Mishima, S.; Suzuki, S. Nippon Kagaku Kaishi **1997**, 33-36.

(59) Llorca, J.; Homs, N.; Sales, J.; de la Piscina, P. R. J. Catal. **2002**, 209, 306-317.

(60) Haga, F.; Nakajima, T.; Miya, H.; Mishima, S. Catal. Lett. **1997**, 48, 223-227.

(61) Haga, F.; Nakajima, T.; Yamashita, K.; Mishima, S. React. Kinet. Catal. Lett. **1998**, 63, 253-259.

(62) Jalama, K.; Coville, N. J.; Hildebrandt, D.; Glasser, D.; Jewell, L. L.; Anderson, J. A.; Taylor, S.; Enache, D.; Hutchings, G. J. Top. Catal. **2007**, 44, 129-136.

(63) Jalama, K.; Coville, N. J.; Xiong, H. F.; Hildebrandt, D.; Glasser, D.; Taylor, S.; Carley, A.; Anderson, J. A.; Hutchings, G. J. Appl. Catal. A **2011**, 395, 1-9.

(64) Leite, L.; Stonkus, V.; Ilieva, L.; Plyasova, L.; Tabakova, T.; Andreeva, D.; Lukevics, E. Catal. Commun. **2002**, 3, 341-347.

(65) Li, J. L.; Jacobs, G.; Zhang, Y. Q.; Das, T.; Davis, B. H. Appl. Catal. A **2002**, 223, 195-203.

(66) Jacobs, G.; Das, T. K.; Zhang, Y. Q.; Li, J. L.; Racoillet, G.; Davis, B. H. Appl. Catal. A **2002**, 233, 263-281.

(67) Yeo, B. S.; Bell, A. T. J. Am. Chem. Soc. **2011**, 133, 5587-5593.

(68) Mennemann, C.; Claus, P. Catal. Lett. **2010**, 134, 31-36.

(69) Park, J. B.; Ratliff, J. S.; Ma, S.; Chen, D. A. J. Phys. Chem. C **2007**, 111, 2165-2176.

(70) Zhou, J.; Ma, S.; Kang, Y. C.; Chen, D. A. J. Phys. Chem. B **2004**, 108, 11633-11644.

(71) Tenney, S. A.; Cagg, B. A.; Levine, M. S.; He, W.; Manandhar, K.; Chen, D. A. Surf. Sci. **2012**, 606, 1233-1243.

(72) Ozturk, O.; Park, J. B.; Black, T. J.; Rodriguez, J. A.; Hrbek, J.; Chen, D. A. Surf. Sci. **2008**, 602, 3077-3088.

(73) Varazo, K.; Parsons, F. W.; Ma, S.; Chen, D. A. J. Phys. Chem. B **2004**, 108, 18274-18283.

(74) Illingworth, A.; Zhou, J.; Ozturk, O.; Chen, D. A. J. Vac. Sci. Technol. B **2004**, 22, 2552-.

(75) Ratliff, J. S. The Morphology and Catalytic Activity of Bimetallic Nanoclusters Supported on TiO_2(110). PhD Dissertation, University of South Carolina, 2009.

(76) Jak, M. J. J.; Konstapel, C.; van Kreuningen, A.; Verhoeven, J.; van Gastel, R.; Frenken, J. W. M. Surf. Sci. **2001**, 494, 43-52.

(77) Kresse, G.; Furthmuller, J. Phys. Rev. B **1996**, 54, 11169-11186.

(78) Kresse, G.; Furthmuller, J. Comput. Mat. Sci. **1996**, 6, 15-50.

(79) Kresse, G.; Hafner, J. Phys. Rev. B **1993**, 47, 558-561.

(80) Perdew, J. P.; Burke, K.; Ernzerhof, M. Phys. Rev. Lett. **1996**, 77, 3865-3868.

(81) Hammer, B.; Hansen, L. B.; Norskov, J. K. Phys. Rev. B **1999**, 59, 7413-7421.

(82) Methfessel, M.; Paxton, A. T. Phys. Rev. B **1989**, 40, 3616-3621.

(83) Makov, G.; Payne, M. C. Phys. Rev. B **1995**, 51, 4014-4022.

(84) Ozturk, O.; Ma, S.; Park, J. B.; Ratliff, J. S.; Zhou, J.; Mullins, D. R.; Chen, D. A. Surf. Sci. **2007**, 601, 3099-3113.

(85) Park, J. B.; Ratliff, J. S.; Ma, S.; Chen, D. A. Surf. Sci. **2006**, 600, 2913-2923.

(86) Zhou, J.; Kang, Y. C.; Chen, D. A. Surf. Sci. **2003**, 537, L429-L434.

(87) Chatain, D.; Rivollet, I.; Eustathopoulos, N. J. Chim. Phys. PCB **1986**, 83, 561.

(88) Sangiorgi, R.; Muolo, M. L.; Chatain, D.; Eustathopoulos, N. J. Am. Ceram. Soc. **1988**, 71, 742.

(89) Chatain, D.; Rivollet, I.; Eustathopoulos, N. J. Chim. Phys.-Chim. Biol. **1987**, 84, 201-203.

(90) Campbell, C. T. Surf. Sci. Rep. **1997**, 27, 1-111.

(91) Binary Alloy Phase Diagrams; 2nd ed.; Massalski, T. B.; International, A.; Okamoto, H., Eds.; ASM International: Materials Park, OH, 1990.

(92) Pesty, F.; Steinrück, H.-P.; Madey, T. E. Surf. Sci. **1995**, 339, 83-95.

(93) Bowker, M.; Fourre, E. Appl. Surf. Sci. **2008**, 254, 4225-4229.

(94) Bennett, R. A.; Stone, P.; Bowker, M. Catal. Lett. **1999**, 59, 99-105.

(95) Bowker, M.; Stone, P.; Morrall, P.; Smith, R.; Bennett, R.; Perkins, N.; Kvon, R.; Pang, C.; Fourre, E.; Hall, M. J. Catal. **2005**, 234, 172-181.

(96) Tauster, S. J.; Fung, S. C.; Garten, R. L. J. Am. Chem. Soc. **1978**, 100, 170-175.

(97) Tauster, S. J. Acc. Chem. Res. **1987**, 20, 389-394.

(98) Tauster, S. J.; Fung, S. C.; Baker, R. T. K.; Horsley, J. A. Science **1981**, 211, 1121-1125.

(99) Diebold, U.; Pan, J. M.; Madey, T. E. Surf. Sci. **1995**, 333, 845-854.

(100) Pan, J. M.; Madey, T. E. J. Vac. Sci. Technol. A **1993**, 11, 1667-1674.

(101) Feldman, L. C.; Meyer, J. W. Fundamentals of Surface and Thin Film Analysis; P T R Prentice-Hall, Inc.: Englewood Cliffs, NJ, 1986.

(102) Surface Analysis: The Principal Techniques; Vickerman, J. C., Ed.; John Wiley and Sons: New York, 1997.

(103) Bridge, M. E.; Comrie, C. M.; Lambert, R. M. Surf. Sci. **1977**, 67, 393-404.

(104) Galhenage, R. P.; Yan, H.; Park, N.; Henkelman, G.; Albrecht, P.; Mullins, D. R.; Chen, D. A. to be sumbmitted to Surf. Sci. **2012**.

(105) NIST-Janaf Thermochemical Tables, J. Phys. Chem. Ref. Data; Fourth ed.; Chase, M. W., Ed.; American Institute of Physics: Melville, NY, 1998; Vol. Monograph 9, pp 1-1951.

(106) Dean, J. A. Lange's Handbook of Chemistry, 15th ed.; McGraw-Hill: New York, 1998.

(107) Hildenbrand, D. L.; Hall, W. F. J. Phys. Chem. **1962**, 66, 754-&.

(108) Baker, T. A.; Kaxiras, E.; Friend, C. M. Top. Catal. **2010**, 53, 365-377.

(109) Diebold, U.; Pan, J. M.; Madey, T. E. Phys. Rev. B **1993**, 47, 3868-3876.

(110) Zhang, L.; Persaud, R.; Madey, T. E. Phys. Rev. B **1997**, 56, 10549-10557.

(111) Jacobsen, C. J. H.; Dahl, S.; Clausen, B. S.; Bahn, S.; Logadottir, A.; Norskov, J. K. J. Am. Chem. Soc. **2001**, 123, 8404-8405.

(112) Peden, C. H. F.; Kidd, K. B.; Shinn, N. D. J. Vac. Sci. Technol. A **1991**, 9, 1518.

(113) Jiang, Q.; Lu, H. M.; Zhao, M. J. Phys. Condens. Matter **2004**, 16, 521-530.

(114) Nilekar, A. U.; Sasaki, K.; Farberow, C. A.; Adzic, R. R.; Mavrikakis, M. J. Am. Chem. Soc. **2011**, 133, 18574-18576.

(115) Gauthier, Y.; Baudoing-Savois, R.; Bugnard, J. M.; Hebenstreit, W.; Schmid, M.; Varga, P. Surf. Sci. **2000**, 466, 155-166.

(116) Menning, C. A.; Chen, J. G. G. J. Chem. Phys. **2009**, 130.

(117) Menning, C. A.; Hwu, H. H.; Chen, J. G. G. J. Phys. Chem. B **2006**, 110, 15471-15477.

(118) Weigand, P.; Novacek, P.; van Husen, G.; Neidhart, T.; Varga, P. Surf. Sci. **1992**, 269-270, 1129-1134.

(119) An, K. S.; Kimura, A.; Ono, K.; Kamakura, N.; Kakizaki, A.; Park, C. Y.; Tanaka, K. Surf. Sci. **1998**, 401, 336-343.

(120) Shen, Y. G.; O'Connor, D. J.; Wandelt, K. Surf. Sci. **1998**, 410, 1-14.

(121) Tanaka, K. I.; Sasahara, A. J. Mol. Catal. A **2000**, 155, 13-22.

(122) Hirano, H.; Yamada, T.; Tanaka, K.; Siera, J.; Nieuwenhuys, B. E. Surf. Sci. **1989**, 222, L804-L808.

(123) Tamura, H.; Tanaka, K. Langmuir **1994**, 10, 4530-4533.

(124) Matsumoto, Y.; Okawa, Y.; Fujita, T.; Tanaka, K. Surf. Sci. **1996**, 355, 109-114.

(125) Bouwman, R.; Sachtler, W. M. H. J. Catal. **1970**, 19, 127-139.

(126) Gao, F.; Wang, Y. L.; Goodman, D. W. J. Phys. Chem. C **2009**, 113, 14993-15000.

(127) Tao, F.; Grass, M. E.; Zhang, Y. W.; Butcher, D. R.; Aksoy, F.; Aloni, S.; Altoe, V.; Alayoglu, S.; Renzas, J. R.; Tsung, C. K.; et. al. J. Am. Chem. Soc. **2010**, 132, 8697-8703.

(128) Tao, F.; Grass, M. E.; Zhang, Y. W.; Butcher, D. R.; Renzas, J. R.; Liu, Z.; Chung, J. Y.; Mun, B. S.; Salmeron, M.; Somorjai, G. A. Science **2008**, 322, 932-934.

(129) Soto-Verdugo, V.; Metiu, H. Surf. Sci. **2007**, 601, 5332-5339.

(130) Dianat, A.; Zimmermann, J.; Seriani, N.; Bobeth, M.; Pompe, W.; Ciacchi, L. C. Surf. Sci. **2008**, 602, 876-884.

(131) Ma, Y. G.; Balbuena, P. B. Surf. Sci. **2009**, 603, 349-353.

(132) Kitchin, J. R.; Reuter, K.; Scheffler, M. Phys. Rev. B **2008**, 77, 075437.

(133) Lovvik, O. M.; Opalka, S. M. Surf. Sci. **2008**, 602, 2840-2844.

(134) Gritsch, T.; Coulman, D.; Behm, R. J.; Ertl, G. Phys. Rev. Lett. **1989**, 63, 1086-1089.

(135) Thiel, P. A.; Behm, R. J.; Norton, P. R.; Ertl, G. J. Chem. Phys. **1983**, 78, 7448-7458.

(136) Tao, F.; Dag, S.; Wang, L. W.; Liu, Z.; Butcher, D. R.; Salmeron, M.; Somorjai, G. A. Nano Lett. **2009**, 9, 2167-2171.

(137) Tao, F.; Dag, S.; Wang, L. W.; Liu, Z.; Butcher, D. R.; Bluhm, H.; Salmeron, M.; Somorjai, G. A. Science **2010**, 327, 850-853.

Chapter 5. Understanding the growth and chemical activity of Co-Pt bimetallic Clusters on TiO2(110): CO adsorption and methanol reaction

5.1 Introduction

Co-Pt bimetallic systems are known to exhibit superior catalytic activity compared to pure Co or pure Pt. Co-Pt bimetallic surfaces have attracted interest as electrocatalysts due to their improved activity for the oxygen reduction reaction (ORR) at the cathode of direct methanol fuel cells (DMFCs).[1-5] While Pt is typically used as the cathode catalyst for ORR, there is an ongoing search for Pt-based alloys that are both more active and more resistant to methanol crossover from the anode to the cathode through the polymer electrolyte membrane.[1,6-11] Co-Pt alloys exhibit higher activity for ORR than Pt alone and are also more active in the presence of methanol.[1-3,12,13] In addition, Co-Pt catalysts have superior properties compared to pure Pt for methanol oxidation at the anode.[1,14-16] As an anode catalyst, Pt has the highest activity for dissociative adsorption of methanol of any of the transition metals,[1] but the kinetics for methanol oxidation are slow, and Pt is easily poisoned by CO, which is a byproduct of methanol oxidation.[1,8,17-19]

The higher activity for Co-Pt in ORR is attributed to electronic modification of Pt by Co.[20] For example, Stamenkovic et al. reported that activity for ORR is 3-4 times greater on an annealed Pt_3Co alloy surface covered by a layer of segregated Pt, as compared to pure Pt.[2,3] Ultraviolet photoemission spectroscopy studies show that the segregated Pt monolayer, or Pt "skin," is electronically modified by the underlying Co, resulting in a shift of the d-band center away from the Fermi level.[2,4,5] Density functional theory (DFT) calculations for a Pt monolayer with Co in the second layer demonstrate that oxygen binds more weakly to this surface than to unmodified Pt,[21-23] and activity is promoted by reducing oxygen poisoning on the Co-modified Pt.[24] DFT calculations by Mavrikakis and coworkers confirm that the binding of oxygen to the Pt monolayer supported on CoPt is

lower than on pure Pt, and this is attributed to the shifting of the d-band away from the Fermi level.[24]

Furthermore, there have been a number of reports of synergistic activity observed on Co-Pt bimetallic surfaces for reactions other than ORR and methanol oxidation. For example, the desorption of H_2 is reported to occur at much lower temperature on Co-Pt bimetallic surfaces compared to pure Co or Pt.[25] Greater activity for hydrogenation has been also observed on the Co-Pt bimetallic systems; low temperature self-hydrogenation of cyclohexene to cyclohexane occurs at 220 K on 1 ML Co films on Pt(111) but does not occur on either Pt(111) or thick Co films on Pt(111).[26] Moreover, higher activity for CO_2 reforming of methane to synthesis gas is observed on supported Co-Pt catalysts due to decreased coking on the bimetallic catalysts.[27] Finally, activity for the hydrogenation of crotonaldehyde to crotyl alcohol has also been observed on Co-Pt particles supported on silica, whereas this reaction does not occur on pure Co or pure Pt surfaces.[28]

In the work reported here, Co-Pt clusters were deposited on TiO_2(110) in order to investigate whether activity for methanol reaction and CO adsorption are altered due to Co-Pt interactions on the bimetallic surfaces. Co-Pt bimetallic clusters were grown via sequential deposition of 0.13 ML of Co on 0.13 ML Pt, or 0.13 ML Pt on 0.13 ML Co. Although the diffusion length of Co is shorter than that of Pt, when the cluster density of the first metal provides sufficient nucleation sites for the growth of the second metal, exclusively bimetallic clusters are formed. The surface compositions of Co-Pt clusters with varying metal fractions are always Pt-rich, but the top monolayer is comprised of both Pt and Co atoms for all compositions studied (30% Co-80% Co). For the adsorption of CO on the bimetallic clusters, desorption from Co and Pt sites is observed at high Co fractions,

and the desorption temperature for CO on Pt decreases with increasing Co fraction. Methanol reaction on the pure and bimetallic Co-Pt clusters produces CO and H_2 as the main products, with methane as a minor product. However, on the bimetallic clusters, C-H bond breaking occurs at higher temperature, and the selectivity for C-O bond scission to produce methane is increased over C-H bond scission to produce CO. Co on Pt and Pt on Co clusters with a 55% Co fraction exhibit nearly identical surface compositions and chemical activity, illustrating the high mobility of atoms within the clusters at room temperature.

5.2 Experimental

All experiments were carried out in two UHV vacuum chambers ($P<1x10^{-10}$ Torr), which have been described in detail elsewhere.[29-36] The first chamber is equipped with a variable-temperature STM (Omicron VT-25), a hemispherical analyzer (Omicron EA125) for low energy ion scattering and X-ray photoelectron spectroscopy experiments, and low energy electron diffraction (LEED) optics (Omicron).[29-34] The second chamber is equipped with a quadrupole mass spectrometer for TPD studies (Hiden HAL 301/3F), a cylindrical mirror analyzer for Auger electron spectroscopy (Omicron CMA 150) and LEED optics (Omicron).[32-36]

Metals were grown on rutile TiO_2(110) crystals (Princeton Scientific Corp., 1 cm x 1 cm x 0.1 cm), which were prepared by multiple cycles of Ar^+ sputtering for 20 min, followed by heating to 950-1000 K for 3 min. This treatment reduced the crystals by removing oxygen and resulted in n-type semiconductors that are sufficiently conductive for STM experiments. The cleanliness and crystallinity of the surfaces were confirmed with a combination of STM, LEIS, Auger electron spectroscopy and LEED experiments.

The crystals were mounted onto Ta back plates using Ta foil straps, and sample heating was achieved via radiative heating from a tungsten filament positioned behind the back plates, as well as by electron bombardment when the samples were held at a positive potential. The temperature of the crystals was measured using either a type K or type C thermocouple spotwelded to the edge of the back plate, and the thermocouples were independently calibrated with an infrared pyrometer (Heitronics).[29]

In the first chamber, Co and Pt were deposited from pure Co and Pt rods (ESPI, 99.95%) using an Oxford electron-beam evaporator (EGC04), and the metal flux was measured with an independently calibrated quartz crystal microbalance (Inficon XTM-2) before every deposition.[37] In the second chamber, Pt was deposited from a Pt rod using an Omicron evaporator (EFM3), while Co was deposited from a homemade source consisting of Co wire (0.25 mm diameter, ESPI, 99.95%) wrapped around a tungsten wire (0.50 mm) through which current was passed. The Co flux was calibrated with a quartz crystal microbalance (QCM) before each deposition; for Pt deposition, the internal flux monitor of the evaporator was used to control Pt flux, and the flux monitor readings were initially calibrated with a QCM. A coverage of one monolayer (ML) of Co or Pt is defined as the packing density of the Co(0001) (1.83×10^{15} atoms/cm^2) or Pt(111) (1.50×10^{15} atoms/cm^2) surface, respectively. The deposition rates were 0.1 ML/min for Co and 0.050-0.1 ML/min for Pt.

The surfaces were exposed to CO (National Welders, 99.99%) and methanol (Fisher Scientific, 99.9%) via a stainless steel directed dosing tube. CO was used as received, and methanol was purified by 3-4 freeze-pump-thaw cycles before each dose. During CO exposure, the sample temperature was held at 300 K, and a saturation exposure

of CO was achieved by leaking in CO at a pressure rise of 3.0×10^{-10} Torr for 3 min. Saturation exposures of methanol at 100 K were determined from the appearance of the methanol multilayer peak in the TPD data. In TPD experiments, the crystal was heated at a constant rate of 2 K/s in front of the mass spectrometer. The crystal was positioned ~2 mm in front of a 4 mm diameter hole cut in the shroud of the mass spectrometer in order to prevent detection of products desorbing from the sample holder. The crystal was biased at -100 V during TPD experiments to prevent damage from the electrons emitted by the mass spectrometer filament. Nine masses were collected in a typical TPD experiment; during wide mass scan experiments to check for additional products, 40 mass channels were monitored in a single experiment. No carbon was detected on the surface in post-TPD Auger experiments after methanol or CO adsorption/reaction.

STM experiments were carried out at a +2.3 V sample bias with tunneling currents of 0.05-0.1 nA. STM tips were prepared by electrochemically etching a 0.38 mm tungsten wire, and tips were also conditioned by Ar^+ sputtering and pulsing to high voltage.[31] Average cluster heights were measured using an in-house program described elsewhere.[33,38] For the surfaces heated to 800 K, all clusters in a 1000 Å x 1000 Å image were analyzed; for all other surfaces, a 1000 Å x 500 Å region was used for the measurement. The number of clusters analyzed in a single image ranged from 300-870. Given that the diameters of the clusters are known to be overestimated due to tip convolution effects,[31,37,39,40] the cluster heights are used as a measure of cluster size. Based on the coverage determination from the QCM, cluster diameters appear to be overestimated by a factor of ~2.2.[31,41]

LEIS data were acquired with a 600 eV He^+ ion beam, a 25 nA current to the sample, a step size of 0.2 eV, and a dwell time of 0.05-0.14 s. The total acquisition time for each spectrum was adjusted to minimize loss of metal from the surface due to He^+ sputtering. In all cases, the Co and Pt signals decreased by less than 10% after seven successive scans, which corresponds to the seven different temperatures investigated. For some cluster compositions, changes in Co and Pt signals as a function of temperature were monitored in two separate experiments in order to minimize beam damage.

5.3 Results

Growth of Bimetallic Clusters

STM images for Pt, Co and Co-Pt clusters deposited on TiO_2(110) at room temperature indicate that bimetallic clusters can be prepared via sequential deposition for both Co on Pt and Pt on Co. Figure 5.1 compares STM images for 0.13 ML of pure Co (Figure 5.1a) and 0.13 ML of pure Pt (Figure 5.1c) deposited on TiO_2; both metals grow as three-dimensional clusters, which are shown as bright features in the STM images. The average cluster height and cluster densities for the Co and Pt clusters are 3.8 ± 1.0 Å and $1.25\text{x}10^{13}\text{cm}^{-2}$ and 5.2 ± 1.7 Å and $1.02\text{x}10^{13}$ cm^{-2}, respectively. The smaller cluster sizes and higher densities for Co demonstrate that the Co atoms are less mobile on the surface than Pt atoms. Furthermore, the higher mobility of Pt atoms on the surface results in a tendency to nucleate at the step edges, which are the preferred low-coordination sites, although Pt clusters nucleate on the terraces as well. In contrast, the Co clusters show no preference for residing at the step edges, implying that the short diffusion length for Co atoms prevents the atoms from reaching the step edges. Previous STM and DFT studies of the growth of Co, Pt and other metals on TiO_2(110) report that the rate of diffusion of

the metals on the TiO_2 surface decreases with increasing metal-titania bonding, which also follows the metal-oxygen bond strengths.[41] Since Pt-O bonds are weaker than Co-O, the diffusion rate of Pt is expected to be higher than that of Co.

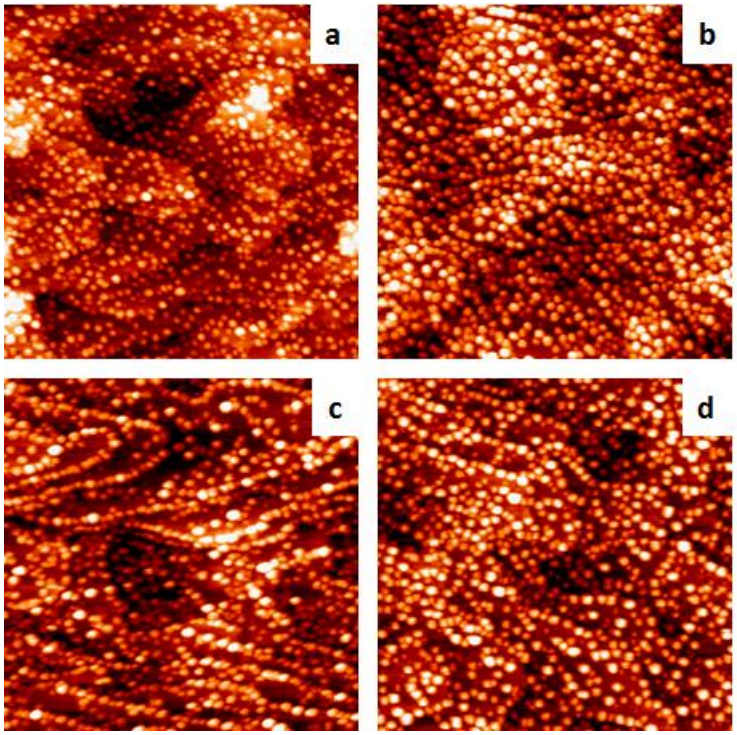

Figure 5.1: Scanning tunneling microscopy images for the following metal coverages deposited on TiO_2(110) at room temperature: a) 0.13 ML of Co; b) 0.13 ML of Co+0.13 ML of Pt; c) 0.13 ML of Pt; and d) 0.13 ML Pt+0.13 ML Co. All images are 1000 Å x1000 Å.

When 0.13 ML of Pt is deposited on top of the 0.13 ML Co seed clusters, the average cluster height increases to 6.1$\pm$1.5 Å, but there is no appreciable increase in cluster density (1.27×10^{13} cm^{-2}), as shown in Figure 5.1b. This behavior implies that the incoming Pt atoms are incorporated into existing Co clusters rather than nucleating new clusters of

pure Pt. For the reverse order of deposition of 0.13 ML Pt + 0.13 ML Co (Figure 5.1d), there is also an increase in average cluster height to 6.8 Å$\pm$1.9 Å, while the cluster density does not change significantly; the 1.05×10^{13} cm^{-2} cluster density is <2% higher than before Co deposition. Despite the fact that the mobility of Pt is higher than Co, mainly bimetallic clusters are formed from deposition of Co on Pt because at these coverages, the number of Pt seed clusters formed is high enough to serve as nucleation sites for all of the deposited Co. However, the cluster sizes are smaller and the cluster densities are larger for bimetallic clusters prepared by depositing Pt on Co. Bimetallic surfaces of varying compositions were prepared by depositing the less mobile Co atoms first and keeping the total metal coverage fixed at 0.25 ML.

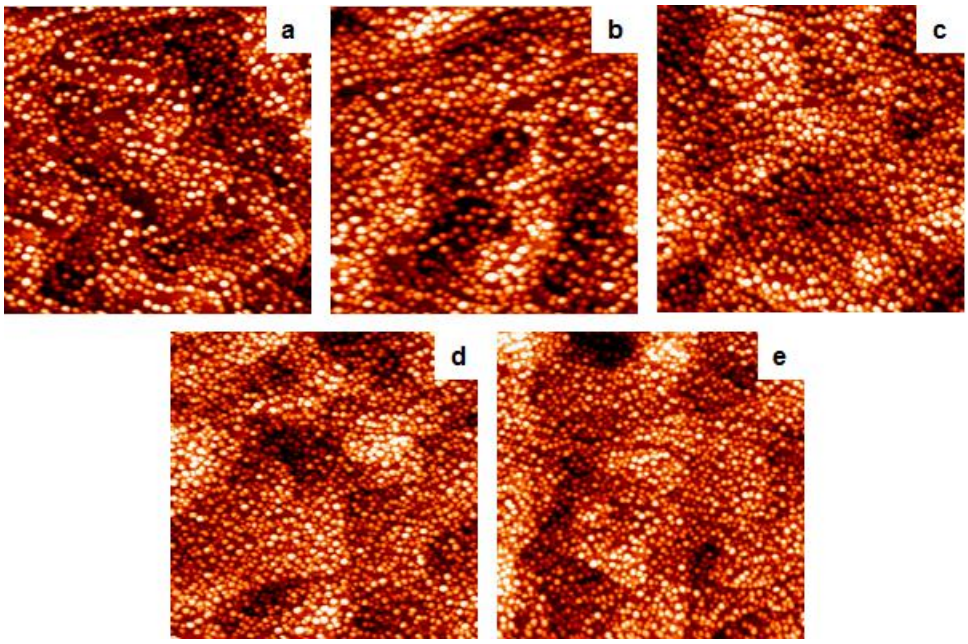

Figure 5.2: Scanning tunneling microscopy images for the following clusters deposited on TiO_2(110) at room temperature at a total metal coverage of 0.25 ML: a) 100% Pt; b) 30% Co+70% Pt; c) 55% Co+ 45% Pt; d) 80% Co+20% Pt and e) 100 % Co. All images are 1000 Å x1000 Å.

Figure 5.2 shows STM images for pure Pt, 30% Co, 55% Co, 80% Co and pure Co clusters. These compositions correspond to 0.25 ML Pt, 0.06 ML Co+0.19 ML Pt, 0.13 ML Co+0.13 ML Pt, 0.19 ML Co+0.06 ML Pt, and 0.25 ML Co, respectively, after accounting for the higher packing density of Co compared to Pt in 1 ML of the metal. For all of the surfaces except for the pure Co clusters, the average cluster heights are similar, ranging from 6.0-6.2 Å (Table 5.1). The pure Co clusters are distinctly smaller with an average height of 5.2+1.5 Å. All of the surfaces exhibit relatively narrow size distributions based on the standard deviations for the average height measurements, which vary from 1.5-2.1 Å.

These same five surfaces were annealed to 800 K for 1 minute in order to understand changes in cluster size upon heating.

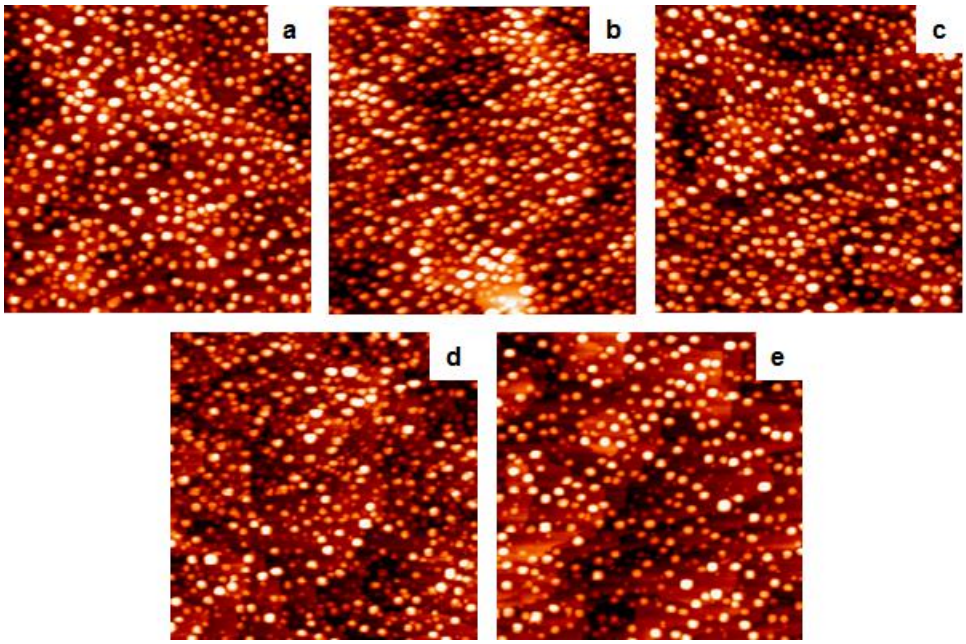

Figure 5.3: Scanning tunneling microscopy images for the following clusters deposited on TiO_2(110) at room temperature at a total metal coverage of 0.25 ML, and then heated to 800 K for 1 minute: a) 100% Pt; b) 30% Co+70% Pt; c) 55% Co+45% Pt; d) 80% Co+20% Pt and e) 100 % Co. All images are 1000 Å x1000 Å.

The resulting STM images demonstrate that the annealed Pt clusters exhibit the largest cluster sizes (9.4±2.7 Å) compared to the other surfaces, which are all in the range of 6.7-7.4 Å (Figure 5.3). Histograms for the cluster heights (Figure 5.4) indicate that the

Table 5.1. Average Cluster Heights for Pt-Co Bimetallic Clusters.

Composition	Height (Å) 300 K	Height (Å) 500 K	Height (Å) 800 K
0.25 ML Co	5.2±1.5	5.4±1.7	7.4±2.9
0.19 ML Co+0.06 ML Pt	6.1±1.7	5.7±1.6	6.7±2.7
0.13 ML Co+0.13 ML Pt	6.1±1.5	6.8±1.9	7.0±2.4
0.13 ML Pt+0.13 ML Co	6.8±1.9	7.2±2.3	7.3±2.4
0.06 ML Co+0.19 ML Pt	6.0±1.8	6.4±2.2	6.7±2.6
0.25 ML Pt	6.2±2.1	7.6±2.3	9.4±2.7

annealed Pt clusters have the highest fraction of large clusters > 10 Å. As the Co fraction is increased from 0-30%, there is a distinct shift in cluster heights to lower values. The 30%-80% Co cluster height distributions are similar except that a sharp peak around 4-5 Å appears in the distribution for the 80% Co clusters. The pure Co clusters exhibit a bimodal distribution with peaks around 8-9 Å and 3-5 Å; although the fraction of large cluster sizes is the same as observed at the 80% Co composition, the number of small Co islands is significantly lower. This loss in cluster density for the pure Co clusters is attributed to desorption of Co from the surface, given that the onset of desorption should occur in this temperature range.[37] The presence of Pt in the clusters appears to inhibit the desorption of Co from the surface, and therefore the 80% Co clusters have the highest cluster density after annealing. The greater Co-Pt bond strength compared to Co-Co (2.97 vs. 1.73 eV)[42] is consistent with decreased Co desorption from the bimetallic clusters. Notably, there is no evidence for significant Co diffusion into $TiO_{2(}$110), given that Co is not observed by X-ray photoelectron spectroscopy (XPS) or STM after the usual cycles of sputtering and

annealing. Also, the XPS Co($2p_{3/2}$) binding energy for the Co clusters has same value as metallic Co[37,41] and does not shift upon annealing, as would be expected if Co were diffusing into titania.

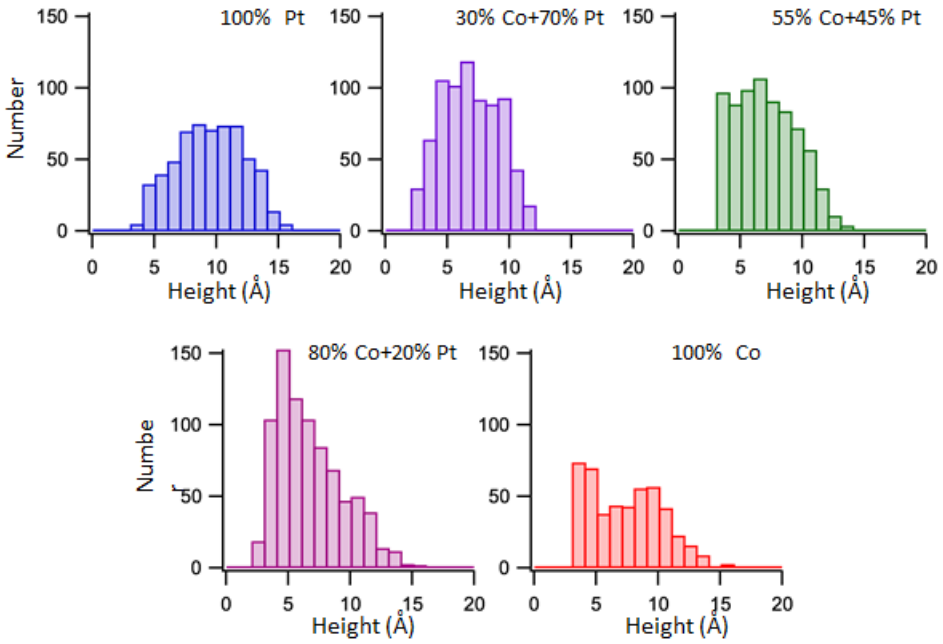

Figure 5.4: Histograms of cluster heights measured from scanning tunneling microscopy images (Figure 5.3) of the pure and bimetallic clusters deposited at room temperature and annealed to 800 K for one minute. For each surface, all clusters in 1000 Åx1000 Å images were measured.

Figure 5.5 and Table 5.2 show cluster densities before (triangles) and after (circles) Pt deposition on Co clusters, as well as after annealing to 500 K and 800 K. Data for the pure Pt and Co clusters (squares) are also shown for comparison, and total metal coverages are fixed at 0.25 ML. For the 80% Co clusters (0.19 ML Co +0.6 ML Pt), the cluster density before Pt deposition (green triangle) is slightly greater than after Pt deposition (green circle), indicating that no new clusters of pure Pt are formed on the surface, and the small decrease is attributed to cluster coalescence.

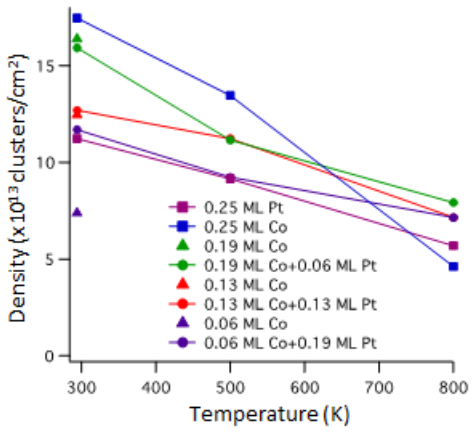

Figure 5.5: Cluster densities for various surfaces at room temperature and after heating to 500 K and 800 K for one minute at each temperature.

As discussed earlier, the cluster densities for the 55% Co surface do not change substantially, regardless of the order of deposition. However, for the 30% Co surface, the number of pure Co clusters formed in the initial deposition is not high enough to provide nucleation sites for all of the deposited Pt, and the cluster density increases from 7.42×10^{12} cm^{-2} to 11.67×10^{12} cm^{-2}. Therefore, the 30% Co surface is the only one that does not consist of exclusively bimetallic clusters, with pure Pt clusters coexisting with Co-Pt clusters. The 80% and 55% Co clusters are expected to have relatively uniform compositions because the incoming Pt atoms are evenly deposited over the surface, and the Co seed clusters are also uniformly dispersed across the surface, as shown for the 0.13 ML Co coverage in Figure 5.1a.

Table 5.2. Average Cluster Densities for Pt-Co Bimetallic Clusters.

Composition	Density (clusters/cm^2) 300 K	Density (clusters/cm^2) 500 K	Density (clusters/cm^2) 800 K
0.25 ML Co	1.75×10^{13}	1.35×10^{13}	4.61×10^{12}
0.19 ML Co+0.06 ML Pt	1.59×10^{13}	1.12×10^{13}	7.96×10^{12}
0.13 ML Co+0.13 ML Pt	1.27×10^{13}	1.13×10^{13}	7.19×10^{12}
0.13 ML Pt+0.13 ML Co	1.05×10^{13}	9.25×10^{12}	5.78×10^{12}
0.06 ML Co+0.19 ML Pt	1.17×10^{13}	9.24×10^{12}	7.15×10^{12}
0.25 ML Pt	1.12×10^{13}	9.19×10^{12}	5.71×10^{12}

After annealing to 500 K, the 20% decrease in cluster density for Co and Pt suggests that the rates of sintering at 500 K are comparable for the two metals. All of surfaces exhibit a relatively small (11-30%) decrease in the number of clusters after heating to 500 K. This decrease appears to be more pronounced for the 100% and 80% Co clusters because the difference in total number of clusters is greatest, but the percent change in cluster density is not substantially different. For all surfaces except the pure Co clusters, the decrease in cluster density at 800 K is ~40-50% of the density at 295 K. In the case of pure Co, the larger decrease in cluster density (75%) is again attributed to desorption of Co from the surface, whereas there is no evidence of Pt desorption at 800 K.

In order to establish the atomic composition of the bimetallic surfaces, LEIS experiments were conducted on various cluster compositions with a total coverage of 0.25 ML. The relative sensitivities for Pt and Co were determined from LEIS experiments on 15 ML films that completely covered the TiO_2 surface so that the Ti peak was fully attenuated. The Pt:Co sensitivity factor was calculated to be 3.0 after correcting for the total surface areas of the Pt and Co films as measured from a numerical integration of the STM images for the films.[30] The plot in Figure 5.6 shows the surface compositions

determined by the LEIS experiments (surface % Co) vs. the ratio of metals deposited (bulk % Co), and the dotted line indicates identical surface and bulk compositions. Based on surface free energies alone, the higher surface free energy for Pt (2.5 J/m^2)[43] compared to Co (1.9 J/m^2)[44-47] suggests that bimetallic clusters formed from deposition of Pt on Co should be core-shell structures with Pt in the core. However, the fact that Co and Pt alloy readily over a wide range of compositions[48] implies that both Co and Pt atoms should reside at the surface. For all of the bimetallic clusters, both Co and Pt atoms are detected at the surface, and cluster surfaces are Pt-rich compared to the bulk. The composition of the 55% Co clusters formed from the deposition of Co on Pt is shown as a blue square in Figure 5.6; deposition of Co on Pt results in a surface composition that is slightly richer in Co (37% vs. 29%). The similarity in surface compositions for the Co+Pt and Pt+Co depositions indicates that the diffusion of metal atoms within the clusters occurs readily at room temperature.

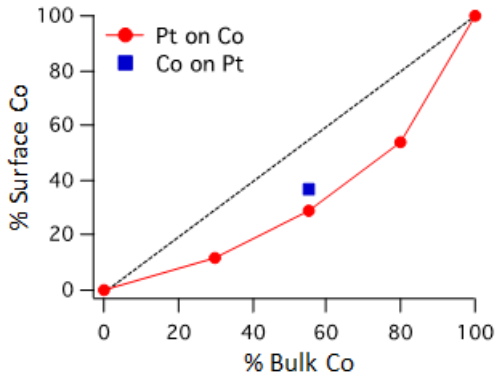

Figure 5.6: A plot of surface Co composition determined from low energy ion scattering experiments as a function of bulk Co composition, which is the ratio of deposited metals.

Changes in surface composition for the bimetallic clusters upon annealing were investigated by LEIS, and data for the Co and Pt signals as a function of temperature are shown in Figure 5.7. For each cluster composition, all signals are normalized to the value at room temperature so that changes in intensity can be observed on the same scale. However, it should be noted that the absolute intensity of the Co signals for the 30% Co and 55% Co clusters are relatively low, constituting only ~20% and 40%, respectively, of the intensity for pure Co clusters at room temperature. The Pt LEIS intensity for the 0.25 ML Pt clusters decreases to ~30% of the room temperature value after heating to 800 K (Figure 5.7a). This dramatic decrease in intensity is attributed to encapsulation of the Pt clusters by titania upon heating, as demonstrated in previous studies of Pt on TiO_2 annealed in UHV.[49-51] Pt does not desorb from the surface at 800 K, and the loss in surface area due to sintering at 800 K also cannot account for the large decrease in Pt intensity.

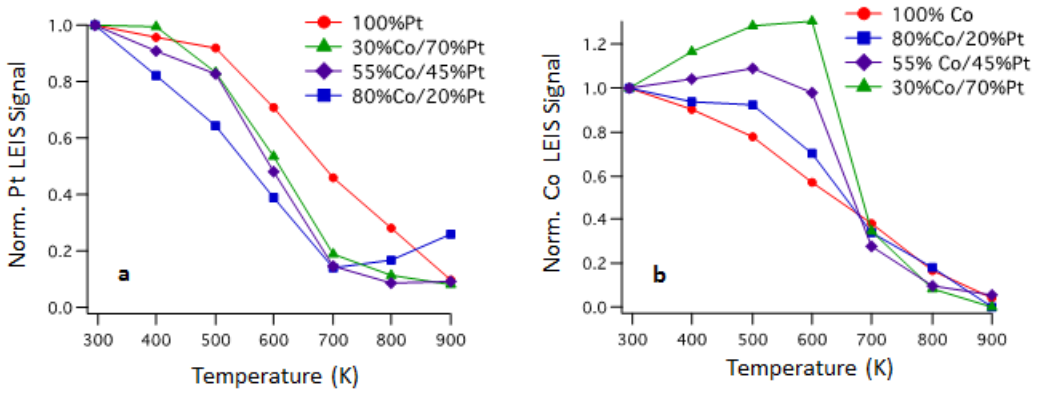

Figure 5.7: Pt (a) and Co (b) low energy ion scattering signals as a function of annealing temperature for various cluster compositions. For each cluster composition, signals are normalized to the initial value at room temperature.

The encapsulation of Pt by the titania support upon heating in a reducing atmosphere such as UHV or H_2 is a well-established phenomenon in the literature and is known as a strong

metal support interaction (SMSI).[52-55] For the bimetallic clusters, the Pt signals all follow similar trends upon heating to 800 K, and the signals at 800 K are even lower than those for the pure Pt clusters, suggesting that either Pt is more easily encapsulated in the presence of surface Co or that Pt is diffusing into the bulk of the cluster upon annealing. For the 80% Co clusters, the small increase in Pt signal at 800 and 900 K is unexpected but has been reproduced in three separate experiments. A possible explanation is that Co desorption at these temperatures increases the fraction of Pt at the cluster surface, and this effect is most pronounced for the bimetallic clusters with the greatest concentration of Co.

For the pure Co clusters, the Co signal (Figure 5.7b) decreases substantially at 800 K, similar to the Pt signal. Previous studies have reported that Co is encapsulated by TiO_2 upon heating in vacuum, given that the loss in Co signal between 295 and 800 K cannot be attributed solely to Co desorption or cluster sintering.[37] All of the Co signals for the bimetallic surfaces are also significantly diminished at 800 K, indicating that the presence of Pt does not prevent encapsulation of Co at the surface. However, the 30% Co clusters exhibit an increase in Co signal between room temperature and 600 K. Similarly, the Co signal intensity for the 55% Co clusters increases between 295 and 500 K, and the intensity at 600 K is comparable to the intensity before heating. The surface Co concentration for the 30% Co clusters corresponds to 16% at 500 K compared to 12% at 295 K, and the surface Co concentration for the 55% Co clusters is 33% at 500 K vs. 29% at 295 K. Thus, annealing has a relatively small effect on the overall surface composition of clusters, given that the change in composition is less than 5%. A possible explanation for the diffusion of Co to the surface after heating is that at room temperature, Co atoms are too strongly bound at the titania interface to diffuse to the surface, but at higher temperatures, diffusion of the

Co from the cluster-support interface to the surface can occur. This effect would be expected to be more pronounced for the low Co fractions, where the concentration of Co atoms in the near-surface region is limited by the diffusion of strongly bound Co atoms away from Co-titania interface.

Chemical Activity

CO Desorption

The chemical activity of the bimetallic clusters was investigated in TPD experiments using CO as a probe molecule (Figure 5.8). Unless otherwise stated, the bimetallic clusters were prepared by deposition of Co seed clusters followed by the more mobile Pt. Notably, CO does not adsorb on the TiO_2 support during dosing at 300 K. On the pure Co clusters, the evolution of CO occurs in a low temperature molecular desorption peak at 375 K and a high temperature peak at 750 K attributed to the recombination of atomic carbon and oxygen from the dissociation of CO.[56] On the pure Pt clusters, CO dissociation does not occur, and only a molecular desorption peak is observed in the lower temperature regime. The maximum CO intensity occurs at ~495 K, and there is also a pronounced shoulder around 420 K; the higher temperature desorption states have been previously attributed to CO adsorption at steps, which are the sites that bind CO the most strongly.[57] At lower CO coverages, the 495 K peak appears first as the step sites are preferentially populated, and the lower temperature states appear only at the higher CO coverages.

For CO adsorption on the 80% Co clusters, two desorption states at 350 and 430 K of comparable intensities are observed. The 350 K peak is assigned to adsorption on Co sites

while the 430 K is assigned to adsorption on Pt sites although neither peak appears at exactly the same temperature as CO desorption from the pure metals. The shift in desorption temperature from 375 K for the pure Co clusters to 350 K for the 80% Co clusters could be explained by the blocking of step sites on the Co surface by Pt. Furthermore, the loss of the 495 K feature from Pt step sites demonstrates that these types of sites are not present on the Co-Pt clusters. Although desorption at 350 K from Co and at 430 K from Pt is the most straightforward explanation of the data in Figure 5.8, it is impossible to rule out contribution from desorption at mixed Co-Pt sites. The decreased intensity for the recombinant peak at 750 K implies that the Pt atoms block the Co sites needed for CO dissociation.

On the 55% Co clusters, the contribution of the 350 K peak diminishes as the 450 K grows, indicating that a greater fraction of CO is now bound to Pt. This behavior is consistent with the decreasing Co fraction at the surface. Since the intensity at 350 K is higher on the pure Pt clusters than on the 55% Co clusters, it is possible that all CO desorption is from Pt; previous studies of Co-Pt alloy surfaces indicate that CO is adsorbed preferentially on Pt compared to Co for surfaces that contain a high fraction of Pt.[58-60] The complete disappearance of the recombinant CO peak demonstrates that all of the Co sites for CO dissociation are blocked by Pt. CO desorption from the 55% Co clusters prepared by the reverse order of deposition (Co on Pt) exhibits a nearly identical desorption profile compared to Pt on Co. Slight differences are observed in the intensity of the desorption peaks and the shift in the leading edge, and although these differences are small, they were found to be highly reproducible.

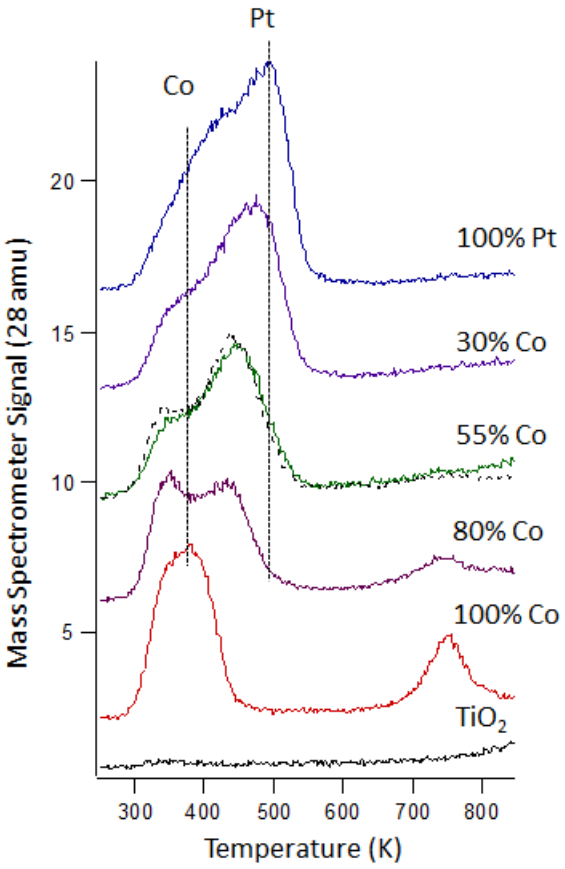

Figure 5.8: Temperature programmed desorption data for a saturation exposure of CO at room temperature on various surfaces. The bimetallic surfaces have a total metal coverage of 0.25 ML. Co deposition was followed by Pt deposition except for the dotted trace for 55% Co, in which the order of deposition was reversed.

Furthermore, for the Co on Pt clusters, there is evidence for CO adsorption on Co, given that the leading edge for CO desorption on this bimetallic surface is slightly lower in temperature than that of CO desorption from the pure Pt clusters. The shift in this edge to lower temperature and the increase in the 350 K peak intensity are both consistent with increased Co at the surface for the Co on Pt clusters.

When the Co content in the bimetallic clusters is reduced to 30%, the CO desorption profile continues to evolve toward that on the pure Pt clusters, as the higher temperature desorption state increases in intensity and shifts toward higher temperatures. The lower temperature state at 350 K does not increase in intensity compared to desorption on the 55% Co clusters and remains less intense than desorption from the pure Pt clusters. Again, the absence of the 750 K recombinant peak on the Co-Pt cluster surfaces that are predominantly Pt shows that this surface is lacking the ensembles of Co sites necessary for CO dissociation.

Methanol Reaction

The TPD data for adsorption of methanol at 100 K on pure 0.25 ML Co clusters and subsequent reaction up to 850 K are shown in Figure 5.9a. The main products from methanol decomposition are gaseous CO (28 amu) and H_2 (2 amu). CO evolves in a molecular desorption peak at 400 K and a higher temperature peak at 750 K assigned to recombinant desorption. The main peak for H_2 evolution is at 360 K although there is a shoulder at 230 K, and a higher temperature tail extends up to 550 K. A small water (18 amu) desorption peak is observed at 230 K and is attributed to reaction of the hydroxyl hydrogens with oxygen from the titania support. The main H_2 desorption peak at 360 K occurs at a lower temperature than CO desorption, implying that C-H bonds are broken before CO begins to desorb from the surface. The desorption of multilayer methanol (32 amu) is observed around 115 K, and molecular methanol desorption is also observed at 280 K. Methane (16 amu) is barely detectable. Methyl radical (15 amu) evolution is observed from methanol reaction on the TiO_2 support around 620 K,[34,61] but the deposition of Co blocks the active sites on titania; the same behavior is observed for other metals on titania

such as Pt.[61] Wide mass scan experiments from 30-110 amu established that no other products were evolved since the only detectable mass signals were from the reported products and their cracking fragments. No carbon was detected on the surface in Auger electron spectroscopy experiments on any of the surfaces after TPD.

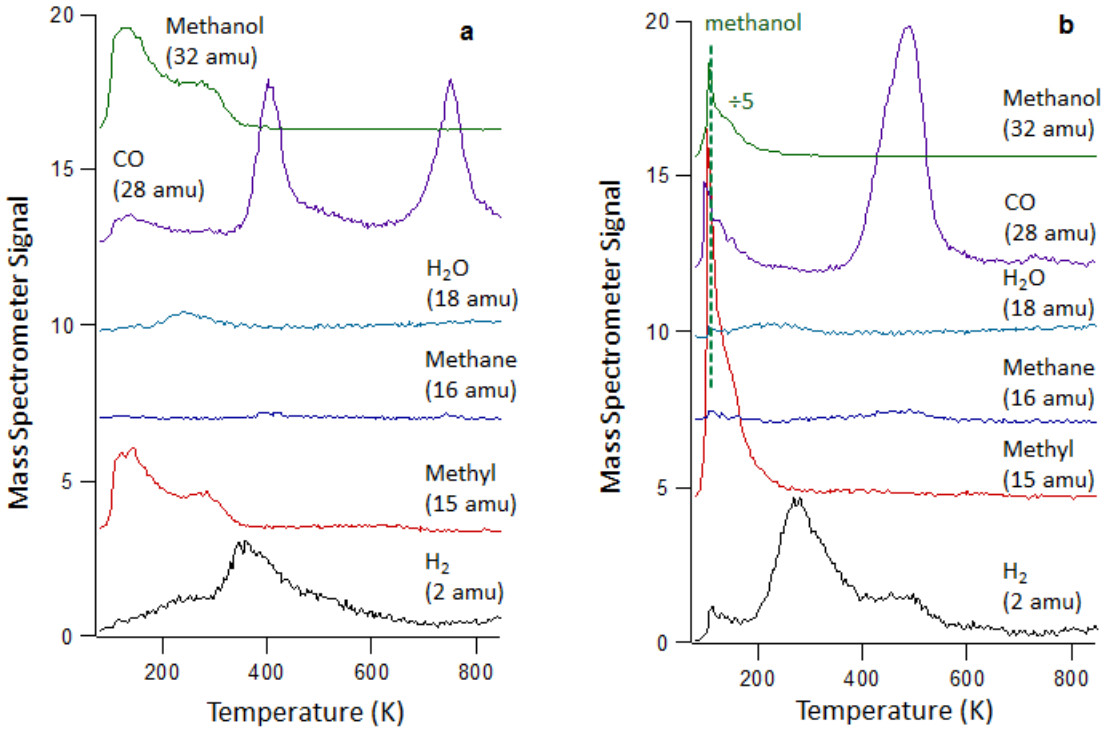

Figure 5.9: Temperature programmed desorption data for a saturation exposure of methanol dosed at 100 K on: a) 0.25 ML Co and b) 0.25 ML Pt clusters. The dotted traces are profiles for the desorption of CO itself after adsorption at room temperature.

TPD data for methanol reaction on pure 0.25 ML Pt clusters on TiO_2(110) has been reported previously,[61] and the main results are summarized briefly here for comparison with pure Co clusters. Reaction on the Pt clusters produces CO at 490 K, with no evidence for recombinant desorption at higher temperature. H_2 desorption occurs in a main peak at

275 K as well as a smaller shoulder at 490 K. A small methane peak is detected at 480 K, and the desorption of water occurs at 230 K. No methyl (15 amu) production is observed, in contrast to the activity on the clean TiO_2(110) surface. The sharp 15 amu peak at 100 K is from fragmentation of the condensed methanol that desorbs at this temperature.

Figure 5.10 (solid traces) shows TPD data for CO evolution from methanol reaction on Pt-Co clusters as a function of Co composition. Previous studies of CO on TiO_2-supported Ni clusters demonstrate that lattice oxygen from titania participates in the removal of carbon from the surface as gaseous CO.[30]

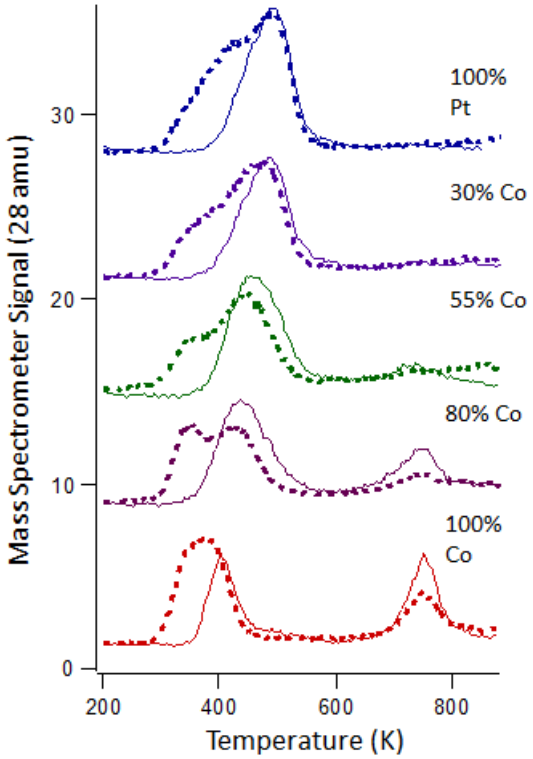

Figure 5.10: Temperature programmed desorption data (28 amu, CO) for a saturation exposure of methanol dosed at 100 K on bimetallic clusters of varying compositions with a total metal coverage of 0.25 ML.

As the fraction of Co is decreased, the recombinant CO peak decreases in both intensity and evolution temperature. At a Co fraction of 30%, the recombinant peak is not observed, indicating that C-O bond scission does not occur in methanol and CO. Furthermore, the lower temperature CO peak shifts from 400 K on the pure Co clusters to 485 K on the 30% Co clusters and 490 K on the pure Pt clusters. The desorption peak widths for all of the bimetallic clusters are comparable to that on the pure Pt clusters, whereas the peak on the pure Co clusters is significantly narrower. For comparison, data for the desorption of CO itself on the clusters of different compositions are overlaid as dotted traces.

On the bimetallic clusters, it appears that CO evolution occurs only from Pt sites since no CO production is observed in the lower temperature regime corresponding to desorption from Co. This result is consistent with previous work that reports preferential binding of CO at Pt sites on Co-Pt alloy surfaces.[58-60] The similarity in temperatures for CO desorption and CO evolution from methanol reaction indicate that the production of CO from methanol is desorption-limited. The greater intensity of CO evolution at 750 K from methanol reaction compared to CO adsorption/desorption implies that C-O bond scission in the methanol reaction intermediate contributes to recombinant CO production at higher temperature.

The H_2 and methane desorption profiles for methanol reaction on the pure and bimetallic clusters, as well as on the TiO_2 support, are shown in Figure 5.11a. On the titania support, H_2 evolution at 220 K is attributed to O-H bond scission to form the methoxy intermediate that decomposes to CH_3 at higher temperatures.[34] The H_2 peak at 360 K, which is characteristic of reaction on the pure Co clusters, is not a prominent feature in the spectra for any of the bimetallic clusters, and this indicates that reaction on the bimetallic

surfaces is not dominated by pure Co sites. In contrast, the main peak from reaction on Pt occurs at 275 K, and a desorption peak at a similar temperature of 300 K is clearly observed in reaction on the 30% Co clusters. For the 55% Co clusters, the H_2 desorption peak at 315 K is also attributed to reaction on Pt sites, but at the lowest Pt fraction (80% Co), there is no clear H_2 desorption state associated with reaction on Pt.

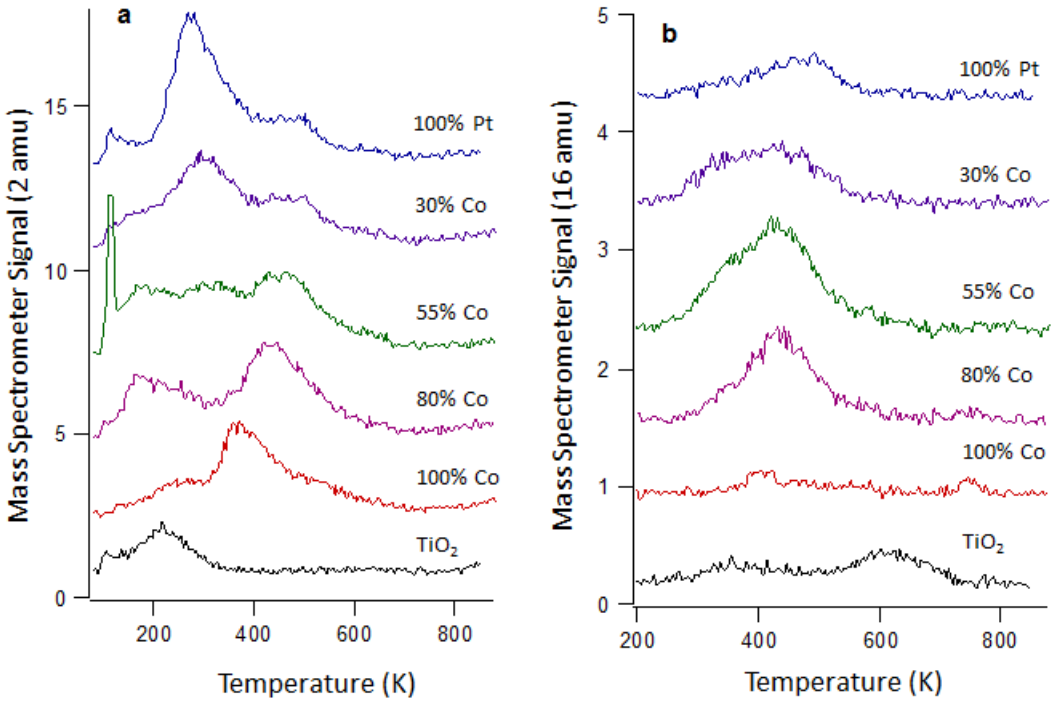

Figure 5.11: Temperature programmed desorption data for a saturation exposure of methanol dosed at 100 K on bimetallic clusters of varying compositions with a total metal coverage of 0.25 ML: a) 2 amu (H_2) and b) 16 amu (CH_4).

The 30% Co clusters have a desorption profile similar to the pure Pt clusters although the 275 K peak is more pronounced on the Pt clusters. However, the 55% and 30% Co clusters exhibit H_2 desorption at 435 K that is more intense than the corresponding peak on pure Pt, and this peak does not appear at all on pure Co; the 435 K feature is therefore attributed

to reaction at mixed Co-Pt sites. For the bimetallic surfaces, there is also a 180 K desorption state that is clearly observedd on the 80% and 55% Co clusters but nonexistent on the pure Co and Pt clusters. Studies by Chen and coworkers have shown that H_2 desorption occurs at temperatures as low as 150 K on Pt-Co-Pt(111) sandwich structures compared to 270-285 K on bulk Pt and Co surfaces and 315 K on Co-Pt-Pt(111).[25] Thus, the low temperature H_2 production is also evidence of activity on the bimetallic surface.

Methane production at 440 K was highest on the bimetallic cluster surfaces and consequently attributed to activity at Co-Pt sites (Figure 5.11b). No methane is produced on the pure Co clusters, and the barely detectable 16 amu signals arise from mass fragmentation of the CO evolved at 400 and 750 K. On the pure Pt clusters, a smaller amount of methane is produced in a broad peak with maximum intensity at ~490 K. The methane yield is greatest on the 55% Co clusters, which produces ~4 times more methane than the pure Pt clusters and ~1.6 times more than the 30% and 80% Co clusters. For the 55% and 80% Co clusters as well as the pure Pt clusters, methane desorption is nearly coincident with the CO and higher temperature H_2 peaks. For the 30% Co clusters, methane evolution occurs in a relatively broad peak that coincides with both high and low temperature H_2 desorption.

Other masses that were specifically monitored in the TPD experiments on the various Co-Pt cluster compositions were: water (18 amu), methyl (15 amu) and methanol (32 amu) (data not shown). Water desorption occurred at 230 K with comparable intensities on all cluster surfaces. Methyl was only observed on the clean TiO_2 surface, and methanol desorbed in a multilayer peak around 110 K. A molecular methanol peak at 285 K was observed on the Co surface, but this feature decreased in intensity with

decreasing Co coverage and was not detected on pure Pt (Figure 5.9a,b). The presence of the higher temperature methanol desorption peak at 285 K on pure Co clusters indicates that total activity is higher on the Pt clusters, where this peak from recombination of methoxy and surface hydrogen is not observed.

5.4 Discussion

Growth and Surface Composition

Co-Pt bimetallic clusters were grown on TiO_2(110) by the sequential deposition of Co on Pt or Pt on Co. In general, bimetallic clusters can be formed when the second metal is more mobile on the surface than the first metal, and therefore all of the metal atoms from the second deposition can be nucleated at existing clusters from the first deposition.[31,33,37,62] Previous work from our group has demonstrated that the relative mobilities of the metals on TiO_2 can be predicted from the strength of the metal-oxygen bonds; specifically, stronger metal-oxygen bonding results in lower mobilities and shorter diffusion lengths.[41] Co is less mobile on the surface than Pt, but exclusively bimetallic clusters are grown from the deposition of 0.13 ML Co on 0.13 ML Pt or 0.13 ML Pt on 0.13 Co; the key here is that the number of nucleation sites created in the first deposition must be sufficient to serve as seed clusters for metal atoms from the second deposition. The deposition of 0.19 ML of Pt on 0.06 ML of Co produced pure Pt clusters coexisting with bimetallic clusters because the low coverage of Co seed clusters did not provide sufficient nucleation sites for all of the Pt atoms from the second deposition. For metals with a greater difference in mobility, such as Au with Ni, Pt or Co, the bimetallic clusters can only be formed when Au is deposited second because the short diffusion lengths of Ni, Pt and Co relative to Au prevents the metal atoms from nucleating exclusively at existing Au clusters.[31,33,37]

The Co and Pt atoms in the bimetallic clusters interdiffuse readily at room temperature, given that the bimetallic clusters formed from both orders of deposition have surface compositions that are nearly identical. The Co on Pt clusters are slightly richer in Co (37% Co) than Pt on Co clusters (29% Co), suggesting that the surface compositions are not completely equilibrated since the surfaces are richer in the metal that was deposited second. Furthermore, the CO TPD data show that the Co on Pt and Pt on Co clusters have indistinguishable activity for CO desorption. Likewise, methanol reaction studied by TPD exhibits the same activity on Co-Pt clusters, regardless of the order of deposition. For Co films deposited on Pt(111), the Co atoms are mobile on the surface at room temperature,[63] but significant diffusion of Co into the bulk occurs only after heating to higher temperatures of 600-700 K.[58,64,65] Thus, interdiffusion at room temperature between the surface and bulk is more pronounced for the clusters than the planar surfaces, and similar effects have been observed for intermixing in TiO_2-supported Pt-Au and Ni-Au clusters[31,33] compared to the corresponding planar bimetallic surfaces.[66-69]

For Co-Pt clusters of varying compositions, the cluster surfaces are found to be 15-25% richer in Pt than the bulk compositions. These surface compositions do not follow the relative surface free energies, as in the case of Au-M (M=Pt, Ni, Co) clusters in which bulk immiscibility of the metals and the lower surface free energy of Au results in surface compositions that are 80-100% Au for bulk Au fractions of >50%.[31,33,37] Because Co and Pt alloy over a wide range of compositions,[48] the lower surface free energy of Co (1.9 J/m^2)[44-47] compared to Pt (2.5 J/m^2)[43] does not result in clusters with near Co shell-Pt core structures. A possible explanation for this behavior is that Co atoms are strongly bound at the interface with titania, and consequently there are fewer Co atoms available for diffusion

to the surface; note that the Co-Pt clusters all have average heights of ~3.5 atomic layers, and therefore it is not surprising that binding with titania should influence surface composition. However, heating the clusters to 500 K, which is below the temperature needed to induce significant encapsulation by titania, increased the Co surface composition by less than 5%, indicating that the Pt-rich surface compositions cannot be solely attributed to trapping of the Co atoms at the titania interface.

Furthermore, there are many studies in the literature reporting Pt surface compositions that are higher than bulk Pt compositions for Pt-Co alloys, and this behavior is consistent with what is observed for the titania-supported Co-Pt clusters. For example, when Co is deposited on Pt(111) and annealed at 700 K, an alloy film with an overall 50% Pt composition is formed with a surface composition of 85% Pt.[58] Other studies of annealed Co films on Pt(111) also report Pt surface compositions of ~75% in the top monolayer.[64] Investigations of $Pt_{25}Co_{75}$(111) bulk alloys show that the surface is enriched up to 50% Pt, [70,71] and $Pt_{75}Co_{25}$ alloys form a top layer of pure Pt after annealing to 1000 K.[3,4] In addition, STEM studies of Pt_3Co nanoparticles supported on carbon demonstrate that the top monolayer is 100% Pt.[23] Theoretical studies also support Pt rich surfaces for the alloys; a study of $Pt_{34}Co_3$ clusters shows that a core shell structure with Co atoms in the interior is more stable than Co at the surface,[60] and DFT calculations for 4-6 layer slab structures indicate that Pt-rich surfaces are favored for PtCo and Pt_3Co alloys.[72] Notably, the enrichment of the top monolayer with Pt results in enrichment of the second layer with Co for the bulk alloys.[2,4,70,71,73]

Chemical Activity

At high Co fractions, TPD experiments for CO desorption on the Co-Pt clusters exhibit two distinct desorption states attributed to desorption from Co and from Pt sites. A comparison of the desorption temperatures for CO on the pure clusters indicates that the binding of CO to Pt is stronger than to Co, and TPD experiments for CO on Co(0001)[74,75] and Pt(111)[76,77] in the literature confirm stronger adsorption of CO to Pt. For the 80% Co clusters, a lower temperature desorption peak assigned to CO at Co sites is observed, and recombinant desorption at 750 K confirms that the surface contains Co atoms, given that Pt does not dissociate CO. At Co fractions of 55% and below, the lower temperature peak from Co is not as pronounced, and there is no recombinant CO desorption. Furthermore, the desorption profiles on these bimetallic clusters are similar to that on pure Pt although the molecular desorption peak is shifted to lower temperatures compared to on the pure Pt clusters; the 30% Co surfaces contain some pure Pt clusters as well as bimetallic clusters, and therefore it is not surprising that these surfaces should exhibit behavior similar to that of pure Pt. Furthermore, investigations of CO on Co-Pt alloy surfaces report that CO preferentially binds to Pt when the surfaces are Pt-rich,[58,59] whereas CO adsorption is observed on Co for alloy surfaces that are Co-rich.[59] Theoretical calculations also support preferential binding of CO to Pt rather than Co on small (~40 atom) Pt-rich clusters.[60]

The higher temperature desorption peak on the Co-Pt clusters assigned to desorption from Pt shifts to lower values as the Co fraction is increased from 0% to 80%. Given that the 495 K peak on Pt surfaces is attributed to CO adsorption at step sites,[57,76] this shift to lower temperature could be attributed to site-blocking when the Co atoms reside at the step edges; since the less strongly adsorbing sites are the only ones available

for CO adsorption, the overall desorption temperature shifts to lower values. As the Co fraction is increased from 0 to 80%, the higher temperature molecular desorption state attributed to Pt gradually shifts from 495 K on pure Pt, to 475 K on 30% Co, to 450 K on 55% Co, to 430 K on 80% Co. This ~60 K shift is comparable to what has been previously observed by our group for CO desorption from Pt-Au clusters on TiO_2.[61] Bimetallic clusters were grown at the same Pt compositions studied here via the deposition of Pt seed clusters followed by Au. In the case of the Au-Pt clusters, the surfaces were initially pure Au at higher bulk Au fractions, but exposure to CO induced the diffusion of Pt atoms to the surface in order to form the strong Pt-CO bonds; CO did not adsorb on pure Au clusters at room temperature. Since the same shift in desorption temperature for CO on Pt is observed in both the Co-Pt and Au-Pt systems, the decrease in CO adsorption energy could be explained solely by site-blocking. However, it is also possible that electronic effects arising from Co-Pt interactions could also contribute to the shifts in desorption temperatures.

Previous work for CO on Co-Pt alloy surfaces reports that CO desorption from Co is shifted to higher temperature while desorption from Pt is shifted to lower temperature, as compared with the respective pure metal surfaces.[59] Studies of CO on bulk Pt-Co alloy surfaces by Al-Shamery and coworkers report that CO is more weakly bound to Pt in the PtCo alloy by 0.15 eV, while CO on pure Co and PtCo have similar adsorption energies within 0.04 eV; in these experiments, Co is deposited on Pt(111) and then heated to various temperatures to make alloys of different compositions.[59,64] It was proposed that the binding of CO at the Pt monolayer is weakened from the lowering of the d-band center due to ligand effects from the Co in the second layer.[59] On the Co-Pt clusters studied here, it is not

always possible to distinguish desorption from Co and desorption from Pt because the desorption profile from Pt itself is broad, extending from 300-550 K. For the 80% Co clusters, the CO desorption peak attributed to Co is not shifted to higher temperatures compared to the pure Co clusters. The peak attributed to desorption from Pt shifts to lower temperature with increasing Co fraction, but the magnitude of this shift is consistent with a site-blocking effect of Co on Pt, as discussed in the preceding paragraph.

Although CO desorption does not clearly demonstrate ligand effects in the Co-Pt clusters, the bimetallic clusters exhibit unusual activity for methanol reaction. Specifically, the reaction intermediate is more stable on the Co-Pt clusters, given that the temperature for reaction-limited H_2 desorption is higher on Co-Pt clusters than on either pure Co or Pt. Methoxy is known to be the surface intermediate formed from methanol reaction via O-H bond scission on single-crystal Pt surfaces like Pt(110)-(2x1)[78,79] as well as Co-Pt surfaces.[65] The inhibition of C-H bond scission in methoxy on the Co-Pt bimetallic clusters suggests that these surfaces should be less susceptible to CO poisoning from methanol crossover in DMFCs. Furthermore, methane production is highest on the bimetallic clusters, indicating that the selectivity of C-O bond scission over C-H bond scission is increased on the Co-Pt clusters compared to either of the pure metals. While this unusual activity could be attributed to the electronic effects that are well-established in Co-Pt bimetallic systems, it is known that selectivity for methane is structure-sensitive on Pt surfaces.[78-80] There is also evidence that a small high temperature H_2 desorption peak around 430 K appears for methanol reaction on Pt(110)-(1x1) but is not observed on (2x1)Pt(110).[80,81] However, it seems unlikely that the high temperature H_2 peak on the Co-Pt clusters originates solely from site-blocking of Co on Pt because the 430 K peak at the

lowest Co fraction is comparable in intensity to the feature on pure Pt clusters, and the 430 K peak is greatest on the 80% Co clusters. Moreover, H_2 desorption at 430 K is not observed from methanol reaction on Au-Pt clusters grown on TiO_2(110) with bulk Au compositions of 50% and 75%. For methanol reaction on Au-Co bimetallic clusters on TiO_2, H_2 production at 430 K does not exceed the intensity observed on pure Co clusters at this temperature, in contrast to the activity on the Co-Pt clusters reported here. The H_2 production at 430 K therefore appears to be unique to the Co-Pt surface, and cannot be assigned to the blocking of active sites on either the Co or Pt surfaces, given that the addition of Au to the pure metal clusters does not result in the same activity. Thus, the greater stability of C-H bonds in the methoxy intermediate is attributed to electronic interactions specific to the Co-Pt bimetallic system, rather than to a change in surface structure due to the addition of the second metal.

The reactions of methanol on the pure Pt and Co clusters are very similar in the sense that gaseous CO and H_2 are the main products. The main difference is that recombinant CO desorption at high temperature is observed on the Co clusters but not on Pt, which does not dissociate C-O bonds. Based on periodic trends, it might be expected that Co as a mid-transition metal would be more active for methanol decomposition than the late-transition metal Pt. However, the Pt clusters have higher activity than the Co clusters as demonstrated by the lower desorption temperature for H_2 on the Pt clusters. The presence of the molecular methanol desorption peak at 250 K on Co but not on Pt suggests that the total methanol activity is lower on Co due to greater recombination of methoxy and surface hydrogen. This behavior is consistent with the fact that desorption of surface hydrogen as H_2 occurs at lower temperature on the Pt clusters, thus preventing

recombination of surface hydrogen with methoxy. The greater activity on Pt is also reflected by the higher product yields: the H_2 and CO production is 20-35% higher on Pt clusters, and methane is evolved from the Pt clusters but not the Co clusters.

5.5 Conclusions

Bimetallic Co-Pt clusters can be grown on TiO_2(110) via the sequential deposition of Pt on Co; despite the higher mobility of Pt on the surface compared to Co, bimetallic clusters are also formed from the deposition of Co on Pt, provided that the initial Pt deposition produces a cluster density that is high enough for all of the Co atoms to nucleate at the existing clusters. The facile diffusion of atoms within the clusters is illustrated by the fact that the bimetallic clusters have nearly identical activities and surface compositions, regardless of the order of deposition. The bimetallic clusters with bulk Co fractions varying from 30-80% all contain a mixture of Co and Pt in the surface monolayer, and in all cases the surface is richer in Pt than the bulk. Studies of methanol reaction on the pure and bimetallic clusters show that C-H bond breaking is inhibited and the selectivity for methane production is increased on the bimetallic clusters compared to the pure clusters. For CO desorption from the bimetallic clusters, a lower and higher temperature peak can be distinguished for adsorption on Co and Pt, respectively, for Co fractions $\geq$55%; the shift in Pt desorption temperature to lower values with increasing Pt fraction can be explained by a site-blocking effect. As a cathode catalyst for ORR, the Co-Pt surfaces should be more resistant to CO poisoning since CO desorption occurs at a lower temperature than on pure Pt. Furthermore, the Co-Pt catalysts in DMFCs should also be less susceptible to CO poisoning from methanol crossover since C-H bond scission in the methoxy intermediate occurs at higher temperature.

5.6 References:

(1) Antolini, E.; Salgado, J. R. C.; Gonzalez, E. R. The Methanol Oxidation Reaction on Platinum Alloys with the First Row Transition Metals - the Case of Pt-Co and -Ni Alloy Electrocatalysts for DMFCs: A Short Review. Appl. Catal. B, **2006**, 63, 137-149.

(2) Stamenkovic, V.; Schmidt, T. J.; Ross, P. N.; Markovic, N. M. Surface Composition Effects in Electrocatalysis: Kinetics of Oxygen Reduction on Well-Defined Pt_3Ni and Pt_3Co Alloy Surfaces. J. Phys. Chem. B, **2002**, 106, 11970-11979.

(3) Stamenkovic, V. R.; Mun, B. S.; Mayrhofer, K. J. J.; Ross, P. N.; Markovic, N. M. Effect of Surface Composition on Electronic Structure, Stability, and Electrocatalytic Properties of Pt-Transition Metal Alloys: Pt-Skin Versus Pt-Skeleton Surfaces. J. Am. Chem. Soc., **2006**, 128, 8813-8819.

(4) Mun, B. S.; Watanabe, M.; Rossi, M.; Stamenkovic, V.; Markovic, N. M.; Ross, P. N. A Study of Electronic Structures of Pt_3M (M=Ti,V,Cr,Fe,Co,Ni) Polycrystalline Alloys with Valence-Band Photoemission Spectroscopy. J. Chem. Phys., **2005**, 123, 204717.

(5) Stamenkovic, V. R.; Mun, B. S.; Arenz, M.; Mayrhofer, K. J. J.; Lucas, C. A.; Wang, G. F.; Ross, P. N.; Markovic, N. M. Trends in Electrocatalysis on Extended and Nanoscale Pt-Bimetallic Alloy Surfaces. Nat. Mater., **2007**, 6, 241-247.

(6) Markovic, N. M.; Ross, P. N. Surface Science Studies of Model Fuel Cell Electrocatalysts. Surf. Sci. Rep., **2002**, 45, 121-229.

(7) Lamy, C.; Lima, A.; LeRhun, V.; Delime, F.; Coutanceau, C.; Leger, J. M. Recent Advances in the Development of Direct Alcohol Fuel Cells (DAFC). J. Power Sources, **2002**, 105, 283-296.

(8) Urban, P. M.; Funke, A.; Muller, J. T.; Himmen, M.; Docter, A. Catalytic Processes in Solid Polymer Electrolyte Fuel Cell Systems. Appl. Catal. A, **2001**, 221, 459-470.

(9) Heinzel, A.; Barragan, V. M. A Review of the State-of-the-Art of the Methanol Crossover in Direct Methanol Fuel Cells. J. Power Sources, **1999**, 84, 70-74.

(10) Cruickshank, J.; Scott, K. The Degree and Effect of Methanol Crossover in the Direct Methanol Fuel Cell. J. Power Sources, **1998**, 70, 40-47.

(11) Gurau, B.; Smotkin, E. S. Methanol Crossover in Direct Methanol Fuel Cells: A Link between Power and Energy Density. J. Power Sources, **2002**, 112, 339-352.

(12) Neergat, M.; Shukla, A. K.; Gandhi, K. S. Platinum-Based Alloys as Oxygen-Reduction Catalysts for Solid-Polymer-Electrolyte Direct Methanol Fuel Cells. J. Appl. Electrochem., **2001**, 31, 373-378.

(13) Salgado, J. R. C.; Antolini, E.; Gonzalez, E. R. Carbon Supported Pt-Co Alloys Electrocatalysts for as Methanol-Resistant Oxygen-Reduction Direct Methanol Fuel Cells. Appl. Catal. B, **2005**, 57, 283-290.

(14) Page, T.; Johnson, R.; Hormes, J.; Noding, S.; Rambabu, B. A Study of Methanol Electro-Oxidation Reactions in Carbon Membrane Electrodes and Structural Properties of Pt Alloy Electro-Catalysts by EXAFS. J. Electroanal. Chem., **2000**, 485, 34-41.

(15) Zhang, X.; Chan, K. Y. Microemulsion Synthesis and Electrocatalytic Properties of Platinum-Cobalt Nanoparticles. J. Mater. Chem., **2002**, 12, 1203-1206.

(16) Zhang, X.; Tsang, K. Y.; Chan, K. Y. Electrocatalytic Properties of Supported Platinum-Cobalt Nanoparticles with Uniform and Controlled Composition. J. Electroanal. Chem., **2004**, 573, 1-9.

(17) Sun, S. G.; Clavilier, J. Electrochemical Study on the Poisoning Intermediate Formed from Methanol Dissociation at Low Index and Stepped Platinum Surfaces. J. Electroanal. Chem., **1987**, 236, 95-112.

(18) Wilhelm, S.; Iwasita, T.; Vielstich, W. COH and CO as Adsorbed Intermediates During Methanol Oxidation on Platinum. J. Electroanal. Chem., **1987**, 238, 383-391.

(19) Markovic, N. M.; Gasteiger, H. A.; Ross, P. N.; Jiang, X. D.; Villegas, I.; Weaver, M. J. Electrooxidation Mechanisms of Methanol and Formic-Acid on Pt-Ru Alloy Surfaces. Electrochim. Acta, **1995**, 40, 91-98.

(20) Nilekar, A. U.; Sasaki, K.; Farberow, C. A.; Adzic, R. R.; Mavrikakis, M. Mixed-Metal Pt Mono Layer Electrocatalysts with Improved CO Tolerance. J. Am. Chem. Soc., **2011**, 133, 18574-18576.

(21) Ma, Y. G.; Balbuena, P. B. Surface Properties and Dissolution Trends of Pt_3M Alloys in the Presence of Adsorbates. J. Phys. Chem. C, **2008**, 112, 14520-14528.

(22) Parteder, G.; Allegretti, F.; Wagner, M.; Ramsey, M. G.; Surnev, S.; Netzer, F. P. Growth and Oxidation of Ni Nanostructures on Stepped Rh Surfaces. J. Phys. Chem. C, **2008**, 112, 19272-19278.

(23) Patrick, B.; Ham, H. C.; Shao-Horn, Y.; Allard, L. F.; Hwang, G. S.; Ferreira, P. J. Atomic Structure and Composition of "Pt_3Co" Nanocatalysts in Fuel Cells: An Aberration-Corrected Stem HAADF Study. Chem. Mat., **2013**, 25, 530-535.

(24) Xu, Y.; Ruban, A. V.; Mavrikakis, M. Adsorption and Dissociation of O_2 on Pt-Co and Pt-Fe Alloys. J. Am. Chem. Soc., **2004**, 126, 4717-4725.

(25) Humbert, M. P.; Chen, J. G. G. Correlating Hydrogenation Activity with Binding Energies of Hydrogen and Cyclohexene on M/Pt(111) (M = Fe, Co, Ni, Cu) Bimetallic Surfaces. J. Catal., **2008**, 257, 297-306.

(26) Khan, N. A.; Murillo, L. E.; Shu, Y. Y.; Chen, J. G. G. Correlating Low-Temperature Hydrogenation Activity of Co/Pt(111) Bimetallic Surfaces to Supported Co/Pt/Gamma-Al_2O_3 Catalysts. Catal. Lett., **2005**, 105, 233-238.

(27) Tang, S.; Lin, J.; Tan, K. L. Characterization and Reactivity of Alpha-Al_2O_3-Supported Pt-Co Bimetallic Catalysts. Surf. Interface Anal., **1999**, 28, 155-158.

(28) Englisch, M.; Ranade, V. S.; Lercher, J. A. Hydrogenation of Crotonaldehyde over Pt Based Bimetallic Catalysts. J. Mol. Catal. A, **1997**, 121, 69-80.

(29) Park, J. B.; Ratliff, J. S.; Ma, S.; Chen, D. A. Understanding the Reactivity of Oxide-Supported Bimetallic Clusters: Reaction of NO with CO on TiO_2(110)-Supported Pt-Rh Clusters. J. Phys. Chem. C, **2007**, 111, 2165-2176.

(30) Zhou, J.; Ma, S.; Kang, Y. C.; Chen, D. A. Dimethyl Methylphosphonate Decomposition on Titania-Supported Ni Clusters and Films: A Comparison of Chemical Activity on Different Ni Surfaces. J. Phys. Chem. B, **2004**, 108, 11633-11644.

(31) Park, J. B.; Conner, S. F.; Chen, D. A. Bimetallic Pt-Au Clusters on TiO_2(110): Growth, Surface Composition and Metal-Support Interactions. J. Phys. Chem. C, **2008**, 112, 5490-5500.

(32) Tenney, S. A.; Ratliff, J. S.; He, W.; Roberts, C. C.; Ammal, S. C.; Heyden, A.; Chen, D. A. Adsorbate-Induced Changes in the Surface Composition of Bimetallic Clusters: Au-Pt on TiO_2(110). J. Phys. Chem. C, **2010**, 114, 21652-21663.

(33) Tenney, S. A.; He, W.; Roberts, C. C.; Ratliff, J. S.; Shah, S. I.; Shafai, G. S.; Turkowski, V.; Rahman, T. S.; Chen, D. A. CO-Induced Diffusion of Ni Atoms to the Surface of Ni–Au Clusters on TiO_2(110). J. Phys. Chem. C, **2011**, 115, 11112-11123.

(34) Tenney, S. A.; Cagg, B. A.; Levine, M. S.; He, W.; Manandhar, K.; Chen, D. A. Enhanced Activity for Supported Au Clusters: Methanol Oxidation on Au/TiO_2(110). Surf. Sci., **2012**, 606, 1233-1243.

(35) Ozturk, O.; Park, J. B.; Black, T. J.; Rodriguez, J. A.; Hrbek, J.; Chen, D. A. Methanethiol Chemistry on TiO_2-Supported Ni Clusters. Surf. Sci., **2008**, 602, 3077-3088.

(36) Varazo, K.; Parsons, F. W.; Ma, S.; Chen, D. A. Methanol Chemistry on Cu and Oxygen-Covered Cu Nanoclusters Supported on TiO_2(110). J. Phys. Chem. B, **2004**, 108, 18274-18283.

(37) Galhenage, R. P.; Ammal, S. C.; Yan, H.; Duke, A.; Tenney, S. A.; Heyden, A.; Chen, D. A. Nucleation, Growth and Adsorbate-Induced Changes in Composition for Co-Au Bimetallic Clusters on TiO_2. J. Phys. Chem. C, **2012**, 116, 24616-24629.

(38) Ratliff, J. S. The Morphology and Catalytic Activity of Bimetallic Nanoclusters Supported on TiO_2(110). Ph.D. Dissertation, University of South Carolina, 2009.

(39) Chen, D. A.; Bartelt, M. C.; McCarty, K. F.; Hwang, R. Q. Self-Limiting Growth of Cu Islands on TiO_2(110). Surf. Sci., **2000**, 450, 78.

(40) Stempel, S.; Bäumer, M.; Freund, H. J. STM Studies of Rhodium Deposits on an Ordered Alumina Film -- Resolution and Tip Effects. Surf. Sci., **1998**, 404, 424-427.

(41) Galhenage, R. P.; Yan, H.; Tenney, S. A.; Park, N.; Henkelman, G.; Albrecht, P.; Mullins, D. R.; Chen, D. A. Understanding the Nucleation and Growth of Metals on TiO_2: Co Compared to Au, Ni and Pt. J. Phys. Chem. C, **2013**, 117, 7191-7201.

(42) Sebetci, A. Density Functional Study of Small Cobalt-Platinum Nanoalloy Clusters. J. Magn. Magn. Mater., **2012**, 324, 588-594.

(43) Jiang, Q.; Lu, H. M.; Zhao, M. Modelling of Surface Energies of Elemental Crystals. J. Phys. Condens. Matter, **2004**, 16, 521-530.

(44) Chatain, D.; Rivollet, I.; Eustathopoulos, N. Thermodynamic Adhesion in Nonreactive Liquid-Alumina Systems. J. Chim. Phys. PCB, **1986**, 83, 561-567.

(45) Sangiorgi, R.; Muolo, M. L.; Chatain, D.; Eustathopoulos, N. Wettability and Work of Adhesion of Nonreactive Liquid-Metals on Silica. J. Am. Ceram. Soc., **1988**, 71, 742-748.

(46) Chatain, D.; Rivollet, I.; Eustathopoulos, N. Estimation of the Thermodynamic Adhesion and the Contact-Angle in the Nonreactive Metal-Ionocovalent Oxide Systems. J. Chim. Phys. PCB, **1987**, 84, 201-203.

(47) Campbell, C. T. Ultrathin Metal Films and Particles on Oxide Surface: Structural, Electronic and Chemisorptive Properties. Surf. Sci. Rep., **1997**, 27, 1-111.

(48) Binary Alloy Phase Diagrams; 2nd ed.; Massalski, T. B.; International, A.; Okamoto, H., Eds.; ASM International: Materials Park, OH, 1990.

(49) Pesty, F.; Steinrück, H.-P.; Madey, T. E. Thermal Stability of Pt Films on TiO_2(110): Evidence for Encapsulation. Surf. Sci., **1995**, 339, 83-95.

(50) Ozturk, O.; Ma, S.; Park, J. B.; Ratliff, J. S.; Zhou, J.; Mullins, D. R.; Chen, D. A. Probing the Interactions of Pt, Rh and Bimetallic Pt-Rh Clusters with the TiO_2(110) Support. Surf. Sci., **2007**, 601, 3099-3113.

(51) Tenney, S. A.; He, W.; Ratliff, J. S.; Mullins, D. R.; Chen, D. A. Characterization of Pt-Au and Ni-Au Clusters on TiO_2(110). Top. Catal., **2011**, 54, 42-45.

(52) Tauster, S. J.; Fung, S. C.; Garten, R. L. Strong Metal-Support Interactions - Group-8 Noble Metals Supported on TiO_2. J. Am. Chem. Soc., **1978**, 100, 170-175.

(53) Tauster, S. J. Strong Metal-Support Interactions. Acc. Chem. Res., **1987**, 20, 389-394.

(54) Tauster, S. J.; Fung, S. C.; Baker, R. T. K.; Horsley, J. A. Strong-Interactions in Supported-Metal Catalysts. Science, **1981**, 211, 1121-1125.

(55) Diebold, U.; Pan, J. M.; Madey, T. E. Ultrathin Metal Film Growth on TiO_2(110): An Overview. Surf. Sci., **1995**, 333, 845-854.

(56) Nowitzki, T.; Borchert, H.; Jurgens, B.; Risse, T.; Zielasek, V.; Baumer, M. UHV Studies of Methanol Decomposition on Mono- and Bimetallic Co-Pd Nanoparticles Supported on Thin Alumina Films. ChemPhysChem, **2008**, 9, 729-739.

(57) Skelton, D. C.; Tobin, R. G.; Lambert, D. K.; DiMaggio, C. L.; Fisher, G. B. Oxidation of CO on Gold-Covered Pt(335). J. Phys. Chem. B, **1999**, 103, 964-971.

(58) Gauthier, Y.; Schmid, M.; Padovani, S.; Lundgren, E.; Bus, V.; Kresse, G.; Redinger, J.; Varga, P. Adsorption Sites and Ligand Effect for CO on an Alloy Surface: A Direct View. Phys. Rev. Lett., **2001**, 87, 036103.

(59) Fenske, D.; Greshnykh, D.; Neuendorf, S.; Hoogestraat, D.; Borchert, H.; Al-Shamery, K. Ligand Effects Observed for the Adsorption of CO on Co-Pt Alloys. Surf. Sci., **2008**, 602, 2101-2106.

(60) Kettner, M.; Schneider, W. B.; Auer, A. A. Computational Study of Pt/Co Core-Shell Nanoparticles: Segregation, Adsorbates and Catalyst Activity. J. Phys. Chem. C, **2012**, 116, 15432-15438.

(61) Tenney, S. A.; Shah, S. I.; Yan, H.; Cagg, B. A.; Levine, M. S.; Rahman, T. S.; Chen, D. A. Methanol Reaction on Pt-Au Clusters on TiO_2(110): Methoxy-Induced Diffusion of Pt. J. Phys. Chem. C, **2013**, 117, 26998-27006.

(62) Park, J. B.; Ratliff, J. S.; Ma, S.; Chen, D. A. In Situ Scanning Tunneling Microscopy Studies of Bimetallic Cluster Growth: Pt-Rh on TiO_2(110). Surf. Sci., **2006**, 600, 2913-2923.

(63) Lundgren, E.; Stanka, B.; Schmid, M.; Varga, P. Thin Films of Co on Pt(111): Strain Relaxation and Growth. Phys. Rev. B, **2000**, 62, 2843-2851.

(64) Fenske, D.; Yim, W. L.; Neuendorf, S.; Hoogestraat, D.; Greshnykh, D.; Borchert, H.; Kluner, T.; Al-Shamery, K. Pitfalls in Interpreting Temperature Programmed Desorption Spectra of Alloys: The CO/Copt Puzzle. ChemPhysChem, **2007**, 8, 654-656.

(65) Skoplyak, O.; Menning, C. A.; Barteau, M. A.; Chen, J. G. G. Experimental and Theoretical Study of Reactivity Trends for Methanol on Co/Pt(111) and Ni/Pt(111) Bimetallic Surfaces. J. Chem. Phys., **2007**, 127, 114707.

(66) Davies, P. W.; Quinlan, M. A.; Somorjai, G. A. The Growth and Chemisorptive Properties of Ag and Au Monolayers on Platinum Single-Crystal Surfaces - an AES, TDS and LEED Study. Surf. Sci., **1982**, 121, 290-302.

(67) Kobiela, T.; Moors, M.; Linhart, W.; Cebula, I.; Krupski, A.; Becker, C.; Wandelt, K. Characterization of Bimetallic Au-Pt(111) Surfaces. Thin Solid Films, **2010**, 518, 3650-3657.

(68) Trant, A. G.; Jones, T. E.; Gustafson, J.; Noakes, T. C. Q.; Bailey, P.; Baddeley, C. J. Alloy Formation in the Au{111}/Ni System - an Investigation with Scanning Tunnelling Microscopy and Medium Energy Ion Scattering. Surf. Sci., **2009**, 603, 571-579.

(69) Katona, G. L.; Erdelyi, Z.; Beke, D. L.; Dietrich, C.; Weigl, F.; Boyen, H. G.; Koslowski, B.; Ziemann, P. Experimental Evidence for a Nonparabolic Nanoscale Interface Shift During the Dissolution of Ni into Bulk Au(111). Phys. Rev. B, **2005**, 71, 115432.

(70) Gauthier, Y.; Baudoing-Savois, R.; Bugnard, J. M.; Hebenstreit, W.; Schmid, M.; Varga, P. Segregation and Chemical Ordering in the Surface Layers of $Pt_{25}Co_{75}$(111): A LEED/STM Study. Surf. Sci., **2000**, 466, 155-166.

(71) Gauthier, Y.; Baudoingsavois, R.; Rosink, J.; Sotto, M. LEED Study of $Pt_{25}Co_{75}$(111). Surf. Sci., **1993**, 297, 193-201.

(72) Hirunsit, P.; Balbuena, P. B. Surface Atomic Distribution and Water Adsorption on Pt-Co Alloys. Surf. Sci., **2009**, 603, 912-920.

(73) Li, J. L.; Jacobs, G.; Zhang, Y. Q.; Das, T.; Davis, B. H. Fischer-Tropsch Synthesis: Effect of Small Amounts of Boron, Ruthenium and Rhenium on Co/TiO_2 Catalysts. Appl. Catal. A, **2002**, 223, 195-203.

(74) Bridge, M. E.; Comrie, C. M.; Lambert, R. M. Chemisorption Studies on Cobalt Single-Crystal Surfaces .1. Carbon-Monoxide on CO(0001). Surf. Sci., **1977**, 67, 393-404.

(75) Lahtinen, J.; Vaari, J.; Kauraala, K. Adsorption and Structure Dependent Desorption of CO on Co(0001). Surf. Sci., **1998**, 418, 502-510.

(76) Gland, J. L.; Kollin, E. B. Carbon Monoxide Oxidation on the Pt(111) Surface: Temperature Programmed Reaction of Coadsorbed Atomic Oxygen and Carbon Monoxide. J. Chem. Phys., **1983**, 78, 963-974.

(77) Ertl, G.; Neumann, M.; Streit, K. M. Chemisorption of CO on Pt(111) Surface. Surf. Sci., **1977**, 64, 393-410.

(78) Franaszczuk, K.; Herrero, E.; Zelenay, P.; Wieckowski, A.; Wang, J.; Masel, R. I. A Comparison of Electrochemical and Gas-Phase Decomposition of Methanol on Platinum Surfaces. J. Phys. Chem., **1992**, 96, 8509-8516.

(79) Wang, J. H.; Masel, R. I. Methanol Adsorption and Decomposition on (2x1) Pt(110)- Enhanced Stability of the Methoxy Intermediate on a Stepped Surface. Surf. Sci., **1991**, 243, 199-209.

(80) Wang, J. H.; Masel, R. I. Structure Sensitivity of Methanol Decomposition on (1x1) and (2x1) Pt(110). J. Vac. Sci. Technol. A, **1991**, 9, 1879-1884.

(81) Wang, J. H.; Masel, R. I. C-O Bond Scission During Methanol Decomposition on (1x1)Pt(110). J. Am. Chem. Soc., **1991**, 113, 5850-5856.

Chapter 6. Characterization of Pt-Re bimetallic clusters on TiO_2(110)

6.1 Introduction

Generation of hydrogen from biofuels has much promise to reduce the dependence on fossil fuels for energy requirements.[1] Hydrogen is a versatile energy carrier with a very high energy density compared to gasoline. Furthermore hydrogen is the promise of clean energy for the future. Research has been done for decades on production of hydrogen via alcohol reforming. Ethanol has become an attractive alcohol because of the availability and the ability of producing it using biomass. Furthermore, ethanol is a nontoxicity alcohol that can be easily transported, and easily stored.[2] Nickel-based catalysts are widely used in ethanol reforming.The drawback of such catalysts is the poisoning by CO, which is a byproduct of the reaction.[3] A catalyst that has more stability towards poisoning and has selectivity to H_2 over hydrocarbons is lacking.

Recently Pt-based catalysts have been proposed for aqueous phase reforming of alcohols but suffer from the lack of stability due to poisoning by CO and other carbonaceous species.[4-8] Addition of a second metal to Pt has shown to increase the stability of the catalyst by reducing the formation of coke.[9] The addition of Re to supported Pt catalysts has shown to enhance the activity due to a smaller degree of CO poisoning of Pt sites.[10,11] The support also plays a significant role in this catalyst; for instance, Pt/TiO_2 interface has activity towards water gas shift (WGS) reaction which acts as sites for the removal of CO.[12] WGS reaction helps to remove the CO which is a byproduct of the reforming reaction to enhance the stability of the reaction and also reduces the methanation of CO which decreases the selectivity for H_2 production. Addition of Re into Pt/TiO_2 known to enhance the activity towards water gas shift reaction by generating a reaction pathway via ReO_x active sites, for the activation of water.[13-16] Furthermore, addition of Re

into the Pt catalyst has also shown to enhance the total conversion of polyols with a small decrease in the selectivity to hydrogen. [17-19] Aqueous phase reforming (APR) activity of glycerol is known to increase the activity upon addition of Re to the Pt catalyst due to Pt-Re interactions.[20] Additionally Pt-Re on titania is shown to have the most activity compared to other supports such as ceria.[20] Also in a different study, Pt-Re/TiO_2 has been shown to have more conversion of xylitol in APR reaction compared to pure Pt.[17] Furthermore addition of Re to Pt/C, increased the total conversion of glycerol to synthesis gas, and this was suggested to be facilitated by providing an additional path for WGS reaction on Re sites and by reducing the strength of the CO bound to Pt, due to Pt-Re interactions.[21,22] In addition, an enhanced activity has been observed for low-temperature water gas shift reactions for Re on Pt/TiO_2 because of the higher dispersion of Pt on Re, where Re acts as an anchor for Pt on the support.[23] Pt-Re on mixed metal oxide supports has also shown greater activity for WGS reaction and assigned the higher activity has been assigned to greater dispersion of Pt.[24] The presence of Re is generally known to improve dispersion Pt on oxide supports which gives the catalyst better thermal stability. Addition of Re to the Pt catalyst, has been shown to reduce the selectivity to structure-sensitive reactions and decrease the amount of poisoning of Pt sites by larger hydrocarbons.[26] These literature studies show promise for the Pt-Re catalysts to have a better activity, selectivity and stability towards the aqueous phase reforming reaction, but the reasons behind this enhanced activity are not well understood. There are few model studies that have been done in order to understand the system better. A model study of Re/Pt(111) has shown the existence of Pt-Re interactions by the adsorption behaviors of H_2 and CO.[27]

Likewise investigating these phenomina using model systems could shed some light to undersatnd the mecahnism by which the enhanced activity is achieved. Bemetallic clusters often show enhanced activity and stability compared to their monometallic counteraprts due to bimetallic effects.[28,29] Few model studies have been done on the Pt-Re bimetallic system, warranting further investigation. Since, atomic level understanding of the industrial catalysts under reaction conditions is challenging, we propose a model system of Pt-Re on TiO_2 (110) to study the fundamental aspect of this system. In this study, we have designed a model system where we have prepared bimetallic clusters of Pt-Re on a single crystal titania rutile support to understand the growth, structure, interactions and activity at a fundamental level. Exclusive bimetallic cluster formation on titania is discussed for different amounts of metal coverages. Bimetallic clusters have found to be Pt rich at surface for all the coverages discussed. Interactions between Pt-Re have been identified using X-ray photoelectron spectrocopy. Strong metal support interactions are also observed for Re at room temperature. CO-TPD was done in order to understand the active sites of the bimetallic system.

6.2 Experimental section

Experiments were carried out in an ultra-high vacuum (UHV) chamber with a base pressure below 1×10^{-10} Torr. The UHV chamber is equipped with a number of surface analytical techniques such as Scanning Tunneling Microscopy (STM, Omicron VT-25), Low Energy Ion Scattering (LEIS), X-Ray Photoelectron Spectroscopy (XPS), and Hemispherical Analyzer (Omicron EA 125) for XPS and LEIS and Auger Electron Spectroscopy (AES)/ Low Energy Electron Diffraction (LEED) system (Omicron Spec 3). The second chamber is equipped with a quadrupole mass spectrometer for TPD studies

(Hiden HAL 301/3F), a cylindrical mirror analyzer for Auger electron spectroscopy (Omicron CMA 150), and LEED optics (Omicron)

The rutile titania (110) (Princeton Scientific Corporation, 1cm x 1cm x 0.1 cm) was used as the substrate to grow Pt/Re bimetallic clusters. The crystal was prepared by using Ar^+ ion sputtering at 1 kV for 20 mins and subsequent annealing to 950 K- 1000 K for 3mins. The crystals were mounted on a Ta back plates using Ta foil straps, and heating of the sample was achieved through radiative heating from a tungsten filament positioned behind the back plates, as well as by electron bombardment when the samples were held at a positive potential. This treatment preferentially removes lattice oxygen to make the crystal an n- type semiconductor that enables ion and electron based spectroscopies and sanning tunneling microscopyexperiments to be conducted. TiO_2 (110)-1x1 LEED pattern was obtained upon this cleaning procedure. Cleanliness and the order were confirmed using a combination of STM, LEED, XPS and AES techniques. The temperature was monitored via a type K thermocouple that was calibrated using an infrared pyrometer.

In the first chamber, Re was deposited by physical vapor deposition of a Re rod (ESPI, 0.08" x 1", 99.99%) using an Oxford electron beam evaporator (EGCO4). Metal flux was determined using a quartz crystal microbalance (QCM, inficon). The QCM was independently calibrated by depositing a sub-monolayer coverage of Au on a Ru(0001) single crystal and calculating the coverage using STM images obtained on these surfaces. In the second chamber, Re was deposited from a Re rod (ESPI, 0.0625" x 1.77", 99.99%) using an Omicron evaporator (EFM3), while Pt was deposited from a homemade source consisting of Pt wire (0.25 mm diameter, ESPI, 99.999%) wrapped around a tungsten wire (0.50 mm) through which current was passed. The Pt flux was calibrated with a QCM

before each deposition; for Re deposition, the internal flux monitor of the evaporator was used to control Re flux, and the flux monitor readings were initially calibrated with a QCM. The metal coverage is given in monolayer (ML) equivalents that correspond to packing density of the corresponding metal. (Re (0001):1.52 x 10^{15} atoms/cm^2, Pt (111): 1.50 x 10^{15} atoms/cm^2). The metal deposition rate was approximately 0.05 - 0.1 ML/min.

STM experiments were carried out to investigate the surface morphology of the Pt/Re bimetallic clusters. The sample was biased at + 2.3 V with respect to the tip, and the images were collected at a constant tunneling current of 0.05 nA – 0.1 nA. Tips were made using a 0.38 mm tungsten wire by electrochemical etching by NaOH and sputtering with an argon ion beam at 3 kV. Clusters in a 500 Å x 500 Å were measured using an inhouse STM stats analysis program.

LEIS experiments were carried out to understand the surface composition. Experiments were conducted with 600 eV helium ion beam and 80 nA current to the sample. Sensitivity to the corresponding metal for LEIS was determined using polycrystalline Pt and Re foils. Foils were sputtered at 5 uA, 1 kV for 15 min and annealed to 900 K for 6 min before taking the scans. The step size for the acquired spectra was 0.2 eV and the dwell time was 0.2 s. The Pt-Re region was collected between 460 eV- 550 eV energy ranges. The XPS data for the Re (4f), Ti(2p) and Pt(4f) regions were collected with an Al Kα source using a 0.2s dwell time and 0.02 eV step size.

The surfaces were exposed to CO (National Welders, 99.99%) and methanol (Fisher Scientific, 99.9%) via a stainless steel directed dosing tube. CO was used as received. During CO exposure, the sample temperature was held at 300 K, and a saturation exposure of CO was achieved by leaking in CO at a pressure rise of 3.0×10^{-10} Torr for 3

min. In TPD experiments, the crystal was heated at a constant rate of 2 K/s in front of the mass spectrometer. The crystal was positioned ~2 mm in front of a 4 mm diameter hole cut in the shroud of the mass spectrometer in order to prevent detection of products desorbing from the sample holder. The crystal was biased at −100 V during TPD experiments to avoid damage from the electrons emitted by the mass spectrometer filament. Nine masses were collected in a typical TPD experiment; during wide mass scan experiments to check for additional products, 40 mass channels were monitored in a single experiment.

6.3 Results

STM images of different compositions of Pt-Re, grown on titania (110) at room temperature, are shown in figure1. Corresponding histograms for cluster heights are presented in figure 6.2. A 0.25 ML coverage of Pt on titania resulted in 3D clusters with an average cluster height of 6.22 ± 2.15 Å and a density of 11.24 x 10^{12} cm^{-2}(figure 6.1a). The same coverage of Re clusters deposited on titania resulted in a narrow cluster distribution with an average cluster height of 3.19 ± 1.06 Å and a density of 28.16 x 10^{12} cm^{-2} (figure 6.1f). Corresponding histograms are shown in figure 6.2a and figure 6.2f. Histograms of the cluster heights indicate that the highest fraction of clusters for 0.25 ML Pt is above 4 Å whereas, for 0.22 ML Re, the highest fraction of the clusters is below 4 Å in height. Growth mode of metals on titania has been known to dictate by the metal-oxygen bond strength.[30] From the STM images for pure Pt and pure Re, it appears that the Pt-Titania bond is weaker compared to the Re-titania bond that resulted in a smaller cluster density and a higher cluster height. In contrast, the growth of Re resembled more 2D cluster growth with a higher cluster densities and a lower cluster heights. A 0.13 ML Pt coverage

was then deposited on titania (figure 6.1b) which resulted in a cluster density of 9.34 x 10^{12} cm^{-2} and an average cluster height of 4.66 ± 1.66 Å. A 0.11 ML Re coveage was then deposited on the 0.13 ML Pt surface as shown in figure 6.1c.

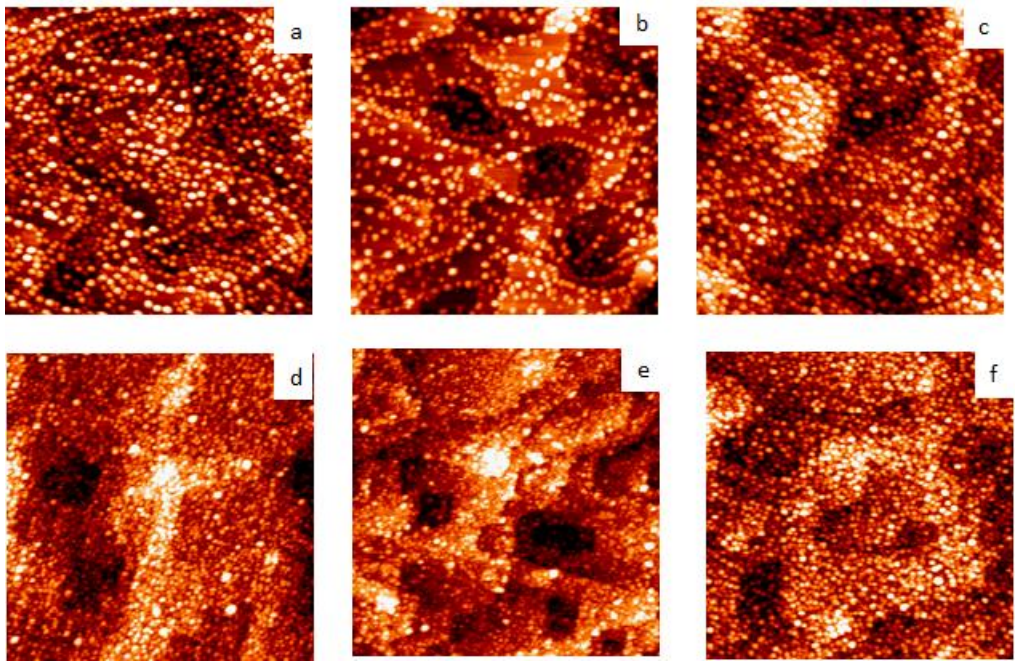

Figure 6.1. STM images of a) 0.25 ML Pt, b) 0.13 ML Pt, c) 0.13 ML Pt + 0.11 ML Re, d) 0.22 ML Re, e) 0.11 ML Re f) 0.11 ML Re + 0.13 ML Pt, deposited at room temperature. All images are 1000 Å x 1000 Å.

Two sizes of clusters can be observed at this compositions. Small clusters were below 4 Å in height and larger clusters were above 4 Å in height. The average cluster height for this composition of Pt+Re is 5.00 ± 1.80 Å and the cluster density is 18.60 x 10^{12} cm^{-2}. Even though the average clusters height is higher than for 0.13 ML Pt, increase of cluster density by a factor of two from the 0.13 ML Pt coverage indicates that there are new nucleation sites after deposition of 0.11 ML Re on 0.13 ML Pt. The histogram for the 0.13 ML Pt + 0.11 ML Re also shows a bimodal distribution that can be attributed to monometallic clusters of pure Re (small clusters) and bimetallic Pt-Re clusters (bigger

clusters). Therefore, in this order of deposition exclusive bimetallic cluster formation was not observed. Figure 6.1d show that 0.11 ML of Re deposited on titania resulted in a cluster density of 31.44 x 10^{12} cm^{-2} and an average height of 2.92 ± 1.05 Å. The average cluster height indicates that Re forms approximately one atomic layer high clusters. Histograms of 0.11 ML Re (Figure 6.2d) and 0.22 ML Re (figure 6.2f) show that they have a similar cluster distribution with a higher fraction of 0.11 ML Re clusters in 1-3 Å range in height, whereas for 0.22 ML Re, clusters are 2-4 Å range in height.

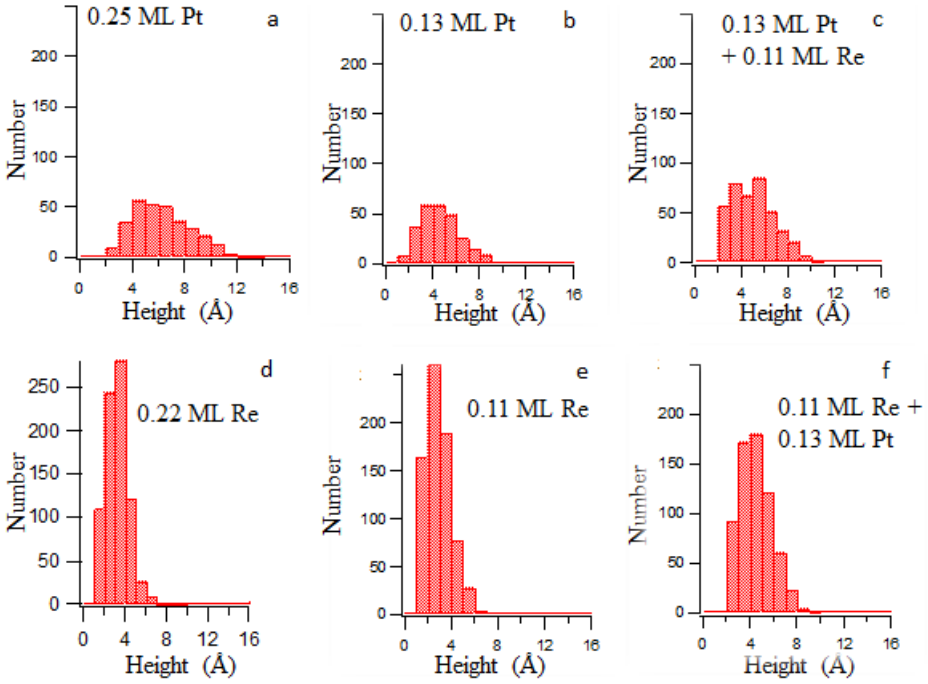

Figure 6.2. Histograms of cluster heights for the STM images in figure 1: a) 0.25 ML Pt, b) 0.13 ML Pt,and c) 0.13 ML Pt + 0.11 ML Re d) 0.22 ML Re, e) 0.12 ML Re, and f) 0.11 ML Re + 0.13 ML Pt. For each surface, all clusters in 500 Å x 500 Å region were measured.

In the second experiment 0.13 ML Pt was deposited on 0.11 ML of Re which resulted in an average clusters of 4.47 ± 1.33 Å and a cluster density of 25.58 x 10^{12} cm^{-2}. The cluster height is higher than that of the cluster height of the 0.11 ML Re, and the density is lower,

which indicates that the deposited Pt has preferentially nucleated on the Re seed clusters. Deposition of Re first provided a sufficient number of seed clusters for the second metal to nucleate at, forming bimetallic clusters. This behavior is in contrast to the deposition 0.13 ML of Pt first which did not provide sufficient number of nucleation sites for all of the Re clusters. A histogram of the cluster height distribution for 0.11 ML Re + 0.13 ML Pt (figure 6.2e) shows a shift to larger cluster sizescompared to histogram for the pure 0.11 ML Re (figure 6.2d); this is consistent with the nucleation of Pt at existing Re clusters.

STM images of clusters heated to 800 K are shown in figure 6.3. Corresponding histograms for cluster height distributions are illustrated in figure 6.4.

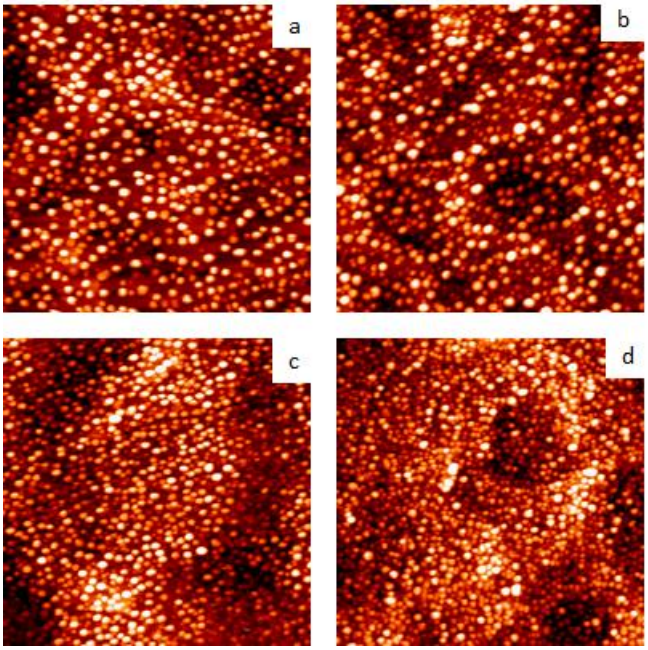

Figure 6.3. STM images of metals deposited at room temperature and then heated to 800 K (a) 0.25 ML Pt, (b) 0.13 ML Pt + 0.11 ML Re, (c) 0.11 ML Re + 0.13 ML Pt and (d) 0.22 ML Re. all images are 1000 Å x 1000 Å.

Heating 0.25 ML of Pt to 800 K resulted in clusters which are ~50% (9.14 ± 2.91 Å) larger in height than the clusters directly after room temperature deposition, and density decreased

by ~50% (5.71 x 10^{12} cm^{-2}). The corresponding histogram (figure 6.4a) for 0.25 ML Pt indicates that the larger clusters are greater than 10 Å and smaller clusters are smaller than 8 Å. After heating the 0.13 ML Pt + 0.11 ML Re surface to 800 K, there are clearly very small clusters as well as larger clusters. (Figure 6.3b) The corresponding histogram also shows a bimodal distribution of cluster heights where smaller clusters peak around 2- 4 Å and larger clusters peak around 9-10 Å.(Figure 6.4b) This behavior was observed even at room temperature due to the formation of monometallic and bimetallic clusters. For 0.13 ML Pt + 0.11 ML Re, the cluster density decreased by 39% (11.26 x 10^{12} cm^{-2}) and the average cluster height increased by 18% (5.91± 3.08 Å).

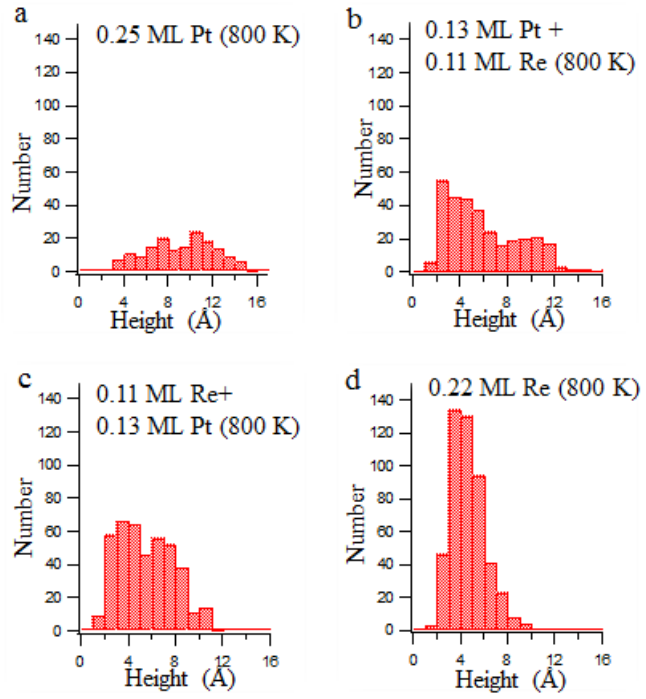

Figure 6.4. Histograms for the STM images in figure 3: a) 0.25 ML Pt, b) 0.13 ML Pt+0.11ML Re, c) 0.11 ML Re+0.13 ML Pt and d) 0.22 ML Re. All clusters in a 500 Å x 500 Å region were measured

For 0.11 ML Re + 0.13 ML Pt (figure 6.4c) an even greater cluster size distribution can be observed. The average cluster height increased by 22 % (5.46 ± 2.25 Å) and the density decreased by 43% (14.61 x 10^{12} cm^{-2}) compared to the clusters before heating. The cluster density of the 0.22 ML Re clusters dropped by 38% (17.51 x 10^{12} cm^{-2}) and the cluster height increased by 31% (4.62 ± 1.44 Å) after annealing to 800 K. Decrease in cluster density for all metal compositions except pure Pt is almost the same. The percent decrease in cluster density is greater on the pure Pt surface than on the Pt-Re surfaces. When Re is present on the surface, the initial cluster density is large and, therefore, after annealing to 800 K the cluster density for these surfaces remains high compared to annealed pure Pt clusters.

Low energy ion scattering data collected for different compositions of Pt-Re at room temperature are shown in figure 6.5a.

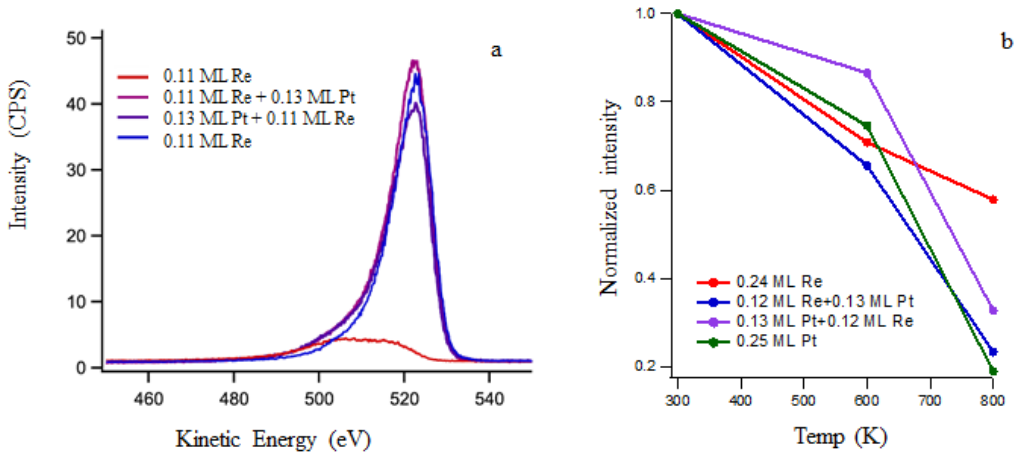

Figure 6.5 Low energy ion scattering spectroscopy studies of different compositions of Pt-Re; a) Pt-Re region at room temperature and b) Pt-Re signal (normalized to the room temperature value) at different temperatures.

The LEIS signals for Pt and Re both fall in the same range of kinetic energy, and therefore it is difficult to get an accurate quantification of the surface composition although a qualitative analysis can be done. The relative sensitivity of LEIS to Pt and Re are determined from polycrystalline Pt and Re foils with same surface area exposed. The calculated sensitivity ratio for Pt: Re is 1.9. Furthermore, the LEIS signal for 0.11 ML Re appears at a slightly lower kinetic energy than that of 0.13 ML Pt. For 0.11 ML Re, the intensity is very small compared to the pure Pt even after correcting for the relative sensitivity. From the STM images, it appears that the cluster density for pure Re is higher than that of pure Pt, which suggests more exposed Re on the surface. This observation could not be confirmed with the LEIS data, even after correcting to the sensitivity. This difference may be due the oxophillic nature of Re, which leads to a reaction with titania upon deposition and encapsulation of Re by titania. Both orders of deposition for 0.11 ML Re/0.13 ML Pt have similar surface compositions at room temperature. The LEIS signal intensity is slightly higher compared to 0.13 ML of Pt when the Pt is deposited second due to greater dispersion of Pt, which nucleates at the Re seed clusters. The difference in dispersion of metal clusters very well observed with the STM iamges, where Re+Pt showed higher cluster density with smaller cluster sizes compared to Pt+Re.

Figure 6.5b shows how the signal intensity changes with annealing to different temperatures with respect to the room temperature values. The signal intensity decreases as the surface is heated to higher temperatures. At 600 K, for bimetallic clusters, the largest decrease (34% from its room temperature value) in signal intensity is observed for 0.11 ML Re +0.13 ML Pt and lowest decrease (13%) is observed for 0.13 ML Pt +0.11 ML Re.

At 800 K, highest decrease in signal intensity is observed for 0.25 ML Pt (81%) and the lowest decrease was observed for 0.22 ML Re (42%).

To understand more about the nature of Pt-Re clusters on titania, higher coverages of Pt-Re were studied. Figure 6 shows the STM images obtained on 1.7 ML Re, 1.7 ML Re + 2 ML Pt, 2ML Pt and 2ML Pt + 1.7 ML Re. Figure 6a shows an STM image of 1.7 ML Re on titania that has a cluster density of 15.49 x 10^{12} cm^{-2} and a cluster height of 4.7 ± 1.0 Å. When 2 ML Pt was deposited on the existing 1.7 ML Re clusters (figure 6b), the cluster density decreased to 10.77 x 10^{12} cm^{-2} and the cluster height increased to 6.3 ± 1.1 Å. The increase in the cluster height and the fact that the lack of increase in cluster density, indicates that Pt deposited second was nucleated on the Re-seed clusters that were deposited first.

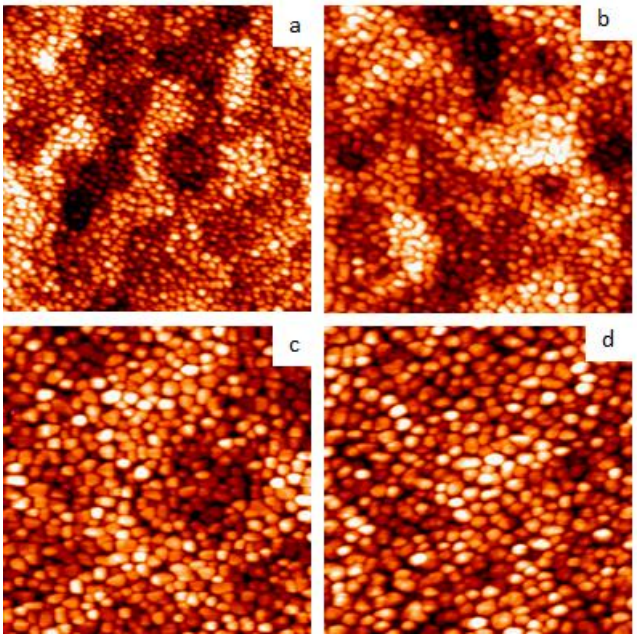

Figure 6.6. STM data for a) 1.7 ML Re, b) 1.7 ML Re + 2ML Pt, c) 2ML Pt, d) 2ML Pt + 1.7 ML Re, all images are 1000 Å x 1000 Å

The cluster coalescence can explain the decrease in the cluster density. When 2 ML Pt was deposited on titania (figure 6.6c), the cluster density (5.66 x 10^{12} cm^{-2}) was much smaller compared to that of 1.7 ML Re and the cluster height (13.2 ± 2.3 Å) was much higher. When 1.7 ML Re was deposited on 2 ML Pt, the cluster height increased to 17.2 ± 3.1 Å, and the cluster density decreased to 5.41 x 10^{12} cm^{-2} indicating the formation of bimetallic clusters. Even though we get bimetallic clusters are formed from both orders of deposition, evidently the surface morphology and the exposed area of metals at the surface are different in each case.

Low energy ion scattering data was obtained on these surfaces and are presented in figure 6.7. The highest LEIS signal is observed for 1.7 ML Re + 2 ML Pt which was even greater than that of 2 ML Pt; this can be explained by the greater dispersion of Pt on smaller Re clusters therefore larger Pt surface area.

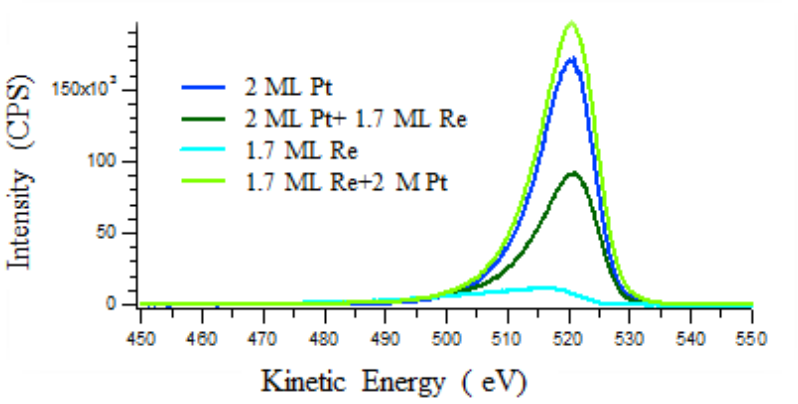

Figure 6.7. Low energy ion scattering spectroscopy studies of different compositions of Pt-Re.

1.7 ML Re shows the lowest signal intensity. The reason may be that the Re is very oxophillic and therefore reacts with titania upon room temperature deposition, resulting in encapsulation of Re by TiO_x. The signal for 2 ML Pt + 1.7 ML Re is lower than that of the reverse order of deposition, partly because the surface area is smaller than for 1.7 ML Re

+ 2 ML Pt due to the lower cluster density. Futhermore, when the Re is deposited second, some amount of Re is probably still present on the surface at room temperature.

Figure 6.8a shows XPS data of Ti ($2p_{3/2}$) peak for 1.7 ML Re and 2 ML Pt on titania at room temperature. When 1.7 ML Re is deposited on titania, a shoulder at lower binding energy appears, which shows that Re reduces the support. In contrast, Pt deposition did not alter the Ti peak shape. Reduction of the titania by Re, support the fact that Re has strong metal support interactions. Furthermore, the LEIS data shown in figure 6.8b shows that titanium peak can never be fully removed by adding higher coverages of Re. This observation suggests that there is a layer of Ti_xO_y on the Re film which is also with the strong Re-titania interactions.

For bimetallic clusters, XPS studies show mixing of Pt and Re, when Re is deposited on Pt seed clusters. Figure 9 shows the Re (4f) region and the Pt (4f) region for these high coverage Pt-Re surfaces.

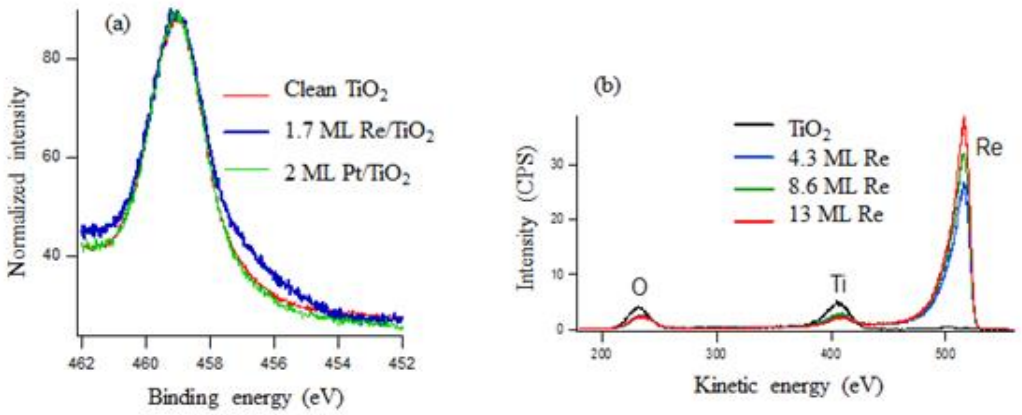

Figure 6.8. a) XPS data for Ti($2p_{3/2}$) peak fro TiO_2 itself and Re and Pt clusters on TiO_2 and b) LEIS data for thick layers of Re on titania

The Pt (4f) peak shifts 0.5 eV to higher binding energies when Re has been deposited on Pt. Binding energy shifts for different metal copositions and coverages are depicted in table 6.1. This shift cannot be attributed to the cluster size effect because that was not present in 2 ML Pt clusters. The shift is therefore assigned to the change the electronic structure in Pt due to the mixing of Re with Pt to make an alloy. The Re(4f) peak is already shifted to higher binding energies compared to its metallic position due to the reaction takes place between the Re and titania upon deposition.

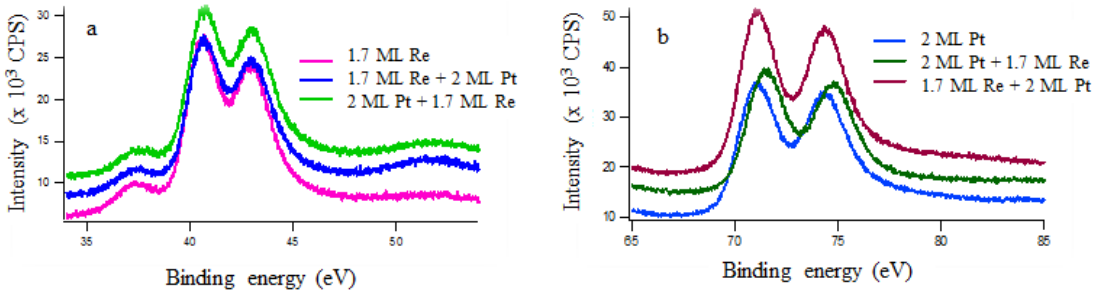

Figure 6.9: XPS data for different compositions of Pt-Re. a) Re(4f), b) Pt(4f)

The chemical activity of bimetallic clusters for lower coverages (0.24 ML total metal coverage) prepared via both orders of deposition was investigated by adsorbing CO at room temperature and observing CO desoprtion upon heating. CO TPD data is shown in figure 6.10. CO does not adsorb on the clean titania surface during exposure at 300 K. On the pure Re clusters there are two distinct desorption peaks at 433 K and 918 K. The low-temperature peak is the molecular desorption peak, whereas the higher temperature peak is the recombinant peak in which the dissociated C and O recombine to form a CO molecule. On the pure Pt clusters, there is one distinct peak at 420 K, which is attributed to the molecular desorption. The high-temperature shoulder that is at 500 K is attributed to the CO desorption from the step sites of Pt.[37, 38]

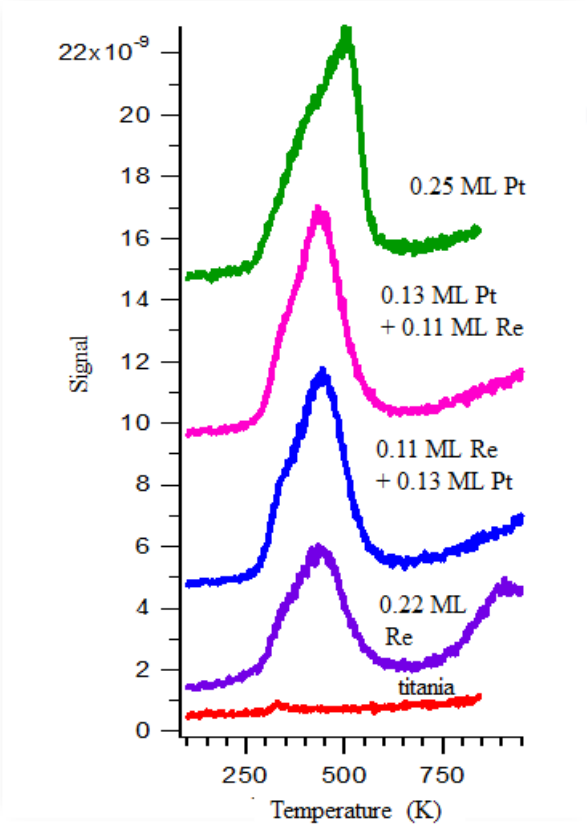

Figure 6.10: TPD data for CO adsorption on different compositions of Pt-Re clusters on TiO_2

When the bimetallic clusters are formed via both orders of deposition at lower coverages (0.24 ML total metal coverage) the molecular desorption peak appeared at 440 K. There was no shoulder to the right of the molecular CO desorption peak that is characteristic for the step sites on Pt. Occupation of these sites by Re is a possible reason for the disappearance of the shoulder. The CO recombinant peak at high temperatures has not been observed on these bimetallic clusters. Strong Re-support interactions may be the cause of the lack of metallic Re for dissociation of the C-O bond. Specifically Re is a highly oxophilic metal, and therefore, Re-TiO_2 interactions are expected.

Table 6.1: Binding energy data obtained from XPS for different compositions of Pt-Re prepared at room temperature

Composition	Pt($4f_{7/2}$)/eV	Re($4f_{7/2}$)/eV
0.25 ML Pt	71.4	
0.13 ML Pt	71.66	
0.13 ML Pt + 0.11 ML Re	71.68	41.14
0.11 ML Re + 0.13 ML Pt	71.6	41.14
0.11 ML Re		41.28
0.22 ML Re		41.14
2ML Pt	71.04	
2ML Pt + 1.7 ML Re	71.5	40.7
1.7 ML Re + 2 ML Pt	71.08	40.64
1.7 ML Re		40.64
0.43 ML Re		41.04
3.5 ML Re		40.54
8.6 ML Re		40.3
13 ML Re		40.3
Re foil		39.98

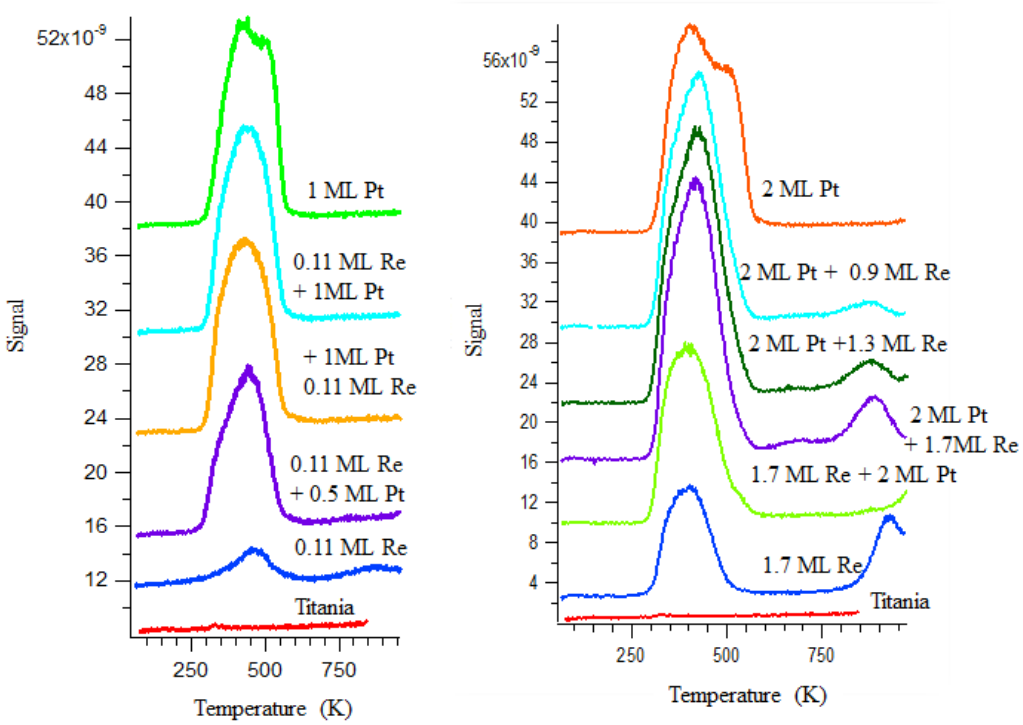

Figure 6.11: TPD data for CO absorption on different compositions of Pt-Re clusters on titania as a function of a) Pt coverage and b) Re coverage.

Mixing Re with the Pt clusters did not cause a significant difference in the absorption behavior of CO on Pt. However, Pt blocked the Re sites that dissociate the CO.

Figure 6.11a show the CO TPD of different coverages of Pt with 0.11 ML Re. Pure Re (0.11 ML Re) shows two CO desorption peaks that correspond to the molecular deposition (low temperature) and CO recombinant peak (high temperature). Pure Pt (1 ML) still shows one molecular desorption peak with a shoulder at high temperatures corresponding to the molecular desorption of CO from step sites. When a small amount of Re was added to the Pt, high-temperature CO desorption peak disappears which indicates that Re has blocked the Pt step sites. When the amount of Pt is decreased by half, the amount of CO desorption was about 70% of that for 1 ML Pt peak. In all other cases, the amount of CO deposition remained almost same on the pure 1 ML Pt.

Figure 11b shows the CO TPD data for 2 ML Pt and different coverages of Re. Only the molecular desorption peak was observed for pure Pt. A molecular desorption peak and a recombinant peak were observed for pure Re. When Re is added to Pt, molecular desorption at step sites on Pt disappears. When Pt is deposited on Re, the recombinant CO desorption peak disappears, which suggests that the Re sites are entirely covered by the Pt. When Re is deposited on Pt, both the molecular peak and the recombinant peaks are observed implying the availability of both Pt and Re on the surface, as also observed in LEIS experiments. The integrated intensity for the molecular desorption peak shows that the highest desorption yield of CO arises from the 2 ML Pt + 1.3 ML Re surface. Lowest from the 1.7 ML Re + 2 ML Pt surface. Desorption temperature of CO did not change significantly for the bimetallic system compared to their monometallic systems.

6.4 Discussion

A comparison of the growth of Pt and Re shows that the dispersion of Re on titania is greater than the dispersion of Pt on titania. Previous studies by our group have shown that the mobility and growth of metals on titania are determined by the affinity of the admetal for oxygen. Pt-O bond strength is lower than the Re-O bond strength and Re is known to be oxophillic in nature, therefore, the observation of high dispersion of Re on titania compared to Pt is expected. Metals with a high mobility, like Au, create 3D clusters on titania while metals with a low mobility, like Re, form 2D islands on titania. The height of 0.11 ML Re, which is 2.92 ± 1.05 Å is close to the thickness of one atomic layer (2.4 Å). Therefore, growth of Re on titania is attributed to 2D growth of clusters in contrast to a 3D growth. This observation demonstrates the strong metal support interactions of Re with titania. Furthermore XPS analysis of the Ti(2p) peak after the deposition of Re also suggest that Re reacts with titania upon deposition at room temperature, and this behavior was not observed for metals such as Pt. Encapsulation of Re by tiatnia due to stromg metal support interactions was confirmed by the LEIS studies. Deposition of thick layers of Re on titania could not completely attenuate the Ti and O LEIS peaks, which suggests that TiO_x atleast partially covere the Re clusters. It has also been suggested that ReO_x diffuses into the titania lattice; temperature programmed reduction studies of Re/TiO_2[31] report that +7 and +4 oxidation states for Re in high loading of Re on titania but for low loading, they only found +4 states. In low loading of Re, only +4 oxidation state is observed due to atomic dispersion of Re in the titania lattice, which prvents it from going to +7. High dispersion of Re on the surface was also observed in our STM experiment. Furthermore, XPS data shows the reduction of Ti(2p) indicating a change in valency of Ti^{4+} that could be caused by diffusion

of Re into the titania lattice. The absenece of a recombinant CO peak in the TPD data for smaller coverages (0.11 ML Re) suggest an absence of therequsite sites or ensembles of Re atoms necessary for CO dissociation. This behavior could be a combination of encapsulation of Re by titania and diffusion of Re on titania lattice that leads to different valencies of Re. Strong metal support interactions that lead to encapsulation of metal clusters by a reducible supports have previously been observed at elevated temperatures and reducing conditions for other metals such as Pt and Co.[32-34]

Formation of bimetallic clusters has been achieved by depositing less mobile Re first followed by Pt for total metal coverage of 0.24 ML. When the more mobile Pt is deposited first followed by Re, a mixture of mono and bimetallic clusters was formed. Despite the fact that different order of Pt deposition results in different cluster densities and sizes, the overall surface compositions are similar. The surfaces are Pt rich for both orders of deposition. In contrast, for higher coverages where the total amount of metal has been fixed at 3.7 ML, both orders of deposition form bimetallic clusters. In both cases, the first deposition provides enough seed clusters for the nucleation of the second metal. However, the cluster density and size distribution are significantly different due to differences in the number of initial seed clusters. LEIS data shows that the Re+Pt is Pt rich where is Pt+Re has a mixture of Pt and Re on the surface. Pt rich surfaces for the bimetallic clusters are consistent with the lower surface free energy of Pt (2.5 J/m^2) compared to Re (3.6 J/m^2). Furthermore, strong interactions of Re with titania also another driving factor for the Re to diffuse to the support. It has also been shown that alloys such as $Pt_{75}Re_{25}$ form a core-shell structure with the Pt at the shell [35,36]

When there is 0.22 ML Re on the surface, a sufficient amount of Re is present, but for the bimetallic clusters with total metal coveraage of 0.24 ML, the CO desorption profiles look similar to CO desorption from pure Pt clusters. Furthermore, the higher desorption peak that is characteristic of presncce of metallic Re was not observed. The CO desorption profile for high coverages of pure Re (1.7 ML) shows more metallic behavior compared to lower coverages. For pure 2 ML Pt, a molecular desorption peak was observed with a higher internsity compared to lower covareges. For all the compositions where Re is deposited second (2 ML Pt+ 1.7 ML Re, 2 ML Pt+1.3 ML Re, 2 ML Pt + 0.9 ML Re) the amount of the higher CO desorption peak at higher temperatures increased as the amount of Re is increased. This suggest that the amount of metallic Re present for the dissociation of C-O bond is proportional to the amount of Re deposited on the Pt. LEIS data also indicates that the surface composition is a mixture of Pt and Re. The yield of lower temperature CO desorption peak that correspond to the molecular desorption of CO is highest for bimetallic Pt-Re compositions compared to pure Pt or pure Re. A similar observation has been reported when Re is deposited on Pt(111), and has been attributed to the electronic interactions between Pt-Re.[27] For the opposite order of deposition (1.7 ML Re + 2ML Pt), no C-O dissociation was observed. The molecular desorption peak also was smaller compared to other bimetallic compositions and as well as pure Pt. This obseravtion is contradictory to the LEIS data, in which the surface Pt is highest for 1.7 ML Re + 2 ML Pt, which in principle should give rise to higher CO desorption. For this composition, the molecular desorption from the step sites of Pt was also not observed. The structure of Pt on the Re/TiO_2 could be different from the structure of Pt on TiO_2 which leads to lower adsorption of CO at room temperature.

CO desorption from the step sites of pure Pt at higher desorption disappears when a small amount of Re is added to the Pt. This behavior can be explained by the blocking of step sites which has been shown for Pt-Au and Pt-Co as well.[37,38] When 1 ML Pt is added to 0.11 ML Re/TiO_2, diffusion of Re to step sites on the Pt seems unlikely given the fact that Re has very strong metal support interactions and higher surface free energy compared to Pt. Another explanation might be that the growth of Pt on Re/TiO_2, could be different compared to the growth of Pt on TiO_2. Re dispersion on the surface of the titania, lattice has also been suggested before. [31] Re is known to modify the oxide supports like alumina as well.[39] When a supported metal on an oxide is prepared from an adsorbed precursor incorporating a noble metal bonded to an oxophilic metal such as Re, the result may be small noble metal clusters nested in a cluster of atoms of the oxophilic metal, which is oxidized and anchored to the support through metal-oxygen bonds.[40,41] Therefore it is possible that Pt grows differently on the Re/TiO_2. However, at this point the structure of the Pt on Re/TiO_2 is not clear.

Heating to elevated temperatures resulted in cluster sintering in both pure and bimetallic clusters. Lowest sintering is observed for pure Re from both STM and LEIS studies. This is partly because Re already has been partially encapsulated with titania and, therefore, both sinter resistant and extent of encapsulation at elevated temperatures is not that significant compared to room temperature. Sintering of bimetallic clusters shows similar behavior as their monometallic counterparts. Decrease in the LEIS signal is attributed to the cluster sintering and encapsulation. Deposition of Re on titania has reduced the titania surface whereas deposition of the same amount of Pt did not reduce the titania support, which suggest the encapsulation of Re by tiatnia at room temperature. At elevated

temperatures, strong metal support interactions are reported for Pt as well.[32] It has been shown that Re prevents Pt from sintering on supports such as titania and carbon.[15,21] This has also been observed in the system we studied because the initial amount of clusters is higher in the presence of Re, and therefore sintering is relatively low at higher temperatures compared to pure Pt. The improved dispersion of Pt on Re, which creates smaller clusters compared to pure Pt growth, is known to reduce the structure-sensitive reaction pathways that lead to poisoning of the Pt sites by carbonaceous species.[26] Similarly it has been shown that the most active Pt-Re bimetallic clusters for water gas shift reaction are produced by sequential impregnation of Re followed by Pt.[42] These observations can be explained by our STM studies, which shows that Pt is deposited on the Re results in a greater number of nucleation sites both at room tmperature and elevated temperatures.

For low coverages, Pt-Re interactions were difficult to determine using XPS, due to cluster size effects. Pt-Re interactions were observed when 1.7 ML Re is deposited on 2 ML Pt. When Pt is deposited second on Re, there were no Pt-Re interactions observed. When Re is deposited first, strong interactions between Re and the support prevent Pt-Re interactions. A study of Pt-Re catalyst is made by impregnation of metals on alumina, has also shown no Pt-Re interactions but a modification of the support due to strong Re-alumina support interactions.[43] Different catalytic pretreatment and preparation methods such as calcination, coimpregnation, successive impregnation reported that Pt-Re interactions.[44,45] This was also observed in our system, when Re was deposited first, Re-Pt interactions were not observed due to the dominant Re-support interactions.

6.5 Conclusions

Re shows strong metal support interactions even at room temperature resulting in highly dispersed Re layers. Encapsulation of Re by TiO_x was observed due to SMSI effects. Pt-Re bimetallic clusters were prepared by depositing less mobile Re first followed by deposition of Pt for sub monolayer coverages. The surface composition of the bimetallic clusters was Pt rich due to the lower surface free energy of Pt and oxophillic nature of Re. CO adsorption behavior of the bimetallic clusters resembled the activity of pure Pt. At higher coverages (3.7 ML total metal coverage) bimetallic clusters were formed by both orders of deposition. (Re on Pt and Pt on Re). When Re was deposited first it resulted in higher nucleation density for bimetallic clusters, and the surface 100% Pt, and the activity resembled that of pure Pt. When Pt was deposited first, the initial seed cluster density was low resulting in a lower density of bimetallic clusters which led to a lower surface area. In this order of deposition surface composition was a mixture of Pt and Re and the activity studies also suggested that both Pt and Re are active sites for the adsorption of CO. Pt-Re interactions were observed when Pt was deposited on titania followed by the deposition of Re.

6.6 References

(1) Sharaf, O. Z.; Orhan, M. F. An overview of fuel cell technology: Fundamentals and applications. Renewable and Sustainable Energy Reviews **2014**, 32, 810-853.

(2) Chheda, J. N.; huber, G. W.; Dumesic, J. A. Liquid-Phase Catalytic Processing of Biomass-Derived Oxygenated Hydrocarbons to Fuels and Chemicals. Angew Chem Int Ed

2007, 46, 7164.

(3) Haryanto, A.; Fernando, S.; Murali, N.; Adhikari, S. Current Status of Hydrogen Production Techniques by Steam Reforming of Ethanol Energy and Fuels **2005**, 19, 2098.

(4) Huber, G. W.; Shabaker, J. W.; Evans, S. T.; Dumesic, J. A. Aqueous-Phase Reforming of Ethylene Glycol over Supported Pt and Pd Bimetallic Catalysts. Appl. Catal. B **2006**, 62, 226.

(5) Shabaker, J. W.; Davda, R. R.; Huber, G. W.; Cortright, R. D.; Dumesic, J. A. Aqueous-Phase Reforming of Methanol and Ethylene Glycol over Alumina-Supported Platinum Catalysts. J. Catal **2003**, 215, 344.

(6) Haryanto, A.; Fernando, S.; Murali, N.; Adhikari, S. Current Status of Hydrogen Production Techniques by Steam Reforming of Ethanol: A Review. Energy and Fuels **2005**, 19, 2098.

(7) Deluga, G. A.; Salge, J. R.; Schimidt, L. D.; Verykios, X. E. Renewable Hydrogen from Ethanol by Autothermal Reforming. Science **2004**, 303, 993.

(8) Sun, J.; Qui, X. P.; Wu, F.; Zhu, W. T. H_2 from Steam Reforming of Ethanol at Low Temperature over Ni/Y_2O_3, Ni/La_2O_3 and Ni/Al_2O_3 Catalysts for Fuel-Cell Application. Int. J. Hudrog. Energy **2005**, 30, 437.

(9) Biswas, J.; Bickle, G. M., Gray, P. G.; Do, D. D.; Barbier, J. The role of Deposited poisons and Crstellite Surface Structure in the Activity and Seclectivity of Refoeming Catalyts. Catal. Rev.-Sci.Eng. **1988,** 30, 161-247

(10) Querini, C. A.; Fung, S. C. Coke and Product Profiles Formed along the Catalyst Bed during n-Heptane Reforming

i. Nonsulfided Pt/Al_2O_3 and $Pt-Re/Al_2O_3$. Journal of Catalysis **1993**, 141, 389-406.

(11) Biswas, J.; Bickle, G. M.; Gray, P. G.; Do, D. D.; Barbier, J. The Role of Deposited Poisons and Crystallite Surface Structure in the Activity and Selectivity of Reforming Catalysts Catal.Rev.-Sci.Eng **1988**, 30, 161-247.

(12) Zhang, L.; karim, A. M.; Engelhard, M. H.; Wei, Z. H.; King, D. L.; Wang, Y. Correlation of Pt-Re Surface Properties with Reaction Pathways for the Aqueous-Phase Reforming of Glycerol. J. Catal **2012**, 287, 37.

(13) Azzam, K. G.; Babich, I. V.; Seshan, K.; Mojet, B. L.; Lefferts, L. Stable and Effecient $Pt-Re/TiO_2$ cata;yts for Water Gas Shift: On the Effect of Rhenium ChemCatChem **2013**, 5, 557-564.

(14) Azzam, K. G.; Babich, I. V.; Sehan, K.; Lefferts, L. Role of Re in $Pt-Re/TiO_2$ catalyts for water gas shift reaction: A mechanistic and Kinetic Study. Applied Catalysis B: Environmental **2008**, 80, 129-140.

(15) Azzam, K.; Babich, I.; Seshan, K.; Lefferts, L. A bifunctional catalyst for the single-stage water–gas shift reaction in fuel cell applications. Part 2. Roles of the support and promoter on catalyst activity and stability. Journal of Catalysis **2007**, 251, 163-171.

(16) Sato, Y.; Terada, K.; Hasegawa, S.; Miyao, T.; Naito, S. Mechanistic study of water–gas-shift reaction over TiO2 supported Pt–Re and Pd–Re catalysts. Applied Catalysis A: General **2005**, 296, 80-89.

(17) Kirilin, A. V.; Tokarev, A. V.; Manyar, H.; Hardacre, C.; Salmi, T.; Mikkola, J. P.; Murzin, D. Y. Aqueous phase reforming of xylitol over Pt-Re bimetallic catalyst: Effect of the Re addition. Catalysis Today **2014**, 223, 97-107.

(18) Zhang, L.; Karim, A. M.; Engelhard, M. H.; Wei, Z.; King, D. L.; Wang, Y. Correlation of Pt–Re surface properties with reaction pathways for the aqueous-phase reforming of glycerol. Journal of Catalysis **2012**, 287, 37-43.

(19) King, D. L.; Zhang, L.; Xia, G.; Karim, A. M.; Heldebrant, D. J.; Wang, X.; Peterson, T.; Wang, Y. Aqueous phase reforming of glycerol for hydrogen production over Pt–Re supported on carbon. Applied Catalysis B: Environmental **2010**, 99, 206-213.

(20) Ciftci, A.; Eren, S.; Ligthart, D. A. J. M.; Hensen, E. J. M. Platinum-Rhenium Synergy on Reducible Oxide Supports in Aqueous-Phase Glycerol Reforming. ChemCatChem **2014**, n/a-n/a.

(21) Kunkes, E.; Simonetti, D.; Dumesic, J.; Pyrz, W.; Murillo, L.; Chen, J.; Buttrey, D. The role of rhenium in the conversion of glycerol to synthesis gas over carbon supported platinum–rhenium catalysts. Journal of Catalysis **2008**, 260, 164-177.

(22) Simonetti, D.; Kunkes, E.; Dumesic, J. Gas-phase conversion of glycerol to synthesis gas over carbon-supported platinum and platinum–rhenium catalysts. Journal of Catalysis **2007**, 247, 298-306.

(23) Iida, H.; Igarashi, A. Structure characterization of Pt-Re/TiO2 (rutile) and Pt-Re/ZrO2 catalysts for water gas shift reaction at low-temperature. Applied Catalysis A: General **2006**, 303, 192-198.

(24) Choung, S. Y.; Ferrandon, M.; Krause, T. Pt-Re bimetallic supported on CeO2-ZrO2 mixed oxides as water–gas shift catalysts. Catalysis Today **2005**, 99, 257-262.

(25) Fung, A. S.; Kelley, M. J.; Konongsberger, D. C.; Gates, B. C. ɣ-Al_2O_3-supported Re-Pt Cluster Catalyst Prepared from $[Re_2Pt(CO)_{12}]$: Characterization by Extended X-ray Absorption Fine Structure Spectroscopy and Catalysis of Methycyclohexane Dehydrogenation. Journal of the American Chemical Society **1997**, 119, 5877-5887.

(26) Ribeiro, F. H.; Bonivardi, A. L.; Kim, C.; Samorjai, G. A. Transformation of Platinum into a Satable, High-Temperature, Dehyrdation-Hydrogenation Catalyts by Ensemble Size Reduction with Rhenium and Sulfur. Journal of Catalysis **1994**, 150, 186-198.

(27) Godbey, D. J.; Somorjai, G. A. The adsorption and Desorption of Hydrogen and Corbon Monoxide on Bimetallic Re-Pt(111) Surfaces. Surface Science **1988**, 204, 301-318.

(28) Cheng, D.; Wang, W.; Huang, S. Core–shell-structured bimetallic clusters and nanowires. Journal of Physics: Condensed Matter **2007**, 19, 356217.

(29) Sinfelt, J. H.: Bimetallic Catalyts: Discopveries, Concepts and Applications: New York: Wiley, 1983.

(30) Galhenage, R. P.; Yan, H.; Tenney, S. A.; Park, N.; Henkelman, G.; Albrecht, P.; Mullins, D. R.; Chen, D. A. Understanding the Nucleation and Growth of Metals on TiO2: Co Compared to Au, Ni, and Pt. The Journal of Physical Chemistry C **2013**, 117, 7191-7201.

(31) Komiyama, M.; Sato, J.; Yamamoto, K.; Ogino, Y. Catalytically Active Species on Titania-Supported Rhenium for Hydrogenation of Carbon Monoxide Langmuir : the ACS journal of surfaces and colloids **1987**, 3, 845-851.

(32) Tenney, S. A.; He, W.; Ratliff, J. S.; Mullins, D. R.; Chen, D. A. Characterization of Pt–Au and Ni–Au Clusters on TiO2(110). Topics in Catalysis **2011**, 54, 42-55.

(33) Galhenage, R. P.; Ammal, S. C.; Yan, H.; Duke, A. S.; Tenney, S. A.; Heyden, A.; Chen, D. A. Nucleation, Growth, and Adsorbate-Induced Changes in Composition for Co–Au Bimetallic Clusters on TiO2. The Journal of Physical Chemistry C **2012**, 116, 24616-24629.

(34) Tauster, S. J. Strong Metal Support Interactions Account of Chemical Research **1987**, 20, 389-394.

(35) Wang, G.; Vanhove, M.; Ross, P.; Baskes, M. Quantitative prediction of surface segregation in bimetallic Pt–M alloy nanoparticles (M=Ni,Re,Mo). Progress in Surface Science **2005**.

(36) Wang, G.; Van Hove, M. A.; Ross, P. N.; Baskes, M. I. Monte Carlo simulations of segregation in Pt-Re catalyst nanoparticles. The Journal of chemical physics **2004**, 121, 5410-5422.

(37) Galhenage, R. P.; Yan, H.; Ahsen, A. S.; Ozturk, O.; Chen, D. A. Understanding the Growth and Chemical Activity of Co–Pt Bimetallic Clusters on TiO2(110): CO Adsorption and Methanol Reaction. The Journal of Physical Chemistry C **2014**, 118, 17773-17786.

(38) Tenney, S. A.; Shah, S. I.; Yan, H.; Cagg, B. A.; Levine, M. S.; Rahman, T. S.; Chen, D. A. Methanol Reaction on Pt-Au Clusters on TiO_2 (110): Methoxy-induced Diffusion of Pt. J.Phys.Chem.C **2013**, 117, 26998–27006.

(39) Huang, Z.; Fryer, J.R.; Park, C.; Stirling, D.; Webb, G.; Transmission Electron Microscopy and Energy Dispersive X-Ray Spectroscopy Studies of Pt-Re/ɣ-Al_2O_3 Catalysts. Jouranl of Catalyis. **1994,** 148, 478-492

(40) Regulbuto, J. Catalyst Preparation Science and Engineering. CRC press, **2006**

(41) Fung, A. S.; Kelley, M. J.; Koningsberger, D. C.; Gates, B. C. ɣ-Al_2O_3 Supported Re-Pt Cluster Catalyst Prepared from $[Re_2Pt(CO)_{12}]$: Characterization by Extended X-Ray Absorption Fine Structure Spectroscopy and Catalysis of Methelycyclohexane Dehdrogenation. J.Am.Chem.Soc. **1997,** 119, 5877-5887

(42) Azzam, K. G.; Babich, I. V.; Seshan, K.; Mojet, B. L.; Leffarts, Leon. Stable and Efficient Pt-Re/TiO_2 Catalysts for Water-Gas-Shift: On the Effect of Rhenium. Chem.Cat.Chem. **2013**, 5, 557-564

(43) Huang, Z.; Fryer, J. R.; Park, C.; Stirling, D.; Webb, G. Transmission Electron Microsocopy and Energy Dispersive X-Ray Spectroscopy Studies of Pt-Re/ ɣ-Al_2O_3 Catalysts. Journal of Catalysis **1994**, 148, 478-492.

(44) Pretsvik, R.; Totdal, B.; Lyman, C. E.; Holmen, A. Bimetallic particles formation in Pt-Re/Al_2O_3 reforming catalysts revealed by energy dispersive X-ray spectrometry in the analytical elctron microscope. Journal of catalysis **1998**, 176, 246-252.

(45) Piek, C. L., Marecot, P., Querini, C. A., Parera, J. M., Barbier, J. Influence of Pt-Re Interactions on Activity and Selectivity of Reforming Catalysts. Appl.Catal. A:General. **1995**, 133, 281-292

Chapter 7. Platinum-Ruthenium bimetallic clusters on graphite: A comparison of vapor deposition and electroless deposition methods

7.1 Introduction

Electrochemical fuel cells have provided an attractive option for portable energy sources that do not rely on fossil fuels.[1-3] In particular, direct methanol fuel cells (DMFCs) have garnered substantial attention due to their high energy density, ease of handling, low operation temperature, and lack of polluting emissions.[1, 2, 4-10] A major challenge for the DMFC is the development of an anode catalyst for efficient electro-oxidation of methanol. Platinum catalysts have been used for the DMFC, and although Pt catalyzes the oxidation of methanol to CO_2, the Pt active sites become poisoned by CO.[1, 2, 6, 11-13] However, bimetallic catalysts such as Pt-Ru supported on carbon are reported to exhibit activity superior to Pt alone.[1, 2, 6, 10, 12, 14,15] The origin of this resistance to poisoning has been explained by two well-established theories: the bifunctional mechanism and ligand effect. According to the bifunctional mechanism, the oxides of Ru provide sites for water dissociation to surface OH, which facilitates the oxidation of the intermediates of methanol decomposition that poison the active Pt sites.[16-20] The ligand (electronic) effect proposes that electronic interactions between Pt and Ru lower the energy of the d band of Pt and cause CO to bind less strongly to Pt.[15, 18, 21-25] In recent studies, the bifunctional mechanism is reported to play the dominant role, with the ligand effect providing a minor contribution to the reduced CO poisoning.[9, 14, 20]

The most active catalysts for methanol electro-oxidation are composed of highly dispersed, nanosized Pt-Ru particles deposited on a carbon support, but small variations in preparation conditions have a significant impact on activity.[1, 12] Conventional impregnation methods have difficulty controlling the dispersion and surface compositions of the Pt-Ru catalysts.[1, 2, 7, 26-29] Although colloidal and microemulsion preparation

methods are known to deposit highly dispersed, nanosized Pt-Ru clusters,[28-35] these methods require complex preparation procedures and expensive starting materials, making them ill-suited for commercial scale up.[1, 2, 28, 30] Therefore, practical preparation methods that produce active Pt-Ru catalysts are still being sought. Monnier and coworkers have demonstrated that electroless deposition (ED) can be used to prepare well-dispersed, exclusively bimetallic clusters in which the two metals are well mixed.[36-42] In this method, the secondary metal in the form of a metallic salt is selectively deposited from solution on the surface of the primary metal, which has been activated by a reducing agent, rather than on the catalyst support.[37, 38, 43-45] Studies by Weidner and coworkers of methanol electro-oxidation with Pt-Ru catalysts on carbon (XC-72) show that 50% Pt-50%Ru catalysts prepared by electroless deposition of Ru on commercial Pt/C have higher activity than the commercial bimetallic catalysts (E-TEK) of the same composition.[46] This higher activity is attributed to better mixing of Pt and Ru on the atomic scale, given that the commercial Pt-Ru catalysts are known to be poorly mixed, with particles of pure Ru and pure Pt coexisting with bimetallic particles.[47, 48]

In this work, the nucleation and growth of vapor deposited Pt, Ru and Pt-Ru clusters on highly ordered pyrolytic graphite (HOPG) are investigated and compared with bimetallic cluster growth via electroless deposition. Unlike vapor deposition, electroless deposition is a method that can be readily adapted for industrial catalyst preparation, given that electroplating has been used commercially for many years in the preparation of thin film coatings.[43] HOPG provides an atomically flat, crystalline surface to serve as a model carbon support for well-characterized bimetallic Pt-Ru clusters, and HOPG is also sufficiently conductive for STM, XPS and LEIS studies. Exclusively bimetallic clusters

can be grown by either deposition of Pt on Ru (Ru+Pt) or Ru on Pt (Pt+Ru), provided that the first metal generates a high enough cluster density to serve as nucleation sites for the second metal. The HOPG surfaces are initially sputtered with Ar^+ before metal deposition to introduce defects that serve as nucleation sites. The surfaces of the bimetallic clusters are Pt-rich, regardless of the order of deposition, implying that the atoms readily diffuse within the clusters to achieve the lowest energy surface. Electroless deposition of Pt on Ru seed clusters on HOPG resulted in the formation of bimetallic clusters. Although electroless deposition of Ru on Pt was also achieved, trace Ag contamination in the $Ru(NH_3)_6Cl_3$ salt caused the deposition of Ag in addition to Ru.

7.2 Experimental

Surface characterization and preparation were carried out in an ultrahigh vacuum (UHV) chamber that has previously been described in detail.[49-54] This chamber has a base pressure below 1×10^{-10} Torr and is equipped with a variable-temperature STM (Omicron VT-25), a hemispherical analyzer (Omicron EA125) for X-ray photoelectron spectroscopy and low energy ion scattering experiments, and a load lock chamber for rapid introduction of new samples.

The HOPG support was purchased from SPI supplies (10 mm x 10mm x 1 mm, SPI 3). The HOPG samples were mounted on a standard Omicron tantalum sample plate and heated via electron bombardment using a tungsten filament positioned behind the sample plate.[55] Before each experiment, a clean surface was prepared by cleaving the surface with adhesive tape in air and reintroducing the sample into the UHV chamber. Approximate temperatures were measured by a K-type thermocouple spot welded to the edge of the sample plate. In order to create surfaces with more defects for metal nucleation, the HOPG

was sputtered with Ar^+ at 500 eV at a current of 0.1 □A and Ar pressure of 3 x 10^{-7} Torr for 30 seconds and 5 minutes. For comparison, the more aggressive sputtering conditions used for cleaning TiO_2(110) and Pt(111) surfaces are 1 kV, 3-5 □A, and 1-5x10^{-6} Torr for 20 min. Following sputtering, the HOPG surfaces were heated to 950-1000 K for 12 min to remove embedded Ar.

Metal deposition was achieved with an electron-beam evaporator (Oxford Applied Research, EGCO4) using a Ru bar (Good Fellow, 99.9%, 2 mm x 2 mm x 25 mm) or a Pt rod (ESPI, 99.99%, 2 mm diameter). During deposition, a +800 V bias was applied to the surface in order to repel the positively charged metal ions that are known to create defect sites for metal nucleation on HOPG.[56] Metal coverages were determined using an independently calibrated quartz crystal microbalance (Inficon, XTM-2),[57] and one monolayer (ML) is defined as the packing density of Pt(111) (1.50 x 10^{15} atoms/cm^2) or Ru(0001) (1.58 x 10^{15} atoms/cm^2).

Procedures for the electroless deposition of Pt and Ru were adapted from previous experiments conducted on Pt and Ru catalysts supported on a powdered carbon support (XC-72).[46] The general procedures for electroless deposition experiments have been described in detail elsewhere.[36, 45, 58] Concentrations of the metals in ppm are calculated from the mass of the metal only divided by the total mass of the solution. For the deposition of Pt on 0.43 ML Ru clusters on HOPG, the electroless deposition (ED) bath consisted of a 100 mL aqueous solution of 20-60 ppm Pt^{+2} (H_2PtCl_6, Sigma-Aldrich) with dimethylamine borane (DMAB, Sigma-Aldrich) as the reducing agent in a 5:1 molar ratio of DMAB:Pt^{+2}. The total deposition time in the Pt ED bath was 60 min, and an additional aliquot of DMAB was added after 30 min in order maintain the 5:1 molar ratio, assuming

that all of the initial DMAB was consumed at this time. The temperature of the ED bath was maintained at either 40 or 70 °C by immersion in a temperature-controlled water bath. The pH was fixed at 11.0 $\pm$ 0.2 through the addition of 1-2 drops of 10 M NaOH, followed by 1 M HCl and 1 M NaOH for fine adjustment, if necessary. The bath for the electroless deposition of Ru on 0.50 ML Pt clusters on HOPG was a 120 mL aqueous solution of 50 ppm Ru^{+3} ($Ru(NH_3)_6Cl_3$, Sigma-Aldrich) and formic acid (Fluka) as the reducing agent in a molar ratio of formic acid:Ru^{+3} of 10:1. The total deposition time in the Ru ED bath was 90 min, and additional aliquots of formic acid solution were added after 30 and 60 min to maintain the 10:1 molar ratio. The temperature of the bath was set at 90 °C, and a pH of 3.5-4 was maintained through the addition of HCl and NaOH. After removal of the HOPG sample from the ED bath, the surface was thoroughly washed with deionized water before transferring into the UHV chamber for surface analysis. All aqueous solutions were prepared with deionized water, experiments were carried out in single-use polypropylene cups, and the ED baths were vigorously stirred during deposition.

STM experiments for clusters on HOPG were carried out with a constant tunneling current of 0.1-0.2 nA and a sample bias of +2-2.3 V with respect to the tip; the clean HOPG surface was imaged with a 0.8 nA tunneling current and +1.0 V bias. STM tips consisted of 0.38 mm diameter tungsten wire that was electrochemically etched in NaOH and conditioned by voltage pulsing and sputtering with Ar^+.[51] Cluster heights are reported as a measure of cluster size since tip convolution effects are known to significantly overestimate diameters.[51, 57, 59, 60] The average cluster heights and standard deviations were determined using an in-house program[53, 61] that measured all clusters in a 100 x 100 nm^2 image. For the following surfaces, 50 clusters were measured manually because the

program was unable to accurately assess the heights of clusters: 0.50 ML of Pt and 0.43 ML of Ru on unmodified HOPG, 0.43 ML Ru+Pt ED (20, 50 ppm Pt^{+2}).

LEIS experiments were carried out with a 600 eV He^{+} beam using a dwell time of 0.2 s and step size of 0.2 s and a current to the sample of 25 □A. Exposure to the ion beam was minimized to prevent damage to the surface during the LEIS experiment. XPS studies were conducted with an AlK□ anode (1486.6 eV) using a dwell time of 0.2 s and step size of 0.02 eV.

7.3 Results

An STM image of the freshly cleaved HOPG surface shows that the surface consists of atomically flat terraces that are as wide as 1000 Å. The terraces are separated steps of 5-10 Å in height, which correspond ~1-3 atomic layers (Figure 7.1a). When 0.25 ML of Pt is deposited on this freshly cleaved surface, three-dimensional clusters are formed with a cluster density of 0.12×10^{12} cm^{-2}, and these clusters are preferentially found at the step edges, which are the preferred coordination sites (Figure 7.1b). The average height for the clusters at the step edge is 33.0 ± 3.7 Å while the larger clusters on the terraces have heights ranging from 40-50 Å. Furthermore, it was difficult to collect high quality images due to the relatively strong interactions between the Pt clusters and the STM tip.

These interactions are a consequence of the weak binding between Pt and the HOPG support,[62] and the fact that the glitches often coincide with the appearance of fully or partially imaged Pt cluster on the terraces suggests that the clusters are picked up or dropped by the STM tip. The presence of the majority of the Pt clusters at the steps implies that Pt atoms are mobile on the surface at room temperature and diffuse to the preferred

step sites; alternatively, it is possible that the STM tip sweeps the clusters across the terraces to the step edges.

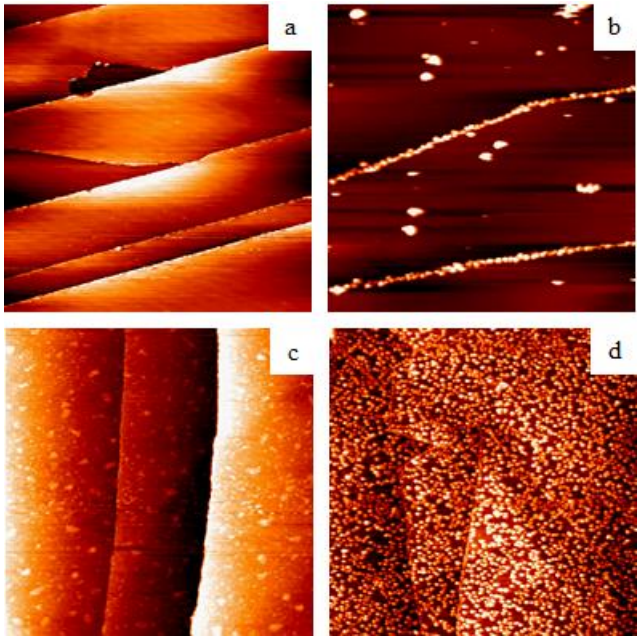

Figure 7.1: Scanning tunneling microscopy images of: a) a freshly cleaved HOPG surface; b) 0.25 ML Pt on HOPG; c) modified HOPG (m-HOPG) prepared by Ar^+ sputtering for 30 s; and d) 0.25 ML Pt on m-HOPG. All images are 4000 Å x 4000 Å.

In order to systematically study nucleation and growth of bimetallic clusters via sequential deposition, a more uniform cluster density over the surface is desirable. Therefore, the HOPG surface was sputtered with Ar^+ to intentionally create surface defects to serve as nucleation sites. After sputtering at 500 eV for 30 s with a 0.1 □A current to the sample, the resulting STM image of the clean HOPG shows that the surface has become more heterogeneous with defect sites appearing on the terraces (Figure 7.1c); this treatment creates the modified HOPG (m-HOPG) surface. In contrast to growth on the unmodified surface, an STM image of 0.25 ML of Pt deposited on m-HOPG shows that the nucleation

density increases by a factor of ~20 (2.25 x 10^{12} cm^{-2}), the average cluster height decreases to 14.6 ± 2.7 Å, and clusters are nucleated uniformly over the surface (Figure 7.1d). Average cluster heights and densities for various surfaces are summarized in Table 7.1. These results are consistent with previous studies reporting that Ar^+ ion sputtering selectively creates nucleation sites for metals on HOPG.[56, 63-68]

A comparison of 0.25 ML and 0.50 ML of Pt on m-HOPG for smaller 1000 Å x 1000 Å images is presented in Figures 2a and b. The cluster density for 0.50 ML of Pt (2.68 x 10^{12} cm^{-2}) is nearly the same as for 0.25 ML, but the average cluster height increases to 16.0 $\pm$ 3.5 Å, implying that the additional Pt atoms contribute to larger cluster sizes rather than nucleating new clusters. Therefore, it appears that almost all of the nucleation sites already are occupied by Pt clusters at a coverage of 0.25 ML. When the HOPG support was sputtered for 5 min to create additional nucleation sites, the deposition of 0.50 ML of Pt on this highly modified surface (hm-HOPG) resulted in the smallest clusters (11.3 $\pm$ 2.7Å) with the highest nucleation density (6.69 x 10^{12} cm^{-2}) (Figure 7.2c).

Bimetallic Pt-Ru clusters are prepared by depositing 0.43 ML of Ru on the 0.50 ML Pt clusters (Pt+Ru) on m-HOPG. A comparison of Figures 2b and 2d indicates that the addition of 0.43 ML of Ru caused a decrease in cluster density from 2.68 to 2.46 x 10^{12} cm^{-2} due to cluster coalescence at the higher coverage, while the average cluster size increased from 16.0 $\pm$ 3.5 Å to 22.8 $\pm$ 6.0 Å. Thus, exclusively bimetallic clusters are formed, given that the incoming Ru atoms nucleate at the existing Pt clusters instead of forming new clusters of pure Ru. Histograms of the cluster heights for all of the clusters imaged over a 1000 Å ×1000 Å region on m-HOPG are presented in Figure B.1 (Appendix B). These height distributions demonstrate that the cluster heights increase with increasing

coverage, and the addition of the second metal results in a shift in the size distribution toward higher values.

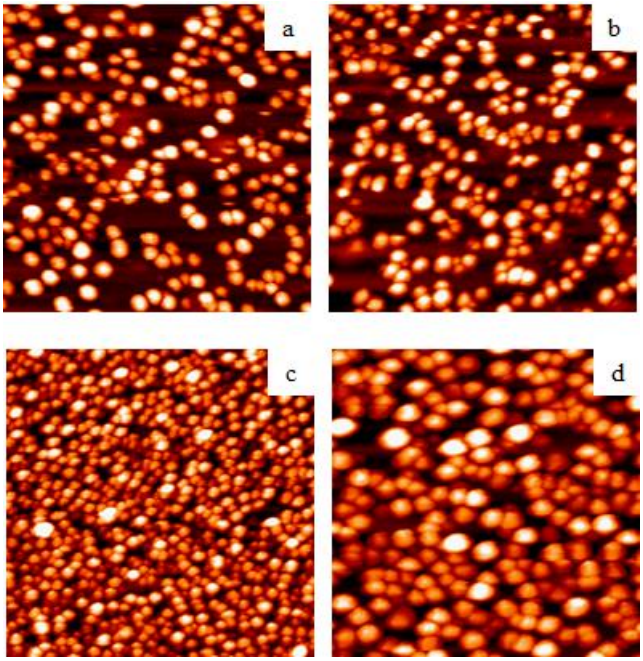

Figure 7.2: Scanning tunneling microscopy images of: a) 0.25 ML Pt on m-HOPG (sputtered 30 s); b) 0.50 ML Pt on m-HOPG; c) 0.50 ML Pt on hm-HOPG (sputtered 5 min); and d) 0.50 ML Pt + 0.43 ML Ru on m-HOPG. All images are 1000 Å x 1000 Å.

The growth of pure Ru clusters on HOPG was also investigated in order to understand the formation of bimetallic clusters via the sequential deposition of Pt on Ru. The deposition of 0.22 ML of Ru on the unmodified HOPG surface (Figure 7.3a,b) demonstrates that the relatively high mobility of the Ru atoms allows the Ru clusters to fill all of the sites at the step edges.

Table 7.1. Average cluster heights and cluster densities for metals on HOPG. All of the surfaces exposed to the Pt ED bath were heated to 130 °C.

Surface	Av. Cluster Height (Å)	Cluster Density ($x10^{12}/cm^2$)
0.25 ML Pt/HOPG	33.0±3.7	0.12
0.25 ML Pt/m-HOPG	14.6±2.7	2.25
0.50 ML Pt/m-HOPG	16.0±3.5	2.68
0.50 ML Pt/hm-HOPG	11.3±2.7	6.69
0.50 ML Pt+0.43 ML Ru/m-HOPG	22.8±6.0	2.46
0.22 ML Ru/HOPG	15.8±3.0	0.19
0.22 ML Ru/m-HOPG	11.7±2.3	2.95
0.43 ML Ru/m-HOPG	17.3±2.9	3.28
0.43 ML Ru+0.50 ML Pt/m-HOPG	19.4±3.9	2.82
0.43 ML Ru+0.50 ML Pt/m-HOPG, 130 °C	22.5±4.7	1.36
0.43 ML Ru+Pt ED (50 ppm Pt^{+2}, 70° C)	34.5±10.9	1.66
0.43 ML Ru+Pt ED (20 ppm Pt^{+2}, 70° C)	24.0±5.9	1.95
0.43 ML Ru+Pt ED (60 ppm Pt^{+2}, 40° C)	22.8±4.6	1.53
0.43 ML Ru+ED bath 40° C, no Pt^{+2}	19.9±4.7	1.58

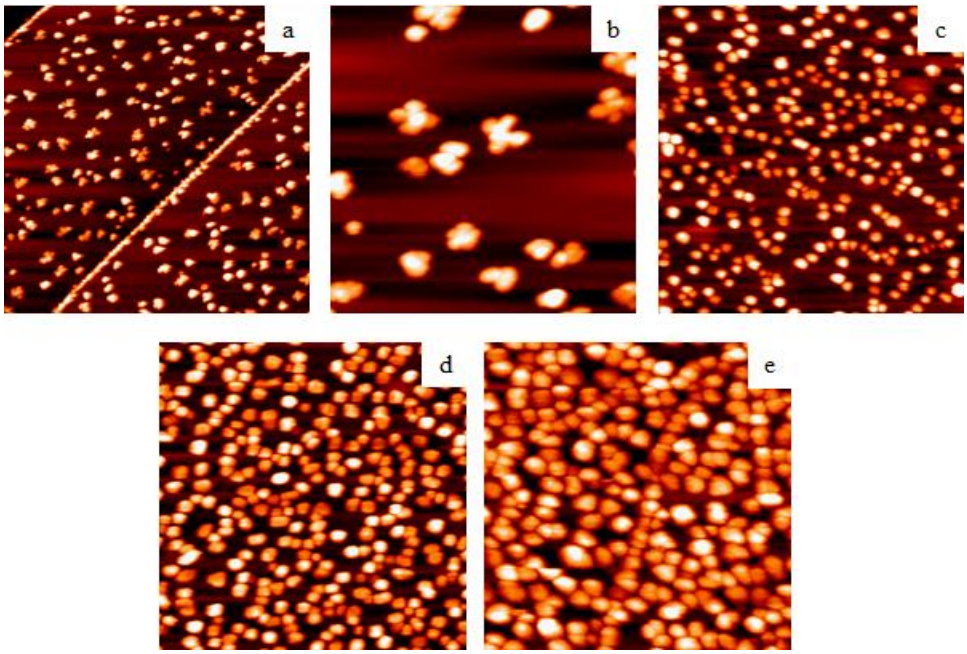

Figure 7.3: Scanning tunneling microscopy images of: 0.22 ML Ru on unmodified HOPG: a) 4000 Åx4000Å and b) 1000 Å x 1000 Å; c) 0.22 ML Ru on modified HOPG (30 s); d) 0.43 ML Ru on m-HOPG; and e) 0.43 ML Ru + 0.50 ML Pt on m-HOPG. Images c-e are 1000 Å x1000 Å.

However, two thirds of the clusters also reside on the terraces, in contrast to the behavior of Pt on unmodified HOPG; this implies that the interaction of the metal clusters with HOPG is weaker in the case of Pt. The average height of clusters on the terraces is 15.8 $\pm$ 3.0 Å while the density of all clusters is 0.19 x 10^{12} cm^{-2}, which is 1.6 times higher than for Pt on HOPG. In general, the clusters at the steps are slightly larger (18.7 $\pm$ 2.0 Å) than at the terraces. Furthermore, the Ru clusters do not have symmetrical shapes but instead exist as clusters of smaller particles.

After modifying the HOPG surface by sputtering for 30 s (m-HOPG), the deposition of 0.22 ML of Ru results in smaller clusters with an average height of 11.7 $\pm$ 2.3 Å and a higher cluster density of 2.95 x 10^{12} cm^{-2} (Table 7.1, Appendix B, Figure B.1).

Increasing the Ru coverage to 0.43 ML m-HOPG produces larger clusters (17.3 $\pm$ 2.9 Å), while the cluster density increases by only ~10% compared to the 0.22 ML coverage (3.28 x 10^{12} cm^{-2}, Figure 7.3c). Both these values are similar to those of 0.50 ML of Pt on m-HOPG, with heights within 10% and cluster densities within 20%. However, a comparison of the histograms (Appendix B Figure 7.1) indicates that there are more small clusters <10 Å for Pt and more large clusters >20 Å for pure Ru, which makes the average cluster height for Ru higher despite the ~20% higher cluster density for Ru. Another difference is that the Ru clusters have more distinctly facetted shapes than Pt, suggesting that the Pt atoms are more mobile within the clusters at room temperature than Ru, and therefore distinct surface facets are not observed for Pt.

After the deposition of 0.50 ML of Pt on the 0.43 ML Ru clusters (Ru+Pt), the cluster density decreases to 2.82 x 10^{12} cm^{-2} as a result of cluster coalescence, and the average cluster height increases to 19.4 $\pm$ 3.9 Å (Figure 7.3e). The larger cluster heights and lower cluster density imply that Pt atoms nucleate at Ru clusters to grow bimetallic clusters, rather than forming new nucleation sites for pure Pt clusters. Notably, the cluster heights and densities are similar for the two bimetallic surfaces although the Pt+Ru surface has a larger average cluster height and lower density due to the initially higher cluster density for pure Ru compared to pure Pt.

LEIS experiments were carried out to evaluate the surface compositions of the Pt+Ru and Ru+Pt bimetallic clusters (Figure 7.4). In order to calculate the surface compositions based on the integrated LEIS peaks, the relative sensitivity factors for Pt and Ru were determined by growing 5 ML Ru and 5 ML Pt films on a Pt foil substrate.

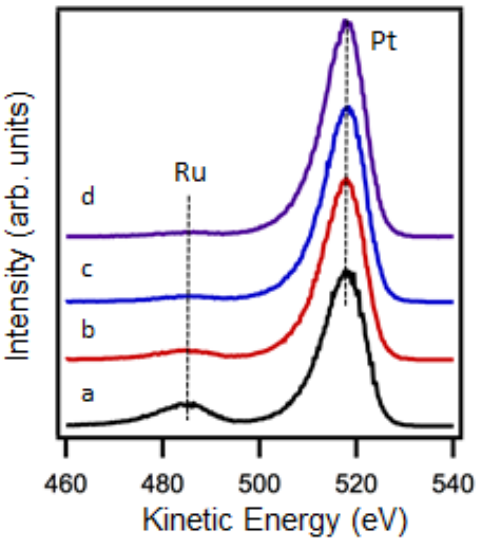

Figure 7.4. Low energy ion scattering data for the following clusters on m-HOPG: a) 0.50 ML Pt+0.43 ML Ru; b) 0.50 ML Pt+0.43 ML Ru heated to 130 °C for 3 min; c) 0.43ML Ru+0.50 ML Pt; and d) 0.43 ML Ru+0.50 ML Pt heated to 130 °C for 3 min.

At this coverage, LEIS experiments showed that the Ru completely covers the Pt foil, given that no Pt signal is detected. The sensitivity for detection of Pt was found to be 1.74 times greater than for Ru, assuming identical surface areas for the films. The surfaces of 0.50 ML Pt+0.43 ML Ru clusters were 80% Pt, whereas the 0.43 ML Ru+0.50 ML Pt clusters were 93% Pt. Furthermore, when the clusters were heated to 130 °C for 3 min, the surface compositions increased to 98-99% Pt for both surfaces. Thus, the bimetallic clusters are rich in Pt regardless of the order of deposition and reach ~100% Pt when the clusters are heated to achieve equilibrium. These results are consistent with the higher surface free energy for Ru (~2.7 J/m^2) compared to Pt (~2.2 J/m^2), which favors Pt at the surface.[69]

Figures 5 and 6 show STM and Pt(4f) XPS data for the electroless deposition of Pt on 0.43 ML Ru clusters on m-HOPG under various conditions (see experimental section for details). No Pt deposition occurs when the freshly cleaved HOPG substrate itself is exposed to the Pt ED bath. All of the surfaces exposed to the ED baths are heated to ~130 °C for 3 min before STM and XPS analysis in order to remove surface contamination that prevents imaging by STM. Since the metal clusters sinter significantly after heating to 130 °C, the ED experiments are compared with vapor deposition experiments in which the surfaces have also been heated to 130 °C. For example, when the vapor deposited 0.43 ML Ru+0.50 ML Pt clusters are heated to 130 °C, a 50% decrease in cluster density is accompanied by an increase in cluster size (Appendix B. Figure 7.1, Table 7.1).

In the first Pt ED experiment with 50 ppm Pt^{+2} at 70 °C, the STM image demonstrates that the surface consists of large clusters with heights ranging from 15 to 65 Å (34.5 ± 10.9 Å) and a cluster density of 1.66 x 10^{12} cm^{-2} (Figure 7.5a). The Pt(4f) region in the XPS data for this surface confirms that Pt was deposited; based on a comparison of the Pt(4f) intensity with that of vapor deposited 0.43 ML Ru+0.50 ML Pt, the Pt coverage in the ED experiment is well over 0.5 ML (Figure 7.6). Due to the high coverage of Pt, it is not possible to determine if Pt deposits selectivity on the Ru seed clusters. Therefore, in the second ED experiment, the Pt^{+2} concentration was decreased to 20 ppm, which resulted in a Pt coverage below 0.5 ML (Figure 7.6). The STM image of this surface (Figure 7.5b) shows clusters with nonuniform heights ranging from 10 to 60 Å (24.0 ± 5.9 Å average height, cluster density of 1.95 x 10^{12} cm^{-2}), and the surface is difficult to image without the tip crashing on the very large clusters.

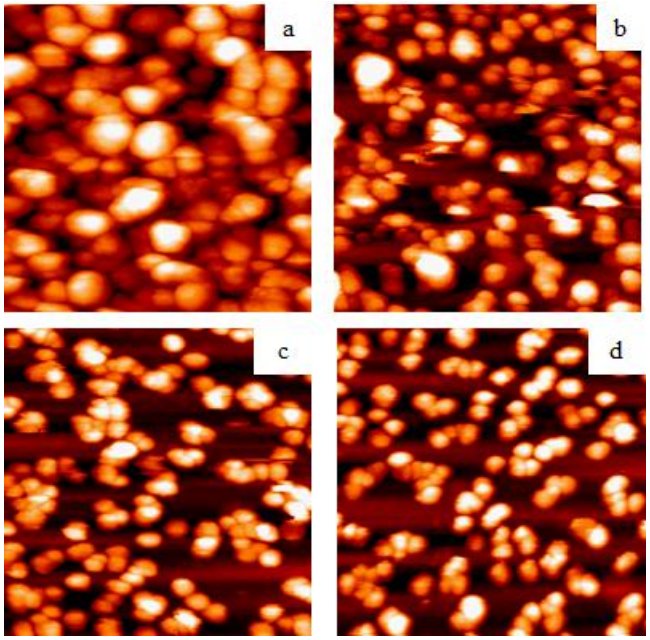

Figure 7.5. Scanning tunneling microscopy images for 0.43 ML Ru on m-HOPG after: a) electroless deposition of Pt (50 ppm of Pt^{+2} at 70℃); b) electroless deposition of Pt (20 ppm of Pt^{+2} at 70℃); c) electroless deposition of Pt (60 ppm of Pt^{+2} at 40℃); and d) exposure to the same electroless deposition conditions in (c) without Pt^{+2}. All surfaces were heated to 130 °C for 3 min, and images are 1000 Å x 1000 Å.

In the third ED experiment, the temperature was reduced to 40 °C in order to decrease the rate of Pt deposition and promote more uniform cluster growth. At a Pt^{+2} concentration of 20 ppm, no Pt was detected by XPS, but a small amount of Pt was deposited from a 60 ppm Pt^{+2} solution at the same temperature (Figure 7.6); this coverage is estimated to be less than 0.1 ML based on the integrated Pt intensity compared to that of the vapor-deposited 0.43 ML Ru+0.50 ML Pt clusters.

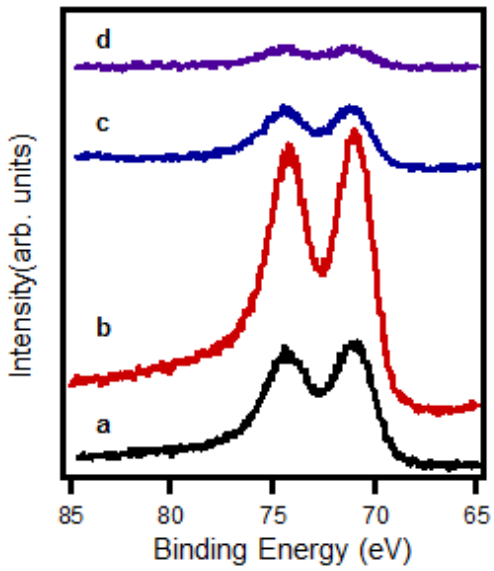

Figure 7.6. X-ray photoelectron spectroscopy data for the Pt(4f) region for 0.43 ML Ru on m-HOPG after the following treatments: a) vapor deposition of 0.50 ML Pt; b) Pt electroless deposition (50 ppm, 70 °C); c) Pt electroless deposition (20 ppm, 70 °C); and d) Pt electroless deposition (60 ppm, 40 °C). All of the surfaces exposed to the ED baths (b-d) were annealed at 130 °C for 3 min.

An STM image of this surface shows clusters with an average height of 22.8 $\pm$ 4.6 Å and a cluster density of 1.53 x 10^{12} cm^{-2} (Figure 7.5c). In order to understand changes due to cluster sintering in the ED bath, 0.43 ML of Ru on m-HOPG was exposed to ED conditions in the absence of the Pt^{+2} salt. XPS data from the resulting surface indicated that no Pt was deposited, and the Ru clusters had an average height of 19.9 $\pm$ 4.7 Å with a cluster density of 1.58 x 10^{12} cm^{-2}. The nearly identical cluster densities and larger cluster sizes for the third Pt ED experiment compared to this surface demonstrate that bimetallic clusters are formed via selective deposition of Pt at the Ru seed clusters.

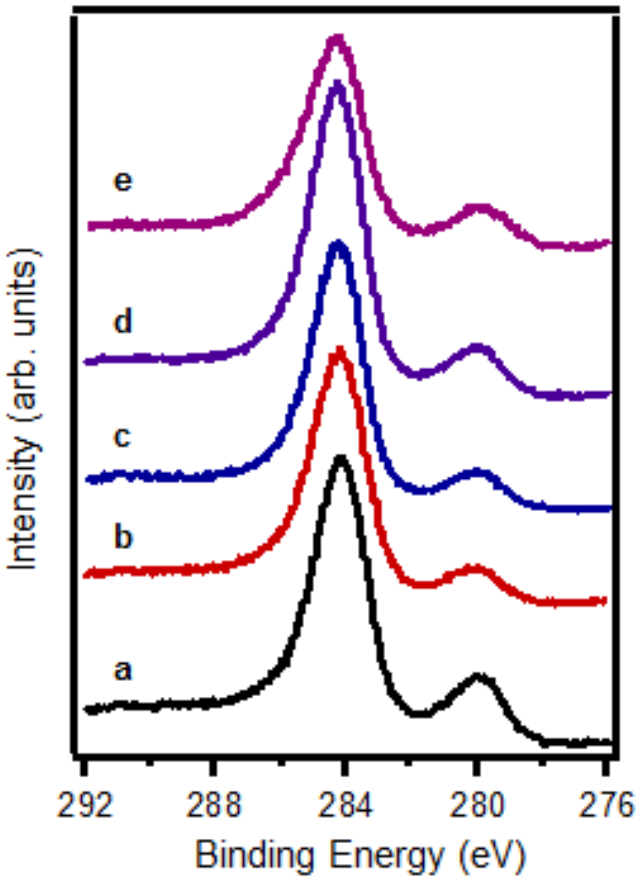

Figure 7.7. X-ray photoelectron spectroscopy data for the Ru(3d)/C(1s) region for 0.43 ML Ru on m-HOPG after the following treatments: a) vapor deposition of 0.50 ML Pt; b) Pt electroless deposition (50 ppm, 70 °C); c) Pt electroless deposition (20 ppm, 70 °C); d) Pt electroless deposition (60 ppm, 40 °C); and e) 0.43 ML Ru exposed to ED bath in (d) without Pt^{+2}. All of the surfaces exposed to the ED baths (b-e) were annealed at 130 °C for 3 min.

The cluster size distributions for these two surfaces confirm that there is a shift to larger sizes after ED of Pt (Appendix B, Figure B.1).

XPS data for the Ru(3d) region are presented in Figure 7, with the Ru($3d_{5/2}$) peak at 280 eV and the Ru($3d_{3/2}$) and C(1s) peaks contributing to the feature at ~284.3 eV. For comparison to the ED experiments, the spectrum of vapor deposited 0.43 ML Ru+0.50 ML Pt appears at the bottom of the figure. The Ru ($3d_{5/2}$) peak is observed for all experiments, indicating that Ru remains on the surface in the ED process. As expected, the intensity of the Ru($3d_{5/2}$) peak decreases with increasing Pt coverage and is attenuated to 40-60% of the intensity of vapor deposited 0.43 ML Ru clusters. Notably, the 0.43 ML Ru clusters exposed to the ED bath without Pt^{+2} also exhibit a 40% decrease in Ru intensity compared to the freshly deposited 0.43 ML Ru clusters despite that fact that no Pt is deposited on the Ru clusters.

Electroless deposition of Ru on Pt seed clusters on hm-HOPG was carried out for 0.50 ML Pt clusters in an ED bath consisting of 50 ppm Ru^{+3} and formic acid (formic acid:Ru^{+3}=10:1) as the reducing agent at a pH of 3.5-4 and temperature of 90 °C; the hm-HOPG was used to create more nucleation sites for Ru deposition and ensure a detectable Ru XPS signal. The appearance of a Ru($3d_{5/2}$) peak indicates that Ru was deposited on the surface, and the Pt(4f) spectrum after deposition shows that Pt remains on the surface after Ru ED (Figure 7.8). However, Ag deposition is also detected by XPS, and inductively coupled plasma emission spectroscopy experiments confirm that there is trace Ag contamination in the $Ru(NH_3)_6Cl_3$ solution. Based on the relative XPS sensitivities for Ag($3d_{5/2}$) and Ru ($3d_{5/2}$),[70] the amounts of Ag and Ru deposited are estimated to be roughly the same.

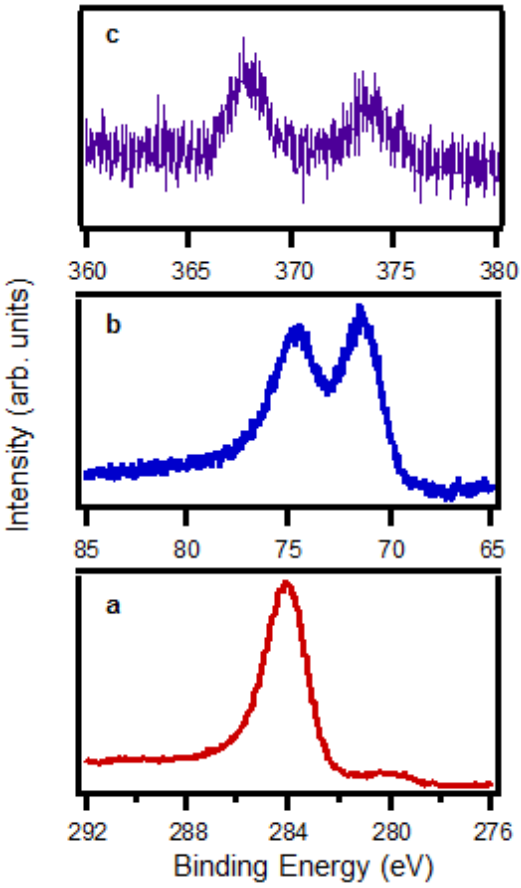

Figure 7.8. X-ray photoelectron spectroscopy data for the: a) Ru(3d)/C(1s); b) Pt(4f); and c) Ag(3d) regions for 0.50 ML Pt on hm-HOPG after exposure to the Ru ED bath. The surface was annealed at 130 °C for 3 min.

LEIS experiments also establish the presence of Ag on the surface. Despite the much higher concentration of Ru^{+3} in solution compared to Ag^{+}, the greater reduction potential for Ag favors the deposition of Ag first, and the relatively small number of surface sites results in comparable coverages of Ru and Ag deposited. Notably, Ag was not detected by XPS for the electroless deposition of Ru using the same $Ru(NH_3)_6Cl_3$ on a commercial

Pt/C catalyst.[46] This behavior is attributed to the greater number of active sites on the powdered carbon support, allowing extensive Ru deposition even after deposition of the Ag contaminant. The use of Pt/C and Pt clusters/HOPG as sacrificial surfaces for the deposition of trace Ag contaminants before exposure to a second Pt/HOPG surface was unsuccessful, given that only Ag was deposited on the second Pt/HOPG surface. Furthermore, other attempts at Ru ED with different Ru salts were not successful because either Ru^{+n} was unstable in solution under ED conditions (K_2RuCl_5, $RuCl_3$, $Ru(NH_3)_6Cl_2$), or the solution was too thermally stable for the reduction of Ru^{+n} ($K_4Ru(CN)_6$). The reduction of Ag^+ contaminants from the Ru^{+3} solution was also attempted using a three-electrode system with potentiostat control, with a Pt wire as the working electrode and a $Hg/HgSO_4$ reference electrode. Given that the standard reduction potential for Ag^+ to Ag is 0.7 V greater than that of $[Ru(NH_3)_6]^{+3}$ to $[Ru(NH_3)_6]^{+2}$, the working electrode was held at a potential close to the value corresponding to the standard potential for reduction of $[Ru(NH_3)_6]^{+3}$ to $[Ru(NH_3)_6]^{+2}$. However, the Ru ED bath prepared from this reduced solution still resulted in the deposition of Ag.

7.4 Discussion

On the unmodified HOPG surface, weak Pt substrate interactions result in high mobility of the Pt atoms and nearly exclusive nucleation of clusters at the step edges. The small fraction of clusters appearing on the terraces is likely due to interactions between the STM tip and Pt clusters that cause cluster displacement. Similarly, other studies of metal clusters such as Pt,[62] Ru[56] and Ag[12, 71, 72] on freshly cleaved HOPG have also shown that weak cluster-support interactions coupled with stronger cluster-tip interactions lead to the tip-induced movement of the clusters on the surface. In general, the mobility of metal

atoms on the unmodified HOPG surface is high at room temperature, and consequently the metal clusters are often found at the favored low-coordinated step sites.[64, 66, 72, 73, 74] However, Ru atoms interact more strongly with HOPG and have decreased mobility, as demonstrated by the higher fraction of Ru clusters found on the terraces and the 60% higher cluster density compared to Pt. Furthermore, the Ru clusters exist on unmodified HOPG as aggregates of smaller particles, and the lack of coalescence of the smaller particles is attributed to different rotational orientations of the crystalline particles with respect to the surface, given that stacking faults preventing coalescence can be formed when particles of two different orientations grow together. In fact, Ru is reported to grow epitaxially on modified HOPG surfaces with two different growth orientations.[75] In both cases, the (0001) face of Ru is parallel to the graphite surface, but one orientation is the same as the graphite lattice whereas the other is rotated by 30°. The aggregates of particles are not observed on m-HOPG, where the Ru clusters have nearly facetted shaped. However, the sizes of the clusters on m-HOPG are generally smaller than the uncoalesced particles on unmodified HOPG due to the shorter Ru diffusion lengths on the more defective m-HOPG.

The nucleation densities of Pt and Ru clusters on HOPG are controlled by creating nucleation sites via Ar^+ ion sputtering. For the same metal coverages, a more highly sputtered surface results in a higher cluster density as well as smaller cluster sizes, and the clusters have a relatively narrow size distribution. Even after sputtering to introduce nucleation sites, the number of clusters for Ru is higher than for Pt, and this is attributed to the higher mobility of Pt atoms on the surface and weaker metal-HOPG interaction for Pt. Furthermore, the difference in cluster densities is greater on the unmodified surface; the Ru density is ~60% higher on the unmodified surface but only 20-30% higher on m-HOPG

for metal coverages of 0.22-0.43 ML. Other literature studies also shown that metal particles with uniform size and spatial distributions are observed after defect sites have been intentionally introduced to the HOPG surface either by sputtering with an inert gas,[56, 63-68] or by sputtering followed by oxidation in air at temperatures above 500 °C.[12, 63, 71, 75]

Bimetallic clusters are formed from sequential vapor deposition of Ru on Pt or Pt on Ru for 0.4-0.5 ML coverages of both metals on m-HOPG. For bimetallic clusters growth on TiO_2(110), our group has shown that exclusively bimetallic clusters can be grown when the less mobile metal is deposited first, followed by the more mobile metal.[51-53, 57, 76, 77] Moreover, it is also possible to form only bimetallic clusters through either order of sequential deposition as long as the number of nucleation sites formed during the deposition of the first metal exceeds the number of nucleation sites required during the deposition of the second metal.[77] In the case of Pt and Ru on m-HOPG, a 0.4-0.5 ML coverage of either metal provides the requisite number of nucleation sites for the 0.4-0.5 ML coverage of the second metal. Furthermore, on m-HOPG the diffusion length is controlled primarily by the number of defect sites induced by sputtering rather than by the intrinsic mobility of the metals. The surface compositions of the bimetallic clusters are close to 100% Pt after heating to 130 °C, and this is consistent with predictions from bulk thermodynamics, given that Pt has a lower surface free energy than Ru (2.2 J/m^2 vs. 2.7 J/m^2).[69] At room temperature, the deposition of Ru on Pt results in cluster surfaces that are only 80% Pt because the atoms have insufficient energy to diffuse within the clusters and achieve the equilibrium surface compositions. However, even at room temperature the diffusion of atoms within a cluster is facile enough to reach an 80% Pt surface composition for Ru deposited on Pt. Although the cluster sizes and densities are similar for the Pt+Ru

and Ru+Pt surfaces, the Ru+Pt surface has a slightly smaller average cluster height (19.4 $\pm$ 3.9 Å vs. 22.8 $\pm$ 6.0 Å) and a 15% higher cluster density because the initial deposition of the Ru seed clusters provides more nucleation sites than the deposition of Pt seed clusters. Previous LEIS studies of Pt-Ru films on HOPG also report a strong tendency for surface segregation of Pt; deposition of 30 Å of Ru on 50 Å of Pt resulted in both Pt and Ru at the surface, whereas 30 Å of Pt on 50 Å of Ru resulted in a pure Pt surface.[78] In addition, encapsulation of Ru and Pt by carbon from the support was observed for 50 Å films deposited on HOPG after heating to 700 °C,[79] but no such cluster encapsulation was observed at 130 °C in this study.

Bimetallic Pt-Ru clusters are grown on m-HOPG using the technique of electroless deposition. Specifically, Pt is deposited from solution onto Ru seed clusters supported on m-HOPG. To our knowledge, this is the first instance in which bimetallic clusters have been grown by electroless deposition and characterized on an atomically flat model support such as graphite. The bimetallic cluster densities are nearly identical to that of the monometallic seed clusters exposed to the ED without Pt^{+2} and heated to 130 °C, while the average cluster heights increase, and the deposition of Pt is confirmed by XPS. The amount of Pt deposited can be controlled by changing the Pt^{+2} concentration in the ED bath, and the rate of metal deposition can be decreased to form more uniformly-sized clusters by decreasing the temperature of the ED bath. Although Ru deposition on Pt seed clusters could be achieved by electroless deposition, the presence of a Ag contaminant in the $Ru(NH_3)_6Cl_3$ salt results in the codeposition of Ag. It should also be noted that electroless deposition is extremely sensitive to trace contaminants of other metals, particularly if the reduction potential for the contaminant metal is significantly higher, as is the case for Ag

and Ru. A Ag contamination level of only 2.5 x 10^{-5} g Ag/g Ru provides enough Ag atoms to completely cover the 0.50 ML Pt clusters on m-HOPG in the Ru^{+3} ED experiment because these model surfaces have a relatively small number of surface sites compared to conventional catalysts on powdered supports. Unlike cluster growth via vapor deposition in vacuum, the technique of electroless deposition is one that is suitable for commercial catalyst preparation, given that electroplating is already widely used in industry. Thus, the ability to grow bimetallic clusters on model, atomically flat surfaces by electroless deposition allows the "materials gap" to be bridged between fundamental investigations of clusters grown on single-crystal support surfaces and studies of industrial catalysts.

7.5 Conclusions

Bimetallic Pt-Ru clusters have been grown on HOPG via vapor deposition in UHV and electroless deposition in solution. The first step in the growth of bimetallic clusters is the deposition of seed clusters of pure Ru or Pt, which serve as nucleation sites for the deposition of the second metal; the higher mobility of Pt on HOPG compared to Ru is attributed to stronger metal-HOPG interactions for Ru. The number of seed clusters on HOPG can be controlled by Ar^+ sputtering, which creates defects that serve as nucleation sites. For the same metal coverages, the cluster density increases with Ar^+ sputtering time, and the average cluster height decreases. Bimetallic clusters can be grown through sequential vapor deposition of either Pt on Ru (Ru+Pt) or Ru on Pt (Pt+Ru), provided that the initial deposition creates a sufficient number of seed clusters for the nucleation of the second metal. Given the lower surface free energy of Pt compared to Ru, the fact that the resulting cluster surfaces are nearly 100% Pt after heating to 130 °C for both orders of deposition demonstrates that diffusion of metal atoms within the clusters occurs readily at

this temperature. Electroless deposition of Pt on Ru seed clusters was achieved using $PtCl_6^{-2}$ with DMAB as a reducing agent, and STM images of the resulting surface indicate that the Pt deposition occurred only at the Ru seed clusters. The electroless deposition of Ru on Pt seed clusters was also carried out from a solution of $Ru(NH_3)_6Cl_3$ with formic acid as a reducing agent, but Ag contamination in the Ru salt resulted in the deposition of Ag as well as Ru.

7.6 References

1. H. S. Liu, C. J. Song, L. Zhang, J. J. Zhang, H. J. Wang and D. P. Wilkinson, J. Power Sources, 2006, **155**, 95.

2. A. S. Arico, S. Srinivasan and V. Antonucci, Fuel Cells, 2001, **1**, 133.

3. A. K. Shukla, A. S. Arico and V. Antonucci, Renew. Sust. Energ. Rev., 2001, **5**, 137.

4. N. M. Markovic and P. N. Ross, Electrochim. Acta, 2000, **45**, 4101.

5. R. Dillon, S. Srinivasan, A. S. Arico and V. Antonucci, J. Power Sources, 2004, **127**, 112.

6. J. M. Leger, S. Rousseau, C. Coutanceau, F. Hahn and C. Lamy, Electrochim. Acta, 2005, **50**, 5118.

7. E. Antolini, Mater. Chem. Phys., 2003, **78**, 563.

8. B. D. McNicol, D. A. J. Rand and K. R. Williams, J. Power Sources, 1999, **83**, 15.

9. S. Wasmus and A. Kuver, J. Electroanal. Chem., 1999, **461**, 14.

10. C. Lamy, J. M. Leger and S. Srinivasan, in Modern Aspects of Electrochemistry, eds. O. M. Bockris, B. E. Conway and R. E. White, Plenum Press, New York, 2000, vol. 34, pp. 53.

11. R. Parsons and T. Vandernoot, J. Electroanal. Chem., 1988, **257**, 9.

12. C. Roth, A. J. Papworth, I. Hussain, R. J. Nichols and D. J. Schiffrin, J. Electroanal. Chem., 2005, **581**, 79.

13. A. Kabbabi, R. Faure, R. Durand, B. Beden, F. Hahn, J. M. Leger and C. Lamy, J. Electroanal. Chem., 1998, **444**, 41.

14. T. Frelink, W. Visscher and J. A. R. Vanveen, Surf. Sci., 1995, **335**, 353.

15. K. Sasaki, J. X. Wang, M. Balasubramanian, J. McBreen, F. Uribe and R. R. Adzic, Electrochim. Acta, 2004, **49**, 3873.

16. M. Watanabe and S. Motoo, J. Electroanal. Chem., 1975, **60**, 267.

17. S. L. Gojkovic, T. R. Vidakovic and D. R. Durovic, Electrochim. Acta, 2003, **48**, 3607.

18. P. Waszczuk, G. Q. Lu, A. Wieckowski, C. Lu, C. Rice and R. I. Masel, Electrochim. Acta, 2002, **47**, 3637.

19. N. M. Markovic, H. A. Gasteiger, P. N. Ross, X. D. Jiang, I. Villegas and M. J. Weaver, Electrochim. Acta, 1995, **40**, 91.

20. C. Lu and R. I. Masel, J. Phys. Chem. B, 2001, **105**, 9793.

21. P. Liu and J. K. Norskov, Fuel Cells, 2001, **1**, 192.

22. F. B. de Mongeot, M. Scherer, B. Gleich, E. Kopatzki and R. J. Behm, Surf. Sci., 1998, **411**, 249.

23. H. Igarashi, T. Fujino, Y. M. Zhu, H. Uchida and M. Watanabe, Phys. Chem. Chem. Phys., 2001, **3**, 306.

24. E. Christoffersen, P. Liu, A. Ruban, H. L. Skriver and J. K. Norskov, J. Catal., 2001, **199**, 123.

25. H. Rauscher, T. Hager, T. Diemant, H. Hoster, F. B. De Mongeot and R. J. Behm, Surf. Sci., 2007, **601**, 4608.

26. J. H. Sinfelt, Bimetallic Catalysts. Discoveries, Concepts, and Applications, John Wiley and Sons, New York, 1983.

27. M. Gotz and H. Wendt, Electrochim. Acta, 1998, **43**, 3637.

28. Z. L. Liu, X. Y. Ling, X. D. Su and J. Y. Lee, J. Phys. Chem. B, 2004, **108**, 8234.

29. T. J. Schmidt, M. Noeske, H. A. Gasteiger, R. J. Behm, P. Britz and H. Bonnemann, J. Electrochem. Soc., 1998, **145**, 925.

30. Z. L. Liu, J. Y. Lee, M. Han, W. X. Chen and L. M. Gan, J. Mat. Chem., 2002, **12**, 2453.

31. Z. L. Liu, J. Y. Lee, W. X. Chen, M. Han and L. M. Gan, Langmuir, 2004, **20**, 181.

32. H. Bonnemann, R. Brinkmann, P. Britz, U. Endruschat, R. Mortel, U. A. Paulus, G. J. Feldmeyer, T. J. Schmidt, H. A. Gasteiger and R. J. Behm, J. of New Mat. for Electrochem. Sys., 2000, **3**, 199.

33. W. Vogel, P. Britz, H. Bonnemann, J. Rothe and J. Hormes, J. Phys. Chem. B, 1997, **101**, 11029.

34. D. R. M. Godoi, J. Perez and H. M. Villullas, J. Electrochem. Soc., 2007, **154**, B474.

35. J. F. Anderson, M. Kuhn, U. Diebold, K. Shaw, P. Stoyanov and D. Lind, Physical Review B-Condensed Matter, 1997, **56**, 9902.

36. K. D. Beard, M. T. Schaal, J. W. Van Zee and J. R. Monnier, Appl. Catal. B, 2007, **72**, 262.

37. M. T. Schaal, A. C. Pickerell, C. T. Williams and J. R. Monnier, J. Catal., 2008, **254**, 131.

38. K. D. Beard, J. W. Van Zee and J. R. Monnier, Appl. Catal. B, 2009, **88**, 185.

39. M. Ohashi, K. D. Beard, S. Ma, D. A. Blom, J. St-Pierre, J. W. Van Zee and J. R. Monnier, Electrochim. Acta, 2010, **55**, 7376.

40. J. Rebelli, A. A. Rodriguez, S. Ma, C. T. Williams and J. R. Monnier, Catal. Today, 2011, **160**, 170.

41. J. Rebelli, M. Detwiler, S. G. Ma, C. T. Williams and J. R. Monnier, J. Catal., 2010, **270**, 224.

42. Y.-J. Song, J. R. Monnier, P. T. Fanson and C. T. Williams, J. Catal., 2014, **315**, 59.

43. S. S. Djokic, in Modern Aspects of Electrochemistry, eds. B. E. Conway and R. E. White, Springer, New York, NY, 2002, vol. 35, pp. 51.

44. K. D. Beard, D. Borelli, A. M. Cramer, D. Blom, J. W. Van Zee and J. R. Monnier, ACS Nano, 2009, **3**, 2841.

45. M. T. Schaal, A. Y. Metcalf, J. H. Montoya, J. P. Wilkinson, C. C. Stork, C. T. Williams and J. R. Monnier, Catal. Today, 2007, **123**, 142.

46. T. R. Garrick, W. Diao, J. M. Tengco, J. R. Monnier and J. W. Weidner, ECS Trans., 2013, **53**, 79.

47. B. L. Garcia, B. Captain, R. D. Adams, A. B. Hungria, P. A. Midgley, S. J. M. Thomas and J. W. Weidner, J. Clust. Sci., 2007, **18**, 121.

48. P. G. Corradini, F. I. Pires, V. A. Paganin, J. Perez and E. Antolini, J. Nanopart. Res., 2012, **14**, 1080.

49. J. B. Park, J. S. Ratliff, S. Ma and D. A. Chen, J. Phys. Chem. C, 2007, **111**, 2165.

50. J. Zhou, S. Ma, Y. C. Kang and D. A. Chen, J. Phys. Chem. B, 2004, **108**, 11633.

51. J. B. Park, S. F. Conner and D. A. Chen, J. Phys. Chem. C, 2008, **112**, 5490.

52. S. A. Tenney, J. S. Ratliff, W. He, C. C. Roberts, S. C. Ammal, A. Heyden and D. A. Chen, J. Phys. Chem. C, 2010, **114**, 21652.

53. S. A. Tenney, W. He, C. C. Roberts, J. S. Ratliff, S. I. Shah, G. S. Shafai, V. Turkowski, T. S. Rahman and D. A. Chen, J. Phys. Chem. C, 2011, **115**, 11112.

54. S. A. Tenney, B. A. Cagg, M. S. Levine, W. He, K. Manandhar and D. A. Chen, Surf. Sci., 2012, **606**, 1233.

55. A. Illingworth, J. Zhou, O. Ozturk and D. A. Chen, J. Vac. Sci. Technol. B, 2004, **22**, 2552.

56. R. M. Nielsen, S. Murphy, C. Strebel, M. Johansson, J. H. Nielsen and I. Chorkendorff, Surf. Sci., 2009, **603**, 3420.

57. R. P. Galhenage, S. C. Ammal, H. Yan, A. Duke, S. A. Tenney, A. Heyden and D. A. Chen, J. Phys. Chem. C, 2012, **116**, 24616.

58. M. T. Schaal, Ph. D. Thesis, University of South Carolina, 2009.

59. D. A. Chen, M. C. Bartelt, K. F. McCarty and R. Q. Hwang, Surf. Sci., 2000, **450**, 78.

60. S. Stempel, M. Bäumer and H. J. Freund, Surf. Sci., 1998, **404**, 424.

61. J. S. Ratliff, Ph.D. Thesis, University of South Carolina, 2009.

62. F. Atamny and A. Baiker, Appl. Catal. A, 1998, **173**, 201.

63. L. L. Wang, X. C. Ma, Y. Qi, P. Jiang, J. F. Jia, Q. K. Xue, J. Jiao and X. H. Bao, Ultramicroscopy, 2005, **105**, 1.

64. A. R. Howells, L. Hung, G. S. Chottiner and D. A. Scherson, Solid State Ionics, 2002, **150**, 53.

65. K. A. Friedrich, F. Henglein, U. Stimming and W. Unkauf, Electrochim. Acta, 2000, **45**, 3283.

66. A. V. Kalinkin, A. M. Sorokin, M. Y. Smirnov and V. I. Bukhtiyarov, Kinet. Catal., 2014, **55**, 354.

67. Y. X. Yao, Q. Fu, Z. Zhang, H. Zhang, T. Ma, D. Tan and X. H. Bao, Appl. Surf. Sci., 2008, **254**, 3808.

68. I. N. Kholmanov, L. Gavioli, M. Fanetti, M. Casella, C. Cepek, C. Mattevi and M. Sancrotti, Surf. Sci., 2007, **601**, 188.

69. W. R. Tyson and W. A. Miller, Surf. Sci., 1977, **62**, 267.

70. C. D. Wagner, W. M. Riggs, L. E. Davis and J. F. Moulder, Handbook of X-Ray Photoelectron Spectroscopy, Perkin Elmer Corporation, Eden Prairie, MN, 1978.

71. H. Zhang, Q. Fu, Y. X. Yao, Z. Zhang, T. Ma, D. L. Tan and X. H. Bao, Langmuir, 2008, **24**, 10874.

72. I. Lopez-Salido, D. C. Lim and Y. D. Kim, Surf. Sci., 2005, **588**, 6.

73. J. Z. Gao and Q. M. Guo, Appl. Surf. Sci., 2012, **258**, 5412.

74. K. A. Wepasnick, X. Li, T. Mangler, S. Noessner, C. Wolke, M. Grossmann, G. Gantefoer, D. H. Fairbrother and K. H. Bowen, J. Phys. Chem. C, 2011, **115**, 12299.

75. Z. Song, T. H. Cai, J. C. Hanson, J. A. Rodriguez and J. Hrbek, J. Am. Chem. Soc., 2004, **126**, 8576.

76. J. B. Park, J. S. Ratliff, S. Ma and D. A. Chen, Surf. Sci., 2006, **600**, 2913.

77. R. P. Galhenage, H. Yan, A. S. Ahsen, O. Ozturk and D. A. Chen, J. Phys. Chem. C, 2014, **118**, 17773.

78. E. M. Fiordaliso, S. Dahl and I. Chorkendorff, J. Phys. Chem. C, 2011, **115**, 25351.

79. A. Guttler, T. Zecho and J. Kuppers, Surf. Sci., 2004, **570**, 218.

Chapter 8. Adsorbate-induced changes in MoS_2 clusters on TiO_2(110)

8.1 Introduction

Layered structures of MoS_2 have been investigated in recent years for their applications in sulfur removal catalysts and photocatalysts.[1-4] MoS_2 nanoclusters are known to show different electronic and geometric structures compared to the bulk MoS_2 in the reactivity.[5] Furthermore, it has also been shown that these structures are active in electrocatalytic water splitting.[6,7] Besenbacher and co-workers have done a tremendous amount of research investigating MoS_2 layered structures on model supports such as gold and titania to inquire into their fundamental structure and activity towards hydrodesulfurization (HDS) reactions.[4,5,8-19] They have investigated the HDS reaction in the context of the metallic edge present in the MoS_2 structures. MoS_2 nanostructures also serve as model systems to obtain an atomic level understanding of the reaction mechanisms which take place at the edges of the more complex MoS_2 structures explained above.[9] Interactions between thiophene and hydrogen with MoS_2, supported on Au(111), have been investigated using high-resolution STM.[5] This study shows that the thiophene reacts on fully sulfided edges, known as brim sites, which exhibit metallic character. DFT studies have identified two metallic states on MoS_2 structures that act as reactive sites.[12,20] This 1-D metallic brim site is known to play a major role in facilitating the HDS reaction.[10] These edge structures that aid reactions are known to be affected by the support.[18] Besenbacher and his co-workers have successfully synthesized MoS_2 on TiO_2 in order to understand the support effect.[18] The structure of TiO_2 has a significant effect on the shape of the supported MoS_2 clusters. Furthermore, they found that strong support interactions arise due to a chemical linkage between the MoS_2 structure and the oxide support. Different oxide supports such as alumina and titania show differences in activity towards the HDS reaction

that suggest that the support has an effect on the reactivity.[18] Reactions such as hydrodeoxygenation and hydrodenitrogenation are reactions that could behave similarly to the HDS reaction. The MoS_2 system is also known to have activity towards the water gas shift reaction[21] and in the formation of alcohols.[22,23] Studying these model systems serves to aid in understanding the fundamental aspects of the surface and to help in the rational design of catalysts.

Although there have been studies done on the synthesis and characterization of MoS_2 nanoparticles on titania, the stability of these structures has not been studied. The objective of this study is to investigate the stability of MoS_2 nano structures on titania as a function of temperature and as a function of reactant gases. We prepared a model surface that consisting of MoS_2 nano structures on titania to investigate the stability of MoS_2 at high temperatures, and the results show that MoS_2 clusters are extremely stable under these conditions. Furthermore, we have investigated these clusters under reactant molecules such as D_2, CO, CH_3OH, H_2O and O_2. Our results show that MoS_2 structures are extremely stable under mildly oxidizing or reducing conditions, such as in the presence of oxygen or hydrogen, but they disintigrate under extremely oxidizing conditions.

8.2 Experimental section

All experiments were carried out in a UHV chamber where the base pressure is kept lower than 5×10^{-11} Torr. This chamber is assembled to perform variable temperature STM (Scanning Tunneling Microscopy), a hemispherical analyzer for LEIS (Low Energy Ion Scattering Spectroscopy) and XPS (X-ray Photoelectron Spectroscopy) and a LEED (Low Energy Electron Diffraction)/AES (Auger Electron Spectroscopy) system.

A rutile titania(110) single crystal (Princeton Scientific Corporation) was used as the substrate to prepare MoS_2. The crystal was mounted on a Ta back plate and cleaned by several cycles of ion sputtering with Ar^+ at 1 kV for 20 minutes with 3.2 uA current to the sample and subsequent annealing at 1030 K for 3 minutes. Heating the crystal was done by electron bombardment of the Ta back plate. This cleaning process drives lattice oxygen out of the bulk, making the crystal an n-type semiconductor, which allows the use of STM and other electronic and ion based microscopies and spectroscopies. Cleanliness and the order of the surface have been confirmed by STM, XPS, LEIS and LEED.

Evaporation of Mo onto the rutile TiO_2 (110) crystal was carried out either from an Omicron doser (Omicron Nanotechnology, EFM 3) or from an Oxford doser (Oxford Applied Research, EGCO4) where Mo rods of diameters 0.0625" (ESPI, 3N8 purity) and 0.080"(ESPI, 3N8 purity) were mounted, respectively. The rods were heated using electron bombardment by tungsten filaments. The MoS_2 surface was prepared by evaporating Mo onto the titania surface, which was kept at a temperature of 400 K – 500 K while in an atmosphere of 5 x 10^{-6} torr H_2S. This surface was then annealed at 950 K for 15 mins in the same sulfiding atmosphere. The preparation of MoS_2 on titania was done according a previously established method.[18] The MoS_2 surface was then exposed to different gases (CO, H_2O, D_2, CH_3OH and O_2) at pressures of ~10^{-7} Torr - 250 Torr to study the effects of different molecules on the morphology and the chemical state of MoS_2.

STM experiments were carried out to investigate the surface morphology of the MoS_2 clusters. Constant tunneling current mode was used, and the tunneling current was in the range of 0.3 nA – 0.32 nA. The sample was positively biased at 1.2 eV with respect to the tip. Tips were made from 0.38 mm tungsten wire that was electrochemically etched

and sputtered with Ar^+ at 3 kV and 8 uA ion current. Widths, lengths and the heights of fifty clusters from each image were analyzed.

XPS experiments were carried out to understand the chemical nature of MoS_2 clusters on rutile TiO_2(110). In all experiments, Al Kα X-rays were used at 15 kV, ~20 mA emission. XPS spectra were collected for the Ti(2p) region (450 eV- 471 eV), Mo(3d) region (220 eV-240 eV) and S(2p) region (153 eV-173 eV). Since the sample was mounted on a Ta support, the Ta(4d) region (210 eV- 230 eV) was subtracted from Mo(3d) region using the spectra acquired on the clean titania sample. For all XPS experiments, the dwell time was 0.2 s, and the step size was 0.02 eV. The cluster analysis was done using XPM pro 2.0. XPS of a MoS_2 single crystal (SPI supplies, 100% natural, 99% purity) was done to compare with the supported clusters. The preparation of the MoS_2 single crystal was done by cleaving the first couple of layers by using adhesive tape.

Temperature Programmed Desorption (TPD) studies were done in order to understand the active sites of prepared MoS_2 nano structures. The surfaces were exposed to CO (National Welders, 99.99%) via a stainless steel directed dosing tube. CO was used as received. During CO exposure, the sample temperature was held at 300 K, and a saturation exposure of CO was achieved by leaking in CO at a pressure rise of 3.0×10^{-10} Torr for 3 min. In TPD experiments, the crystal was heated at a constant rate of 2 K/s in front of the mass spectrometer. The crystal was positioned ~2 mm in front of a 4 mm diameter hole cut in the shroud of the mass spectrometer in order to prevent detection of products desorbing from the sample holder. The crystal was biased at −100 V during TPD experiments to avoid damage from the electrons emitted by the mass spectrometer filament.

Nine masses were collected in a typical TPD experiment; and 40 mass channels were monitored in a single experiment to check for additional products.

8.3 Results

Preparation of MoS_2 was done according to the procedure developed by Kibsgaard et al.[18] They have done atom resolved STM to image the supported nanoclusters, and found the interatomic spacing of perfectly crystalline basal plane to be 3.15 Å, which agrees with the interatomic spacing of bulk MoS_2(0001) facet. Figure 8.1 shows the growth of Mo and MoS_2 on titania. Mo on titania was prepared exactly the same way as MoS_2 was prepared except for the H_2S environment that was present in the preparation of MoS_2.

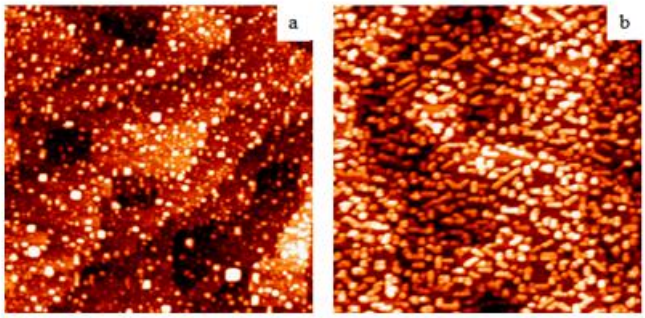

Figure 8.1 STM images of a) 0.1 ML Mo on titania deposited at 400 K and subsequently annealed to 950 K for 15 minutes , b) 0.1 ML MoS_2: prepared by depositing 0.1 ML Mo on titania at 400 K in 5 x 10^{-6} Torr H_2S and subsequently annealed to 950 K for 15 minutes in the same H_2S environment. All images are 100 nm x 100 nm.

Pure Mo formed small, round-shaped clusters (0.5 ± 0.1 nm in height, 2.9 ± 0.4 nm in width) while the MoS_2 clusters formed rectangular-shaped clusters that have an average height of 0.7 ± 0.1 nm, an average length of 5.6 ± 0.9 nm and an average width of 2.3 ±

0.4 nm. In Figure 8.2, the size distribution of clusters is shown in histograms. Figure 8.2a displays the length distribution of 50 clusters selected from Figure 8.1b. These elongated structures are understood to be single layer high MoS_2 clusters by atom resolved STM.[18] The clusters show a bimodal distribution around 5 nm and 6 nm. The average width (2.3 nm) and height (0.6 nm) are comparable to what is reported in the literature (3.3 nm and 0.5 nm, respectively).[18] The small differences in the size distribution of MoS_2 clusters compared to the values declared in the literature could be due to the slight differences in heating and the sulfiding environment.

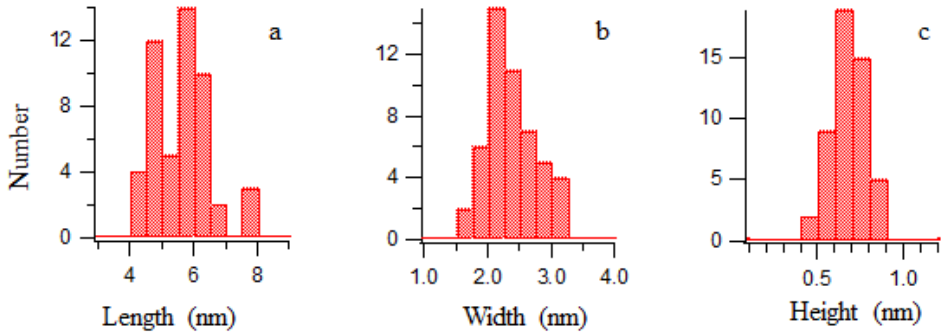

Figure 8.2. Histograms for length, width and height of clusters in Figure 1b (0.1 ML MoS_2) in nanometers.

Kibsgaard et al. have showed that a 50 K difference in heating could generate slightly different size distributions.[18] There were features which were more round in shape which can attributed MoS_x, which were not completely sulfided to form elongated MoS_2 structures. MoS_2 clusters have been heated to different temperatures to understand the stability at elevated temperatures. STM images of 0.1 ML MoS_2 after heating to 400 K, 600 K and 800 K are shown in Figure 8.3. Table 8.1 represents the cluster analysis on the

Table 8.1. Cluster size analysis of MoS_2 on titania at different temperatures

Composition	Height/Å	Length/Å	Width/Å
0.1 ML MoS_2	6.0 ± 1.1	61.8 ± 8.7	24.7 ± 4.0
0.1 ML MoS_2 - D_2	7.4 ± 1.4	69.0 ± 18.4	24.3 ± 3.3
0.1 ML MoS_2 - CO	5.5 ± 0.9	59.8 ± 12.4	23.6 ± 3.1
0.1 ML MoS_2 - MeOH	5.8 ± 1.0	62.2 ± 10.0	28.8 ± 3.2
0.1 ML MoS_2 - H_2O	6.5 ± 1.1	-	30.4 ± 4.6
0.1 ML MoS_2 – O_2	6.4 ± 1.0	64.3 ± 10.5	25.3 ± 3.2

STM images collected on MoS_2 at different temperatures. Changes in the average cluster height, length, and width are compared to the room temperature measurements. The changes in the height and width of MoS_2 clusters are within 10% of the values at room temperature, and the changes in the average length are within 15%, which suggests that MoS_2 structures on titania are stable at higher temperatures. MoS_2 clusters were then exposed to different probe molecules to understand the stability of the structure in the presence of various reactant molecules. The probe molecules used in this experiment were D_2, H_2O, CH_3OH, O_2 and CO. STM images of the surfaces that were exposed to different gas molecules at a pressure at 1 x 10^{-7} Torr are shown in Figure 8.4.

An analysis of cluster sizes of these images is depicted in Table 8.2. Changes in the cluster height of the MoS_2 structures after exposure to gases are within 10% of the characteristic MoS_2 height except for the surface expose to D_2 where a change of 23% was observed. The length also did not change substantially and was within 10% with the exception of the surface to H_2O where we could not grow longer clusters in the initial synthesis of MoS_2.

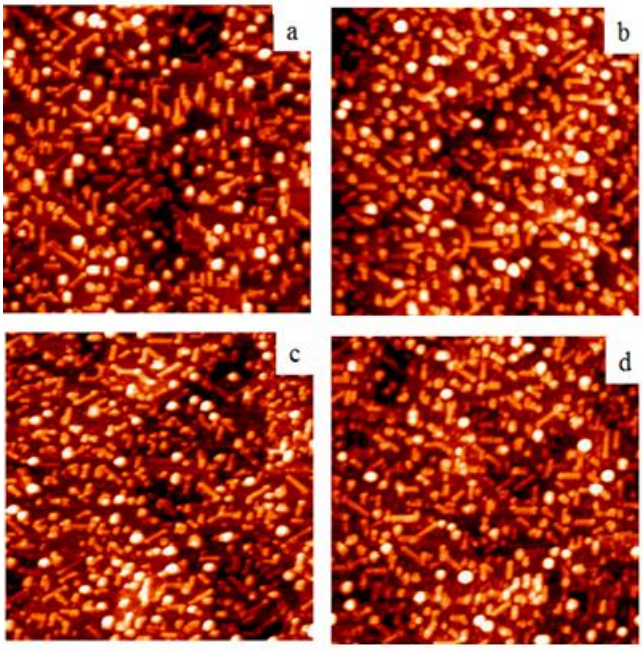

Figure 8.3. STM images of a) 0.1 ML MoS_2, heated to b) 400 K, c) 600 K and d) 800 K. All images are 100 nm x 100 nm.

The width of the clusters increased approximately 20% when the surfaces were exposed to H_2O and methanol; whereas, the change was within 5% for other gas molecules. When the pressure of the reactant molecules was increased to 10 Torr, for H_2O, methanol and O_2, the increase in width was about 20% while the height remained almost constant. STM images for the exposures at 10 Torr are shown in Figure 5. Long MoS_2 structures remained after the exposure to methanol, but after exposing to H_2O and O_2 longer structures were rarely found on the surface. STM images collected after exposing the MoS_2 structures to O_2 at 250 Torr for 2.5 hours and to air for 2.5 hours are shown in Figure 8.6. Under these more extensive oxidizing conditions, the MoS_2 structures were destroyed.

Table 8.2. Cluster size analysis of MoS_2 which was exposed to different gases at a pressure 1 x 10^{-7} Torr

Composition	Height/Å	Length/Å	Width/Å
0.1 ML MoS_2	6.0 ± 1.1	61.8 ± 8.7	24.7 ± 4.0
0.1 ML MoS_2 - D_2	7.4 ± 1.4	69.0 ± 18.4	24.3 ± 3.3
0.1 ML MoS_2 - CO	5.5 ± 0.9	59.8 ± 12.4	23.6 ± 3.1
0.1 ML MoS_2 - MeOH	5.8 ± 1.0	62.2 ± 10.0	28.8 ± 3.2
0.1 ML MoS_2 - H_2O	6.5 ± 1.1	-	30.4 ± 4.6
0.1 ML MoS_2 – O_2	6.4 ± 1.0	64.3 ± 10.5	25.3 ± 3.2

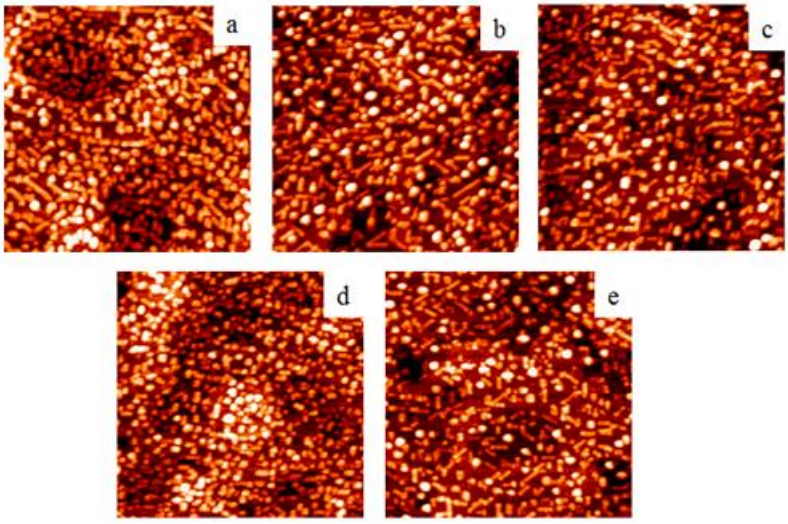

Figure 8.4. STM images of, A 0.1 ML MoS_2 was exposed to different gas molecules at 1 x 10^{-7} Torr for 5 min a) D_2, b) CO, c) CH_3OH, d) H_2O, e) O_2. All images are 100 nm x 100 nm.

XPS data for the Mo(3d) region for Mo/TiO_2, MoS_2/TiO_2, and MoS_2 single crystal are shown in Figure 8.7. The Mo ($3d_{5/2}$) peak for Mo clusters appeared at 228.3 eV. This value is shifted by +0.6 eV from the metallic position given in standard XPS data books. The shift in the oxidation state could either be a factor of the cluster size effect or the oxidation of Mo by lattice oxygen in titania. Oxidation of Mo is supported by the reduction of Ti substrate as shown in Figure 8.8.

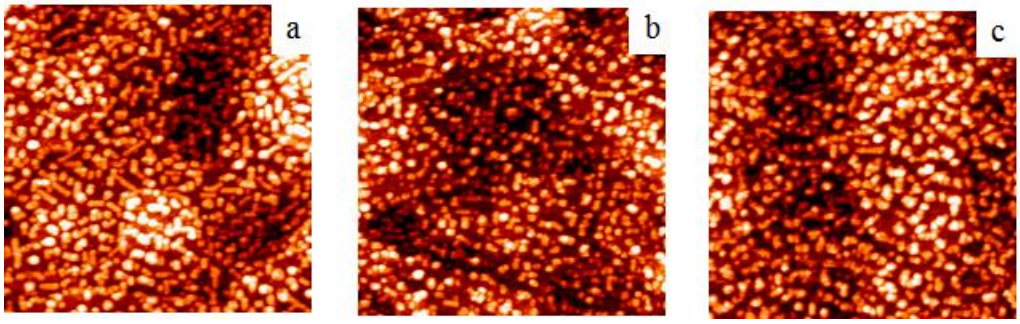

Figure 8.5. STM: A 0.13 ML coverage of MoS_2 surface was exposed to different gas molecules at 10 Torr for 2.5 hours a) CH_3OH b) H_2O, c) O_2. All images are 100 nm x100 nm.

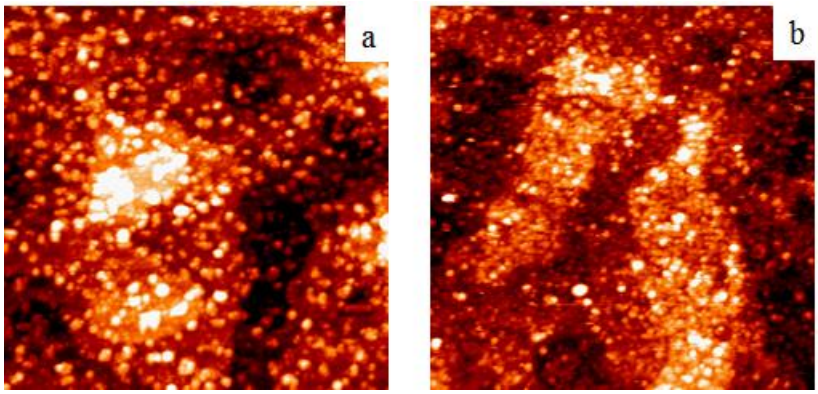

Figure 8.6. STM: A 0.1 ML coverage of MoS2 was exposed to a) O_2 at 250 Torr for 2.5 hours and b) Air for 2.5 hours. All images are 100 nm x 100 nm.

A comparison of XPS data of Ti($2p_{3/2}$), for clean titania, Mo/titania, and MoS_2/Titania, is illustrated in Figure 8.8. The shoulder at lower binding energy, shows the reduction of titania upon deposition of Mo. This observation support the oxidation of Mo clusters upon deposition. Mo(3d) peak for the supported MoS_2 clusters appeared at 228.0 eV.

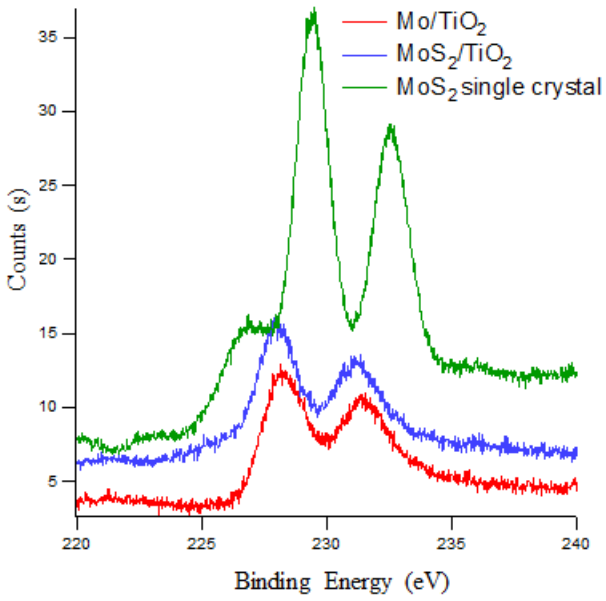

Figure 8.7. Comparison of the Mo(3d) peak of Mo, MoS_2 and MoS_2 single crystal

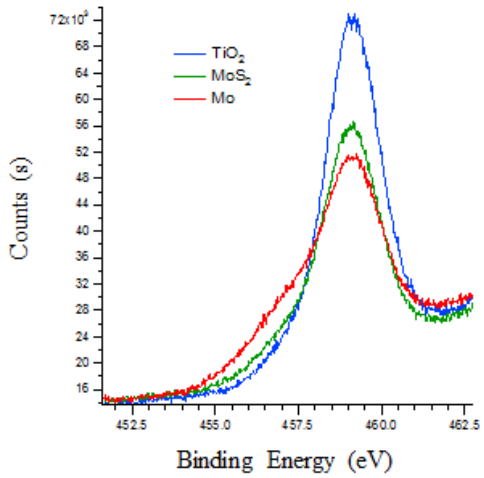

Figure 8.8. XPS data for the Ti($2p_{3/2}$) region for Mo and MoS_2 on titania compared to a clean titania surface.

It has been shifted towards the binding energy for metallic Mo and the shoulder that represents the reduction of titania was no present. Therefore, the +0.6 eV shift could be an effect of oxidation of Mo by the suppport. However, the Mo ($3d_{5/2}$) peak for MoS_2/Titania

is shifted by -1.5 eV compared to the Mo($3d_{5/2}$) for the MoS_2 single crystal. This could be due to the difference in clusters on titania compared to the bulk MoS_2 in a single crystal. S(2s) peak appears at 226.7 eV and can be seen clearly in the MoS_2 single crystal but not very prominent in MoS_2/titania due to the low concentration of S on the MoS_2 clusters. XPS data for the oxidation of Mo and MoS_2 at 1 x10 $^{-7}$ Torr of oxygen are shown in Figure 8.9. Mo(3d) peak for Mo clusters has shifted to higher binding energies whereas; Mo(3d) peak for MoS_2 did not shift upon oxidizing at this oxidizing conditions. MoS_2 was then exposed to 10 Torr of O_2, H_2O, and MeOH.

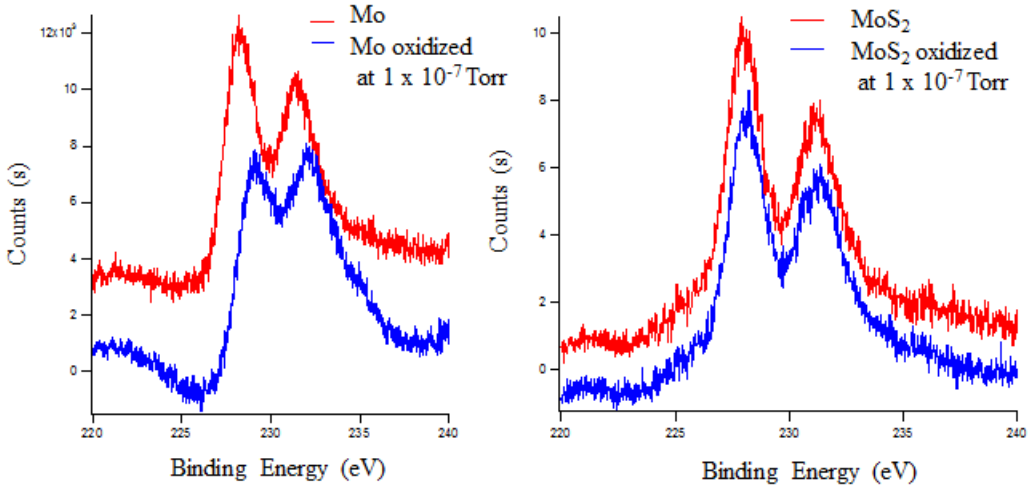

Figure 8.9. XPS data for the Mo(3d) region a) Mo clusters and b) MoS_2 cluster on TiO_2 before and after oxidation of 1 x10^{-7} Torr O_2 for 5 min at room temperature.

XPS data for Mo (3d) peak after exposing the MoS_2 clusters to CH_3OH, O_2 and H_2O are shown in Figure 8.10. The binding energy shfits are not prominent when the surface was exposed to CH_3OH and H_2O.

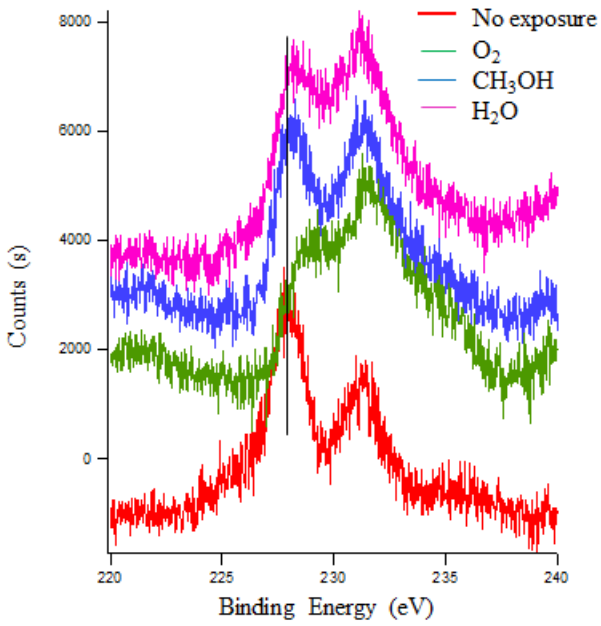

Figure 8.10. XPS data for the Mo(3d) region for MoS_2 on TiO_2 exposed to different gases at a pressure of 10 Torr.

A significant shift in Mo (3d) was observed when MoS_2 was exposed to O_2. A complete cluster collapse (Figure 8.6) was observed in highly oxidizing conditions such as 250 Torr of O_2 and in air. Under these oxidizing conditions, the Mo(3d) peak has shifted significantly in the MoS_2 clusters which was resistant to oxidation in mildly oxidizing conditions such as at 1 x 10^{-7} Torr O_2.

CO-TPD data are shown in Figure 8.12. A significant desorption CO peak was not observed on clean titania or on sulfided titania except for the multilayer desorption peak at low temperatures. A broad CO desorption feature at ~ 280 K was observed for Mo clusters deposited on TiO_2 at room temperature. However, Mo clusters deposited at 400 K and heated to 950 K, the exact same procedure of synthesizing MoS_2 except the H_2S environment, did not show the broad feature for CO desorption. Encapsulation of Mo was

not extensively studied, but metals such as Pt, Co and Re become encapuslated by titania at higher temperatures.[25, 26, 29] Therefore, it could be that the Mo has encapsulated by titania during the deposition and subsequent annealing in the preparation, and consequently the sites responsible for CO desorption at high temperature are blocked. For MoS_2, there was a significant desorption peak that appeared at 280 K. This desorption peak falls around the desorption peak that was observed on Mo/TiO_2 therefore, could be attributed to desorption of CO from the metallic sites present in the MoS_2 structures.

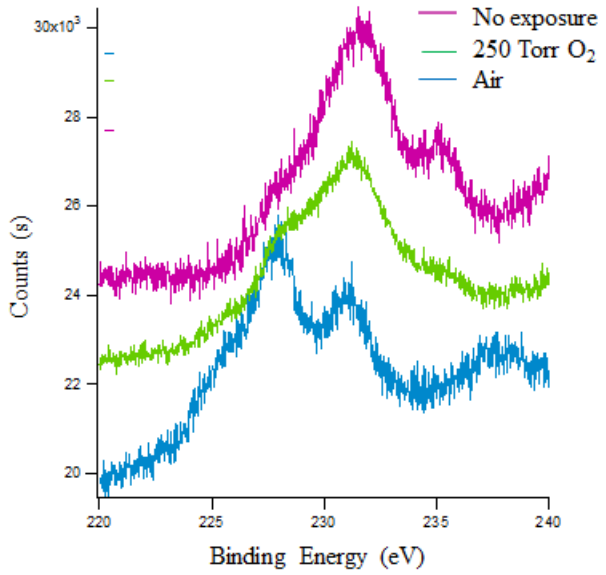

Figure 8.11. XPS data for the Mo(3d) region for MoS_2 on titania exposed to O_2 and air for 2.5 hours.

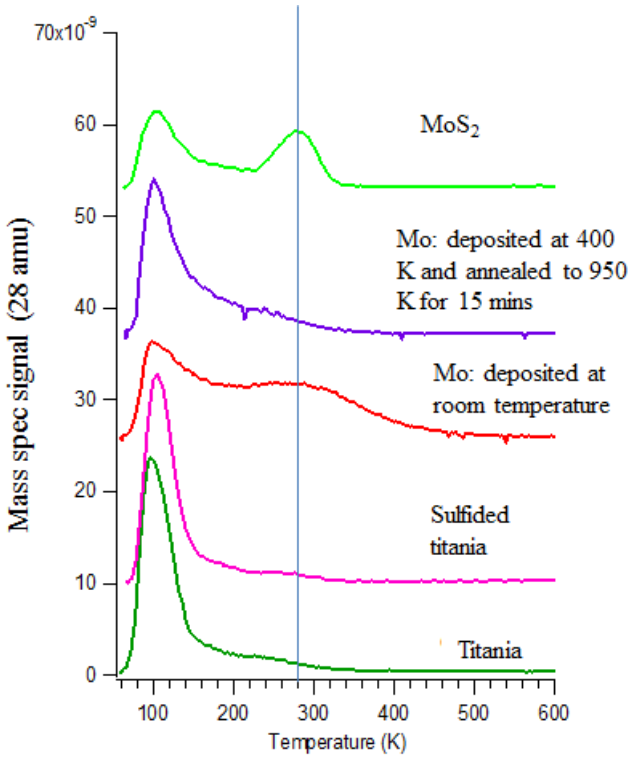

Figure 8.12. TPD data for CO desorption

8.4 Discussion

MoS_2 nanoclusters were formed on a titania support using previously adopted synthetic procedure.[18,24] Characteristic widths and lengths of the prepared MoS_2 nanoclusters were comparable with the literature studies. The differences in the characteristic measurements could be due to the changes in the temperature and the sulfiding atmosphere. It has been shown that the subtle changes in these parameters have an effect on the width and the length of the MoS_2 nanoclusters.[14,18] XPS data for Mo(3d) peak for MoS_2 single crystal compard to the clusters supported on titania were different. Cluster support interactions may have an affect on this change in the binidng energy. Cluster support interactions have been observed for MoS_2 nanoclusters synthesized on

various supports.[10,18,24] High-resolution STM experiments has shown that the cluster support interactions control the shape of the MoS_2 structures.[18] MoS_2 clusters on titania were stable upon heating to temperatures up to 800 K. Metals such as Co, Pt, Au and Ni show cluster sintering therefore a decrease in surface area at high temperatures such as at 800 K.[25-29] MoS_2 did not show such effects upon annealing, possibly due the chemical linkage between the MoS_2 structure and the support.[18]

Mo reduces the support upon deposition due to the oxophillic nature of Mo. When MoS_2 was synthessized on titania, a reduction of the titania support was not observed. Mo in MoS_2 is metallic in nature compared to the bare Mo clusters on titania. The metallic brim sites in MoS_2 has been previously reported in many studies.[5,8,10,14,15,17,18,20,24,30] Oxidation of Mo/TiO_2 was easily achieved compared to the oxidation of Mo in MoS_2. Stability of MoS_2 appeared to be excellent at pressures of 1×10^{-7} Torr with reactant molecules such as D_2, CH_3OH, CO, O_2, and H_2O. The height of the clusters that correspond to one layer of MoS_2 did not change upon exposing to these molecules which implies that the layered structure remained stable. Under these conditions MOS_2 retained its structure and chemical nature. However, oxidizing environments, such as exposing to O_2 at pressures of 250 Torr was able to destroy the structures of MoS_2. Furthermore, exposing the MoS_2 clusters to air also completely destroyed the characteristic structure and oxidized the Mo. Oxidation of MoS_2, however, could not be achieved at mild oxidation conditions that oxidized the pure Mo. The metallic edges present in these structures which is known to be the reactive site seem susceptible towards oxidation at highly oxidizing conditions.

CO-TPD studies which were done on MoS_2 has showed a distinct desorption peak at 280 K. A broader desorption peak of CO was observed for pure Mo on titania as well,

but this feature was disappeared when the Mo is deposited at 400 K and heated to 950 K for 12 mins. The latter experiment, when Mo surface was prepared in the same way as MoS_2 except for the H_2S environment, was done inorder to make sure that the distinct desorption that was observed on MoS_2 does not arise from Mo itself. Encapsulation of Mo by titania could explain the absence of metallic Mo to adsorb CO. The metallic edge that present in MoS_2 nano clusters can be explained by adsorption of CO on MoS_2. It has been reported that the metallic edge sites present in MoS_2 nano structures exhibit adsorption properties of reactants.[14] DFT calculations were done by our collaborators to calculate the binding energy of CO to unsupported MoS_2 and supported MoS_2.[31] DFT studies also shows that CO adsorb on both supported MoS_2 and unsupported MoS_2 clusters. DFT studies did not show strong evidence to show a significant role of the support in the CO adsorption.

8.5 Conclusions

MoS_2 nanostructures were successfully prepared on a TiO_2(110) single crystal. Heating to temperatures up to 800 K did not disintegrate the characteristic structure of the MoS_2 which shows the stability of MoS_2 at this conditions. Exposing MoS_2 clusters show great stabiliyt upon exposure to rectant gassses (D_2, CO, CH_3OH, H_2O and O_2) at low pressures but disintegrated at highly oxidizing conditions. MoS_2 was able to adsorb CO which could attributed to metallic characteristic of the clusters.

8.6 References

(1) Paek, S.-M.; Jung, H.; Park, M.; Lee, J.-K.; Choy, J. H. An Inorganic Nanohybrid With High Specific Surface Area TiO_2-Pillared MoS_2. Chem Mater **2005**, 17, 3492-3498.

(2) Benavente, E.; Ana, M. A. S.; Mendiza, F.; Gonzalez, G. Intercalation Chemistry of Molybdenum Disulfide. Corrdination Chemistry Reviews **2002**, 224, 87-109.

(3) Lee, Y.-H.; Zhang, X.-Q.; Zhang, W.; Chang, M.-T.; Lin, C.-T.; Kai-Di; Chang, Y.-C. Y.; Wang, J. T.-W.; Chang, C.-S.; Li, L.-J.; Lin, T.-W. <Synthesis of Large-Area MoS2 Atomic Layers with Chemical Vapor Deposition.pdf>.

(4) Schweiger, H. Shape and Edge Sites Modifications of MoS2 Catalytic Nanoparticles Induced by Working Conditions: A Theoretical Study. Journal of Catalysis **2002**, 207, 76-87.

(5) Lauritsen, J. V.; Nyberg, M.; Nørskov, J. K.; Clausen, B. S.; Topsøe, H.; Lægsgaard, E.; Besenbacher, F. Hydrodesulfurization reaction pathways on MoS2 nanoclusters revealed by scanning tunneling microscopy. Journal of Catalysis **2004**, 224, 94-106.

(6) Chen, Z. B.; Cummins, D.; Reinecke, B. N.; Clark, E.; Sankara, M. K.; Jaramillo, T. F. Core-Shell MoO_3-MoS_2 Nanowires for Hydrogen Evolution Reaction: A Functional Design for Electrocatalytic Materials Nano letters **2011**, 11, 4168-4175.

(7) Li, Y. G.; Wang, H. L.; Xie, L. M.; Liang, Y. Y.; Hong, G. S.; Dai, H. J. MoS_2 Nanoparticles Grown on Graphene: An Advanced Catalyst for the Hydrogen Evolution Reaction. Journal of the American Chemical Society **2011**, 133, 7296-7299.

(8) Kibsgaard, J.; Tuxen, A.; Levisen, M.; Laegsgaard, E.; Gemming, S.; Seifert, G.; Lauritsen, J. V.; Besenbacher, F. Atomic Scale Structure of Mo_6S_6 Nanowires. Nano letters **2008**, 8, 3928-3931.

(9) Helveg, S.; Lauritsen, J. V.; Lægsgaard, E.; Stensgaard, I.; Nørskov, J. K.; Clausen, B. S.; Topsøe, H.; Besenbacher, F. Atomic Scale Structure of Single Layer MoS_2 Nano Clusters. Physical Review Letters **2000**, 84, 951.

(10) Kibsgaard, J.; Lauristen, J. V.; Laesgaard, E.; Clausen, B. S.; Topsoe, H.; Besenbacher, F. Cluster-Support Interactions and Morphology of MoS_2 Nanoclusters in a Graphite-Supported Hydrotreating MOdel Catalyst. Journal of the American Chemical Society **2006**, 128, 13950-13958.

(11) Tuxen, A.; Kibsgaard, J.; Gobel, H.; Laegsgaard, E.; Topsoe, H.; Lauristen, J. V.; Besenbacher, F. Size Theshold in the Dibenzothiophene Adsorption on MoS_2 Nanoclusters Acs Nano **2010**, 4, 4677-4682.

(12) Bollinger, M.; Lauritsen, J.; Jacobsen, K.; Nørskov, J.; Helveg, S.; Besenbacher, F. One-Dimensional Metallic Edge States in MoS2. Physical Review Letters **2001**, 87.

(13) Lauritsen, J. Atomic-Scale Structure of Co–Mo–S Nanoclusters in Hydrotreating Catalysts. Journal of Catalysis **2001**, 197, 1-5.

(14) Lauritsen, J. V.; Bollinger, M. V.; Lægsgaard, E.; Jacobsen, K. W.; Nørskov, J. K.; Clausen, B. S.; Topsøe, H.; Besenbacher, F. Atomic-scale insight into structure and morphology changes of MoS2 nanoclusters in hydrotreating catalysts. Journal of Catalysis **2004**, 221, 510-522.

(15) Lauritsen, J.; Kibsgaard, J.; Olesen, G.; Moses, P.; Hinnemann, B.; Helveg, S.; Norskov, J.; Clausen, B.; Topsoe, H.; Lagsgaard, E. Location and coordination of promoter atoms in Co- and Ni-promoted MoS2-based hydrotreating catalysts. Journal of Catalysis **2007**, 249, 220-233.

(16) Lauritsen, J. V.; Kibsgaard, J.; Helveg, S.; Topsoe, H.; Clausen, B. S.; Laegsgaard, E.; Besenbacher, F. Size-dependent structure of MoS2 nanocrystals. Nature nanotechnology **2007**, 2, 53-58.

(17) Besenbacher, F.; Brorson, M.; Clausen, B. S.; Helveg, S.; Hinnemann, B.; Kibsgaard, J.; Lauritsen, J. V.; Moses, P. G.; Nørskov, J. K.; Topsøe, H. Recent STM, DFT and HAADF-STEM studies of sulfide-based hydrotreating catalysts: Insight into mechanistic, structural and particle size effects. Catalysis Today **2008**, 130, 86-96.

(18) Kibsgaard, J.; Clausen, B. S.; Topsøe, H.; Lægsgaard, E.; Lauritsen, J. V.; Besenbacher, F. Scanning tunneling microscopy studies of TiO2-supported hydrotreating catalysts: Anisotropic particle shapes by edge-specific MoS2–support bonding. Journal of Catalysis **2009**, 263, 98-103.

(19) Le, D.; Sun, D.; Lu, W.; Bartels, L.; Rahman, T. S. Single layer MoS_{2} on the Cu(111) surface: First-principles electronic structure calculations. Physical Review B **2012**, 85.

(20) Li, T.; Galli, G. Electronic Properties of MoS_2 Nanoparticles. J. Phys. Chem. C **2007**, 111, 16192-16196.

(21) Hou, P.; Meeker, D.; Wise, H. Kinetic Studies with a Sulfur-Tolerent Water Gas Shift Catalyts. J. Catal **1996**, 80, 280-285.

(22) Surisetty, V. R.; Tavasoli, A.; Dalai, A. K. Synthesis of Higher Alcohols from Syngas Over Alkali Promoted MoS_2 CAtalyts Supported on Multi Walled CArobon Nanotubes. Appl Catal A **2009**, 365, 243-251.

(23) Surisetty, V. R.; Dalai, A. K.; Kozinski, J. Alcohols as Alternative Fuels: An overview Appl Catal A-Gen **2011**, 404, 1-11.

(24) Kibsgaard, J. Atomic Scale Investigation of MoS_2 Based Hydrotreating Model Catalyst University of Aarhus, Denmark, 2008.

(25) Tenney, S. A.; He, W.; Ratliff, J. S.; Mullins, D. R.; Chen, D. A. Characterization of Pt–Au and Ni–Au Clusters on TiO2(110). Topics in Catalysis **2011**, 54, 42-55.

(26) Galhenage, R. P.; Ammal, S. C.; Yan, H.; Duke, A. S.; Tenney, S. A.; Heyden, A.; Chen, D. A. Nucleation, Growth, and Adsorbate-Induced Changes in Composition for Co–Au Bimetallic Clusters on TiO2. The Journal of Physical Chemistry C **2012**, 116, 24616-24629.

(27) Tenney, S. A.; Cagg, B. A.; Levine, M. S.; He, W.; Manandhar, K.; Chen, D. A. Enhanced activity for supported Au clusters: Methanol oxidation on Au/TiO2(110). Surface Science **2012**, 606, 1233-1243.

(28) Tenney, S. A.; Shah, S. I.; Yan, H.; Cagg, B. A.; Levine, M. S.; Rahman, T. S.; Chen, D. A. Methanol Reaction on Pt-Au Clusters on TiO_2 (110): Methoxy-induced Diffusion of Pt. J.Phys.Chem.C **2013**, 117, 26998–27006.

(29) Galhenage, R. P.; Yan, H.; Ahsen, A. S.; Ozturk, O.; Chen, D. A. Understanding the Growth and Chemical Activity of Co–Pt Bimetallic Clusters on TiO2(110): CO Adsorption and Methanol Reaction. The Journal of Physical Chemistry C **2014**, 118, 17773-17786.

(30) Petukhov, M.; Rizzi, G. A.; Domenichini, B.; Granozzi, G.; Bourgeois, S. Scanning tunneling microscopy and spectroscopy of Mo clusters grown on TiO2(110). Surface Science **2007**, 601, 3881-3885.

(31) Rawal, T. B.; Le, D.; Rahman, T. S. Effect of TiO_2 support on the adsorption of CO and NO on MoS_2: insights from ab-initio calculations. In preparation.

Appendix A. Supplemental figures for chapter 4

Average cluster heights and height distributions for Co-Au clusters of various compositions at 295 K and after heating to 800 K; and the most stable structures for the 50%M-50%Au (M=Pt, Ni, Co) bimetallic surfaces used in the DFT calculations for CO adsorption.

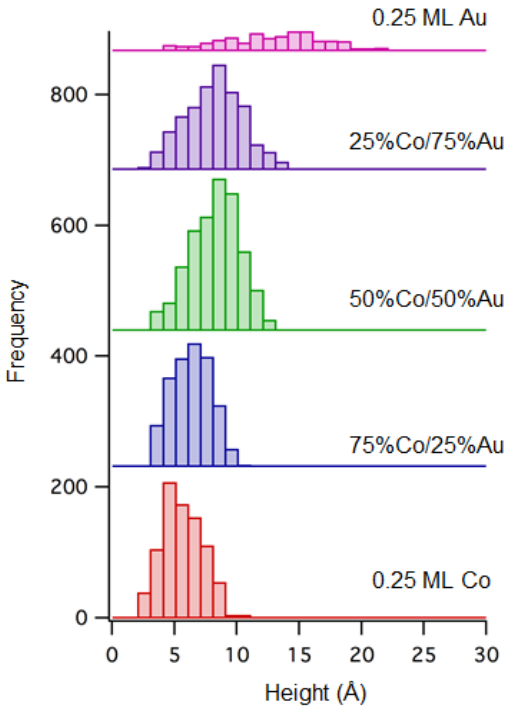

Figure A.1. Cluster height distributions for the pure and bimetallic clusters after room temperature deposition. Total coverages were all 0.25 ML. Distributions were determined by measuring all of the clusters in: 1000Å x1000Å images for the 100% Au, 25% Co and 50% Co clusters; and 500Å x1000Å images for the 100% Co and 75% Co clusters.

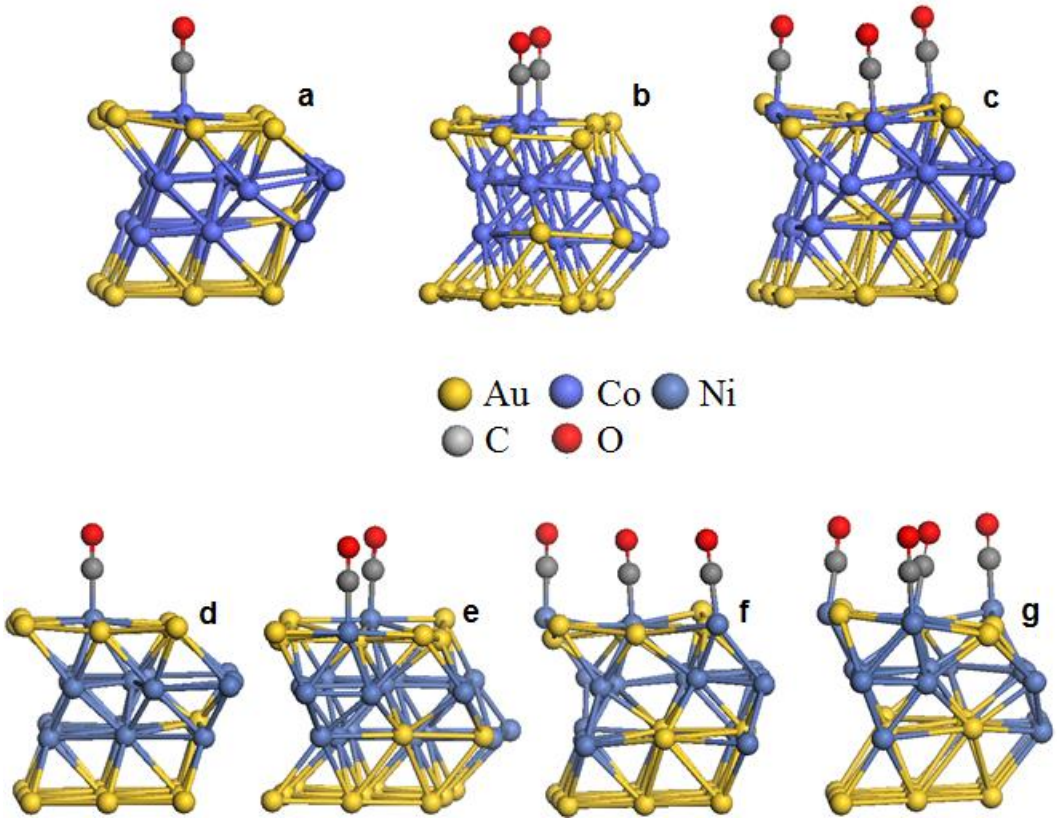

Figure A.2. The most stable structures for the 50%M/50%Au (M = Co, Ni) bimetallic surfaces in the presence of CO. (a)-(c) correspond to the structures 1Co···1CO, 2Co···2CO, and 3Co···3CO, respectively, shown in the phase diagram of Figure 11a. (d)- (g) correspond to the structures 1Ni···1CO, 2Ni···2CO, 3Ni···3CO, and 4Ni···4CO, respectively, shown in the phase diagram of Figure 11b. For all these structures, the most stable positions for the exchanged Au atoms were found to be in the third layer.

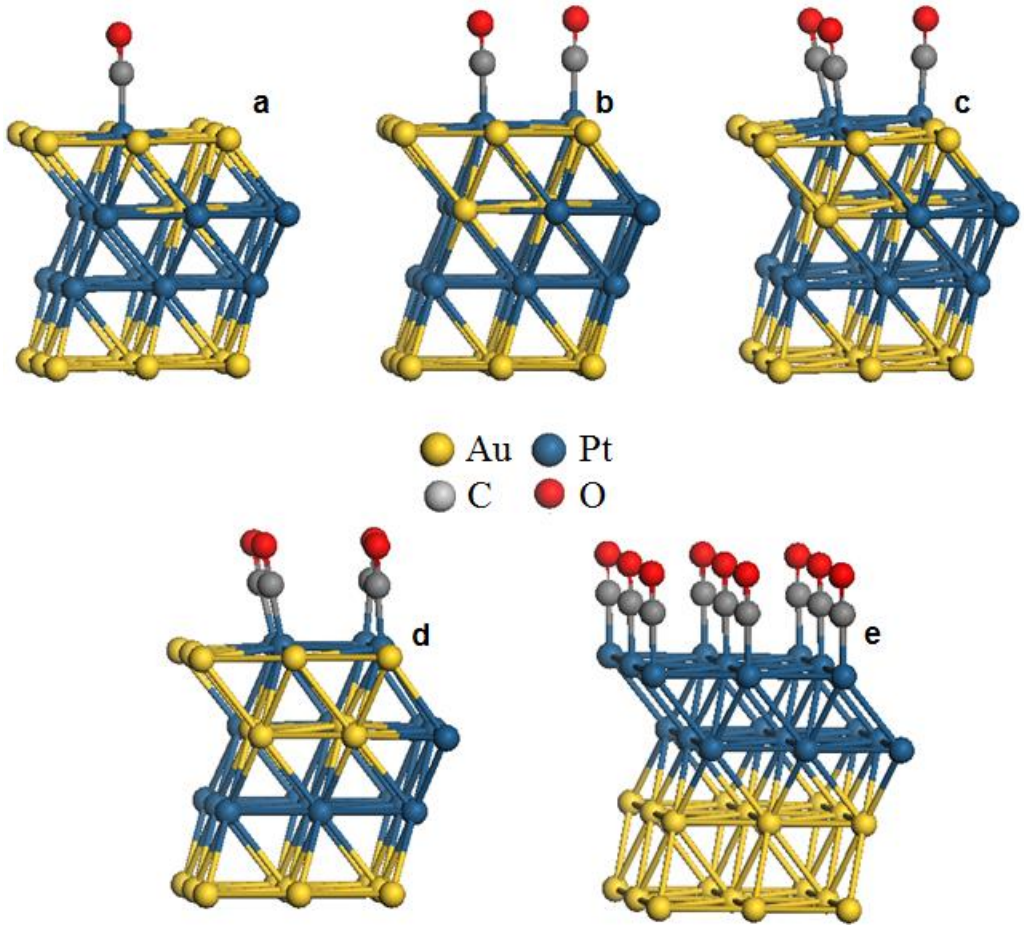

Figure A.3. The most stable structures for the 50% Pt/50% Au surface in the presence of CO. (a)-(e) correspond to the structures 1Pt⋯1CO, 2Pt⋯2CO, 3Pt⋯3CO, 4Pt⋯4CO, and 9Pt⋯9CO, respectively, shown in the phase diagram of Figure 11c. In contrast to the Co-Au and Ni-Au cases, the structures with exchanged Au atoms in the second or third layer have very similar energies. In the presence of 1ML CO (9CO), the structure with all Pt atoms in the first two layers becomes more stable due to the strong Pt-Pt and Pt-CO bonds.

Appendix B. Supplemental figures for chapter 7

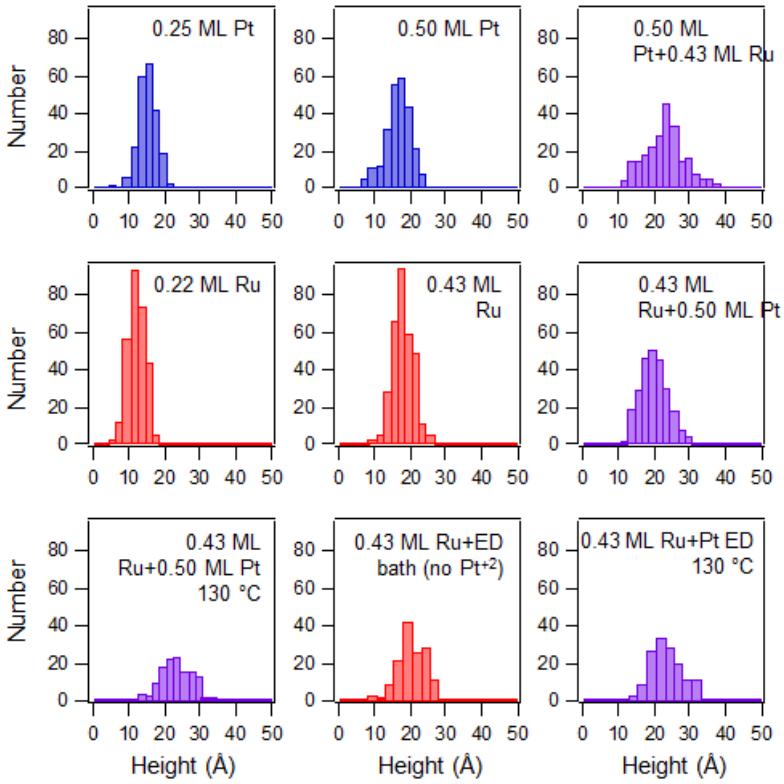

Figure B.1. Histograms of cluster heights for various metals on modified HOPG (m-HOPG). Surfaces exposed to the ED baths were heated to 130 °C for 3 min.

Appendix C. Permission to reprint: chapter 3

1/12/2015 Rightslink® by Copyright Clearance Center

Home Account Info Help Live Chat

Title: Understanding the Nucleation and Growth of Metals on TiO2: Co Compared to Au, Ni, and Pt

Logged in as: Randima Galhenage

LOGOUT

Author: Randima P. Galhenage, Hui Yan, Samuel A. Tenney, et al

Publication: The Journal of Physical Chemistry C

Publisher: American Chemical Society

Date: Apr 1, 2013

PERMISSION/LICENSE IS GRANTED FOR YOUR ORDER AT NO CHARGE

This type of permission/license, instead of the standard Terms & Conditions, is sent to you because no fee is being charged for your order. Please note the following:

- Permission is granted for your request in both print and electronic formats, and translations.
- If figures and/or tables were requested, they may be adapted or used in part.
- Please print this page for your records and send a copy of it to your publisher/graduate school.

Appropriate credit for the requested material should be given as follows: "Reprinted

(adapted) with permission from (COMPLETE REFERENCE CITATION). Copyright (YEAR) American Chemical Society." Insert appropriate information in place of the capitalized words.

- One-time permission is granted only for the use specified in your request. No additional uses are granted (such as derivative works or other editions). For any other uses, please submit a new request.

BACK CLOSE WINDOW

Appendix D. Permission to reprint: chapter 4

1/12/2015 Rightslink® by Copyright Clearance Center

RightsLink®

Home | Account Info | Help | Live Chat

Title: Nucleation, Growth, and Adsorbate-Induced Changes in Composition for Co–Au Bimetallic Clusters on TiO2

Randima Galhenage

LOGOUT

Author: Randima P. Galhenage, Salai C. Ammal, Hui Yan, et al

Publication: The Journal of Physical Chemistry C

Publisher: American Chemical Society

Date: Nov 1, 2012

PERMISSION/LICENSE IS GRANTED FOR YOUR ORDER AT NO CHARGE

This type of permission/license, instead of the standard Terms & Conditions, is sent to you because no fee is being charged for your order. Please note the following:

- Permission is granted for your request in both print and electronic formats, and translations.
- If figures and/or tables were requested, they may be adapted or used in part.
- Please print this page for your records and send a copy of it to your publisher/graduate school.

Appropriate credit for the requested material should be given as follows: "Reprinted

(adapted) with permission from (COMPLETE REFERENCE CITATION). Copyright (YEAR) American Chemical Society." Insert appropriate information in place of the capitalized words.

- One-time permission is granted only for the use specified in your request. No additional uses are granted (such as derivative works or other editions). For any other uses, please submit a new request.

BACK CLOSE WINDOW

Appendix E. Permission to reprint: chapter 5

1/12/2015 Rightslink® by Copyright Clearance Center

Logged in as:

Randima Galhenage

LOGOUT

Title: Understanding the Growth and Chemical Activity of Co–Pt Bimetallic Clusters on TiO2(110): CO Adsorption and Methanol Reaction

Author: Randima P. Galhenage, Hui Yan, Ali S. Ahsen, et al

Publication: The Journal of Physical Chemistry C

Publisher: American Chemical Society

Date: Aug 1, 2014

- Permission is granted for your request in both print and electronic formats, and translations.
- If figures and/or tables were requested, they may be adapted or used in part.
- Please print this page for your records and send a copy of it to your publisher/graduate school.

Appropriate credit for the requested material should be given as follows: "Reprinted (adapted) with permission from (COMPLETE REFERENCE CITATION). Copyright (YEAR) American Chemical Society." Insert appropriate information in place of the capitalized words.

- One-time permission is granted only for the use specified in your request. No additional uses are granted (such as derivative works or other editions). For any other uses, please submit a new request.

BACK CLOSE WINDOW